V. 122, NO. 1
JANUARY 2025

ACI MATERIALS JOURNAL

A JOURNAL OF THE AMERICAN CONCRETE INSTITUTE

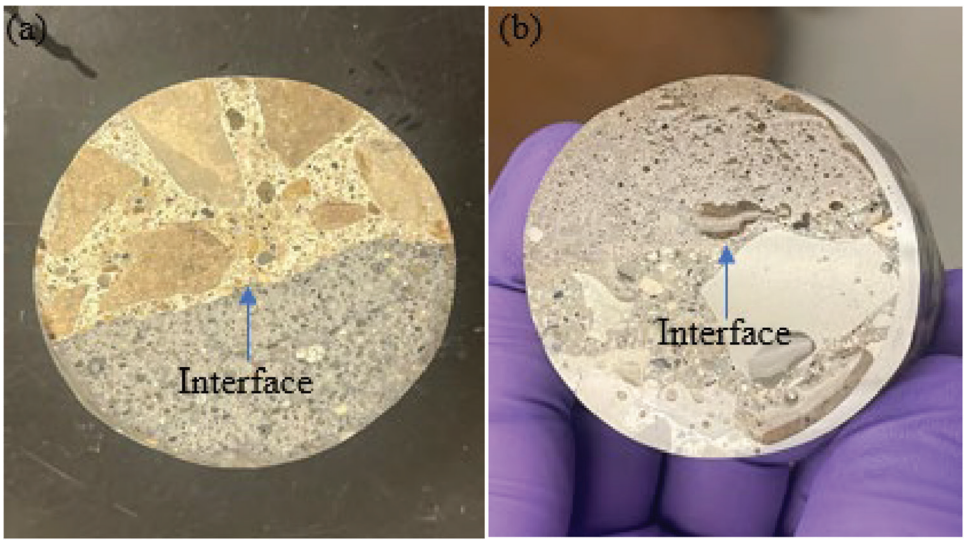

American Concrete Institute

CONTENTS

PRINTED WITH SOY INK

ACI MATERIALS JOURNAL

JANUARY 2025, V. 122, NO. 1

A JOURNAL OF THE AMERICAN CONCRETE INSTITUTE
AN INTERNATIONAL TECHNICAL SOCIETY

The *ACI Materials Journal* (ISSN 0889-325x) is published bimonthly by the American Concrete Institute. Publication office: 38800 Country Club Drive, Farmington Hills, MI 48331. Periodicals postage paid at Farmington, MI, and at additional mailing offices. Subscription rates: $210 per year, payable in advance. POSTMASTER: Send address changes to: *ACI Materials Journal*, 38800 Country Club Drive, Farmington Hills, MI 48331.

Canadian GST: R 1226213149.

Direct correspondence to 38800 Country Club Drive, Farmington Hills, MI 48331. Telephone: +1.248.848.3700.
Website: http://www.concrete.org.

MEETINGS

FEBRUARY 2025

10-13—2025 ACPA Pipe School, Columbus, OH, https://pipeschool.org

12-13—Canadian Concrete Expo, Toronto, ON, Canada, https://canadianconcreteexpo.com

MARCH 2025

9-11—2025 ASA Shotcrete Convention and Technology Conference, Savannah, GA, www.shotcrete.org/convention

16-18—ACPA 2025 Annual Business Meeting, Isle of Palms, SC, www.concretepipe.org/events

23-28—RILEM Spring Convention & Conference on Durability of Building Materials and Systems in the Transportation Infrastructure, Mendrisio, Switzerland, www.rilem.net/agenda/rilem-spring-convention-confernece-on-durability-of-building-materials-and-systems-in-the-transportation-infrastructure-1532

APRIL 2025

7-9—CRSI 2025 Spring Business & Technical Meeting, Atlanta, GA, www.crsi.org/event/2025-spring-business-technical-meeting

7-13—bauma 2025, Munich, Germany, https://bauma.de/en/trade-fair

13-16—2025 ICRI Spring Convention, Austin, TX, www.icri.org/event/2025-icri-spring-convention

14-16—The Masonry Society 2025 Spring Meeting, Spokane, WA, https://masonrysociety.org/event/2025-spring-meeting

14-17—International Conference on Advances in Structural and Geotechnical Engineering (ICASGE'25), Hurghada, Egypt, https://icasge.conferences.ekb.eg

17—Concrete Durability and Structural Integrity, Beirut, Lebanon, https://acts-int.com/conferences/Concrete-Durability-and-Structural-Integrity

MAY 2025

4-7—2025 PTI Spring Convention, Phoenix, AZ, www.post-tensioning.org/events/conventions.aspx

12-14—11th International Conference on Analytical Models and New Concepts in Concrete and Masonry Structures (AMCM 2025), Łódź, Poland, www.amcm2024.p.lodz.pl/index2.php

14-16—2025 International *fib* Symposium on Conceptual Design of Concrete Structures, Rio de Janeiro, Brazil, https://fib.abece.com.br

ACI CONCRETE CONVENTION: FUTURE DATES

2025—Mar. 30-Apr. 2, Sheraton Centre Toronto Hotel, Toronto, ON, Canada
2025—October 26-29, Hilton Baltimore & Baltimore Marriott Inner Harbor, Baltimore, MD
2026—Mar. 29-Apr. 1, Hyatt Regency O'Hare Chicago, Rosemont/Chicago, IL
2026—Oct. 11-14, Hilton Atlanta, Atlanta, GA

For additional information, contact:
Event Services, ACI
38800 Country Club Drive
Farmington Hills, MI 48331
Telephone: +1.248.848.3795
email: conventions@concrete.org

ON FRONT COVER: 122-M05, p. 56, Fig. 6—Polished samples: (a) concrete-cementitious grout; and (b) concrete-epoxy grout.

Contributions to *ACI Materials Journal*

The *ACI Materials Journal* is an open forum on concrete technology and papers related to this field are always welcome. All material submitted for possible publication must meet the requirements of the "American Concrete Institute Publication Policy" and "Author Guidelines and Submission Procedures." Prospective authors should request a copy of the Policy and Guidelines from ACI or visit ACI's website at **www.concrete.org** prior to submitting contributions.

Papers reporting research must include a statement indicating the significance of the research.

The Institute reserves the right to return, without review, contributions not meeting the requirements of the Publication Policy.

All materials conforming to the Policy requirements will be reviewed for editorial quality and technical content, and every effort will be made to put all acceptable papers into the information channel. However, potentially good papers may be returned to authors when it is not possible to publish them in a reasonable time.

Discussion

All technical material appearing in the *ACI Materials Journal* may be discussed. If the discussion is received within four months of the paper's print publication, it will appear in the issue dated ten months from this journal's date. Discussion material received after specified dates will be considered individually for publication or private response. ACI Standards published in ACI Journals for public comment have discussion due dates printed with the Standard. Discussion should be complete and ready for publication, including finished, reproducible illustrations. Discussion must be confined to the scope of the paper and meet the ACI Publication Policy.

Follow the style of the current issue. Discussions should not exceed 1800-word equivalents (illustrations and tables count as 300 words each). References should be complete. Do not repeat references cited in original paper; cite them by original number. Numbering of additional references, figures, tables, and equations should follow sequentially from the original manuscript throughout the discussion. The discusser must indicate the month, year, volume number, issue number, authors' names, and manuscript number of the original manuscript. Closures responding to a single discussion should not exceed 1800-word equivalents in length, and to multiple discussions, approximately one half of the combined lengths of all discussions. Closures are published together with the discussions.

Discuss the paper, not some new or outside work on the same subject. Use references wherever possible instead of repeating available information.

Discussion offered for publication should offer some benefit to the general reader. Discussion which does not meet this requirement will be returned or referred to the author for private reply.

Send manuscripts to:
http://mc.manuscriptcentral.com/aci

Send discussions to:
Journals.manuscripts@concrete.org

ACI MATERIALS JOURNAL TECHNICAL PAPER

Title No. 122-M01

Improving Fatigue Properties of Reinforcing Steel Bars

by J. Gonzalez, S. S. K. Dolati, A. Suselo, D. Stalheim, A. Araujo, and W. M. Ghannoum

Low-cycle fatigue and monotonic tension tests were performed on steel reinforcing bars microalloyed using niobium and vanadium and processed by various hot-rolling and post-rolling cooling production strategies. The objective was to identify beneficial alloy designs and production techniques that deliver cross-diameter microstructures at different strength levels with improved fatigue properties. Bars were sourced from the United States and China to represent a range of alloy designs and production methods common in those countries. Parameters considered included the microalloying content of vanadium (V) and/or niobium (Nb), carbon content (C), overall alloy content (CE), hot-rolling/post-rolling cooling strategies, microstructures/grain size, stress-strain tensile curve shape, hardness, and rib geometry. Ferrite fraction and grain size, average cross-section hardness, and bar deformations were found to be influential on fatigue life. Bar chemistries and processing techniques that result in increased ferrite fraction and reduced grain size are recommended to improve the low-cycle fatigue performance of reinforcing bars.

Keywords: low-cycle fatigue; microalloying (MA); niobium (Nb); reinforcing bars.

INTRODUCTION

Even in modern seismically designed structures, seismic hazards can lead to extensive damage that can hinder the recovery of communities after an earthquake event (Eguchi et al. 2012; Zaki 2020). Reinforced concrete structures in seismic regions are designed such that reinforcing bars dissipate energy from seismic waves through relatively large inelastic deformations. In seismically detailed concrete structures, adequate confinement of concrete reduces the likelihood of concrete degradation during strong earthquake motions, whereby ultimate loss of strength often initiates due to fracture of longitudinal bars or lateral instability (Zhong et al. 2021). Recent studies quantifying the low-cycle (high-strain) fatigue performance of reinforcing bars in production in the United States have shown fatigue lives that can be an order of magnitude different from one manufacturing process (MP) to another (Ghannoum and Slavin 2016; Slavin and Ghannoum 2015; Sokoli et al. 2019). This is despite bars satisfying ASTM A706/A706M-16 (2016) specifications for the seismic grade of reinforcing bars and being produced at an equivalent cost. These findings are prompting a closer look at reinforcing bar steel production strategies, with the goal of identifying the strategies that achieve improved fatigue performance in reinforcing bars, particularly under inelastic strain demands. Ultimately, the work aims to guide the industry in alloy and processing strategies that improve the fatigue life of reinforcing bars without appreciably increasing production costs.

A national effort is underway focused on enhancing the seismic performance of infrastructure, moving practice from targeting the most basic collapse prevention performance objective to investigating means to achieve post-event functional recovery (Sattar et al. 2021). Within the functional recovery performance objective, structures would be designed not only to survive a seismic event but also to sustain limited damage such that they can be returned to full operation within a short time frame. Reinforcing bars with improved fatigue life can result in delayed bar fractures in structures subjected to major earthquakes (Zhong et al. 2021), which reduces the likelihood of seismic collapse while also improving post-event outcomes, such as damage extent and resistance to aftershocks. Therefore, improvements to the fatigue life of reinforcing bars, the primary energy dissipation elements in concrete structures, have the potential to move closer to the functional recovery objective without triggering disruptive changes in construction practices or additional costs.

While traditional reinforcing bars in the United States typically comprise relatively high amounts of carbon and manganese (Mn), high concentrations of these elements can lead to a loss of ductility, resulting in brittle failures (Slavin and Ghannoum 2015). To limit this detrimental effect, the chemical composition of the reinforcing bars can be altered by decreasing concentrations of deleterious chemicals and adding other elements, such as niobium (Nb), that can have a beneficial impact on strength and ductility properties. Nb is commonly used as an alloying element to improve steel performance in a wide range of industries requiring metallurgy that delivers high strength and ductility. In the aviation industry, Nb alloys have been used to provide aircraft shells with higher temperature capabilities and reduced weight (Heisterkamp and Carneiro 2001). Adding relatively small amounts of Nb, along with other elements such as vanadium (V), also tends to increase the strength of steel, a process often referred to as microalloying (MA). When Nb is added to steel, it can considerably improve structurally desirable properties, with superior strength, ductility, toughness, and weldability (Davis 2001). Additionally, it can enhance hardenability, which can compensate for strength reductions when lower carbon and manganese levels are used (Jansto 2010). Given the emergence of Nb as a beneficial alloy in different industries, attempts by the construction industry are

ACI Materials Journal, V. 122, No. 1, January 2025.

MS No. M-2023-139.R2, doi: 10.14359/51743282, received September 26, 2024, and reviewed under Institute publication policies.

ongoing to implement it effectively in reinforcing bars, with particular emphasis on improving bar toughness and fatigue life.

RESEARCH SIGNIFICANCE

The effects of different industrial production strategies, coupled with Nb chemistries, on the mechanical properties of steel reinforcing bars, especially ductility and low-cycle fatigue, were investigated. Monotonic tension-test properties and low-cycle fatigue properties were measured for 18 different production variations. In addition, bar microstructures and fracture-surface analyses were quantified. Bars were sourced from within and outside the United States to expand the range of test parameters. Bar chemistry and microstructural properties influencing fatigue life were identified. Recommendations for key alloy, processing, and microstructural features to improve the low-cycle fatigue performance of reinforcing bars are provided.

BACKGROUND

Low-cycle fatigue performance of reinforcing bars

The phenomenon of weakening of a material as the result of repeated load cycles, or material fatigue, can be the cause of critical failures or collapses in structures (Sokoli and Ghannoum 2016; Sokoli et al. 2020; To and Moehle 2020; Zhong et al. 2021). Low-cycle fatigue occurs due to a relatively low number of cycles at relatively large inelastic strain demands that are typical under earthquake loading. The low-cycle fatigue behavior of reinforcing bars, which are used in concrete construction, has been shown to be influenced by several variables, summarized as follows.

Bar buckling was found to increase strain demands and concentration in bars and lead to a lower fatigue life than bars that do not buckle under inelastic demands (Restrepo-Posada et al. 1994; Sokoli and Ghannoum 2016; Sokoli et al. 2020). Strain amplitude was found to have a linear relation with the number of cycles to fracture in log space (Brown and Kunnath 2004; Sokoli et al. 2020). Bar size was also found to influence fatigue life (Brown and Kunnath 2004), even when chemistries were not altered.

Ghannoum and Slavin (2016) and Sokoli et al. (2019) investigated the fatigue life of Grade 60 (60 ksi [420 MPa]) to Grade 100 (100 ksi [690 MPa]) reinforcing steel bars by conducting low-cycle fatigue air tests. Bars from several mills using the typical U.S. production methods were tested, including quenching and tempering (QT) and microalloying (MA). Correlations were identified between the fatigue life of bars and various bar parameters, including deformation patterns, production methods, bar strength, buckling length, strain amplitude, and chemical compositions.

Previous research on the effects of bar deformations has shown that abrupt changes in the geometrical form of deformations cause stress concentrations on the surface of a bar (Jhamb and MacGregor 1974a; Fei and Darwin 1999; Ghannoum and Slavin 2016). These concentrations have been found to have a pronounced influence on the initiation of fatigue cracks (Hanson et al. 1968). Jhamb and MacGregor (1974b) showed that the ratio of the radius at the base of a rib (r) to the rib height (h) had the most pronounced effect on stress concentrations. The value of the stress concentration factor decreased with an increase in r/h value. Zheng and Abel (1998) observed that bars with transverse ribs normal to the bar axis had a lower fatigue life than bars with ribs angled to the bar axis. Furthermore, they found that stress concentrations increase as the rib spacing approaches zero. Burton (1965) conducted fatigue tests on bars in concrete beams, which indicated that the maximum stress concentrations and fracture initiation occurred at the junction between bar longitudinal and transverse ribs.

However, although bar deformations are known to have a significant impact on fatigue life, international reinforcing bar specifications, such as ASTM A706/A706M and GB/T 1499.2-2018 (2018), can differ greatly in rib design/geometry requirements.

Metallurgy of reinforcing bars

The strength, ductility, and fatigue toughness of reinforcing bars are primarily derived from the cross-diameter final grain/packet size, homogeneity of that grain/packet size, and the final microstructural phase volume fraction that is produced (Stalheim et al. 2021). Specifically, for a given cross-diameter microstructure, strength is driven by the average grain/packet size, while ductility is driven by the average grain/packet size plus homogeneity (Isasti et al. 2014a,b). Due to the influence of cross-diameter properties, hot-rolling temperatures and post-rolling cooling rates in bars of different diameters can influence their fatigue performance (Stalheim et al. 2021).

Chemistry design and processing design strategy/capability (total hot-rolling deformation and temperature followed by post-rolling cooling using either air or water) determine the final cross-diameter grain/packet size, homogeneity of that grain/packet size, and the final microstructural phase volume fraction. Hot-rolling deformation strategies coupled with the temperature result in the refinement and homogeneity of the cross-sectional austenite grain-size evolution. The final cooling rate determines the final ferrite grain size, microstructural phases, and, in some cases, the cross-sectional homogeneity (Enloe et al. 2020; Subramanian 2007).

Stable higher strength properties are metallurgically influenced by finer grain/packet size, good homogeneity, and harder microstructural phases. Optimum ductility properties, such as elongation, fracture toughness, low-cycle fatigue, and formability/bendability, are also metallurgically influenced by finer final grain/packet size and homogeneity but with a minimum of harder microstructural phases. Therefore, optimizing the aforementioned cross-diameter properties is required to achieve the desired combinations of strength and ductility properties.

Typical chemistry design for reinforcing bar strengths up to 80 ksi (550 MPa) yield strength and processed through hot rolling followed by post-rolling cooling in air and/or light water cooling consists of carbon in the 0.20 to 0.40 wt. % range, manganese in the 1.00 to 1.60 wt. % range, silicon in the 0.15 to 0.80 wt. % range, and microalloy additions of either V in the 0.020 to 0.050 wt. % range or Nb (columbium) in the 0.010 to 0.025 wt. % range (Zhang et al. 2018).

The amounts of carbon, manganese, or silicon used are driven by the steel production routes of either basic oxygen furnace (BOF) melt or electric arc furnace (EAF) scrap melt. BOF melt with low residuals of copper, nickel, chromium, and molybdenum tends to use higher levels of manganese and silicon, while EAF scrap melt, which contains relatively high residual levels of copper, nickel, chromium, and molybdenum, tends to use lower levels of manganese and silicon. Carbon equivalent (CE), as measured by the International Institute of Welding (IIW), typically ranges from 0.45 to 0.60. These chemistry designs plus processing strategies result in microstructural phases predominately ferritic with various volume fractions of pearlite depending on carbon/manganese (C/Mn) content and post-rolling cooling rate. However, higher overall CE and/or the presence of larger than desired austenite grain size prior to transformation, depending on post-rolling cooling rate, can result in an increase in higher-hardness bainitic microstructural phases, which can reduce the ductility performance of the cross-sectional microstructure. Thermomechanical controlled processing (TMCP) followed by post-rolling water cooling has recently been developed and implemented in reinforcing bar production. TMCP hot deformation results in controlling key per-pass temperatures and deformations using strain-induced Nb precipitation to retard the austenite recrystallization evolution, resulting in a finer austenite grain size entering the post-rolling water cooling. This hot-rolling and post-rolling water cooling results in an improvement (finer and more homogeneous) in cross-sectional ferrite/pearlite grain size, which can achieve strength and improved ductility performance. TMCP has typically been used in high-strength steel, with optimum ductility performance in flat products, and has now been developed and implemented into reinforcing bar equipment design. One of the bar batches tested in this study was produced using TMCP.

Reinforcing bar producers using quenching and self-tempering (QST) post-rolling cooling processing typically use carbon, manganese, and silicon only, regardless of the steel production melting method, to achieve the desired strength levels. Occasionally, V microalloying may be used, but it is not typical in this processing design. This process results in the formation of a self-tempered martensitic shell around a ferrite/pearlite core (Rocha et al. 2016). While this cross-sectional microstructure results in the desired strength, the ductility can be significantly decreased by the presence of the harder microstructural phases versus that of the other reinforcing bar metallurgical production routes. Due to this potential for reduction in ductility performance, the Chinese reinforcing bar standard GB/T 1499.2-2018, developed after the devastating 2008 Sichuan earthquake in China, does not allow for QST type of cross-sectional metallurgy/microstructural phase features to be used.

As can be seen from the various alloy/processing strategies, various levels of cross-sectional grain-size fineness and homogeneity can be achieved. Adding post-rolling water cooling improves the fineness of the cross-sectional grain size, and implementing TMCP hot rolling using Nb plus post-rolling water cooling further refines the cross-sectional grain size and improves the homogeneity. Improved cross-sectional grain-size fineness and homogeneity, along with the desired microstructural phases, will improve important ductility performance properties of fatigue and formability/dependability in reinforcing bars used in concrete structural members.

EXPERIMENTAL PROGRAM

The experimental program focused on evaluating production strategies and their effect on the low-cycle fatigue performance of reinforcing bars and, hence, on their total energy dissipation potential. Parameters considered include the MA content of V and/or Nb, the hot-rolling/cooling strategy implemented in production, and rib geometry. Bars were sourced from the United States and China to capture a wider range of production methods. The experimental design of this study purposely replicates research done by Ghannoum and Slavin (2016) and Sokoli et al. (2019) to provide direct behavioral comparisons between bars of common production in the United States and bars of experimental chemistries (particularly using Nb) and processing strategies.

Three test phases were conducted. In the first phase, 16 production permutations were tested under monotonic tension and inelastic cyclic loading. In the second phase, No. 5 (5/8 in. [16 mm]) bars of Phase 1 were machined to remove their bar deformations and were cycled inelastically. Phase 2 testing allowed more direct investigation of the effects of microstructure on fatigue life by removing the effects of bar deformations. In Phase 3, an additional fifth batch produced in the United States was investigated, with altered chemistry aimed at improving grain refinement and fatigue life. Additional details about the testing program and results can be found in Gonzalez (2022).

Directly controlled parameters

The parameters that were controlled were: 1) MP strategy; 2) steel grade or strength; 3) bar size; 4) unbraced or clear span of bars; 5) strain protocol; and 6) chemical composition.

Manufacturing process—Low-cycle fatigue tests were performed on bars produced from four different MPs. MP 1 is representative of the current production methods in the United States using MA. MPs 2, 3, and 4 are representative of production methods in China. MP 1 used an EAF melting process with post-rolling air cooling. MP 2 used a BOF melting process with post-rolling water cooling. MP 3 used a TMCP that consisted of two stages in a series: controlled rolling and a subsequent accelerated cooling process. MP 4 used a BOF melting process with post-rolling air cooling, similar to MP 1.

Steel grade or strength—Two different grades of steel were tested for MP 1: Grades 60 and 80 ksi (420 and 550 MPa) bars satisfying ASTM A615/A615M-16 (2016) and ASTM A706/A706M-16 were tested. The term "grade" is used to refer to the specified yield strength of a reinforcing bar in ksi. For MP 2, 3, and 4, steel grades were HRB400 and HRB500. HRB stands for hot-rolled ribbed bars with reinforcing bar yield strengths of 58 ksi and 72 ksi (400 MPa and 500 MPa), respectively.

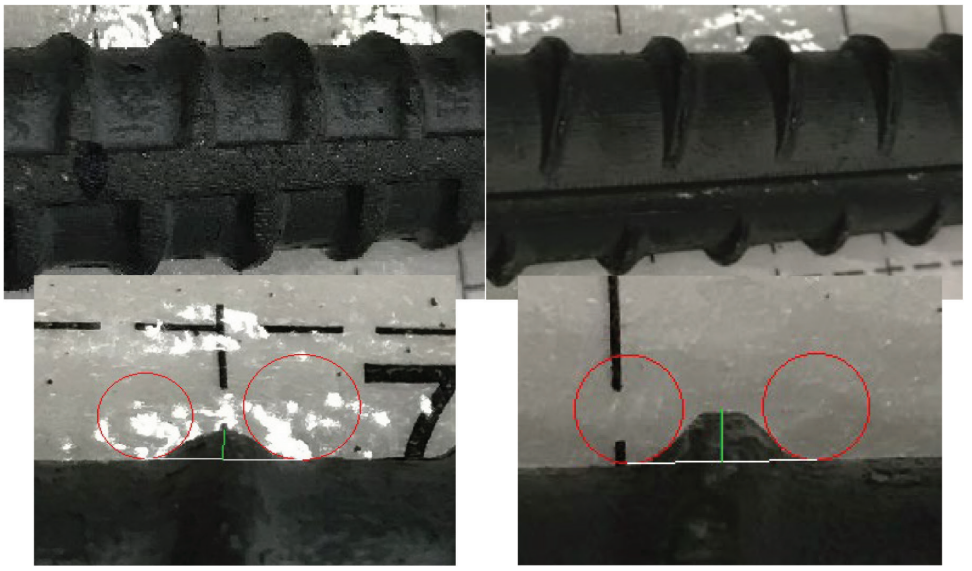

Fig. 1—Bar deformation geometries and base radii for: (left) MP 1; and (right) MPs 2 to 4.

Bar size—Two common bar sizes used in concrete building structures were tested. No. 5 bars having a diameter of 5/8 in. (16 mm) were selected to represent bars typically used as transverse reinforcement, and No. 8 bars (1 in. [25 mm] diameter) were chosen to represent longitudinal reinforcement.

Unbraced or clear span of bars—Bars were gripped at two clear spans: $4d_b$ and $6d_b$ (where d_b is the nominal bar diameter) to explore the interactions between bar buckling and low-cycle fatigue performance.

Strain protocol—Tests were conducted with a partially reversed cyclic loading protocol bound by a compression strain of –1% and a larger tension strain of +4%. This loading protocol is representative of the strains experienced in longitudinal bars of concrete frame members sustaining large inelastic deformations (Slavin and Ghannoum 2015; Sokoli et al. 2019).

Chemical composition—Manufacturer mill reports indicated the percent composition of 11 elements in the steel: carbon, Nb, manganese, phosphorus, sulfur, silicon, copper, nickel, chromium, molybdenum, and V. When these elements were alloyed, focus was primarily placed on the Nb. Nb content ranged from 0.002 to 0.024% (based on weight). One notable difference is that Chinese bar production limits carbon content to 0.25% for HRB400 and HRB500 (GB/T 1499.2-2018), while ASTM A706/A706M-16 allows more carbon, limiting its content to 0.30%.

Non-controlled parameters

Bar deformations, or ribs, varied based on MP and region of manufacture but were not controlled directly in the study. The surface geometry differed between U.S. production (MP 1) and Chinese production due to the applicable specifications. The ASTM A706/A706M-16 and GB/T 1499.2-2018 specifications provide dimensions and allowable deviations for the spacing of traverse ribs, angle of rib inclinations, and rib heights.

MP 1 bars had angled transverse ribs that met a longitudinal rib along the bar axis, as stated in ASTM A706/A706M-16. The measured rib angle ranged between 45 and 70 degrees from the longitudinal axis. MPs 2 to 4 bars also had angled transverse ribs with angles ranging between 45 and 70 degrees. MP 1 transverse ribs intersected longitudinal ribs without tapering, while the transverse ribs of MPs 2 to 4 bars gradually terminated before intersecting the longitudinal rib (Fig. 1).

The majority of MP 1 bars had relatively large rib base radius (r) to rib height (h) compared to the other bars. As seen in Fig. 1, the U.S.-manufactured bars display a soft curvature at the base of the deformations, thus yielding higher r values. On the other hand, Chinese-manufactured bars display a sharper curvature at the base of the deformations, resulting in relatively lower r values. An exception to this was observed from MP 2 batch 02 (m2_02_D400Nb#8). It is believed that this batch had a production error.

Indirectly controlled parameters

As a result of attempting to directly control MA chemistries and production methods, the microstructural characteristics of bars and their hardness values were affected indirectly.

Microstructural properties—Light optical microscopy (LOM) was used to analyze microstructural details and inclusions in the bars tested in this study. Bars were prepared and polished to a fine, mirror-like finish conforming to ASTM F728-81 (2003). To reveal grain boundaries and phases, chemical solutions known as etchants were used. Phase fraction measurements were performed considering ferrite and pearlite. The remainder of the constituents, quantified as "others," consisted of bainite, acicular ferrite, and/or martensite-austenite phases. Ferrite grain sizes were measured for all bars except bars that had low fractions present in their microstructure. The microstructural properties of Phase 1 bars are summarized in Table 1.

In addition, a microstructural characterization was performed on sample bars through a field-emission gun scanning electron microscope (FEG-SEM). Four representative samples from each manufacturer were analyzed. Analyses

Table 1—Microstructural properties of bars

MP	Batch No.	Grade	Microalloying	Bar size	Ferrite fraction, %	Pearlite fraction, %	Other phases, %	Ferrite diameter grain size mills (μm)
1	01	80	Nb + V	No. 5	51.1	48.2	0	0.31 (8)
	01	80	Nb + V	No. 8	53	47	0	0.39 (9.9)
	02	60	Nb	No. 5	23.2	35.5	41.3	—
	03	60	Nb	No. 5	38.4	48.9	12.7	0.30 (7.7)
	03	60	Nb	No. 8	35.8	57.2	7	0.41 (10.5)
	04	60	Nb	No. 5	32.2	32.8	35	—
	04	60	Nb	No. 8	32.3	31.4	36.3	—
2	01	400	Nb	No. 5	55.3	41.1	3.7	0.32 (8.1)
	02	400	Nb	No. 8	49.4	46	4.5	0.36 (9.2)
	03	500	Nb + V	No. 5	39.2	60.6	0	0.24 (6)
	03	500	Nb + V	No. 8	44.6	55.4	0	0.31 (8)
3	01	400	Nb	No. 5	59.2	40.8	0	0.28 (7.2)
4	01	400	V	No. 5	56.7	43.4	0	0.28 (7.2)
	01	400	V	No. 8	58.3	41.7	0	0.32 (8.2)
	02	500	V	No. 5	51.5	48.5	0	0.35 (8.9)
	02	500	V	No. 8	54.4	45.6	0	0.24 (6.1)

Note: No. 5 bars are 5/8 in. (16 mm) diameter; No. 8 bars are 1 in. (25 mm) diameter.

were conducted to identify phase distribution in the various alloys as well as associated grain sizes.

At low magnifications, the MP 1 bars displayed mainly ferritic and pearlitic microstructure (Fig. 2), in accordance with the measurements from the optical micrograph. However, at higher magnifications, the presence of other phases, such as martensite-austenite (M/A), phases of considerable size were detected (Fig. 2).

Similarly, at low magnifications, MP 2 exhibited mainly ferritic and pearlitic microstructure, while at higher magnifications, the presence of M/A islands was detected. Both MP 3 and MP 4 microstructures were observed to be ferritic and pearlitic. At higher magnifications, the presence of M/A islands was very scarce for both manufacturers.

The presence of M/A and acicular constituents in MPs 1 and 2 agrees with the lower yield plateau length detected in the monotonic tensile tests (Pang et al. 1981).

The microstructural properties of bars tested in Phase 1 are shown in Table 1. Overall, higher percentages of ferrite fraction were observed in MPs 2 to 4, while MP 1 had the lowest ferrite fraction percentage and highest pearlite and "Other" fraction percentages.

Hardness—Hardness was measured over the cross section for each bar type by performing a Vickers hardness traverse test following ASTM E92-17 (2017). The unit of hardness derived from the test is known as the Vickers Pyramid Number (HV). The higher the HV value, the higher the resistance at the bar surface.

Monotonic tension tests

Monotonic tension tests were conducted to identify the material properties of the steel bars and explore correlations with fatigue life. The tests were performed conforming to the procedures specified in ASTM A370-16 (2016) and ASTM E8/E8M-16a (2016). The material properties obtained from the stress-strain response include yield strength, tensile strength, elastic modulus, yield strain, hardening strain, yield plateau length, uniform strain, and fracture strain. Hardening strain was defined as the strain at which the stress first reaches 1% over yield. The yield plateau length was calculated by subtracting the hardening strain from the yield strain. Uniform strain was defined as the strain at tensile strength and was calculated in accordance with ASTM E8/E8M-16a. Lastly, the ratio of the tensile strength to yield

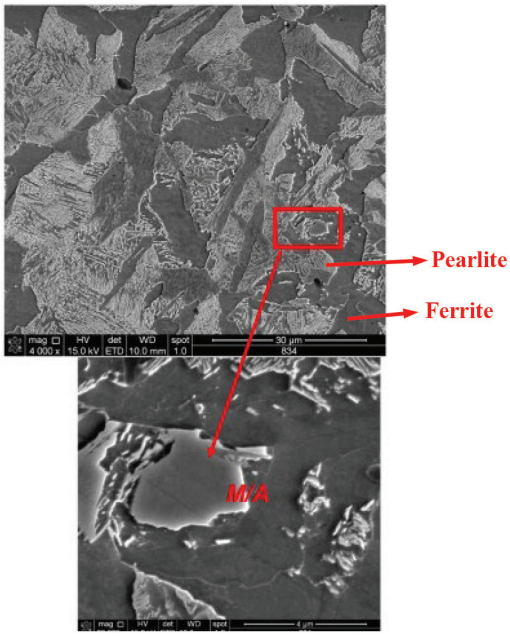

Fig. 2—FEG-SEM analysis for MP 1.

strength (T/Y) and the ratio of the fracture strain to uniform strain (F/U) were calculated from the monotonic test data.

Low-cycle fatigue tests

Cyclic testing to inelastic strain demands was conducted similarly to work by Ghannoum and Slavin (2016) and Sokoli et al. (2019). Specimens were cycled until fracture occurred. All the specimens selected did not contain bar markings. If bar fracture occurred at or near the gripping mechanisms, the test was deemed unsuccessful and removed from subsequent analysis. All cyclic tests were conducted at a strain rate not exceeding 0.0008/s. All tests were conducted so that tension strains were imposed first prior to reserving loading direction. The applied strain was sinusoidal with respect to time. At least three successful tests per bar type and test parameters were performed.

The following test sample nomenclature was used for cyclic tests.

Example: Cm1_04_A60Nb#5_N10P40_6db

Bar type nomenclature

Type of test: C is cyclic; M is monotonic

Manufacturing process: m1; m2; m3; m4

Batch: 01; 02; 03; 04

ASTM specification: A is A615/A615M; B is A706/A706M; C is dual A615/A615M and A706/A706M; D is HRB

Grade: 60; 80; 400; 500

Primary microalloying: Nb is niobium; NbV is niobium and vanadium; V is vanadium

Bar size: No. 5 (5/8 in. [16 mm]); No. 8 (1 in. [25 mm])

Test type nomenclature

Strain protocol: N10P40 (negative 1.0%, positive 4.0% strain)

Clear unbraced length: $4d_b$; $6d_b$

Instrumentation

Loads applied to the specimens were recorded from the load cell of the testing machine. Strains and deformations of the bars were obtained from high-resolution images recorded at a rate of several frames per second using a specialized vision digital camera. A digital image correlation (DIC) system (Sokoli et al. 2014; Ghannoum et al. 2021) dubbed the Civil Infrastructure Vision (CIV) system was used to track the two-dimensional location of surface targets on the bars between subsequent frames. The strain between targets at the grip edges was used to control the tests and achieve the intended strain range.

PHASE 1 TEST RESULTS

In this section, test results are presented for Phase 1, with trends highlighted. Discussions pertaining to test results and the effects of test parameters on fatigue results are presented in the subsequent section. Phase 2 and 3 results are presented subsequently and discussed considering Phase 1 results.

Monotonic tension tests

Three monotonic tension tests were conducted for each bar type. The average was calculated for the mechanical properties of the specimens. Typical stress-strain curves are plotted in Fig. 3 for No. 5 (5/8 in. [16 mm]) bars from each manufacturer in Phase 1.

As anticipated, higher-grade bars exhibited lower T/Y ratios. Uniform and fracture strains were generally larger for MPs 2 to 4 than for MP 1.

MP 1 batch 01 bars were the only batch from the first manufacturer that did not have a continuous stress-strain curve, as depicted in Fig. 3. Instead, the stress-strain curves had a clear yield plateau at approximately 80 ksi (550 MPa). Batch 01 also displayed lower T/Y than batches 02 to 04 from MP 1. Overall, MP 1 had the lowest yield plateau lengths compared to other manufacturers.

Low-cycle fatigue tests

A total of 96 fatigue tests were conducted in the first phase of this study. Tests involved pulling the bar specimens to +4.0% strain in tension before reversing loading to a compressive strain of –1.0%. During the low-cycle fatigue tests, bars experienced varying degrees of strength degradation, mainly due to buckling and cracking. The number of half-cycles to bar fracture is the main performance measure used in this study to quantify the fatigue life of bars. Table 2 shows the average number of half-cycles to fracture for three tests per specimen type and test parameters.

The number of half-cycles varied with clear gripping span and between MPs. Representative stress-strain responses of No. 5 (5/8 in. [16 mm]) bars tested at a $6d_b$ clear span for each MP are presented in Fig. 4. For the most part, bars gripped at $6d_b$ experienced more pronounced buckling and cyclic strength degradation than the equivalent bars tested at $4d_b$, resulting in a smaller number of half-cycles to fracture. For the most part, bars from MPs 2 to 4 experienced more half-cycles to fracture than MP 1 bars. As seen in Fig. 4, MP 1 bars typically suffered less cyclic strength degradation before fracture relative to bars from other processes, but they experienced a more brittle fracture. Alternatively, bars produced by MPs 2 to 4 usually sustained gradually widening fatigue cracks that resulted in more cycles to fracture and greater cyclic strength degradation before fracture occurred.

A key difference between Grades 60 and 80 ksi (420 and 550 MPa) bars is their buckling behavior. At a clear span of $6d_b$, Grade 80 bars experienced increased buckling deformations due to the higher loads on them. This behavior increased strain concentrations in Grade 80 bars compared with their Grade 60 counterparts, which reduced the Grade 80 bar fatigue life, irrespective of other bar properties. Previous research (Sokoli et al. 2019) found that Grade 80 bars tested in low-cycle fatigue at a gripping span of $5d_b$ showed comparable fatigue performance to Grade 60 bars gripped at $6d_b$. At a span of $4d_b$, both grades experienced limited buckling, making fatigue-life comparisons between grades more appropriate at that clear span.

Fractographic analysis from fatigue samples—A fractographic analysis was conducted to analyze fracture surface details. The following representative samples from each MP were studied: m1_03_A60Nb#5, m2_01_D400Nb#5, m3_01_D400Nb#5, and m4_01_D400V#5. At low magnifications, it was possible to identify three areas with distinctive

surface properties on the fracture surfaces of MPs 1 and 2 and two areas for MPs 3 and 4 (Fig. 5). For all samples, fatigue cracks would nucleate at the surface and propagate during cycling over a fatigue region until final fracture occurred. MP 1 bars typically had the smallest fatigue crack propagation area (Wang 1996), followed by bars from MP 2, then MP 3, and finally MP 4 (Fig. 5). Bars from MPs 1 and 2 had a final failure that was mainly brittle, as opposed to bars from MPs 3 and 4, which had a ductile final failure mode. Additional details from fractographic analyses can be found in Gonzalez (2022).

Table 2—Average number of half-cycles for $4d_b$ and $6d_b$ clear gripping spans

MP	Batch No.	Grade	Chemistry	Bar size	Half-cycles	
					$4d_b$	$6d_b$
1	01	80	NbV	No. 5	9.37	6.25
	01	80	NbV	No. 8	14.02	9.75
	02	60	Nb	No. 5	19.66	9.66
	03	60	Nb	No. 5	17.61	15.09
	03	60	Nb	No. 8	27.30	14.64
	04	60	Nb	No. 5	14.45	11.21
	04	60	Nb	No. 8	30.62	15.10
2	01	400	Nb	No. 5	41.93	28.39
	02	400	Nb	No. 8	47.69	12.47
	03	500	NbV	No. 5	22.32	23.88
	03	500	NbV	No. 8	34.43	17.98
3	01	400	Nb	No. 5	30.42	30.48
4	01	400	V	No. 5	65.79	25.71
	01	400	V	No. 8	36.27	25.92
	02	500	V	No. 5	29.91	17.93
	02	500	V	No. 8	30.98	19.88

Note: No. 5 bars are 5/8 in. (16 mm) diameter; No. 8 bars are 1 in. (25 mm) diameter.

PHASE 1 DATA ANALYSES AND DISCUSSIONS

Tensile properties

Several correlations were uncovered between microstructural and monotonic tensile properties. In this section, red data points refer to bars conforming to ASTM standards, while blue data points conform to GB/T 1499.2-2018. Average hardness across the section of bars showed, as would be expected, increasing yield strength. Decreasing ferrite grain size showed increasing yield strength (Fig. 6). This increasing yield strength with decreasing ferrite grain size is due to the use of Nb microalloying to increase bar strength through various modifications of the austenite conditioning recrystallization behaviors during hot rolling, including hot deformation, plus solute Nb. This results in a finer final ferrite grain size upon cooling transformation. In steels without Nb microalloying present, such as plain C/Mn or V microalloyed steels, there is only a single influence on the austenite conditioning recrystallization behavior (hot deformation only), which results only in a slightly finer ferrite grain size upon cooling transformation (Enloe et al. 2020; López et al. 2018; Samuel et al. 1988).

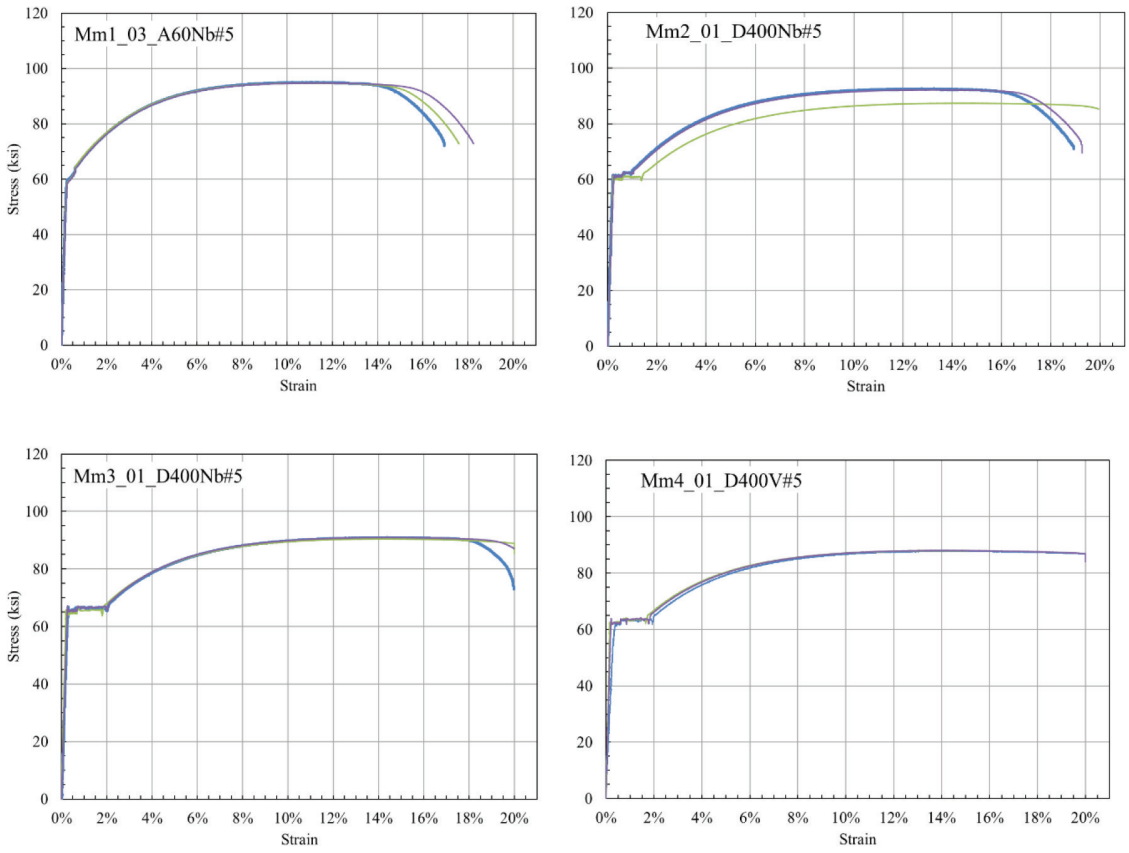

Fig. 3—Typical monotonic stress-strain curves for No. 5 bars from each manufacturing process. (Note: 1 ksi = 6.89 MPa.)

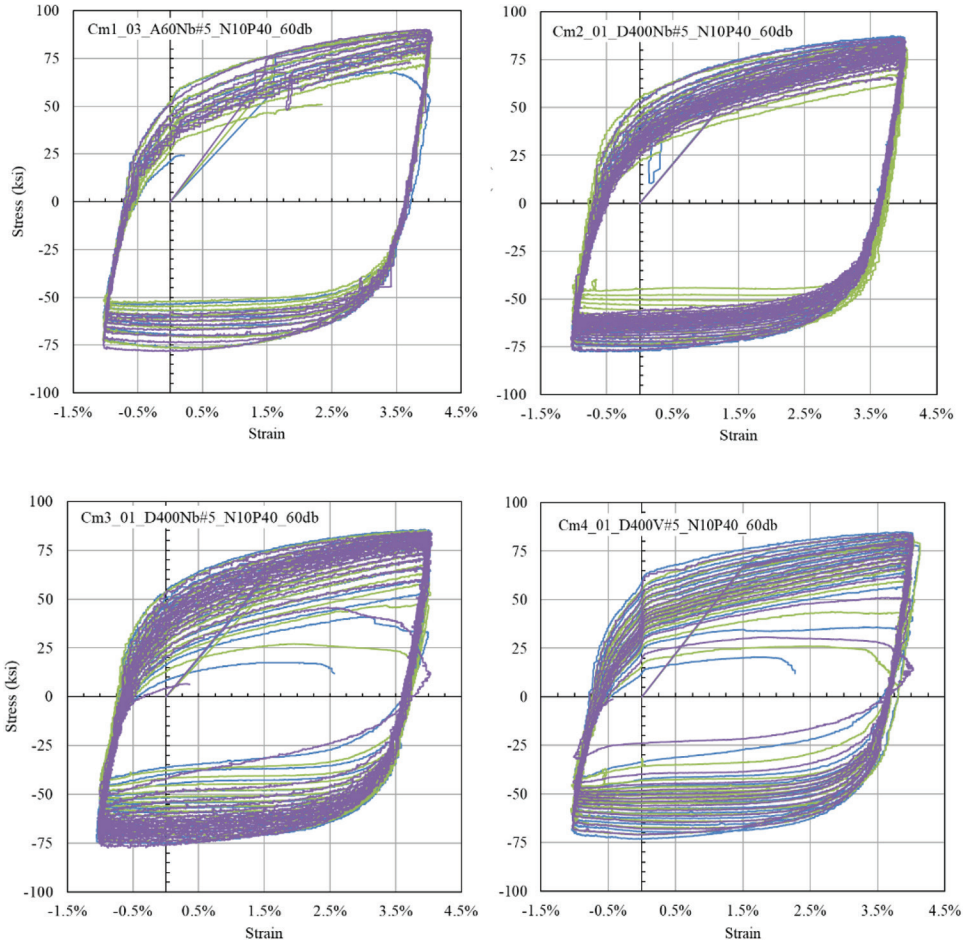

Fig. 4—Typical cyclic stress-strain curves for No. 5 bars at $6d_b$ from each manufacturing process. (Note: 1 ksi = 6.89 MPa.)

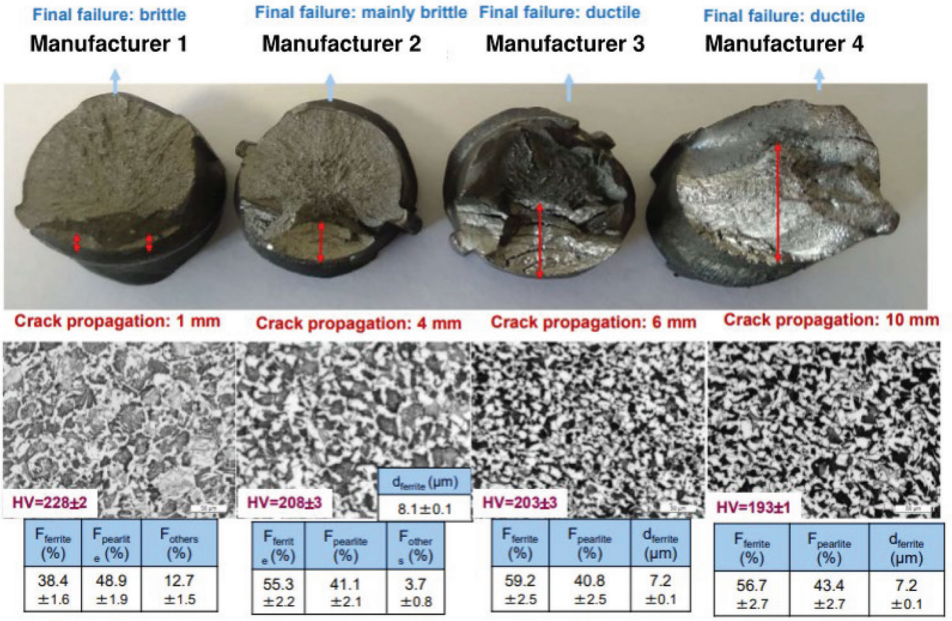

Fig. 5—Fractographic analysis for all manufacturing processes and corresponding microstructural properties. (Note: 1 μm = 0.039 mils.)

This strengthening method is often referred to as the grain-boundary strengthening method, which strengthens steel alloys by changing their average crystallite size (Hall-Petch relationship) (Callister 2001). Vanadium does not influence final ferrite grain size in structural steels but can contribute to strength, which can be enhanced with the addition of Nb through post-rolling precipitation-hardening mechanisms (Zajac 2005; Gladman 1999).

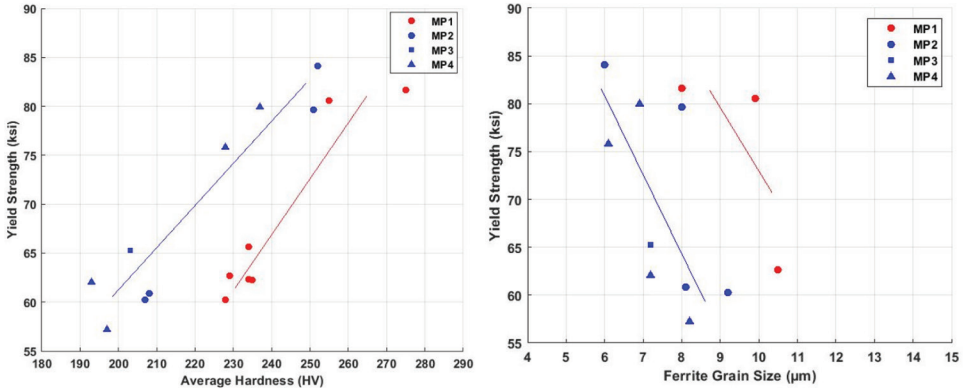

Fig. 6—Correlations between microstructural properties and yield strength. (Note: 1 ksi = 6.89 MPa; 1 μm = 0.039 mils.)

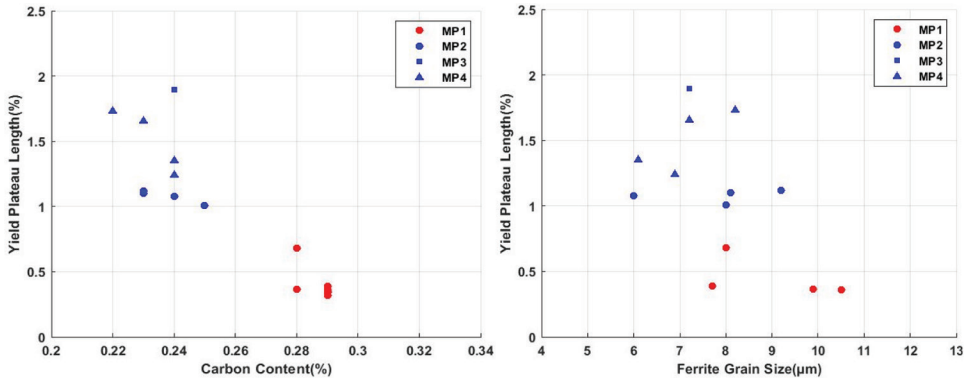

Fig. 7—Negative correlations between carbon content, ferrite grain size, and yield plateau length. (Note: 1 μm = 0.039 mils.)

Yield plateau length, uniform strain, and fracture strain were found to correlate positively with ferrite fraction. Results, therefore, indicate that higher ferrite fraction increases bar ductility. Previous studies (Bannister 1998; Hall 1970) indicated that the yield plateau length is not an intrinsic material property and is dependent on the MP, chemical composition, and grain size. Focusing on the yield plateau length, inverse correlations are shown with carbon content and ferrite grain size in Fig. 7.

Fatigue life

Test data were analyzed to identify correlations between test parameters and the fatigue life of bars. It is noted that bar m2_02_D400Nb#8 was believed to be an outlier due to odd rib geometry values and microstructure based on the production method. Data from this batch are tagged in all plots as "outlier." Discussions in this section are centered around data from tests conducted at a clear span of $6d_b$. However, the trends discussed are similar for both clear spans of $4d_b$ and $6d_b$.

Overall, bars conforming to GB/T 1499.2-2018 (MPs 2 to 4), despite having lower deformation r/h values, generally sustained a greater number of half-cycles to fracture than ASTM-conforming bars (MP 1). Fatigue cracks were often observed to initiate in the MP 1 bars at the interface between the transverse and longitudinal ribs. This region is known to have high stress concentrations during bar loading (Burton 1965). MPs 2 to 4 bars, however, had transverse ribs that did not intersect the longitudinal ones, which may have contributed to the improved fatigue life of those bars compared to MP 1 bars. Due to differing rib geometries, data analyses were conducted separately for MP 1 and other bars, while Phase 2 looked at machined samples to remove bar deformations and their influence on fatigue.

MP 1 bars had the highest carbon content for all batches because the ASTM specifications allow higher carbon content than the GB/T specifications. This difference may also have contributed to the lower MP 1 bar fatigue life. However, within each specification, the carbon content was relatively constant, which did not allow the study to explore the effects of carbon content on fatigue life more directly.

The bars produced by the TMCP production method (MP 3) exhibited the highest number of half-cycles to fracture overall. This was expected as TMCP can produce enhanced grain refinement, which tends to improve fatigue life and toughness of steel elements (Du et al. 2021). Bars produced using the TMCP MP 3 also contained some of the highest amounts of Nb. However, as can be seen in Fig. 8, Nb content by itself is not a sufficient indicator of fatigue life, as processing conditions play an important role in the Nb benefits with respect to fatigue life.

Higher levels of V were used in all cases to increase bar strength from 60 to 80 ksi (420 to 550 MPa). This mechanism used to increase yield strength is known as precipitation strengthening (Gladman 1999). However, the resulting increase of precipitates can have a deleterious effect on low-cycle fatigue life, reducing the number of half-cycles to fracture, as seen in Fig. 8. In the figure, total MA content is calculated as the sum of V and Nb contents.

Figure 5 summarizes results from fracture surface analyses, microstructure analysis, and hardness tests. To

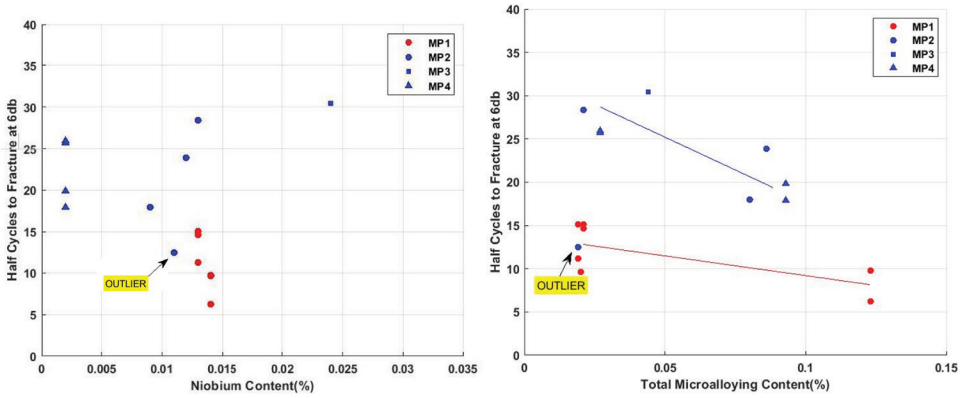

Fig. 8—Niobium content and total microalloying content versus half-cycles to fracture.

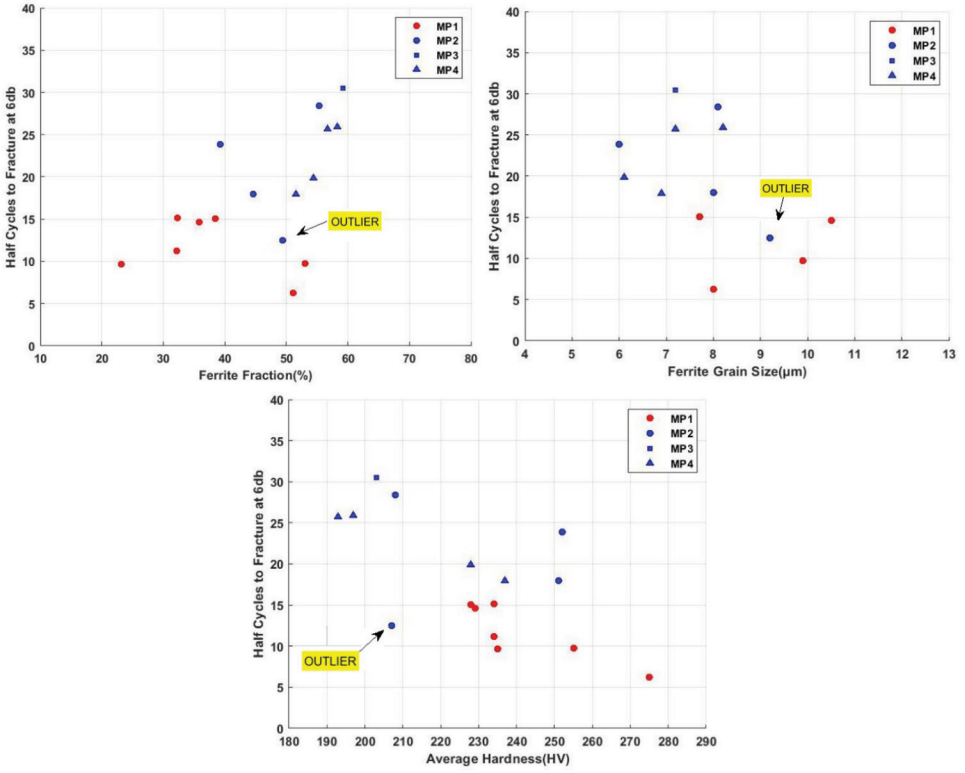

Fig. 9—Ferrite fraction, ferrite grain size, and average hardness versus half-cycles to fracture.

identify trends between the properties summarized in Fig. 5 and fatigue life, the number of half-cycles to fracture are plotted versus ferrite fraction, ferrite grain size, and average cross-sectional hardness in Fig. 9.

Fractographic analysis of test specimens showed that MPs 1 and 2 had a brittle fatigue failure, while MPs 3 and 4 had a more ductile failure. In their microstructural images shown in Fig. 5, it can be seen that the grain size and corresponding microstructural phases differ from one MP to another. For MP 1, mainly coarse dark phases, consisting of pearlite and/or various forms of bainite, are present. Pearlitic and various forms of bainitic phases are known to be harder and, hence, more brittle. They are characterized by their high strength, low fracture resistance, and low ductility, which can contribute to brittle fatigue failure. MPs 3 and 4 microstructures show relatively finer grains and corresponding microstructural phases of pearlite, less bainitic phases, and lighter microstructural phases of ferrite. Ferrite is a softer and more ductile microstructural phase than other larger and harder microstructural phases. These microstructural characteristics were found to correlate with the fatigue fracture surfaces and fatigue life. More so, a direct relationship between the microstructure's ferrite fraction and the number of half-cycles to fracture was observed (Fig. 9). An increase in ferrite fraction exerted a positive influence on the low-cycle fatigue life. An inverse relationship was observed between the ferrite grain sizes and the fatigue life (Fig. 9). When looking at the microstructural images from MP sample bars in Fig. 5, the grain sizes are smaller and more refined for MPs 3 and 4 than for MPs 1 and 2. This refinement, also known as the Hall-Petch effect (Callister 2001), has a positive effect on the number of half-cycles to fracture the bars can sustain.

For the steels with more conventional MA additions (all Grade 60 ksi [420 MPa] bars) that do not use a

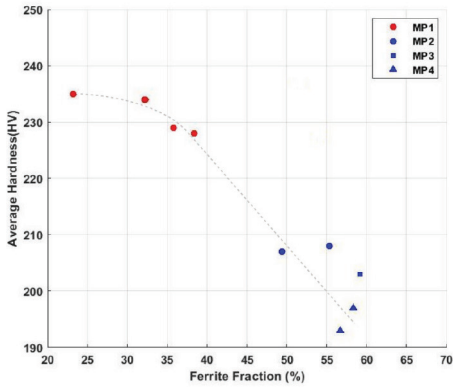

Fig. 10—Relationship between ferrite fraction and average cross-sectional hardness (Grade 60 ksi [420 MPa] bars).

precipitation-strengthening mechanism, the ferrite fraction was correlated to the average section hardness (Fig. 10). A higher ferrite fraction percentage led to lower hardness values. To further investigate, average hardness values were plotted against half-cycles to failure, and as expected, because ferrite grains tend to be softer than other grains, an inverse relationship was found (Fig. 9). A decrease in hardness resulted in higher half-cycles to failure.

Several correlations were identified between tensile properties and fatigue life. Yield strength had an inverse relationship with half-cycles to fracture; as yield strength increased, low-cycle fatigue life decreased. This trend was more severe at a gripping span of $6d_b$ due to increased buckling of higher strength bars but was also manifest at a gripping span of $4d_b$. Precipitates resulting from V microalloying used to increase bar yield strength can have a negative impact on fatigue life.

Referring to the final fracture failure analysis and the corresponding monotonic stress-strain curves, a pattern was observed with the yield plateau length (Fig. 5). As the yield plateau recorded in tension testing increased in strain length, larger crack propagation areas were noted in fractographic analyses. Yield plateau lengths also exhibited a positive correlation with the ferrite fraction. A longer yield plateau correlated with a larger ferrite fraction in the microstructure. This may explain the brittle and ductile final fracture failures experienced during low-cycle fatigue testing. The yield plateau length was clear on the low-cycle fatigue, as shown in Fig. 11. The longer the yield plateau was sustained, the greater the number of half-cycles.

Lastly, a direct correlation between the uniform strain and low-cycle fatigue life was also observed. The uniform strain is a good indicator of a material's ductility. The greater the uniform strain value, the more pronounced the ability of the material to change its shape without deforming/necking. In this study, bars withstanding a higher number of half-cycles also exhibited relatively large uniform strains.

ADDITIONAL TESTS

Phase 2 machined bars

Because the bar deformation geometries differ substantially between production methods and owing to previous findings that highlighted the significant effects of bar deformation on fatigue life (Ghannoum and Slavin 2016), No. 5

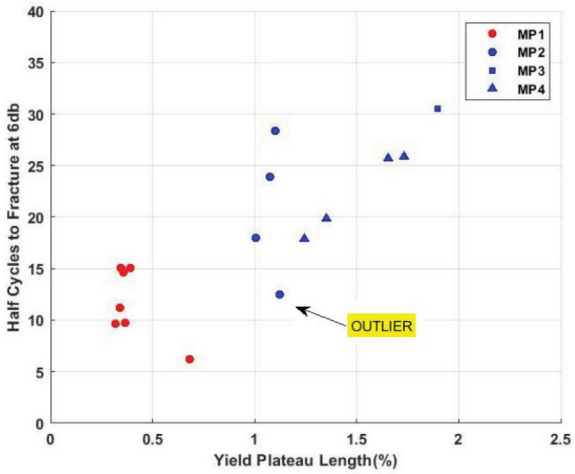

Fig. 11—Direct relationship between yield plateau length and number of half-cycles.

(5/8 in. [16 mm]) bars from all four MPs were machined to dog-bone coupons per ASTM E606/E606M-19 (2019) to remove their surface deformations. By removing bar deformations, it was possible to directly compare the effects of chemistry and microstructure on fatigue life. The coupons were machined to a diameter of 1/4 in. (6.4 mm) and a clear span to the end of the prismatic portion of the coupon of 1.5 in. (38 mm). This resulted in a clear span of $6d_b$.

As seen in Fig. 12, the same trends are observed between fatigue life, hardness, and ferrite fraction in both Phase 2 and Phase 1 tests conducted at $6d_b$ gripping span. This finding demonstrates that lower hardness and higher ferrite fraction tend to increase the fatigue life of reinforcing bars, regardless of the geometry of their deformations. The machined samples had significantly higher fatigue lives than their non-machined counterparts. This corroborates prior findings that indicated the deleterious effects of bar deformations on their fatigue life. Ferrite grain size and fatigue life did not appear correlated in Phase 2 testing, possibly owing to the limited grain-size range in the coupons. On the other hand, positive correlations were found between coupon fatigue life, yield plateau length, and uniform strain elongation, as was found in Phase 1 tests. Additionally, a clearer negative correlation between equivalent carbon content and half-cycles to fracture was observed in the coupon tests than in tests on non-machined bars (Fig. 12).

Additional MP 1 U.S. bar batch

Adjustments to the chemistry of bars using MP 1 were undertaken to explore whether grain refinement translating into increasing ferrite content, decreasing grain size, and lower hardness could yield improvements in fatigue life. An additional Grade 60 batch 05 was produced using MP 1, without modifying the hot-rolling or post-rolling cooling, but with chemical adjustments to optimize various contributions from key alloying elements toward the final microstructural phase and gain-size formation. Differences in batch 05 consisted mainly of reducing Mn and balancing that reduction in Mn for strength purposes with small Nb and V additions. With solute Nb contributing to final ferrite

grain-size refinement and improved microstructural phase formation and V contributing post-rolling precipitation strengthening, both additions offset the Mn reduction for strength. These alloy modifications were roughly cost-neutral on bar production.

As seen in Table 3, at $6d_b$, both No. 5 (5/8 in. [16 mm]) and No. 8 (1 in. [25 mm]) bars of batch 05 had the highest number of half-cycles of all MP 1 bars. On average, batch 05 bars exhibited an increase in the number of half-cycles to fracture compared to previous Grade 60 batches of 58% for No. 5 bars and 30% for No. 8 bars across both clear gripping spans. These results indicate that simple cost-neutral changes to chemistry optimization for the existing processing conditions can result in substantial improvements in reinforcing bar fatigue life.

The trends between hardness, ferrite fraction, and ferrite grain size with respect to fatigue life can be seen in Fig. 13 for all bar batches. As seen in the figure, the additional batch data fit well within the overall trends, supporting the observation that these three microstructure measures are correlated with the fatigue life of bars and that realized improvements in them in batch 05 followed the same trends toward an increased fatigue performance of that batch.

COMPARISON WITH EXISTING LOW-CYCLE FATIGUE TESTS

The fatigue life of bars representing current production in the United States and recently tested for low-cycle fatigue by Sokoli et al. (2019) and those tested in this study, including Nb-based chemistries, are compared in this section. The mean values of half-cycles to fracture of bars produced using various MPs are compared with those obtained

Table 3—Average number of half-cycles for all U.S. bars

MP	Batch No.	Grade	Chemistry	Bar size	Half-cycles	
					$4d_b$	$6d_b$
1	01	80	NbV	No. 5	9.37	6.25
	01	80	NbV	No. 8	14.02	9.75
	02	60	Nb	No. 5	19.66	9.66
	03	60	Nb	No. 5	17.61	15.09
	03	60	Nb	No. 8	27.30	14.64
	04	60	Nb	No. 5	14.45	11.21
	04	60	Nb	No. 8	30.62	15.10
	05	60	NbV	No. 5	23	21.94
	05	60	NbV	No. 8	37.11	19.83

Note: No. 5 bars are 5/8 in. (16 mm) diameter; No. 8 bars are 1 in. (25 mm) diameter.

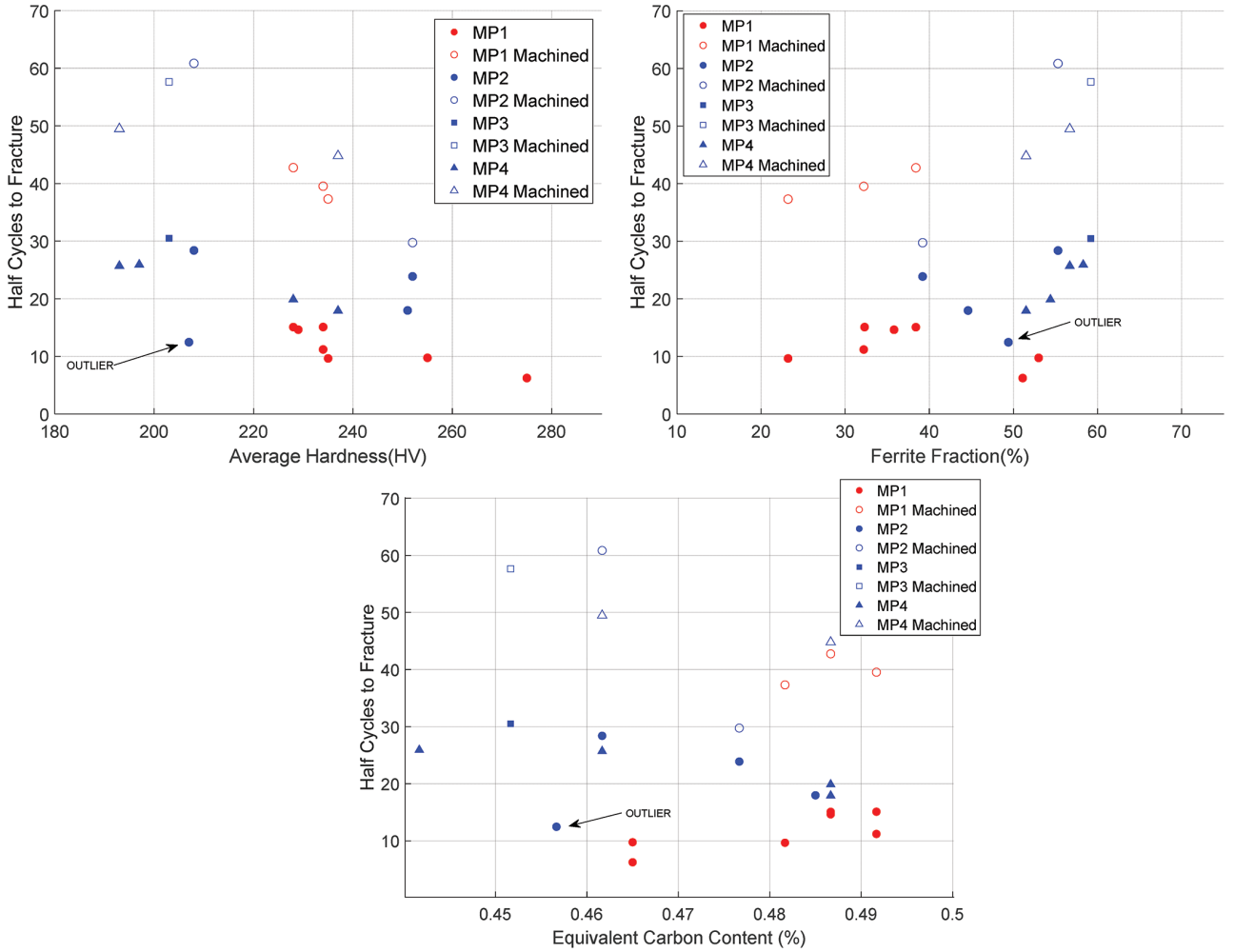

Fig. 12—Machined coupon fatigue life trends with Phase 1 tests at $6d_b$ clear span.

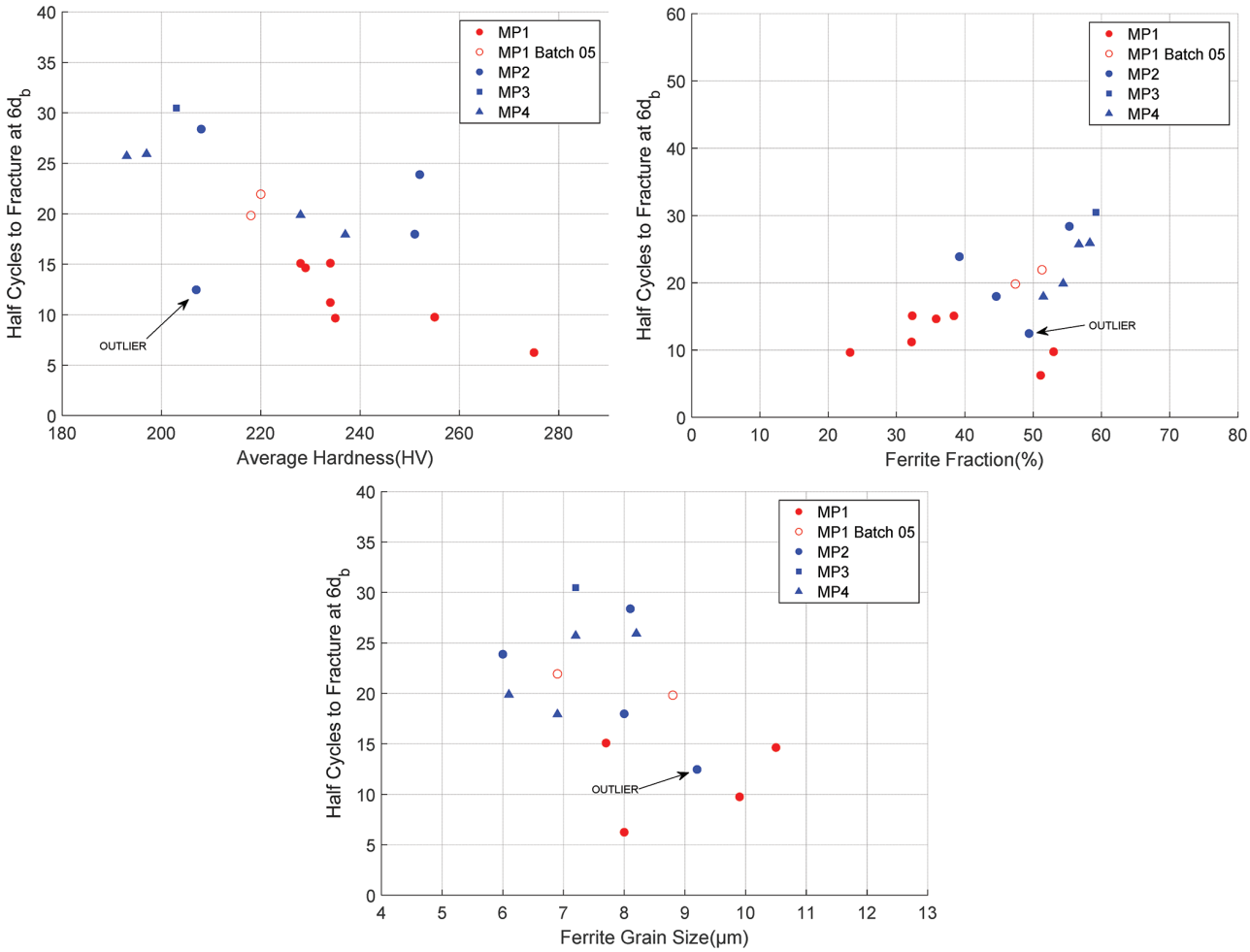

Fig. 13—Additional U.S. batch 05 results with improved grain refinement (6d_b clear span). (Note: 1 μm = 0.039 mils.)

by Sokoli et al. (2019) for bars covering the full range of production methods in the United States. The comparison is made by providing the percentiles of the number of half-cycles to fracture from U.S.-produced bars that correspond to the mean values of half-cycles to fracture for each batch of this study. Comparisons were made using data with the same gripping span, strain amplitude, and steel grade, as presented in Table 4. In the table, the percentiles provided indicated the percentage of bars in current U.S. production that have lower fatigue life than the mean for the bars tested in this study. For both gripping spans, MP 1 bars from batches 01 to 04 produced in the United States exhibited comparable performance to current production (between approximately the 10th and 50th percentiles). This indicates that the first trials using MP 1 in this study did not appreciably improve the fatigue performance of the bars. However, for batch 05, produced later in the study, fatigue life was generally better than approximately 75% of bars in current U.S. production. MPs 2 to 4 bars, for the most part, exhibited substantially superior fatigue life compared with current U.S. production, with percentiles generally exceeding the 75th percentile and even higher than the 99th in several cases. This finding indicates that methods used in the last MP 1 batch 05 and for MPs 2 to 4 bars can significantly improve the fatigue life of bars in the United States. Additionally, bar deformation patterns used in MPs 2 to 4 bar productions may be worth pursuing in the United States as an additional low-cost method for improving fatigue life.

CONCLUSIONS

Several manufacturing processes (MPs) and chemistries were explored to identify practices that can improve the low-cycle fatigue life and ductility of reinforcing bars. Correlations between bar properties, such as microstructural properties, chemical composition, and bar deformations, were explored with respect to fatigue life. Key findings include:

1. Yield plateau length, uniform strain, and fracture strain were found to correlate positively with ferrite fraction. This indicates that ferrite fraction is a key parameter in determining these tensile properties and enhances ductile bar behavior.

2. Furthermore, ferrite fraction, in combination with ferrite grain size, was found to have a positive effect on fatigue life. These parameters are key to improving the strength and fatigue mechanical properties of bars.

3. Conversely, average hardness across a bar cross section was found to have a strong negative correlation with fatigue life.

4. Bar deformations are found to have deleterious effects on the fatigue life of bars. Machined coupons for which deformations were removed exhibited substantially

Table 4—Average number of half-cycles and percentiles of existing bar production in United States

MP	Bar	Percentile of half-cycles to fracture of U.S. bars corresponding to mean values of bars tested in this study	
		$4d_b$	$6d_b$
Grade 60 ksi (420 MPa) bars			
1	m1_02_B60Nb#5	10th	10th
1	m1_03_A60Nb#5	5th	40th
1	m1_03_C60Nb#8	25th	40th
1	m1_04_A60Nb#5	<5th	15th
1	m1_04_C60Nb#8	55th	40th
1	m1_05_C60NbV#5	15th	80th
1	m1_05_C60NbV#8	90th	75th
2	m2_01_D400Nb#5	>99th	>99th
2	m2_01_D400Nb#8 (outlier)	>99th	20th
3	m3_01_D400Nb#5	55th	>99th
4	m4_01_D400V#5	>99th	>99th
4	m4_01_D400V#8	85th	>99th
Grade 80 ksi (550 MPa) bars			
1	m1_01_A80NbV#5	10th	<5th
1	m1_01_B80NbV#8	60th	10th
2	m2_03_D500NbV#5	>99th	85th
2	m2_03_D500NbV#8	>99th	75th
4	m4_02_D500V#5	>99th	75th
4	m4_02_D500V#8	>99th	80th

improved fatigue performance compared with their non-machined counterparts.

5. Equivalent carbon content followed that of hardness and was found to be negatively correlated with the fatigue life of bars, particularly for machined bars where deformations and their effects were removed.

6. Precipitation strengthening generated by microalloying (MA) with vanadium (V) to increase bar strength from 60 to 80 ksi (420 to 550 MPa) is shown to have a deleterious effect on the low-cycle fatigue life of reinforcing bars, reducing the number of half-cycles to fracture at both $4d_b$ and $6d_b$ clear spans. The presence of V microalloy contributed to an increased average hardness while not contributing metallurgically to the final ferrite grain size.

7. Bars conforming to GB/T 1499.2-2018 that were processed using thermomechanical controlled processing (TMCP) with water cooling during rolling, and containing the highest amount of niobium (Nb), had the highest number of half-cycles to fracture. These bars exhibited fatigue performance better than 99% of the bars currently in production in the United States and had some of the highest ferrite content, smallest grain size, and lowest hardness values. This finding indicates that grain refinement through TMCP and Nb microalloying can improve fatigue performance significantly.

It is recommended that adjustments to reinforcing bar production be pursued in the United States to improve ductility and fatigue life. This study demonstrated that improvement in excess of 50% in the fatigue lives of bars can be achieved without increasing the cost of production.

To improve the ductility and low-cycle fatigue performance of reinforcing bars, it is recommended to use production methods that result in: 1) reduced cross-section hardness; 2) increased ferrite fractions; and 3) decreased ferrite grain size. Optimization of the overall alloy design with the addition of Nb for an existing hot-rolling and cooling reinforcing bar production can help in achieving those goals. Adding an optimized overall alloy design with enhancements to thermal control during and post-rolling can further enhance the goals of improved ductility and low-cycle fatigue performance. It is also recommended to explore alternate rib geometries for reinforcing bars that can reduce stress concentrations and improve fatigue life. Particularly, rib geometries that do not have intersecting transverse and longitudinal ribs should be pursued.

FURTHER RESEARCH

Additional tests of Nb-based bars need to be conducted to better understand their effects on the low-cycle fatigue of reinforcing bars. Further investigation into the effects of bar deformation geometry and its effect on fatigue life is necessary to establish standard specifications to ensure adequate and consistent fatigue life. Likewise, additional MPs should be investigated to further understand the relationship between bar microstructure and low-cycle fatigue performance.

AUTHOR BIOS

Jessica Gonzalez *is a Civil/Structural Engineering Associate at Wiss, Janney, Elstner Associates, Inc.*

ACI member **Seyed Sasan Kedmatgozar Dolati** *is a PhD Candidate at The University of Texas at San Antonio, San Antonio, TX. He is a member of ACI Committees 369, Seismic Repair and Rehabilitation, and 374, Performance-Based Seismic Design of Concrete Buildings. His research interests include the nonlinear behavior of reinforced concrete structures, finite element analyses, and repair and rehabilitation of concrete structures.*

ACI member **Ariel Suselo** *is a Civil/Structural Engineering Associate at Wiss, Janney, Elstner Associates, Inc. His research interests include the nonlinear behavior of reinforced concrete structures, structural nondestructive testing and evaluation, and repair and rehabilitation strategies for civil structures.*

Douglas Stalheim *is President of DGS Metallurgical Solutions, Inc., a technical consultant to the steel industry. He received his BS in metallurgical engineering. He has over 42 years of practical steel alloy/process/production experience in both flat and long structural steel products.*

Ana Araujo *is a Technical Market Development Specialist serving the steel industry in North America. She received her MS in metallurgical engineering from the Colorado School of Mines, Golden, CO.*

ACI member **Wassim M. Ghannoum** *is a Professor at The University of Texas at San Antonio. He is a member of the ACI Technical Activities Committee and ACI Committee 318, Structural Concrete Building Code. His research interests include the behavior of reinforced concrete structures at high damage states, the use of novel materials in concrete construction, and the lifespan extension of concrete structures.*

ACKNOWLEDGMENTS

This project was made possible by funding from CBMM. The assistance of M. Enloe in sourcing bars and Ceit, San Sebastián, Spain, for detailed metallographic characterization, is gratefully acknowledged.

REFERENCES

ASTM A370-16, 2016, "Standard Test Methods and Definitions for Mechanical Testing of Steel Products," ASTM International, West Conshohocken, PA, 49 pp.

ASTM A615/A615M-16, 2016, "Standard Specification for Deformed and Plain Carbon-Steel Bars for Concrete Reinforcement," ASTM International, West Conshohocken, PA, 8 pp.

ASTM A706/A706M-16, 2016, "Standard Specification for Deformed and Plain Low-Alloy Steel Bars for Concrete Reinforcement," ASTM International, West Conshohocken, PA, 7 pp.

ASTM E8/E8M-16a, 2016, "Standard Test Methods for Tension Testing of Metallic Materials," ASTM International, West Conshohocken, PA, 30 pp.

ASTM E92-17, 2017, "Standard Test Methods for Vickers Hardness and Knoop Hardness of Metallic Materials," ASTM International, West Conshohocken, PA, 27 pp.

ASTM E606/E606M-19, 2019, "Standard Test Method for Strain-Controlled Fatigue Testing," ASTM International, West Conshohocken, PA, 16 pp.

ASTM F728-81(2003), 2003, "Standard Practice for Preparing An Optical Microscope for Dimensional Measurements (Withdrawn 2003)," ASTM International, West Conshohocken, PA.

Bannister, A. C., 1998, "Contribution to Sub-Task 2.3: Assessment of the Occurrence and Significance of Yield Plateaus in Structural Steels," Report No. SINTAP/BS/19, Brite-Euram BE 95-1426, British Steel plc, Rotherham, UK.

Brown, J., and Kunnath, S. K., 2004, "Low-Cycle Fatigue Failure of Reinforcing Steel Bars," *ACI Materials Journal*, V. 101, No. 6, Nov.-Dec., pp. 457-466.

Burton, K. T., 1965, "Fatigue Tests of Reinforcing Bars," *Journal of the PCA Research and Development Laboratories*, V. 7, No. 3, Sept., pp. 13-23.

Callister, W. D. Jr., 2001, *Fundamentals of Materials Science and Engineering: An Integrated Approach*, second edition, John Wiley & Sons, Inc., Hoboken, NJ, 824 pp.

Davis, J. R., ed., 2001, "High-Strength Low-Alloy Steels," *Alloying: Understanding the Basics*, ASM International, Materials Park, OH, pp. 193-209.

Du, B.; Sheng, L.; Cui, C.; Hu, Z.; and Sun, X., 2021, "Effects of Grain Refinement on the Low-Cycle Fatigue Behavior of IN792 Superalloys," *Crystals*, V. 11, No. 8, Aug., Article No. 892. doi: 10.3390/cryst11080892

Eguchi, R.; Elwood, K. J.; Lee, E. K.; Berger, J.; Boulanger, R.; Buckle, I.; Comerio, M. C.; Davidson, R.; Greene, M.; Fritz, H.; Furukawa, T.; Mahin, S.; Robertson, I. N.; Sakamoto, Y.; Sutton, J.; and Tsugawa, M., 2012, "The 2010 Canterbury and the 2011 Christchurch New Zealand Earthquakes and the 2011 Tohoku Japan Earthquake: Emerging Research Needs and Opportunities; Workshop Report," Earthquake Engineering Research Institute, Oakland, CA, 59 pp.

Enloe, M.; Stalheim, D.; and Bastos, F., 2020, "Niobium Metallurgy in Rebar Steels," CBMM training presentation, Oct., CBMM North America, Inc., Houston, TX.

Fei, J., and Darwin, D., 1999, "Fatigue of High Relative Rib Area Reinforcing Bars," SM Report No. 54, University of Kansas Center for Research, Inc., Lawrence, KS, July, 83 pp.

GB/T 1499.2-2018, 2018, "Steel for the Reinforcement of Concrete – Part 2: Hot Rolled Ribbed Bars," General Administration of Quality Supervision, Inspection and Quarantine of the People's Republic of China, Beijing, China, 31 pp.

Ghannoum, W. M., and Slavin, C. M., 2016, "Low-Cycle Fatigue Performance of High-Strength Steel Reinforcing Bars," *ACI Materials Journal*, V. 113, No. 6, Nov.-Dec., pp. 803-814. doi: 10.14359/51689116

Ghannoum, W. M.; Diaz, M.; Rajaei, S.; Banjade, S.; Chapagain, B.; and Hogsett, G., 2021, "CIV – Civil Infrastructure Vision© v1.0: Bridge Calibration User Manual and Validation Manual," Report No. FHWA/TX-21/0-6950-1, The University of Texas at San Antonio, San Antonio, TX, 85 pp.

Gladman, T., 1999, "Precipitation Hardening in Metals," *Materials Science and Technology*, V. 15, No. 1, pp. 30-36.

Gonzalez, J., 2022, "Improving Fatigue Properties of Reinforcing Steel Bars," master's thesis, The University of Texas at San Antonio, San Antonio, TX, 143 pp.

Hall, E. O., 1970, *Yield Point Phenomena in Metals and Alloys*, Springer, New York, 296 pp.

Hanson, J. M.; Burton, K. T.; and Hognestad, E., 1968, "Fatigue Tests of Reinforcing Bars - Effect of Deformation Pattern," *Journal of the PCA Research and Development Laboratories*, V. 10, No. 3, Sept., pp. 2-13.

Heisterkamp, F., and Carneiro, T., 2001, "Niobium: Future Possibilities – Technology and the Market Place," *Niobium, Science & Technology: Proceedings of the International Symposium Niobium 2001*, Orlando, FL, Dec., pp. 1109-1162.

Isasti, N.; Jorge-Badiola, D.; Taheri, M. L.; and Uranga, P., 2014a, "Microstructural Features Controlling Mechanical Properties in Nb-Mo Microalloyed Steels. Part I: Yield Strength," *Metallurgical and Materials Transactions A: Physical Metallurgy and Materials Science*, V. 45, No. 11, Oct., pp. 4960-4971. doi: 10.1007/s11661-014-2450-7

Isasti, N.; Jorge-Badiola, D.; Taheri, M. L.; and Uranga, P., 2014b, "Microstructural Features Controlling Mechanical Properties in Nb-Mo Microalloyed Steels. Part II: Impact Toughness," *Metallurgical and Materials Transactions A: Physical Metallurgy and Materials Science*, V. 45, No. 11, Oct., pp. 4972-4982. doi: 10.1007/s11661-014-2451-6

Jansto, S., 2010, "Niobium-Bearing Structural Steels for the 21st Century," *Niobium Bearing Structural Steels*, S. G. Jansto and J. Patel, eds., The Minerals, Metals & Materials Society (TMS), Pittsburgh, PA, pp. 1-27.

Jhamb, I. C., and MacGregor, J. G., 1974a, "Effect of Surface Characteristics on Fatigue Strength of Reinforcing Steel," *Fatigue of Concrete*, SP-41, American Concrete Institute, Farmington Hills, MI, pp. 139-167.

Jhamb, I. C., and MacGregor, J. G., 1974b, "Stress Concentrations Caused by Reinforcing Bar Deformations," *Fatigue of Concrete*, SP-41, American Concrete Institute, Farmington Hills, MI, pp. 169-182.

López, B.; Pereda, B.; Bastos, F.; Rebellato, M.; and Rodriguez-Ibabe, J. M., 2018, "Challenges of Nb Application in Thermomechanical Processes of Steels for Long Products," *Materials Science Forum*, V. 941, pp. 386-393. doi: 10.4028/www.scientific.net/MSF.941.386

Pang, G.-Y.; Zhang, J.-M.; Zhang, H.-T.; Liu, C.-B.; Wang, R.-Z.; and Wan, Y., 1981, "The Relationship of Microstructure and Mechanical Properties of Hot Rolled Nb-Microalloyed High Strength Rebar Steel," Central Iron & Steel Research Institute, Beijing, China.

Restrepo-Posada, J. I.; Dodd, L. L.; Park, R.; and Cooke, N., 1994, "Variables Affecting Cyclic Behavior of Reinforcing Steel," *Journal of Structural Engineering*, ASCE, V. 120, No. 11, Nov., pp. 3178-3196. doi: 10.1061/(ASCE)0733-9445(1994)120:11(3178)

Rocha, M.; Brühwiler, E.; and Nussbaumer, A., 2016, "Geometrical and Material Characterization of Quenched and Self-Tempered Steel Reinforcement Bars," *Journal of Materials in Civil Engineering*, ASCE, V. 28, No. 6, June, p. 04016012. doi: 10.1061/(ASCE)MT.1943-5533.0001355

Samuel, F. H.; Barbosa, R.; Boratto, F.; Yue, S.; and Jonas, J. J., 1988, "Laboratory Simulation of Flow Stresses During Strip Rolling Using High Strain Rate Torsion Testing," *International Conference on Physical Metallurgy of Thermomechanical Processing of Steels and Other Metals: Proceedings of THERMEC-88*, I. Tamura, ed., Tokyo, Japan.

Sattar, S.; Ryan, K.; Arendt, L.; Bonowitz, D.; Comerio, M.; Davis, C.; Deierlein, G.; and Johnson, K. J., 2021, "Recommended Options for Improving the Built Environment for Post-Earthquake Reoccupancy and Functional Recovery Time," NIST-FEMA Special Publication FEMA P-2090/NIST SP-1254, Federal Emergency Management Agency (FEMA), Washington, DC, and National Institute of Standards and Technology (NIST), Gaithersburg, MD, Jan., 135 pp.

Slavin, C. M., and Ghannoum, W. M., 2015, "Defining Structurally Acceptable Properties of High-Strength Steel Bars through Material and Column Testing: Part I: Material Testing Report," CPF Research Grant Agreement No. 05-14, Charles Pankow Foundation, Haymarket, VA, 135 pp.

Sokoli, D., and Ghannoum, W. M., 2016, "High-Strength Reinforcement in Columns under High Shear Stresses," *ACI Structural Journal*, V. 113, No. 3, May-June, pp. 605-614. doi: 10.14359/51688203

Sokoli, D.; Hogsett, G.; Limantono, A. A.; Suselo, A.; Al-Tarafany, D.; and Ghannoum W. M., 2019, "Acceptable Elongations and Low-Cycle Fatigue Performance for High-Strength Reinforcing Bars," CPF Research Grant Agreement No. 03-16, Charles Pankow Foundation, Haymarket, VA, 213 pp.

Sokoli, D.; Limantono, A.; and Ghannoum, W. M., 2020, "Special Moment Frames with High-Strength Reinforcement—Part 2: Columns," *ACI Structural Journal*, V. 117, No. 2, Mar., pp. 253-265.

Sokoli, D.; Shekarchi, W.; Buenrostro, E.; and Ghannoum, W. M., 2014, "Advancing Behavioral Understanding and Damage Evaluation of Concrete Members Using High-Resolution Digital Image Correlation Data," *Earthquakes and Structures*, V. 7, No. 5, Nov., pp. 609-626.

Stalheim, D.; Slifka, A.; Lucon, E.; Uranga, P.; and Kang, D.-H., 2021, "Effect of Through-Thickness Microstructural Homogeneity on Fatigue Performance of Structural Steels in Air and Hydrogen Environments," *AISTech 2021—Proceedings of the Iron & Steel Technology Conference*, J. M. Emling and E. C. Williams, eds., Nashville, TN, pp. 924-934. doi: 10.33313/382/09110.33313/382/091

Subramanian, S. V., 2007, "Thermo-mechanical Processing Options of High Niobium Microalloyed Steel Line Pipe Applications," CBMM/CITIC Metal Pipeline Seminar, Beijing, China.

To, D. V., and Moehle, J. P., 2020, "Special Moment Frames with High-Strength Reinforcement—Part 1: Beams," *ACI Structural Journal*, V. 117, No. 2, Mar., pp. 239-252.

Wang, C.-H., 1996, "Introduction to Fracture Mechanics," Report No. DSTO-GD-0103, DSTO Aeronautical and Maritime Research Laboratory, Melbourne, VIC, Australia, July, 82 pp.

Zajac, S., 2005, "Precipitation of Microalloy Carbo-nitrides Prior, During and After γ/α Transformation," *Materials Science Forum*, V. 500-501, Nov., pp. 75-86.

Zaki, A., 2020, "More Buildings and Construction Projects Set to Open in Christchurch This Year," accessed 9/7/2020, Radio New Zealand (RNZ), Wellington, New Zealand, Jan. 20, https://www.rnz.co.nz/news/national/407665/more-buildings-and-construction-projects-set-to-open-in-christchurch-this-year. (last accessed Dec. 19, 2024)

Zhang, Y.; Guo, A.; and Yong, Q., 2018, "Strengthening Effects of Niobium on High Strength Rebars," *Journal of Mechanics Engineering and Automation*, V. 8, No. 2, pp. 82-91. doi: 10.17265/2159-5275/2018.02.005

Zheng, H., and Abel, A., 1998, "Stress Concentration and Fatigue of Profiled Reinforcing Steels," *International Journal of Fatigue*, V. 20, No. 10, Nov., pp. 767-773. doi: 10.1016/S0142-1123(98)00051-6

Zhong, K.; Ghannoum, W. M.; and Deierlein, G. G., 2021, "Influence of High-Strength Reinforcing Bars on Seismic Safety of Concrete Frames," *ACI Structural Journal*, V. 118, No. 5, Sept., pp. 299-311.

ACI MATERIALS JOURNAL TECHNICAL PAPER

Title No. 122-M02

Effect of Cement Replacement by Bauxite Residue on Mechanical Properties of Concrete

by Yassine Brahami, Mathieu Fiset, Ali Saeidi, Kadiata Ba, and Rama Vara Prasad Chavali

Concrete, a highly energy-intensive material, contributes approximately 10% of global carbion dioxide (CO_2) emissions. To address this issue, incorporating industrial residues in concrete production has emerged as a viable solution, reducing natural resource consumption and lowering the CO_2 footprint. Using bauxite residues in concrete has proven to be an environmentally friendly and sustainable approach. In this study, cement mass was partially replaced with bauxite residues (at 5%, 10%, 15%, and 20%), with variations in residue diameter (300 µm, 600 µm, and 2 mm) and in liquid form. The concrete's workability, air content, density, mechanical strength, elasticity, Poisson's ratio, and porosity were assessed with each replacement percentage. The study revealed that bauxite residues can effectively replace up to 20% of cement in a concrete mixture. Although their use slightly affects the fresh properties of concrete, it significantly enhances its mechanical properties. With this approach, a sustainable and eco-friendly concrete without compromising its performance can be created.

Keywords: bauxite residue; cement; mechanical properties.

INTRODUCTION

The modern world is facing several challenges originating from the construction industry, which revolve mainly around the use of natural resources along with the carbon dioxide (CO_2) emissions generated during cement production. Approximately 5 to 10% of greenhouse gas (GHG) emissions are attributed to cement production and that percentage is expected to increase to 10 to 15% the coming years, or 12 to 15% of the total industrial energy consumption (Hossain et al. 2021). Recent years have seen the emergence of new energy and environmental requirements and challenges giving rise to multiple reflections in different sectors, and more particularly in the construction industry. In this context, the use of industrial by-products to produce concretes and mortars appears as an environmental solution for their disposal as well as the development of ecological and sustainable concretes. One of the environmentally hazardous wastes is bauxite residue from the aluminum industry. Approximately 4 billion tons of bauxite residue is produced each year around the world (Liu et al. 2021). However, industrial use of bauxite residue is very limited, and its quantity is increasing in storage areas.

Bauxite residues can contaminate surrounding soil and water, posing risks to human health and the environment, including toxic effects on flora and fauna. Storing red mud presents significant waste management challenges as it requires large areas and strict measures to prevent leaks and accidental spills. In concrete, bauxite residues are used to partially replace cement, reducing cement consumption, which is a major source of CO_2 emissions. Several studies suggest that bauxite residues chemically react with cement components to form hydrated cementitious products, enhancing the mechanical properties of the concrete, particularly at an early age. The alkaline components of bauxite residues can be immobilized in the cement matrix, limiting their mobility and potential for contamination. Few authors found that when properly incorporated into concrete, bauxite residues are chemically stabilized, thus it can be stated that the presence of red mud in concrete would not make negative influence on the leaching (Tang et al. 2019).

The source of bauxite and the aluminum extraction process significantly influence their chemical and mineral composition, as well as their physical characteristics such as particle size, pH, and particle type. Each bauxite deposit has a unique composition, and processes such as the Bayer, Pederson, and combination methods variably alter these residues (Liu et al. 2007). These differences directly impact the properties of concrete when mixed with bauxite residues (Di Mare et al. 2021). For instance, particle size and alkalinity can affect the mechanical strength and durability of concrete. The chemical composition of bauxite residues also influences the setting time and porosity of concrete.

Several works have been published on the use of bauxite residues in conventional concretes. For example, Sunitha and Prakash (2014) investigated the use of washed and unwashed bauxite residues in concrete for partial cement replacement at grades of 0 to 20% with a 2% range. They found that shear strength, compressive strength, and tensile strength measured by bending and splitting increased with an increasing amount of bauxite residue washed up to 8% and unwashed up to 8%; thereafter, a reduction in resistance was observed. Also, water absorption and sorptivity were observed to decrease with increasing bauxite residue in concrete. The strength, workability, and sorptivity of washed bauxite residue concrete were superior to those of unwashed residue. Shetty et al. (2014) investigated the strength aspects of self-consolidating concrete prepared by partially replacing cement with bauxite residues at 1, 2, 3, and 4% and, in the same mixture, partial sand replacement was carried out with iron ore residues at percentages of 10, 20, 30, and 40%. Each mixture with bauxite and iron ore

ACI Materials Journal, V. 122, No. 1, January 2025.
MS No. M-2023-253.R3, doi: 10.14359/51744374, received November 8, 2024, and reviewed under Institute publication policies.

residue replacement achieved higher strengths than a control concrete. After 28 days of curing, the control blend reached a compressive strength, f_c' of 32.8 MPa. The mixture with 2% bauxite residue and 30% iron ore residue achieved the greatest compressive strength and tensile strength, with approximately 22% and 26% increase over the control concrete, respectively. Raj and Rajab (2018) examined the strength of self-consolidating concrete in which portland cement was partially replaced with bauxite residue at proportions of 1, 2, 3, and 4% in 30 MPa grade concrete. Their findings indicated that the incorporation of bauxite residue enhanced the compressive strength of each mixture compared to the control mixture. At 28 days, the mixture with 2% bauxite residue showed a significant increase in both compressive and flexural strengths compared to the control concrete. Illavarason et al. (2018) replaced the cement with residues at proportions of 0, 5, 10, 15, and 20% bauxite residues, and a constant amount of hydrated lime of 5% in 30 MPa conventional concrete. Compressive and tensile strength results demonstrated an increase to 5, 10, and 15%, then a decrease to 20% with a 10% and 14% increase in compressive and tensile strength, respectively. Ye et al. (2018) proposed using bauxite residue to partially replace fly ash (12.5, 25, and 50%) in self-consolidating concrete. The test results revealed that the addition of bauxite residue caused a considerable loss of fluidity and that the mechanical strength of the concrete increased with increasing bauxite residue content. The samples of 50% bauxite residue provided the best results in terms of compressive strength, with an increase of 7% compared to the control concrete. On the other hand, for the tensile strength, the mixtures of 25% bauxite residues gave the best results with an increase of 5% compared to the control concrete. Bayat et al. (2018) replaced slags with bauxite residues at percentages of 0, 10, 20, 30, and 40% by weight of the slag. The authors found that the mixtures containing 10 and 20% bauxite residue showed a higher compressive strength at 7 and 28 days than the control mixture of portland cement concrete. Thus, it can be deduced that a higher content of bauxite residue leads to a lower uniaxial compressive strength of the concrete. The tensile strength measured by a bending test of all slag concrete and bauxite residue specimens was lower than that of slag-alone concrete and the control mixture. Most recently, Song et al. (2022) found optimal mixture proportions of autoclave aerated concrete with 22.5% of bauxite residue replacement of fly ash along with the use of polycarboxylic acid.

RESEARCH SIGNIFICANCE

Previous studies have demonstrated the effective use of bauxite residues in replacing cement in various types of concrete; however, the specific use of bauxite residues from the Saguenay–Lac-Saint-Jean (SLSJ) region for concrete applications remains unexplored. To date, the SLSJ bauxite residues have not been studied with respect to particle size and replacement levels up to 20%. This research fills a critical knowledge gap by providing, for the first time, detailed insights into the impact of these residues on concrete performance. The study is conducted with the aim of reducing GHG emissions and mitigating the environmental impact of bauxite residue disposal. Furthermore, when developing new types of concrete, it is essential to verify the equations predicting the mechanical properties to incorporate the parameter representing bauxite residues into the concrete formulation that complies with current standards and regulations.

With an estimated production of 1 million tons of bauxite residue annually in the SLSJ region, it is imperative to conduct a localized investigation to assess the performance of bauxite residue-based concrete and promote its widespread adoption. This study specifically examines the effects of partial cement replacement with SLSJ bauxite residues on the physico-mechanical behavior of specialized concrete (Rio Tinto 2016). Various substitution levels and particle sizes were considered to optimize economic benefits and enhance residue reuse. The properties of both fresh and hardened concrete were evaluated to ensure a comprehensive understanding of the design parameters. Moreover, building on existing predictive models, new equations were proposed to accurately assess the mechanical properties of bauxite residue-based concrete as a function of the substitution rate, ensuring compliance with current standards and regulations.

PHYSICOCHEMICAL PROPERTIES OF BAUXITE RESIDUES

Bauxite residues' colors are often gray-white to red, depending on the existing amount of iron oxide. The melting point, density, and bulk density of bauxite residues are between 1100 and 1500°C, 2700 and 3200 kg/m^3, and 750 and 1000 kg/m^3, respectively (Anagnostopoulos et al. 2021; Atan et al. 2021; Hong et al. 2021; Sun et al. 2021). Bauxite tailings have a pH between 10 and 12.5, which is highly alkaline. The plasticity index is 17.2 to 30.5 (Panda et al. 2017; Wang et al. 2021).

The grain size of the bauxite residue is extremely fine. Kumar and Kumar (2013) used a laser particle size analyzer to determine the particle size distribution of bauxite residue and found that its distribution was narrower than the one of fly ash used in concrete. The surface area of bauxite residues is approximately 12 to 59 m^2/g, and the grain diameter is between 3 and 75 μm. Consequently, bauxite residues indicate excellent adsorption. For practical uses, the majority of studies focused on the particle size and fineness of bauxite residue as a substitute for cement powder.

Al_2O_3, Fe_2O_3, SiO_2, Na_2O, CaO, MgO, and K_2O are the main chemical compounds of the bauxite residue. Table 1 shows the typical chemical composition of bauxite residue from different aluminum manufacturing processes and compares it to portland cement. Bauxite residue can also be weakly radioactive due to the presence of metals, rare earths, and traces of radioactive elements such as uranium and thorium (Hong et al. 2021; Milačič et al. 2012; Paramguru et al. 2004; Wang et al. 2021). Due to regional variations in raw resources, aluminum manufacturing procedures, and technical advances, the chemical composition of bauxite residue varies from one production location to another. The estimated chemical compositions of bauxite

Table 1—Chemical composition of portland cement and bauxite residues

Composition	Portland cement, %	Bauxite residue		
		Manufacturing process		
		Bayer, %	Pedersen, %	Combination, %
CaO	61 to 70	1 to 9	45 to 49	43.5 to 47
SiO_2	20 to 25	4 to 20	22 to 23	20 to 21
Al_2O_3	3.5 to 7.5	12 to 24	4 to 7	5.5 to 7.5
Fe_2O_3	1.5 to 6	35 to 65	6 to 10	6 to 7.5
MgO	1.5 to 4	0.2 to 0.3	1.3 to 1.6	—
SO_3	0.05 to 3.5	0.60 to 0.8	—	—
K_2O	0.05 to 1.4	0.04 to 0.05	0.3 to 0.4	0.4 to 0.7
Na_2O	0.05 to 0.7	3 to 10	2.5 to 3.5	2.7 to 3
Chloride	0 to 0.1	—	—	—
Insoluble	0.05 to 1.2	—	—	—
Fire losses	0.2 to 3	10 to 16	7 to 10	—
Free lime	1.0	—	—	—

Fig. 1—Bauxite residues used.

residue generated by Bayer, sintering, and combination processes are shown in Table 1 (Liu et al. 2021). Compared to the bauxite residue produced by the sintering process, the bauxite residue from the Bayer process has a lower content of calcium and silicon and a higher concentration of Al, Fe, and Na, as shown in Table 1.

EXPERIMENTAL PROCEDURE

To be able to characterize the physical and mechanical properties of concretes with different percentages of bauxite and bauxite residue diameters, tests in fresh condition and in the hardened state are determined for the formulation of the control concrete with a grade of 30 MPa and bauxite residue formulations.

The mechanical properties are limited to compressive strength, tensile strength, modulus of elasticity, Poisson's ratio, and porosity available to water in compliance with CSA A23.1 (2019) and CSA A23.2 (2019) standards. The slump and air content tests were also carried out to know the properties in the fresh state of the concrete. Specimens made of 300 µm diameter bauxite residue concrete and control mixtures of portland cement concrete were placed and cured for 7, 28, 90, and 180 days, while the bauxite residue concretes—of diameters 600 µm and 2 mm and liquid red mud—were tested at 7 and 28 days only.

Bauxite residues

The bauxite residues used in this study are those produced by the Rio Tinto refinery in the SLSJ region, province of Quebec, through the Bayer process. The bauxite residues were collected as red mud (Fig. 1) dried at 110 ± 5°C in a muffle oven for 48 hours. Subsequently, the dried residue was crushed and sieved manually to different sizes: 300 µm, 600 µm, and 2 mm (Fig. 2).

Cement

The portland cement used was manufactured by a Canadian cement plant. It was GUL type (portland-limestone cement for general use), characterized by a bulk density of 3220 kg/m^3 and a specific surface of 3275 cm^2/g.

Aggregates

A crushed fine aggregate with a specific gravity of 2.56, fineness modulus of 2.6, water absorption of 1.01%, and maximum size of 5 mm conforming to CSA A23.1-19, was used. Similarly, coarse aggregate with a density of 2.67 g/cm^3, maximum size of 20 mm, and water absorption

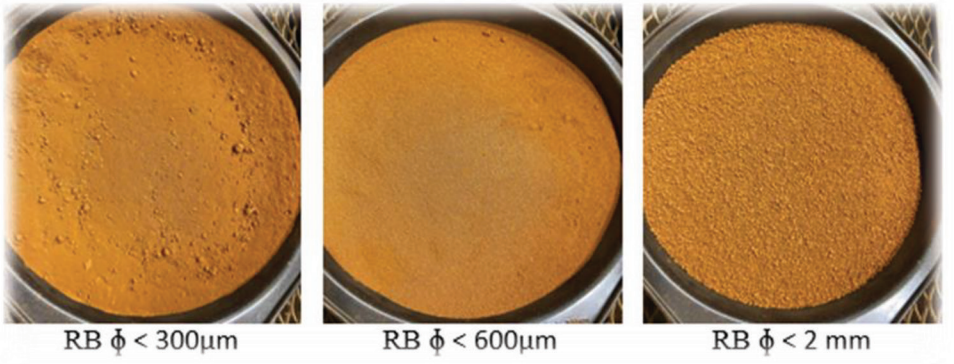

Fig. 2—Sieve analysis of bauxite residues.

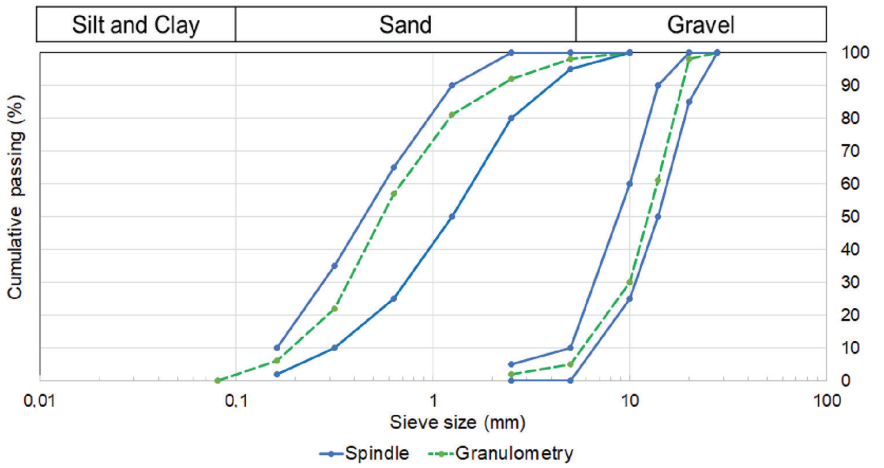

Fig. 3—Particle size distribution curves for aggregates (CSA A23.2-19).

of 1.39% was used. Aggregate particle size curves can be seen in Fig. 3.

Additive

The proportion of high-range water-reducing admixture (HRWRA) used is 0.55% by weight of binder. The HRWRA was used to improve the workability of the concrete and reduce segregation. The extra type of air entrainer was used in a proportion of 0.85% by weight of binder. Dispersant was added at 0.80% by weight binder.

Mixture composition

The design of the mixture was carried out in accordance with CSA A23.1-19. The control concrete mixture (only portland cement) used in this experimental program aimed for a uniaxial compressive strength of 30 MPa at 28 days, with a water-cement ratio (*w*/*c*) of 0.45 dosed at 370 kg/m^3 and an aggregate ratio of 60% gravel and 40% sand. The concrete mixtures based on bauxite residues were made by replacing the cement with 5, 10, 15, and 20% of bauxite residue for each of the bauxite residue diameters: 300 µm, 600 µm, 2 mm, and in liquid form (Table 2).

The concrete was mixed in a concrete mixer with a capacity of 70 kg. In the first mixing step, the two types of aggregates were added separately and mixed for 2 minutes with the air-entraining agent and one-third the amount of water used. In the second stage, the bauxite residues, cement, and dispersant were added separately and mixed for 1 more minute. In the last step, two-thirds of the amount of water and the HRWRA were added and mixed thoroughly for another 5 minutes to obtain a homogeneous mixture. Prior to placing the concrete in the molds, the workability of each mixture was measured using the slump cone test as well as air content and density. The molds were filled with concrete in three layers; in each layer, 20 mallet strokes were given. Once the mold was filled, the excess concrete was removed, and the surface was levelled using a trowel. Twenty-four hours after casting, the specimens were removed from the mold and cured at 100% humidity. A total of 222 cylindrical specimens (75 x 150 mm) were subsequently cast and tested to determine compressive strength, tensile strength, modulus of elasticity, and Poisson's ratio at various ages.

For each of the mixtures tested, three specimens were tested for each of the tests. The uniaxial compression tests were carried out according to the CSA A23.2-19 standard with a universal testing machine at the University of Quebec at Chicoutimi. The specimens were subjected to a preload of 0.8 kN and then loaded at a rate of 1.14 kN/s until failure. The compressive strength was obtained by taking the average of the three specimens. Stress-strain curves for each blend were obtained by testing the cylindrical specimens under uniaxial compression. The data-acquisition system consisted of a 100 mm vertical extensometer cell and a horizontal extensometer mounted on a belt to measure the load and corresponding displacements of the specimens.

Table 2—Concrete formulation

	Bauxite residue content	Cement, kg	Fine aggregates, kg	Coarse aggregates, kg	Bauxite residues, kg	Water, L
Control concrete	0%	370.0	767.5	1151.3	0	166.5
Bauxite residue diameter < 300 µm	5%	351.5	766.0	1149.0	18.5	169.0
	10%	333.0	764.5	1146.5	37.0	171.5
	15%	314.5	762.7	1144.0	55.5	174.0
	20%	296.0	761.1	1141.6	74.0	176.5
Bauxite residue diameter < 600 µm and < 2 mm	5%	351.5	766.0	1149.0	18.5	166.5
	10%	333.0	764.5	1146.5	37.0	166.5
	15%	314.5	762.7	1144.0	55.5	166.5
	20%	296.0	761.1	1141.6	74.0	166.5
Bauxite residues in liquid form	5%	351.5	766.0	1149.0	18.5	161.5
	10%	333.0	764.5	1146.5	37.0	156.7
	15%	314.5	762.7	1144.0	55.5	152.0
	20%	296.0	761.1	1141.6	74.0	147.5

Note: All mixtures included 1.000 L of air-entraining agent, 0.925 L of dispersant, and 0.650 L of HRWRA.

The tensile strength was measured by the Brazilian tests according to CSA A23.2. Three concrete cylinders for each mixture were tested by the Brazilian testing machine with a preload of 0.8 kN and a load rate of 1.14 kN/s. The tensile strength was obtained by taking an average of the three samples.

The calculation of the tensile strength is carried out using Eq. (1)

$$f_{ct} = \frac{2P}{\pi l d} \quad (1)$$

where f_{ct} is tensile strength measured by splitting (MPa); P is maximum load applied (N); l is length of the specimens (mm); and d is specimen diameter (mm).

The water-accessible porosity was measured using the water absorption test by immersion at atmospheric pressure. After demolding, three specimens of each percentage of bauxite residue from the 300 µm series as well as the control concrete were kept in a humid room at 20 ± 2°C, with over 95% relative humidity until 180 days of age. At this point of the water-accessible porosity test, the specimens were weighed and exposed to drying at a temperature of 110 ± 5°C for 48 hours. Then the specimens were also weighed after drying. The porosity is expressed as a percentage of the dry mass of the specimen. Indeed, to obtain the porosity of a concrete, it is enough to multiply the water absorption by immersion (in %) by the dry specific mass of this concrete, expressed in kg/dm^3.

EXPERIMENTAL RESULTS AND DISCUSSION

Fresh-state properties

Workability—The workability of all mixtures was measured between the 16th and 18th minute after water-binder contact using a slump cone tester according to CSA A23.2. The measured values for the mixtures are shown in Fig. 4. According to the developed method of the control concrete, the slump value should be between 50 and 110 mm

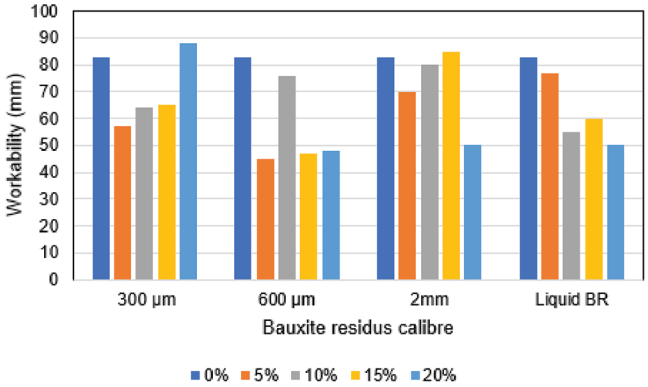

Fig. 4—Effects of bauxite residue on mixture slump.

(plastic concrete). It can be seen from Fig. 4 that the control concrete meets this requirement with a slump of 83 mm. The substitution of cement by bauxite residues in the concrete reduced the slump, thereby decreasing its workability. A similar observation of decrease in workability for identical mixtures was mentioned by other researchers (Liu and Poon 2016). For very-fine-grained mixtures (300 µm), it was necessary to increase the water content by 1.5% for each 5% of bauxite residue to maintain workability and acceptable slump. This need for additional water can be explained by the high water absorption by the bauxite residue (Table 2), which has been observed by other researchers (Bayat et al. 2018; Tang et al. 2018). Finally, as can be seen in Fig. 4, the slump value respects the prescribed limits with the initial dosage, without water modification, for the bauxite residues of 600 µm and 2 mm. It can also be seen for the mixtures of 600 µm and 2 mm that the size of the bauxite residues have an influence on the workability of the concrete. For mixtures with liquid bauxite residues, the amount of water was fixed with the assumption of 40% solid and 60% liquid in liquid bauxite residue. However, the decrease in workability of concrete with increase of liquid bauxite residues indicates a possible high percentage of solids in liquid bauxite residue.

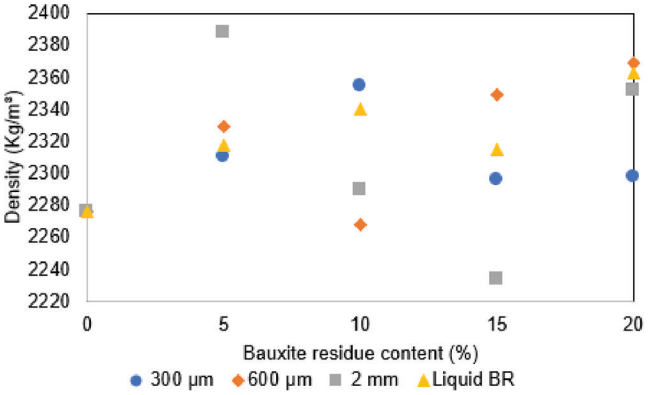

Fig. 5—Effects of bauxite residues on mixture density.

Density—The density of concrete was determined according to CSA A23.2. The results obtained are shown in Fig. 5. It can be seen that the density of the bauxite residue concrete is slightly higher than that of the control concrete. Otherwise, for the different diameters, it is found that there is no apparent effect on the density. According to CSA A23.2, the density of standard portland cement concrete typically ranges from 2250 to 2350 kg/m^3. For the mixtures tested, the density of the bauxite residue concrete varies from 2200 to 2500 kg/m^3, which remains similar to conventional portland cement concrete. It can also be seen that the mixtures with lower density exhibited high workability as compared to denser mixtures for all combinations.

Air content—The entrained air content was determined according to standard CSA A23.2. Figure 6 shows the results obtained for the different proportions and sizes of bauxite residue. A slight decrease in the amount of entrained air in the range of 3.2 to 7% is observed as the amount of bauxite residue increases in the concrete mixture. According to CSA A23.2, the entrained air value varies from 5 to 8%, which is the case for the control concrete with a value of 6%.

Hardened-state properties

After wet properties were measured, the mixtures were cast into cylinders 76.2 mm in diameter by 152.4 mm high, in accordance with CSA A23.2 to measure certain properties in the cured state. All specimens underwent wet curing for a period varying from 7 to 180 days before being tested by a uniaxial compression or splitting test (Brazilian tests) according to CSA A23.2. These tests made it possible to measure the compressive strength, tensile strength, stress-strain behavior, stiffness, and Poisson's ratio.

Compressive strength—Figure 7 presents the average resistance (average of three cylinders) in compression of the partially replaced concrete versus various percentages of bauxite residues of different diameters. The results indicate that the strength of bauxite residue concrete increases with addition of residue content up to 10% and with curing time. The enhanced strength of bauxite residue concrete with curing regime can be attributed to the formation of calcium-silicate-hydrates (C-S-H gel) in the presence of calcium and silica. Beyond 10%, further addition of bauxite residue content resulted in reduction of strength. The reduction in strength of concrete can be attributed to limited pozzolanic

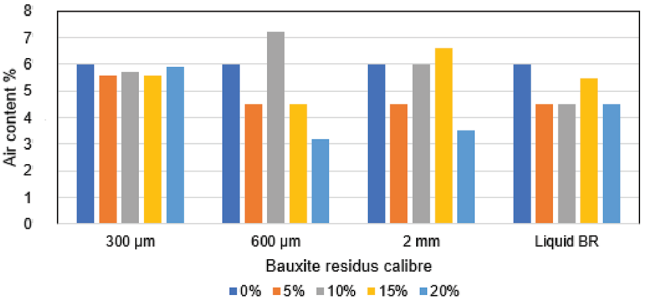

Fig. 6—Effects of bauxite residues on air content of mixtures.

reaction owing to inadequate water at higher proportions of residue replacement (Tang et al. 2018). The effects of bauxite residue content on improving compressive strength were more pronounced at rates of 5 and 10% for the four different diameters, while compressive strength decreased as their proportion rose. This observation is analogous to studies by Illavarason et al. (2018). The strength of bauxite residue concrete for all tested mixtures ranges from 21.4 to 41.0 MPa after 28 days of curing, which means a decrease of 23% and an increase of 45% compared to the control concrete, respectively. On the other hand, for the series of 600 µm, 2 mm, and liquid form, the strength is variable according to the content of residue. However, up to 20% replacement, the concrete exhibits compressive strength similar to the portland cement control concrete, without bauxite residue. Figure 8 shows fracture of bauxite residue concrete as a function of bauxite residue content. With the 5 and 10% bauxite residue, the concrete had a lot of fresh breaks in the gravel. On the other hand, for 15 and 20%, much more tearing of the concrete paste was seen.

Figure 9 shows the curing rate of bauxite residue concrete and control concrete between the seventh and 28th days for all mixtures. According to CSA A23.3 (2019), conventional concrete reaches approximately 80% of its compressive strength measured between the seventh and the 28th days. In this study, the control concrete, without bauxite residue, showed an 84% increase in its compressive strength from 7 to 28 days. In comparison, bauxite residue concrete has a faster rate of curing, of up to 93% of its predicted compressive strength on day 28 after only 7 days. On the other hand, there does not seem to be a clear trend of the effect of bauxite residue particle size on the rate of curing as observed in Fig. 9.

Table 3 compares the average compressive strengths measured with those predicted with Eq. (2) of the compressive strength given by the *fib* Model Code for Concrete Structures (2010). The results show that the predicted strength value of the bauxite residue concretes as well as the control concrete is always higher than the average experimental value measured. The difference between the resistances obtained shows that there is a certain difference while increasing the contents of bauxite residues and the duration of cure.

$$f_c(t) = \beta_{cc}(t) \cdot f_c' \tag{2}$$

where

$$\beta_{cc}(t) = \exp\left\{s\left[1 - \left(\frac{28}{t}\right)^{0.5}\right]\right\} \tag{3}$$

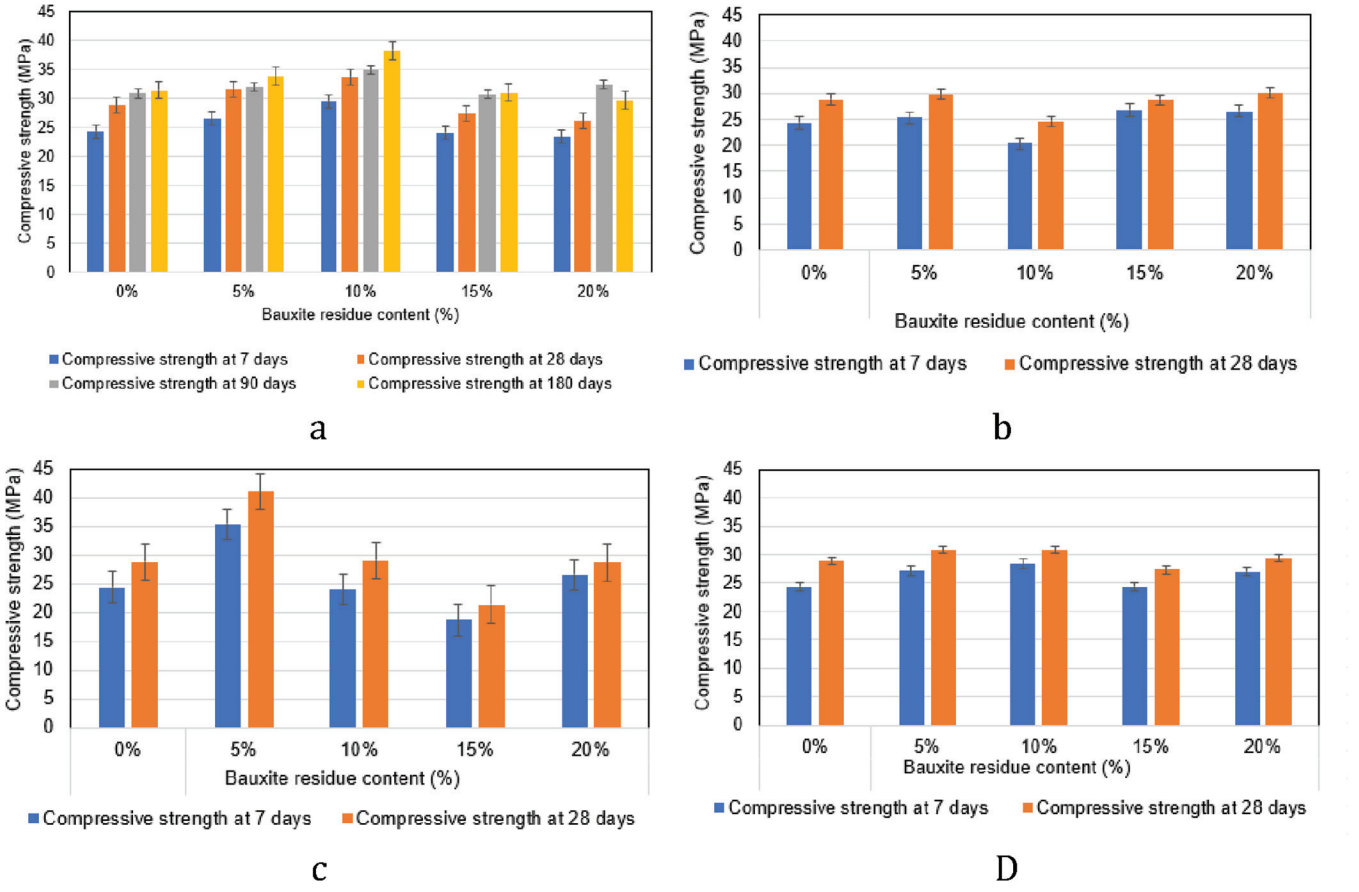

Fig. 7—Uniaxial compressive strength measured on cylinder for different curing times and for maximum dry particle size of bauxite residue of: (a) 300 µm; (b) 600 µm; (c) 2 mm; and (d) as raw liquid.

f_c' is the average compressive strength at an age (t) that can be estimated by $f_c(t)$, according to Eq. (2). $\beta_{cc}(t)$ is a function that describes the development of resistance with time depending on two parameters, where t depends on the age of concrete and s is a coefficient that depends on the class of the strength of the cement. The value of s varies between 0.20 and 0.38, while the cement used in this study has a value of $s = 0.25$.

To accurately predict the compressive strength of bauxite residue concretes, the authors defined the relationship between the parameter s of Eq. (3) and the bauxite residue content from the experimental results. Figure 10 presents the value of the optimal coefficient s as a function of the bauxite residue content. The results show that the value of s decreases with the increase in the amount of bauxite residue in the concrete, which means that the curing of the concrete is faster with the increase in the content of bauxite residue. From Fig. 10, it can be concluded that there is a linear relation between s and the content of bauxite residues with a coefficient of determination $R^2 = 0.65$ defined by Eq. (4), where BR is the bauxite residue content expressed as a percent. This relationship is valid for the range of experimental bauxite residue content data.

$$s = 0.17 - 0.14(BR) \quad (4)$$

The maturity equation allows for predicting the gain in mechanical strength of concrete over time, which is essential for determining when the concrete has reached sufficient strength to be loaded. In other words, this equation helps estimate the time required for fresh concrete to achieve the desired strength, a vital parameter for construction planning and timeline optimization.

Tensile strength—The indirect tensile strength was determined by the Brazilian test at day 28, according to CSA A23.2. Figure 11 shows the tensile strength for the 300 µm mixtures and the control concrete after 28 days of curing. By comparing the tensile strengths measured with those measured in compression (Fig. 7(a)), it is possible to observe that the tensile strength represents approximately 10% of the compressive strength. A slight increase in tensile strength is observed for the mixtures containing 5 and 10% bauxite residue, with an increase of 0.2 and 0.4 MPa, respectively, compared to the control mixture of portland cement concrete. For higher bauxite residue contents of 15 and 20%, the tensile strength is approximately 0.25 MPa lower than that of the cement concrete control mixture.

The results of the direct tensile strength (f_{ct}) predicted by Eq. (5) (ACI Committee 318 2019) as well as the experimental results obtained for different bauxite residue contents are presented in Table 4. The error between the theoretically calculated value according to the CSA standard and the experimental results is generally low.

$$f_{ct} = 0.56\sqrt{f_c'} \quad (5)$$

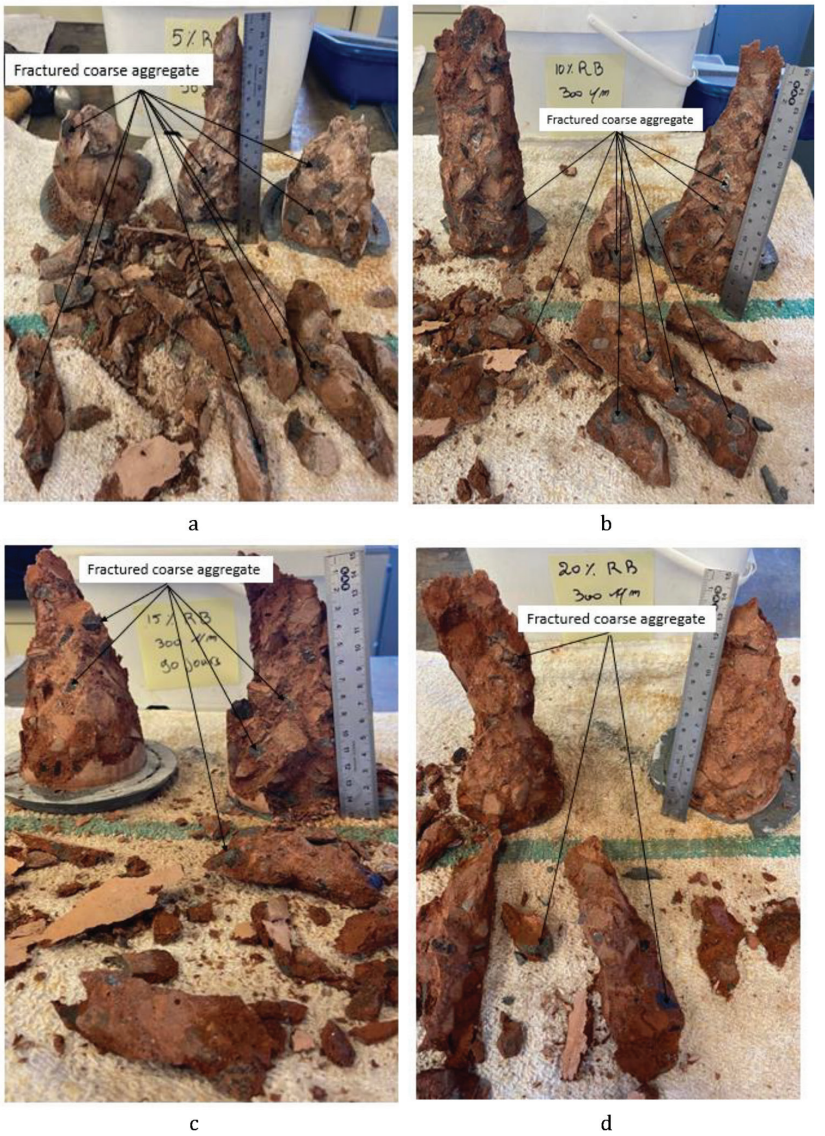

Fig. 8—Typical specimen photo after rupture by compression testing for contents of: (a) 5%; (b) 10%; (c) 15%; and (d) 20%.

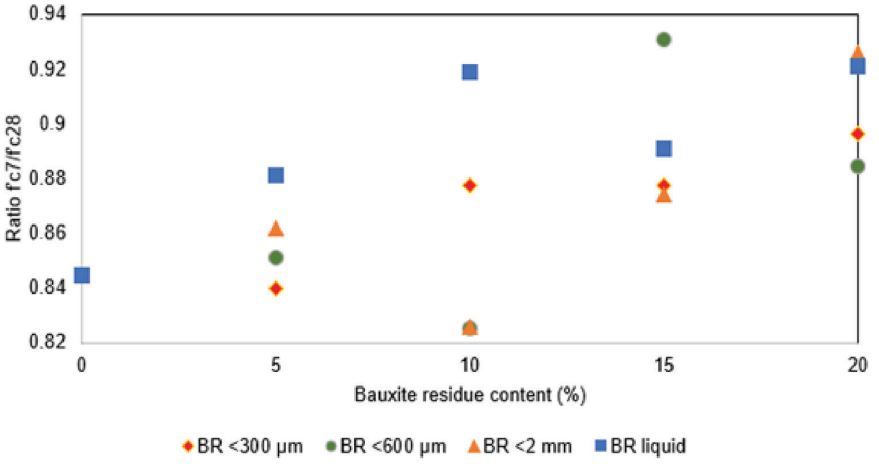

Fig. 9—Concrete curing rate as function of time.

Elasticity module—Figure 12 shows the modulus of elasticity on the different specimens during uniaxial compression tests, after different curing times, and for different contents and sizes of bauxite residues used in the mixtures. The modulus of elasticity was measured at 7, 28, 90, and 180 days for the 300 µm series while for the 600 µm, 2 mm, and liquid series, the tests were carried out on days 7 and 28. It is possible to see that with the increase in the bauxite residue

Table 3—Average compressive strength experimentally measured and predicted by *fib* Model Code for Concrete Structures 2010

Compressive strength (RB < 300 µm)		0%	5%	10%	15%	20%
7 days	Experimental, MPa	24.4	26.6	29.6	24.1	23.4
28 days	Prediction, MPa	31.2	34.1	38.0	30.9	30.1
	Experimental, MPa	28.8	31.6	33.7	27.5	26.1
	Error, %	7.7	7.3	11.3	11.0	13.3
90 days	Prediction, MPa	32.2	35.3	37.6	30.7	29.2
	Experimental, MPa	30.9	33.6	37.3	29.2	28.8
	Error, %	4.1	4.8	0.8	4.9	1.4
180 days	Prediction, MPa	33.6	36.9	39.3	32.0	30.5
	Experimental, MPa	31.5	33.8	38.3	30.5	29.7
	Error, %	6.3	8.4	2.5	4.7	2.6

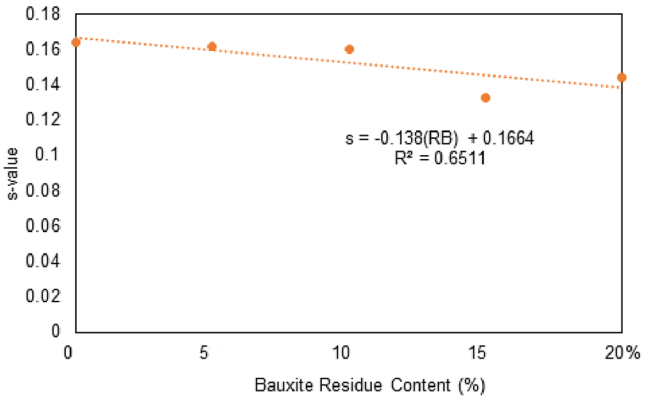

Fig. 10—Value of parameter s *as function of bauxite residue content on day 7.*

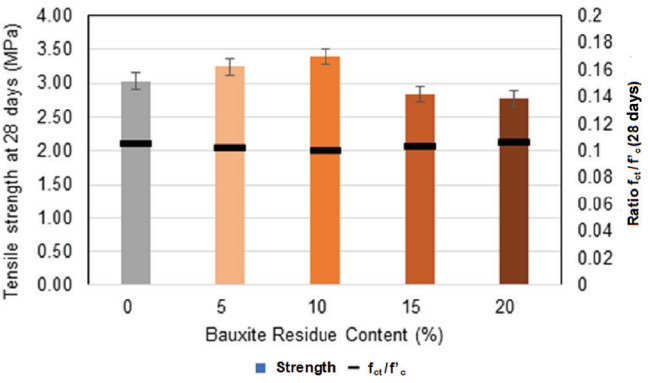

Fig. 11—Tensile strength on day 28 (RB < 300 µm).

content (from 5 to 20%), the elastic modulus of the bauxite residue concrete is generally higher than that of the control concrete. According to these results, it can be concluded that increasing the amount of bauxite residues in the concrete has only a negligible effect on the modulus and elasticity of the mixtures. In fact, the mixtures of the 300 µm series demonstrated a remarkable decrease after 28 days compared to the rest of the mixtures, A decrease of approximately 2 GPa is obtained for all the mixtures of the 300 µm series. After that, the modulus increased on average by 4 GPa at 90 days, followed by a slight decrease after 180 days (refer to Fig. 12(a)). Figure 12(b) presents the results of the modulus

Table 4—Average tensile strength measured experimentally and predicted by Eq. (5)

Tensile strength (RB < 300 µm)	Prediction, MPa	Experimental, MPa	Error, %
0%	2.85	3.03	5.94
5%	3.02	3.25	7.07
10%	3.10	3.40	8.82
15%	2.78	2.84	2.11
20%	2.71	2.79	2.86

of elasticity of the 600 µm series. It was found that only with the 10% of bauxite residues, the modulus of elasticity decreased with time. On the other hand, the modulus of elasticity of the mixtures of 5, 15, and 20% had a gain in rigidity with time. For the 2 mm series and liquid bauxite tailings, the modulus of elasticity increased over time (refer to Fig. 12(c) and (d)).

Table 5 presents the modulus of elasticity calculated according to CSA A23.2 by Eq. (6) (in MPa). The results show that the value of the predicted elastic modulus is always lower than the measured experimental value. The error between the obtained elastic modulus values shows that there are some errors while increasing the bauxite residue contents and the curing time.

$$E_c = 4500\sqrt{f_c'} \quad (6)$$

To minimize the error of the modulus of elasticity of the bauxite residue concrete, Eq. (7) was developed based on the experimental results of the compressive strength and corresponding modulus of elasticity. For each of the specimens tested for all mixtures and at all curing ages, while dividing the value of the modulus of elasticity by the square root of the compressive strength, an average value of 5200 (f_c' in MPa) was obtained.

$$E_c = 5200\sqrt{f_c'} \quad (7)$$

Typically, engineers use the compressive strength measured uniaxially on a cylinder and increased by a power

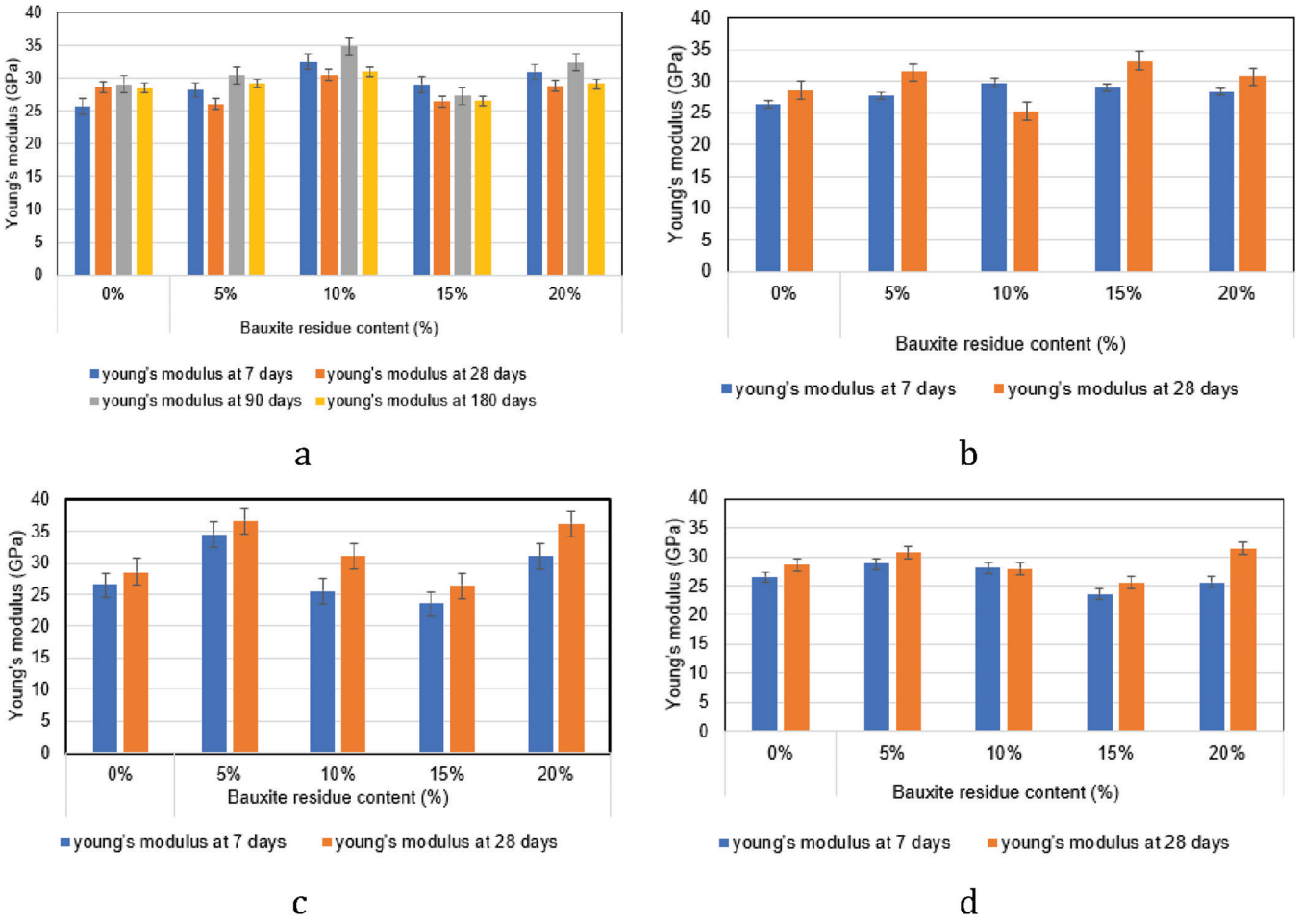

Fig. 12—Modulus of elasticity measured on cylinder at different curing times for maximum dry bauxite residue particle size of: (a) 300 µm; (b) 600 µm; (c) 2 mm; and (d) for bauxite residue liquid.

Table 5—Mean elastic modulus determined experimentally and predicted by Eq. (6)

Elasticity module E_c (RB < 300 µm)		0%	5%	10%	15%	20%
7 days	Prediction, MPa	23.2	23.9	24.8	23.1	22.9
	Experimental, MPa	25.7	28.2	32.5	29.1	31.0
	Error, %	9.73	15.25	23.69	20.62	26.13
28 days	Prediction, MPa	24.6	25.5	26.1	24.2	23.8
	Experimental, MPa	28.6	26.0	30.5	26.4	28.8
	Error, %	13.99	1.92	14.43	8.33	17.36
90 days	Prediction, MPa	25.2	26.0	27.0	24.7	24.6
	Experimental, MPa	29.1	30.4	34.9	27.3	32.4
	Error, %	13.40	14.47	22.64	9.52	24.07
180 days	Prediction, MPa	25.4	26.1	27.3	25.1	24.9
	Experimental, MPa	28.5	29.2	31.0	26.6	29.2
	Error, %	10.88	10.62	11.94	5.64	14.73

of 1/2 to estimate the modulus of elasticity of concrete. Figure 13 shows the relationship between the modulus of elasticity and the square root of the compressive strength. The results reveal that the mixtures tested in this study are generally stiffer than the normal predictions anticipated by the ACI 363 standard model (Eq. (8)) and the CSA A23.3 standard model given by Eq. (6). However, due to the low range of compressive strengths tested (f_c' varying between 21 and 41 MPa at 28 days), it is difficult to establish a relationship between the bauxite residue content, the compressive strength and the modulus of elasticity. Nevertheless, the distribution obtained is similar to that observed on conventional portland cement concretes (Paultre 2017).

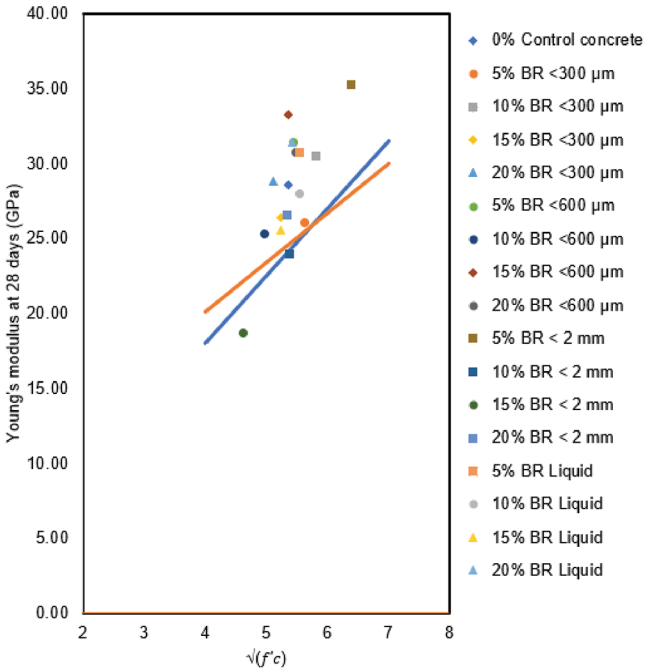

Fig. 13—Modulus of elasticity as function of compressive strength.

$$E_c = \left(3300\sqrt{f_c'} + 6900\right)\left(\frac{\gamma_c}{2300}\right)^{1.5} \quad (8)$$

where E_c is the modulus of elasticity (MPa); f_c' is compressive strength (MPa); and γ_c is density (kg/m^3).

Poisson's ratio—The Poisson's ratio is estimated at an average value of 0.20 according to the *fib* Model Code for Concrete Structures 2010 and CSA A23.2. According to the results of this study, the bauxite residue content had a few effects on the Poisson's ratio. The various Poisson's ratios of the mixtures experimentally determined for each of the 300 µm bauxite residue grades presented in Fig. 14 show that the values for all the mixtures are between 0.17 and 0.18, which is equal to or less than the value determined for the control concrete of 0.18.

Porosity—The variation in porosity with bauxite residue content is shown in Fig. 15. The results show that the porosity of the control concrete is approximately 9.5%. On the other hand, the addition of bauxite residues makes it possible to reduce the porosity between 7.5 and 9%.

CONCLUSIONS

In this paper, the influence of the percentage and the diameter of bauxite residue on the fresh and hardened properties of concrete have all been presented. Therefore, the following conclusions can be drawn:

1. The addition of bauxite residues in concrete has a slightly negative impact on the workability and the air content owing to high water absorption by the bauxite residue.

2. Bauxite residue concretes exhibited quick compressive strength gain in early age compared to control concrete.

3. Grain size and bauxite residue content affect concrete strength. The optimum value of bauxite residues in concrete is 10% of the cement amount. Limited pozzolanic reaction

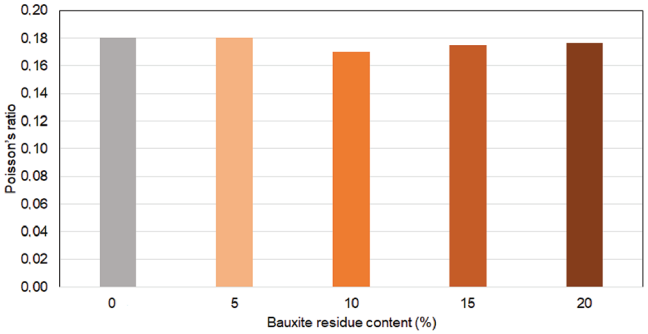

Fig. 14—Poisson's ratio on day 28 (RB < 300 µm).

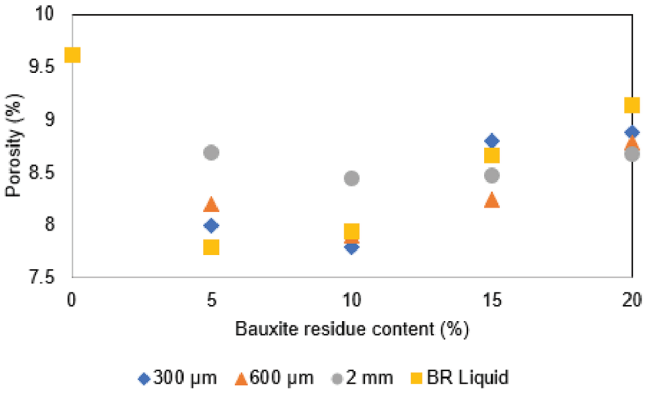

Fig. 15—Porosity of bauxite residue concrete.

owing to inadequate water at higher proportions of residue replacement caused reduction in strength of concrete.

4. The tensile strengths were similar to those of conventional concretes. A mixture of 5% and 10% bauxite residues gave good tensile strengths.

5. Bauxite residues can be used effectively as a replacement material up to 20% of the cement amount, which allows a large use of waste.

AUTHOR BIOS

Yassine Brahami *is Project Manager and Estimator at the civil engineering company Excavations G. Larouche (EGL). He received his master's degree in civil engineering (civil and industrial construction) from the University of Djillali Liabès, Sidi Bel Abbès, Algeria, and his PhD in civil engineering from the Université of Québec at Chicoutimi (UQAC), Saguenay, QC, Canada. His research interests include the development of concrete behavior based on bauxite residue.*

Mathieu Fiset *is a Professor in civil engineering at UQAC and a regular member of the research center on concrete infrastructures. His research interests include structural behavior, shear strengthening, and bond behavior in reinforced concrete structures; the development of innovative low-carbon and geopolymer concrete; the interaction between concrete, in terms of mixture constituents, properties, and pathologies; and the implications for the durability, structural performance, and safety of concrete structures.*

Ali Saeidi *is a Professor of geomechanics at UQAC and holds the Canada Research Chair on forecasting and preventing risks related to hydro-geotechnical hazards. He received his PhD in geomechanics (risk analysis) from the Institut National Polytechnique de Lorraine, Nancy, France. His research interests include risk assessment at the geotechnical level, particularly in relation with the instability of mining stopes, landslides, seismicity, and the erosion of rock masses at dam spillways.*

Kadiata Ba *is a Professor in mechanical engineering at UQAC. She received her PhD in mechanical engineering from the Laval University, Québec, QC, Canada, in 2017. Her research interests include aluminum and composite material, characterization, computer-aided design, numerical*

simulations of manufacturing processes such as friction stir welding and forging, mechanical assembly, and heat treatment.

Rama Vara Prasad Chavali *is a Geotechnical Researcher and an Associate Professor at Velagapudi Ramakrishna Siddhartha Engineering College, Vijayawada, Andhra Pradesh, India. He received his PhD from National Institute of Technology Warangal, Hanamkonda, India, and completed postdoctoral studies at UQAC. His research interests include landslides and permafrost in Canada, soil behavior in changed and extreme environments, and ground improvement and landslides, aiming for safer and more sustainable infrastructure.*

ACKNOWLEDGMENTS

The authors wish to express their gratitude to the Canada Research Chair program grant number 950-232724, and Le Centre de Recherche sur les Infrastructures en Béton (Research Center on Concrete Infrastructures) for financing this research work. The authors also acknowledge the support provided by Rio Tinto, G. Simard, and the research group CURAL-Bauxite-Residue.

REFERENCES

ACI Committee 318, 2019, "Building Code Requirements for Structural Concrete (ACI 318-19) and Commentary (ACI 318R-19) (Reapproved 2022)," American Concrete Institute, Farmington Hills, MI, 624 pp.

Anagnostopoulos, A.; Navarro, M. E.; Stefanidou, M.; Ding, Y.; and Gaidajis, G., 2021, "Red Mud-Molten Salt Composites for Medium-High Temperature Thermal Energy Storage and Waste Heat Recovery Applications," *Journal of Hazardous Materials*, V. 413, p. 125407. doi: 10.1016/j.jhazmat.2021.125407

Atan, E.; Sutcu, M.; and Cam, A. S., 2021, "Combined Effects of Bayer Process Bauxite Waste (Red Mud) and Agricultural Waste on Technological Properties of Fired Clay Bricks," *Journal of Building Engineering*, V. 43, p. 103194. doi: 10.1016/j.jobe.2021.103194

Bayat, A.; Hassani, A.; and Azami, O., 2018, "Thermo-Mechanical Properties of Alkali-Activated Slag–Red Mud Concrete," *Road Materials and Pavement Design*, V. 21, No. 2, pp. 411-433. doi: 10.1080/14680629.2018.1500299

CSA A23.1-19, 2019, "Concrete Materials and Methods of Concrete Construction," CSA Group, Toronto, ON, Canada.

CSA A23.2-19, 2019, "Test Methods and Standard Practices for Concrete," CSA Group, Toronto, ON, Canada.

CSA A23.3-19, 2019, "Design of Concrete Structures," CSA Group, Toronto, ON, Canada.

Di Mare, M.; Monteiro, V. N.; Brial, V.; Ouellet-Plamondon, C. M.; Fortin, S.; Tsesmelis, K.; Montini, M.; and Rosani, D., 2021, "A Calculator for Valorizing Bauxite Residue in the Cement Industry," *Journal of Cleaner Materials*, V. 1, p. 100009. doi: 10.1016/j.clema.2021.100009

fib, 2010, fib *Model Code for Concrete Structures 2010*, Ernst and Sohn, Lausanne, Switzerland.

Hong, Q.; Wang, P.; Chen, Z.; Huang, Z.; Shen, L.; and Song, T., 2021, "Evaluation of Red Mud as Oxygen Carrier for Chemical Looping Combustion of Methane and Biomass in Fluidized Bed," *Fuel Processing Technology*, V. 222, p. 106964. doi: 10.1016/j.fuproc.2021.106964

Hossain, M. U.; Cai, R.; Ng, S. T.; Xuan, D.; and Ye, H., 2021, "Sustainable Natural Pozzolana Concrete–A Comparative Study on its Environmental Performance against Concretes with Other Industrial By-Products," *Construction and Building Materials*, V. 270, p. 121429. doi: 10.1016/j.conbuildmat.2020.121429

Illavarason, P.; Renjit, A.; and Mohan Kumar, P., 2018, "Clinical Evaluation of Functional Vision Assessment by Utilizing the Visual Evoked Potential Device for Cerebral Palsy Rehabilitation," *Procedia Computer Science*, V. 132, pp. 128-140. doi: 10.1016/j.procs.2018.05.174

Kumar, A., and Kumar, S., 2013, "Development of Paving Blocks from Synergistic Use of Red Mud and Fly Ash Using Geopolymerization," *Construction and Building Materials*, V. 38, pp. 865-871. doi: 10.1016/j.conbuildmat.2012.09.013

Liu, C.-J.; Li, Y.-Z.; Luan, Z.-K.; Chen, Z.-Y.; Zhang, Z.-G.; and Jia, Z.-P., 2007, "Adsorption Removal of Phosphate from Aqueous Solution by Active Red Mud," *Journal of Environmental Sciences*, V. 19, No. 10, pp. 1166-1170. doi: 10.1016/S1001-0742(07)60190-9

Liu, R.-X., and Poon, C.-S., 2016, "Utilization of Red Mud Derived from Bauxite in Self-Compacting Concrete," *Journal of Cleaner Production*, V. 112, pp. 384-391. doi: 10.1016/j.jclepro.2015.09.049

Liu, X.; Han, Y.; He, F.; Gao, P.; and Yuan, S., 2021, "Characteristic, Hazard and Iron Recovery Technology of Red Mud - A Critical Review," *Journal of Hazardous Materials*, V. 420, p. 126542. doi: 10.1016/j.jhazmat.2021.126542

Milačič, R.; Zuliani, T.; and Scancar, J., 2012, "Environmental Impact of Toxic Elements in Red Mud Studied by Fractionation and Speciation Procedures," *The Science of the Total Environment*, V. 426, pp. 359-365. doi: 10.1016/j.scitotenv.2012.03.080

Panda, I.; Jain, S.; Das, S. K.; and Jayabalan, R., 2017, "Characterization of Red Mud as a Structural Fill and Embankment Material Using Bioremediation," *International Biodeterioration & Biodegradation*, V. 119, pp. 368-376. doi: 10.1016/j.ibiod.2016.11.026

Paramguru, R. K.; Rath, P. C.; and Misra, V. N., 2004, "Trends in Red Mud Utilization – A Review," *Mineral Processing and Extractive Metallurgy Review*, V. 26, No. 1, pp. 1-29. doi: 10.1080/08827500490477603

Paultre, P., 2017, *Structures en Béton Armé: Analyse et Dimensionnement*, V. 2, Presses Internationales Polytechnique, Montreal, QC, Canada.

Raj, R. K., and Rajab, P. M., 2018, "Effect of Red Mud and Iron Ore Tailings on the Strength of Self Compacting Concrete with Polypropylene Fibre," *International Journal of Civil Engineering and Technology*, V. 9, No. 13, pp. 456-471.

Rio Tinto, 2016, "PUBLIC CONSULTATION REPORT on the Vaudreuil Project beyond 2022," https://transfertconsult.ca/wp-content/uploads/2017/02/Rapport_consultation_Vaudreuil_au-dela_2022_VF4.pdf. (in French) (last accessed Dec. 18, 2024)

Shetty, K. K.; Nayak, G.; and Vijayan, V., 2014, "Effect of Red Mud and Iron Ore Tailings on the Strength of Selfcompacting Concrete," *European Scientific Journal*, V. 10, No. 21.

Song, Y.; Dong, M.; Wang, Z.; Qian, X.; Yan, D.; Shen, S.; Zhang, L.; Sun, G.; Lai, J.; and Ruan, S., 2022, "Effects of Red Mud on Workability and Mechanical Properties of Autoclaved Aerated Concrete (AAC)," *Journal of Building Engineering*, V. 61, p. 105238. doi: 10.1016/j.jobe.2022.105238

Sun, Y.; Li, J.-S.; Chen, Z.; Xue, Q.; Sun, Q.; Zhou, Y.; Chen, X.; Liu, L.; and Poon, C. S., 2021, "Production of Lightweight Aggregate Ceramsite from Red Mud and Municipal Solid Waste Incineration Bottom Ash: Mechanism and Optimization," *Construction and Building Materials*, V. 287, p. 122993. doi: 10.1016/j.conbuildmat.2021.122993

Sunitha, M. P., and Prakash, K. B., 2014, "Effect of Replacement of Cement by Red Mud on the Properties of Concrete," *International Journal of Scientific and Engineering Research*, V. 5, No. 9, pp. 805-814.

Tang, W. C.; Wang, Z.; Donne, S. W.; Forghani, M.; and Liu, Y., 2019, "Influence of Red Mud on Mechanical and Durability Performance of Self-Compacting Concrete," *Journal of Hazardous Materials*, V. 379, p. 120802. doi: 10.1016/j.jhazmat.2019.120802

Tang, W. C.; Wang, Z.; Liu, Y.; and Cui, H. Z., 2018, "Influence of Red Mud on Fresh and Hardened Properties of Self-Compacting Concrete," *Construction and Building Materials*, V. 178, pp. 288-300. doi: 10.1016/j.conbuildmat.2018.05.171

Wang, S.; Jin, H.; Deng, Y.; and Xiao, Y., 2021, "Comprehensive Utilization Status of Red Mud in China: A Critical Review," *Journal of Cleaner Production*, V. 289, p. 125136. doi: 10.1016/j.jclepro.2020.125136

Ye, J.; Hu, A.; Ren, G.; Chen, M.; Tang, J.; Zhang, P.; Zhou, S.; and He, Z., 2018, "Enhancing Sludge Methanogenesis with Improved Redox Activity of Extracellular Polymeric Substances by Hematite in Red Mud," *Water Research*, V. 134, pp. 54-62. doi: 10.1016/j.watres.2018.01.062

ACI MATERIALS JOURNAL TECHNICAL PAPER

Title No. 122-M03

Analytical Model of Concrete Cyclic Behavior in Compression

by Sama Mohammed Saleem, Salman A. Alshamrani, and Hayder A. Rasheed

The modeling of concrete constitutive relationships in cyclic compression has attracted a lot of research attention. In this study, a normalized envelope stress-strain curve made for concrete in uniaxial compression is mathematically derived. The compression loops are formulated using a bilinear unloading path followed by a linear reloading path based on thorough observations and calibrations of available experimental data. The proposed normalized model is calibrated against a set of experimental cyclic stress-strain data. This model is shown to yield robust results by proving it successful in capturing five other independent experimental cyclic stress-strain curves. This proposed model may prove valuable for the implementation and analysis of members subjected to cyclic loading in numerical finite element analysis.

Keywords: compression loading; cyclic loops; envelope curve; stress-strain curve.

INTRODUCTION

The response of concrete to cyclic loading is characterized by several phenomena, including stiffness degradation, strength reduction, and energy dissipation. These behavior indicators are influenced by numerous factors, such as the loading history, loading frequency, stress amplitude, and concrete composition. Thus, understanding the cyclic behavior of concrete subjected to compression loads is a critical topic in the field of constitutive modeling.

Even though conducting experimental testing can provide tangible results for investigating the nonlinear behavior of reinforced concrete (RC) structures, several factors can directly influence the accuracy of the testing, such as specimen sizes, shapes, loading, and boundary conditions. As a result, developing a model that can accurately predict the response of concrete structures subjected to cyclic loading has become an attractive research subject. Accurate modeling of concrete under cyclic loads enables engineers to predict the lifespan and maintenance needs of structures more accurately. This is particularly important in regions susceptible to seismic activity, where structures are regularly exposed to cyclic loading. Concrete exhibits a gradual loss of stiffness under repeated loading, which can be attributed to the formation and propagation of microcracks within the material.[1-5] The cyclic loading leads to a reduction in compressive strength due to cumulative damage.[6-9] Additionally, concrete dissipates energy through hysteresis during cyclic loading, which is a crucial factor in assessing its damping capacity.[10]

Furthermore, the development of an analytical model that comprehensively captures the features of the cyclic behavior of concrete becomes essential in enhancing the understanding of how structures respond to repeated loading. Several models have been developed to simulate the behavior of concrete under cyclic compression. These include empirical models, analytical models, and advanced numerical methods such as finite element analysis (FEA). Empirical models are based on experimental data and provide simplified equations to predict concrete behavior under cyclic loads.[11-17] Analytical approaches often involve constitutive models that describe the stress-strain relationship of concrete under cyclic loads.[18-21] FEA has become a powerful tool in simulating the complex behavior of concrete structures under cyclic loading, enabling detailed analysis of stress distribution and crack propagation.[22-25] The following are examples of available modeling studies in the literature in more detail.

Yankelevsky and Reinhardt[13] developed a one-dimensional empirical model for the cyclic compressive behavior of concrete. To predict the linear branch of the unloading and reloading paths, a set of focal points was determined. According to the authors, a complete cyclic loop can be constructed graphically for any starting point on the envelope curve without the need for any calculations. The results of the model showed good agreement with various experimental data.

An analytical model was established by Sima et al.[18] to simulate the hysteretic behavior of concrete subjected to cyclic loading in both compression and tension directions. To capture the degradation of concrete under increasing loads in compression and tension, two independent damage parameters were developed. In the case of cyclic compression, an exponential equation was developed to define the envelope stress-strain curve based on parameters from monotonic tests. Unloading followed an exponential curve with varying characteristics due to damage accumulation, while reloading was linear. The results of the proposed model showed good agreement with available experimental data on concrete with different strengths and cyclic histories.

Aslani and Jowkarmeimandi[21] further developed a constitutive model for the cyclic response of concrete. This model was based on experimental observations and previous analytical studies. In their approach, they used a power-type equation to model the nonlinear curve of the unloading path, while the reloading was modeled as linear with the consideration of stiffness degradation. Their model demonstrated

ACI Materials Journal, V. 122, No. 1, January 2025.
MS No. M-2024-019.R3, doi: 10.14359/51744376, received June 29, 2024, and reviewed under Institute publication policies.

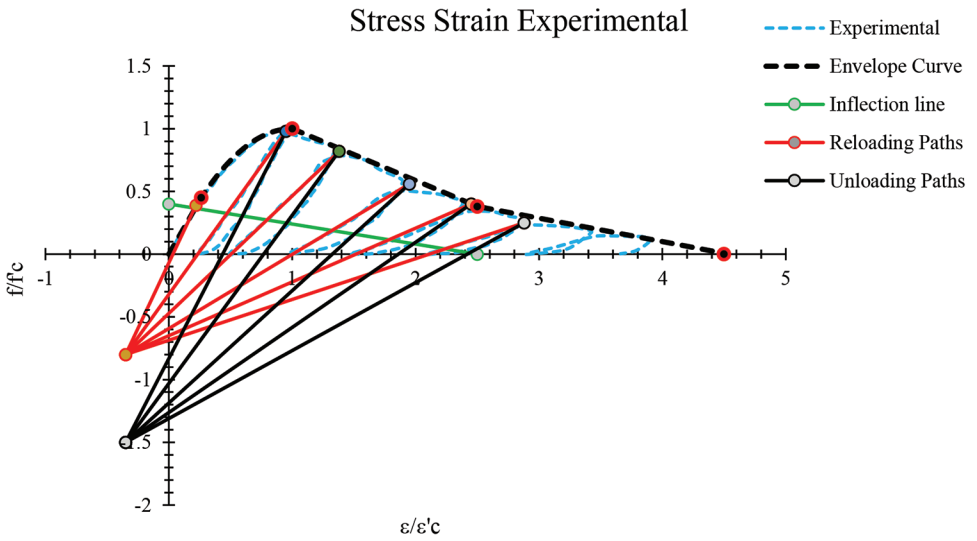

Fig. 1—Unloading and reloading slopes intersection points for cyclic compression loading using experimental data from Tanigawa and Uchida.[27]

the capability to simulate the cyclic response of concrete members with both normal and high strength. Validation of the model resulted in a suitable agreement with the experimental data.

A numerical model was established by Varma et al.[24] to simulate the response of carbon fiber-reinforced polymer (CFRP)-confined concrete elements subject to monotonic and cyclic loadings. This research study developed a numerical model to simulate the monotonic and cyclic behavior of CFRP-confined RC columns. Tests showed that the monotonic stress-strain curves serve as envelopes for cyclic loading curves. The monotonic stress-strain curve has three branches: a linear first branch governed by concrete and reinforcement, a nonlinear third branch governed by CFRP confinement, and a second branch ensuring continuity, affected by all three components. The model predicts stress-strain responses for any loading path and accurately simulates the degradation in load capacity and stiffness observed during unloading/reloading cycles based on nonlinear relationships between stress and strain.

This paper aims to develop an analytical modeling approach that addresses the complexities of concrete behavior under cyclic compression using a simple yet very accurate representation. This is made possible by approximating the unloading path with a bilinear curve that accurately depicts the inflection point. Furthermore, the envelope curve is composed of a combination of straight lines and a parabola characterized by controlling stress-strain boundary conditions. The analytical model is shown to predict the cyclic response of concrete under compression loading and the envelope curve very accurately and efficiently.

RESEARCH SIGNIFICANCE

The need for a simplified model to accurately predict the cyclic response of concrete subjected to compression loading is crucial. Thus, this research study presents an uncomplicated mathematical model that successfully projects the normalized envelope backbone stress-strain curve and cyclic loops for unconfined concrete. The model was calibrated and verified against a set of independent experimental data, resulting in an excellent matching. The ability of the proposed model to capture cyclic response and envelope curves presents an opportunity to simulate the response of structures subjected to cyclic loading and its implementation in numerical FEA.

DESCRIPTION OF FUNDAMENTAL MODEL DEVELOPMENT

Envelope curve

For plain concrete in cyclic compression loading, the envelope curve is divided into two regions: the pre-peak and post-peak regions. The pre-peak region is divided into two curves. The first is a linear curve terminating at a stress of $0.45f_c'$. This line represents the elastic secant modulus according to ACI 318-19.[26] The second curve is a parabola defined by three stress-strain boundary conditions—namely, the strain corresponding to $0.45f_c'$, the strain corresponding to $f_c'(\varepsilon_c')$, and the slope of zero of this curve, which is located at the strain corresponding to $f_c'(\varepsilon_c')$. The post-peak region that defines the softening response is simplified as two descending linear curves. The first line occurs between the compressive strain value ε_c' and the strain value corresponding to $2.5\varepsilon_c'$. The other line occurs between the compressive strain value of $2.5\varepsilon_c'$ and the compressive strain value of $4.5\varepsilon_c'$. To maintain a versatile model, the strains are normalized by ε_c', while the stresses are normalized by f_c'. Another important observation that was drawn from the experimental data indicates that an inflection point for every compressive cycle is seen to have a locus falling along a line that starts at a normalized stress of 0.4, corresponding to a normalized strain of zero, and linearly descending to a normalized stress of zero, corresponding to a normalized strain of 2.50, as shown in Fig. 1. This observation simplifies the modeling of the unloading path to a bilinear curve.

Cyclic loops

In this study, a normalized envelope stress-strain model of concrete in compression is initially derived, as described

Table 1—Specimen sizes and test setup of experimental data used for validation

Experimental study	Sample shape	Height, mm (in.)	Diameter or width, mm (in.)	Length, mm (in.)	Loading type
Tanigawa and Uchida[27]	Cube	150 (6)	150 (6)	150 (6)	Uniaxial compression loading
Bahn and Hsu[14]	Cylinder	150 (6)	75 (3)	NA	Uniaxial compression loading
Xu et al.[29]	Prism	300 (12)	150 (6)	150 (6)	Uniaxial compression loading

in the previous "Envelope curve" section. On the other hand, the unloading compression cyclic paths are observed to gradually degrade such that they all meet at a common pivot point. Furthermore, the reloading compression cyclic paths intersect at another common pivot point (refer to Fig. 1). It is further observed that unloading inflection points exist on all compression loops aligned along a strain-dependent declining line. This observation leads to the hypothesis that these compression loops assume a bilinear unloading path followed by a linear reloading path. These paths are identifiable through the envelope departure point, the inflection point, and the residual point on the strain axis for the unloading curve, as well as the same residual point, back to the envelope departure point for the reloading line.

MODEL CALIBRATION

The present model was calibrated using normalized variables from data reported by Tanigawa and Uchida.[27] The specimen size, specimen type, and test setup are listed in Table 1.

Envelope curve

Equations (1) to (5) can be used to determine the envelope curve as follows:

For the elastic range of the envelope curve, where the normalized strain is $0.00 \le (\varepsilon_c/\varepsilon_c') \le (5.0/19)$, the corresponding normalized stress can be found using the following equation

$$\frac{\sigma_c}{f_c'} = 1.71\frac{\varepsilon_c}{\varepsilon_c'} \tag{1}$$

where

$$\varepsilon_c' = 1.71\frac{f_c'}{E_c} \tag{2}$$

where σ_c is the compressive stress at different levels of loading; ε_c is the compressive strain at different levels of loading; E_c is the elastic modulus of the concrete; f_c' is the unconfined compressive strength of the concrete; and ε_c' is the strain corresponding to f_c'.

The second curve is part of the pre-peak response, where the normalized strain is $(5.0/19) \le (\varepsilon_c/\varepsilon_c') \le 1.00$, and the corresponding normalized values of stress can be computed using Eq. (3).

$$\frac{\sigma_c}{f_c'} = a_0 + a_1\frac{\varepsilon_c}{\varepsilon_c'} + a_2\left(\frac{\varepsilon_c}{\varepsilon_c'}\right)^2 \tag{3}$$

By applying the following boundary conditions

$$\frac{\sigma_c}{f_c'} = 0.45;\ \frac{\varepsilon_c}{\varepsilon_c'} = \frac{5}{19}$$

$$\frac{\sigma_c}{f_c'} = 1.00;\ \frac{\varepsilon_c}{\varepsilon_c'} = 1.00$$

$$\frac{\varepsilon_c}{\varepsilon_c'} = 1.00;\ \text{slope} = 0.00$$

Equation (3) results in

$$\frac{\sigma_c}{f_c'} = a_0 + a_1\left(\frac{5}{19}\right) + a_2\left(\frac{5}{19}\right)^2$$

$$\frac{\sigma_c}{f_c'} = \alpha_0 + \alpha_1(1) + \alpha_2(1)^2$$

$$\frac{d\frac{\sigma_c}{f_c'}}{d\frac{\varepsilon_c}{\varepsilon_c'}} = \alpha_1 + 2\alpha_2(1) = 0$$

The foregoing equations are arranged in a matrix form to compute the unknown coefficients, as follows.

$$\begin{bmatrix} 1 & \frac{5}{19} & \left(\frac{5}{19}\right)^2 \\ 1 & 1 & 1 \\ 0 & 1 & 2 \end{bmatrix} \begin{Bmatrix} a_0 \\ a_1 \\ a_2 \end{Bmatrix} = \begin{Bmatrix} 0.45 \\ 1 \\ 0 \end{Bmatrix} \tag{4}$$

Solving the matrix system in Eq. (4)

$\alpha_0 = -0.0130102$, $\alpha_1 = 2.02602041$, and $\alpha_2 = -1.0130102$

Substituting the foregoing coefficients in Eq. (3)

$$\frac{\sigma_c}{f_c'} = -0.013 + 2.026\frac{\varepsilon_c}{\varepsilon_c'} - 1.013\left(\frac{\varepsilon_c}{\varepsilon_c'}\right)^2 \tag{5}$$

To find the post-peak part of the envelope curve, Eq. (6) and (7) were developed.

For $1.00 \le (\varepsilon_c/\varepsilon_c') \le 2.50$, the boundary conditions are as follows:

At a normalized strain of $\varepsilon_c/\varepsilon_c' = 1.00$, the corresponding stress value is $\sigma_c/f_c' = 1.00$.

At a normalized strain of $\varepsilon_c/\varepsilon_c' = 2.50$, the corresponding stress value is $\sigma_c/f_c' = 0.38$.

The value of $(\sigma_c/f_c') = 0.38$ is extracted from the stress-strain curve used for calibration. After applying the two boundary conditions, the normalized stress-strain line can be recovered by Eq. (6).

$$\frac{\sigma_c}{f_c'} = -0.413\frac{\varepsilon_c}{\varepsilon_c'} + 1.413 \quad (6)$$

For $2.5 \leq (\varepsilon_c/\varepsilon_c') \leq 4.50$, the boundary conditions are as follows:

At a normalized strain of $\varepsilon_c/\varepsilon_c' = 2.50$, the corresponding stress value is $\sigma_c/f_c' = 0.38$.

At a normalized strain of $\varepsilon_c/\varepsilon_c' = 4.50$, the corresponding stress value is $\sigma_c/f_c' = 0.00$.

After applying the boundary conditions, the normalized stress-strain line can be recovered by Eq. (7).

$$\frac{\sigma_c}{f_c'} = -0.19\frac{\varepsilon_c}{\varepsilon_c'} + 0.855 \quad (7)$$

Cyclic loops

The current model is based on careful experimental observations from available data. Based on these observations, the following assumptions were made:

1. The coordinate of the normalized pivot point at which all the unloading paths intersect if extended linearly is at (–0.35, –1.50).

2. The coordinate of the normalized pivot point at which all the reloading paths intersect if extended linearly is at (–0.35, –0.80).

3. The inflection point on the unloading path is assumed to lie along a diagonal line between the points (0.00, 0.40) and (2.50, 0.00), as shown in Fig. 1.

Unloading path

The slope of any unloading path can be calculated using Eq. (8)

$$S_u = \frac{y_e + 1.5}{x_e + 0.35} \quad (8)$$

where y_e and x_e are the normalized y and x departure point coordinates on the envelope curve; and S_u is the slope of the unloading path.

Reloading path

The slope of any reloading path can be calculated using Eq. (9)

$$S_R = \frac{y_e + 0.80}{x_e + 0.35} \quad (9)$$

where S_R is the slope of the reloading path.

To locate the coordinate of the x-intercept of any reloading path, Eq. (10) can be used.

$$x_{int} = \frac{-0.35S_R + 0.80}{S_R} \quad (10)$$

Inflection and x-residual points

The inflection points can be determined by the intersection of the unloading line and the descending inflection line, defined in the third assumption in the previous "Cyclic loops" section, leading to Eq. (11) and (12)

$$x_i = \frac{0.35S_u - 1.90}{-0.16 - S_u} \quad (11)$$

$$y_i = -0.16x_i + 0.40 \quad (12)$$

where y_i and x_i are the normalized y and x inflection point coordinates on the unloading path.

To locate the coordinate of the residual point for any loop using the reloading path (normalized x-intercept), Eq. (13) can be applied.

$$x_{res} = \frac{-0.35S_R + 0.80}{S_R} \quad (13)$$

After developing all the necessary equations, the model was calibrated against the original experimental data from Tanigawa and Uchida[27] to verify its accuracy. The results recovered from this calibration, along with the experimental curve, are presented in Fig. 2. Further blind validation was conducted to assess the applicability of the present model using other experiments, as explained in the next section.

MODEL VERIFICATION

The data used for the verification examples are retrieved from several research studies, including Sinha et al.,[11] Okamoto et al.,[28] Tanigawa and Uchida,[27] Bahn and Hsu,[14] and Xu et al.[29] tests data of concrete subjected to compressive cyclic loading. It is important to mention that the test data of Sinha et al.[11] and Okamoto et al.[28] were adapted from Aslani and Jowkarmeimandi[21] because the original two papers were written in Japanese with no translation available to the authors. On the other hand, the test parameters for the studies by Tanigawa and Uchida,[27] Bahn and Hsu,[14] and Xu et al.[29] are listed in Table 1. A spreadsheet was used to formulate the present cyclic compression model. The comparison results between the present model and the original experimental data demonstrate a very good agreement, leading to the conclusion that the developed model effectively represents the behavior of plain concrete under compression cyclic loads. It is evident that the validation in Fig. 3 compares generally very well against experimental data for the envelope curve and cyclic loops. The minor discrepancies are to be expected for a simplified model with a limited number of parameters to tune. Figure 4 reflects an excellent agreement, while Fig. 5 shows very good agreement with experimental data curves. The envelope curve in Fig. 6 overestimates the experimental backbone curve, while the opposite is true in Fig. 7. Nevertheless, both verification curves reflect excellent correspondence with the cyclic test loops. Thus, the model can serve as a valuable tool for predicting the complex stress-strain response of concrete members under repeated loading and can be adapted for other numerical research work.

CONCLUSIONS

The present model proposed for cyclic compression loading considers the fundamental understanding of concrete damage response, which is reflected in the stiffness and strength degradation from carefully observing

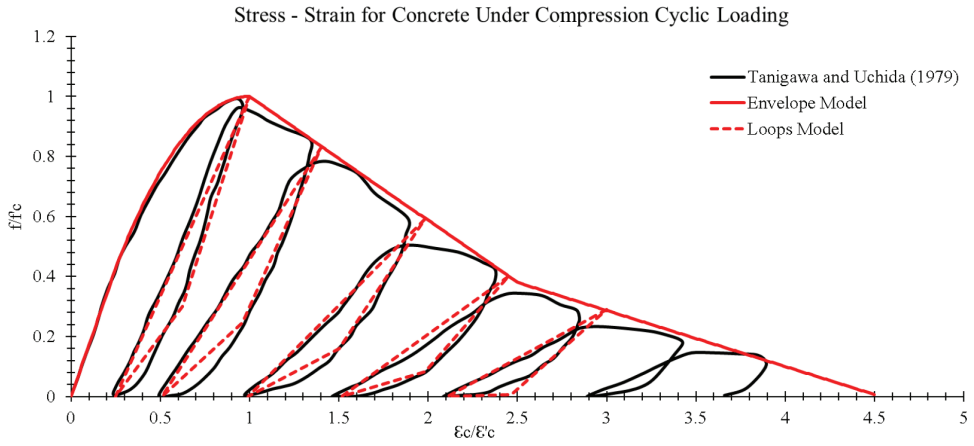

Fig. 2—Model calibration with experimental data from Tanigawa and Uchida.[27]

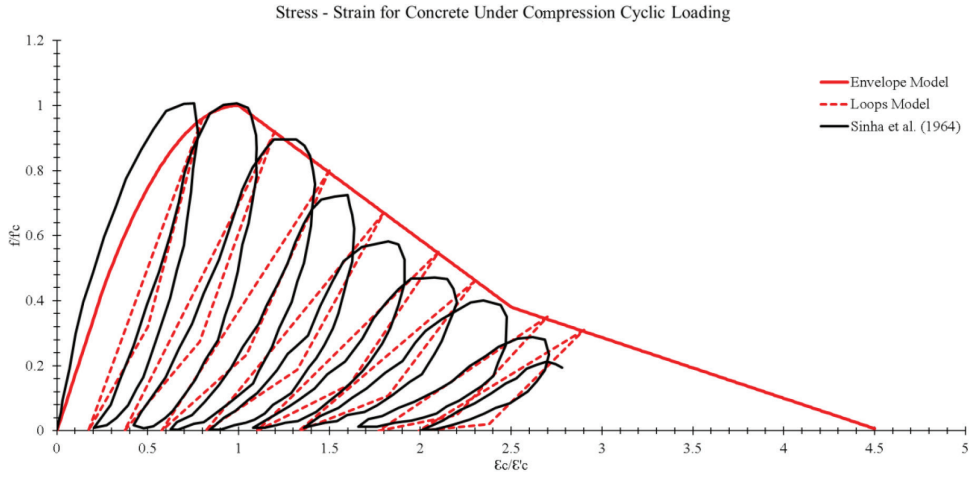

Fig. 3—Cyclic compression experimental data from Sinha et al.[11] versus proposed model.

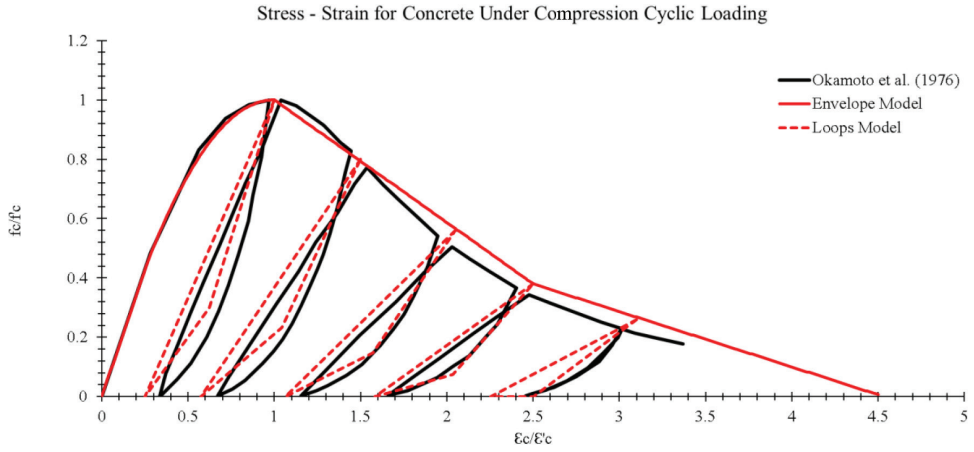

Fig. 4—Cyclic compression experimental data from Okamoto et al.[28] versus proposed model.

the experimental data. The envelope curve for the cyclic compression loading is simulated using normalized stress-strain values from key points in a linear function, followed by a parabolic curve in the pre-peak region. These points are normalized stress-strain sets at (0, 0) to (5/19, 0.45) (for the linear portion) and (5/19, 0.45) to (1.0, 1.0) (for the parabolic portion). The post-peak region is defined by two linear descending lines from (1.0, 1.0) to (2.5, 0.38) and (2.5, 0.38) to (4.5, 0). The experimental test data are used to extract a phenomenological cyclic model, which was characterized by two pivot points at which all the unloading lines and reloading lines met. Furthermore, the locus of the inflection points is characterized by a descending line that can be used to extract the coordinates of these inflection points for different loading cycles. The bilinear unloading function terminates at the residual points, which are determined by the intersection of the reloading lines between the envelope departure points and the reloading pivot point. The

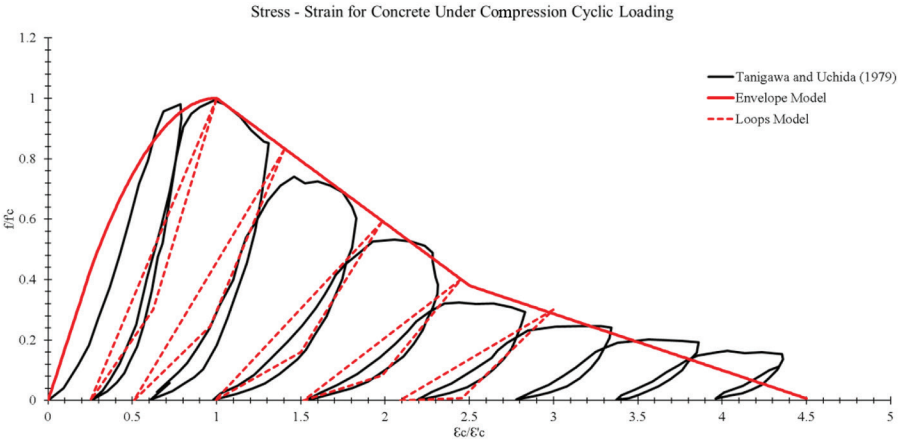

Fig. 5—Cyclic compression experimental data from Tanigawa and Uchida[27] versus proposed model.

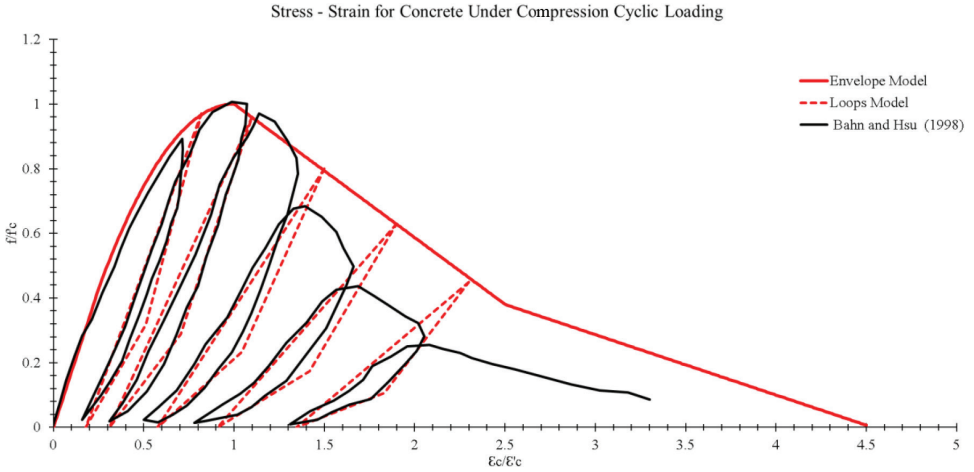

Fig. 6—Cyclic compression experimental data from Bahn and Hsu[14] versus proposed model.

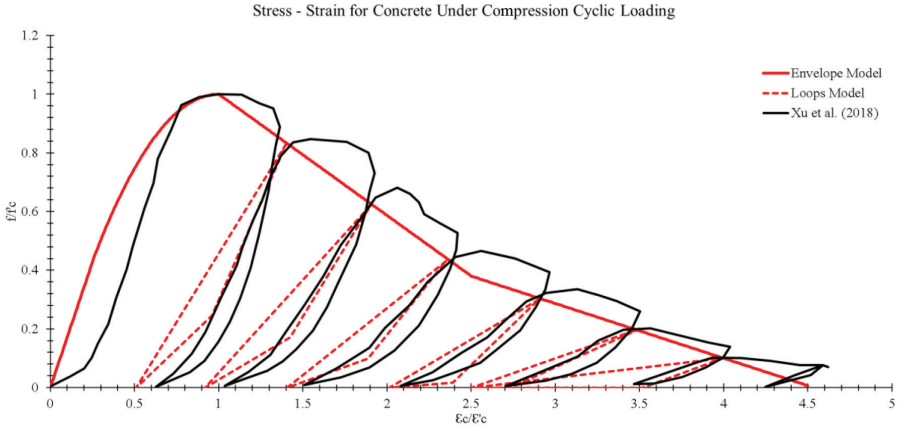

Fig. 7—Cyclic compression experimental data from Xu et al.[29] versus proposed model.

compression cyclic loading model was able to capture the complex behavior of concrete when blindly verified on five other experimental data sets. This model is expected to be a valuable tool for numerical finite element analysis (FEA) due to its simplicity and versatility.

AUTHOR BIOS

Sama Mohammed Saleem *is a Structural Designer at L.A. Fuess Partners. She received her BS in architectural engineering from the University of Sharjah, Sharjah, UAE, and her MS from Kansas State University, Manhattan, KS. Her research interests include fiber-reinforced polymer (FRP)-strengthened concrete beam-column joints under seismic effects and nonlinear analysis of concrete members.*

ACI member **Salman A. Alshamrani** *is an Assistant Professor in the Civil Engineering Department, College of Engineering, University of Bisha, Bisha, Saudi Arabia. He received his PhD from Kansas State University in 2024. His research interests include FRP-strengthened concrete beams under seismic effects, modeling of FRP-concrete bond, and nonlinear analysis of concrete members.*

Hayder A. Rasheed, *FACI, is a Professor of structural engineering at Kansas State University. He received his PhD from The University of Texas at Austin, Austin, TX, in 1996. He is a member of ACI Committees 369, Seismic Repair and Rehabilitation, and 440, Fiber-Reinforced Polymer Reinforcement; and Joint ACI-ASCE Committee 441, Reinforced Concrete Columns. His research interests include the behavior of reinforced/prestressed concrete and advanced composites.*

REFERENCES

1. Wang, H. C.; Zhao, J.; Li, J.; Braithwaite, C. H.; and Zhang, Q. B., "Progressive Fracturing of Concrete under Biaxial Confinement and Repetitive Dynamic Loadings: From Damage to Catastrophic Failure," *International Journal of Impact Engineering*, V. 165, July 2022, Article No. 104232. doi: 10.1016/j.ijimpeng.2022.104232

2. Keerthana, K., and Chandra Kishen, J. M., "Micromechanics of Fracture and Failure in Concrete under Monotonic and Fatigue Loadings," *Mechanics of Materials*, V. 148, Sept. 2020, Article No. 103490. doi: 10.1016/j.mechmat.2020.103490

3. Kumar, B., and Ray, S., "An Analytical Approach for the Fracture Characterization of Concrete under Cyclic Loading," *Materials Today: Proceedings*, 2023, (in press). doi: 10.1016/j.matpr.2023.04.075

4. Zhang, J.; Yu, Z.; Tang, Y.; Shen, J.; and Chen, H., "Fracture Properties of Concrete under Cyclic Loading," *Construction and Building Materials*, V. 281, Apr. 2021, Article No. 122610. doi: 10.1016/j.conbuildmat.2021.122610

5. Monnamitheen Abdul Gafoor, A. H., and Dinkler, D., "A Macroscopic Gradient-Enhanced Damage Model for Deformation Behavior of Concrete under Cyclic Loadings," *Archive of Applied Mechanics*, V. 90, No. 5, May 2020, pp. 1179-1199. doi: 10.1007/s00419-020-01669-4

6. Lu, J.; Zhu, K.; Tian, L.; and Guo, L., "Dynamic Compressive Strength of Concrete Damaged by Fatigue Loading and Freeze-Thaw Cycling," *Construction and Building Materials*, V. 152, Oct. 2017, pp. 847-855. doi: 10.1016/j.conbuildmat.2017.07.046

7. Kunnath, S. K., and Chai, Y. H., "Cumulative Damage-Based Inelastic Cyclic Demand Spectrum," *Earthquake Engineering & Structural Dynamics*, V. 33, No. 4, Apr. 2004, pp. 499-520. doi: 10.1002/eqe.363

8. Xiao, J.-Q.; Ding, D.-X.; Jiang, F.-L.; and Xu, G., "Fatigue Damage Variable and Evolution of Rock Subjected to Cyclic Loading," *International Journal of Rock Mechanics and Mining Sciences*, V. 47, No. 3, Apr. 2010, pp. 461-468. doi: 10.1016/j.ijrmms.2009.11.003

9. Isojeh, B.; El-Zeghayar, M.; and Vecchio, F. J., "Concrete Damage under Fatigue Loading in Uniaxial Compression," *ACI Materials Journal*, V. 114, No. 2, Mar.-Apr. 2017, pp. 225-235. doi: 10.14359/51689477

10. Wang, C.; Wu, H.; and Li, C., "Hysteresis and Damping Properties of Steel and Polypropylene Fiber Reinforced Recycled Aggregate Concrete under Uniaxial Low-Cycle Loadings," *Construction and Building Materials*, V. 319, Feb. 2022, Article No. 126191. doi: 10.1016/j.conbuildmat.2021.126191

11. Sinha, B. P.; Gerstle, K. H.; and Tulin, L. G., "Stress-Strain Relations for Concrete Under Cyclic Loading," *ACI Journal Proceedings*, V. 61, No. 2, Feb. 1964, pp. 195-211.

12. Karsan, I. D., and Jirsa, J. O., "Behavior of Concrete Under Compressive Loadings," *Journal of the Structural Division*, ASCE, V. 95, No. 12, Dec. 1969, pp. 2543-2564. doi: 10.1061/JSDEAG.0002424

13. Yankelevsky, D. Z., and Reinhardt, H. W., "Model for Cyclic Compressive Behavior of Concrete," *Journal of Structural Engineering*, ASCE, V. 113, No. 2, Feb. 1987, pp. 228-240. doi: 10.1061/(ASCE)0733-9445(1987)113:2(228)

14. Bahn, B. Y., and Hsu, C.-T. T., "Stress-Strain Behavior of Concrete under Cyclic Loading," *ACI Materials Journal*, V. 95, No. 2, Mar.-Apr. 1998, pp. 178-193.

15. Chang, G. A., and Mander, J. B., "Seismic Energy Based Fatigue Damage Analysis of Bridge Columns: Part I—Evaluation of Seismic Capacity," Technical Report NCEER-94-0006, National Center for Earthquake Engineering Research, State University of New York at Buffalo, Buffalo, NY, Mar. 1994, 244 pp.

16. Mansour, M., and Hsu, T. T. C., "Behavior of Reinforced Concrete Elements under Cyclic Shear. II: Theoretical Model," *Journal of Structural Engineering*, ASCE, V. 131, No. 1, Jan. 2005, pp. 54-65. doi: 10.1061/(ASCE)0733-9445(2005)131:1(54)

17. Palermo, D., and Vecchio, F. J., "Compression Field Modeling of Reinforced Concrete Subjected to Reversed Loading: Formulation," *ACI Structural Journal*, V. 100, No. 5, Sept.-Oct. 2003, pp. 616-625.

18. Sima, J. F.; Roca, P.; and Molins, C., "Cyclic Constitutive Model for Concrete," *Engineering Structures*, V. 30, No. 3, Mar. 2008, pp. 695-706. doi: 10.1016/j.engstruct.2007.05.005

19. Chen, X.; Xu, L.; and Bu, J., "Experimental Study and Constitutive Model on Complete Stress-Strain Relations of Plain Concrete in Uniaxial Cyclic Tension," *KSCE Journal of Civil Engineering*, V. 21, No. 5, July 2017, pp. 1829-1835. doi: 10.1007/s12205-016-0802-0

20. Chen, E.-S., and Buyukozturk, O., "Constitutive Model for Concrete in Cyclic Compression," *Journal of Engineering Mechanics*, ASCE, V. 111, No. 6, June 1985, pp. 797-814. doi: 10.1061/(ASCE)0733-9399(1985)111:6(797)

21. Aslani, F., and Jowkarmeimandi, R., "Stress–Strain Model for Concrete under Cyclic Loading," *Magazine of Concrete Research*, V. 64, No. 8, Aug. 2012, pp. 673-685. doi: 10.1680/macr.11.00120

22. Castaldo, P.; Gino, D.; Bertagnoli, G.; and Mancini, G., "Resistance Model Uncertainty in Non-linear Finite Element Analyses of Cyclically Loaded Reinforced Concrete Systems," *Engineering Structures*, V. 211, May 2020, Article No. 110496. doi: 10.1016/j.engstruct.2020.110496

23. El Yassari, S., and El Ghoulbzouri, A., "Numerical Simulation of Fiber-Reinforced Concrete under Cyclic Loading Using Extended Finite Element Method and Concrete Damaged Plasticity," *International Journal of Engineering*, V. 36, No. 10, Oct. 2023, pp. 1815-1826. doi: 10.5829/IJE.2023.36.10A.08

24. Varma, R. K.; Barros, J. A. O.; and Sena-Cruz, J. M., "Numerical Model for CFRP Confined Concrete Elements Subject to Monotonic and Cyclic Loadings," *Composites Part B: Engineering*, V. 40, No. 8, Dec. 2009, pp. 766-775. doi: 10.1016/j.compositesb.2009.05.005

25. Vecchio, F. J., "Towards Cyclic Load Modeling of Reinforced Concrete," *ACI Structural Journal*, V. 96, No. 2, Mar.-Apr. 1999, pp. 193-202.

26. ACI Committee 318, "Building Code Requirements for Structural Concrete (ACI 318-19) and Commentary (ACI 318R-19) (Reapproved 2022)," American Concrete Institute, Farmington Hills, MI, 2019, 624 pp.

27. Tanigawa, Y., and Uchida, Y., "Hysteretic Characteristics of Concrete in the Domain of High Compressive Strain," *Proceedings*, Annual Architectural Institute of Japan (AIJ) Convention, Tokyo, Japan, 1979, pp. 449-450.

28. Okamoto, S.; Shiomi, S.; and Yamabe, K., "Earthquake Resistance of Prestressed Concrete Structures," *Proceedings*, Annual Architectural Institute of Japan (AIJ) Convention, Tokyo, Japan, 1976, pp. 1251-1252.

29. Xu, L.; Li, B.; Ding, X.; Chi, Y.; Li, C.; Huang, B.; and Shi, Y., "Experimental Investigation on Damage Behavior of Polypropylene Fiber Reinforced Concrete under Compression," *International Journal of Concrete Structures and Materials*, V. 12, No. 1, Dec. 2018, Article No. 68. doi: 10.1186/s40069-018-0302-3

ARE YOU A RESEARCHER?

SIGN UP FOR ORCID TODAY!

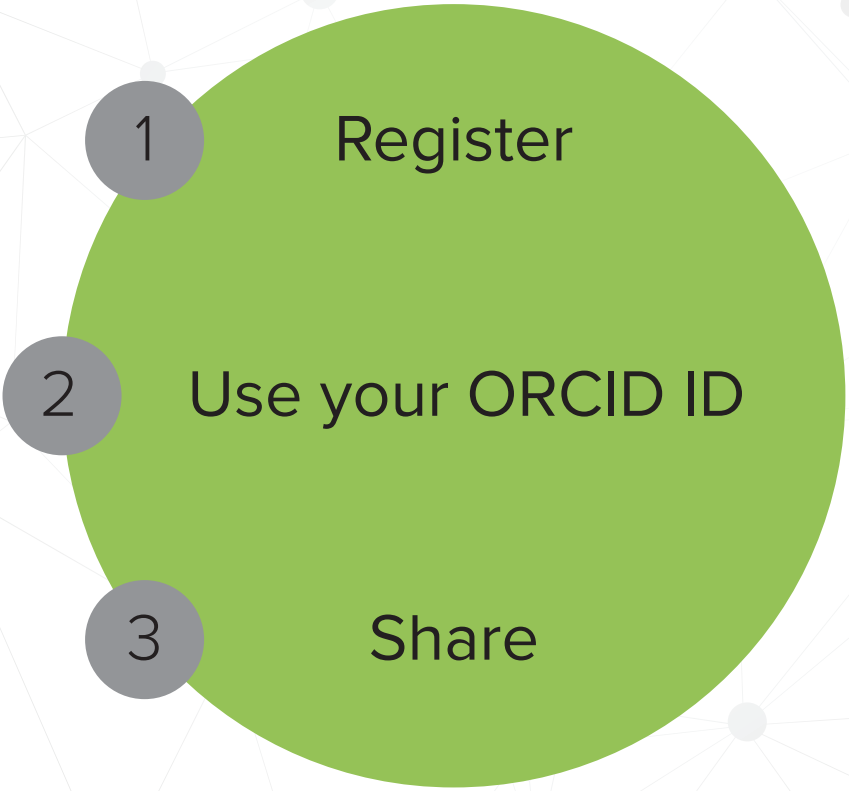

ORCID provides a digital identifier that distinguishes you from every other researcher and, through integration in key research workflows such as manuscript and grant submission, supports automated linkages between you and your professional activities, ensuring that your work is recognized.

ORCID services are FREE and it's as easy as **1-2-3**.

WWW.ORCID.ORG

ACI MATERIALS JOURNAL TECHNICAL PAPER

Title No. 122-M04

Mechanical Degradation of Ferritic Stainless-Steel (410L) Reinforcing Bar due to Corrosion

by Ankit Kumar Jaiswal and Sangeeta Gadve

Corrosion of carbon-steel reinforcement in marine environments is a significant problem, prompting the use of materials with higher corrosion resistance, such as stainless steel. Despite stainless steel's superior durability, especially in aggressive environments such as marine structures, it remains vulnerable to localized pitting corrosion, which can be more detrimental than the corrosion observed in carbon steel. The scientific challenge addressed in this study is the lack of extensive research on the degradation of mechanical properties in corroded stainless-steel reinforcing bar. The novelty of this research lies in its focus on ferritic stainless-steel reinforcing bar (SS410L) and the detailed quantification of the relationship between corrosion-induced mass loss and mechanical strength deterioration. An experimental investigation was conducted to assess the impact of different corrosion levels (5, 10, and 20% mass loss) induced using an accelerated impressed-current technique. Tensile tests on both uncorroded and corroded samples provided insights into the reduction of yield load, ultimate load, and elongation. The results revealed that for mass loss percentages of 3.73%, 10.72%, and 23.76%, there was a corresponding reduction in yield load of 6.21%, 29.09%, and 46.56%; ultimate load reductions were 3.43%, 23.91%, and 42.69%; and elongation decreased by 19.45%, 31.28%, and 41.52%, respectively. This study also proposes regression models to predict mechanical property degradation and establishes a relationship between percentage mass loss and cross-sectional area loss, highlighting the severe effect of pitting corrosion on mechanical properties based on experimental results.

Keywords: accelerated corrosion; corrosion; experimentation; mechanical properties; stainless-steel reinforcing bar; tensile test.

INTRODUCTION

Reinforced concrete structures stand as pillars in the construction industry, valued for their durability, accessibility, and robustness. However, a significant challenge faced by steel-reinforced concrete is the corrosion induced by carbon dioxide and chloride ions upon contact with the steel reinforcing bar's surface. Particularly in coastal regions, chloride ions infiltrate the reinforcing bar surface, compromising its passive layer and inciting corrosion at a much-accelerated rate.[1] This corrosion process leads to the generation of voluminous corrosion products, culminating in heightened internal pressure within the concrete, resulting in cracks and spalling.[2] The presence of these corrosion products affects concrete in diverse ways, such as diminishing the bond strength between the reinforcing bar and concrete, reducing the reinforcing bar's diameter, and instigating cracks in the concrete, thereby decreasing its cross-sectional stiffness and the capacity of the members.[3] Addressing this issue has prompted the development of several methods to impede corrosive agents from accessing the reinforcing bar surface. These methods encompass the use of epoxy-coated reinforcing bars, galvanized coatings, enamel coatings, and inhibitors, and decreasing the permeability of concrete by using novel materials such as polypropylene fibers, alkali-activated concrete (AAC), fly ash, and ground-granulated blast-furnace slag (GGBS), among others.[4-9] While these approaches effectively delay corrosion, it is critical to note that once the protective layer incurs damage from mechanical actions, the corrosion of these reinforcing bars can escalate faster than that of unprotected ones.[10] The focus of these reinforcing bar coating methods primarily revolves around altering the reinforcing bar's surrounding environment rather than augmenting the reinforcing bar's inherent corrosion resistance. Considering this perspective, stainless-steel alloys, renowned for their significantly superior corrosion-resistant properties compared to conventional carbon reinforcing bars, emerge as a promising alternative. Although the use of stainless-steel reinforcing bar is not novel and has been within the purview of engineers for a considerable time, its adoption has been limited by cost considerations. While the cost of stainless-steel alloys notably exceeds that of carbon steel—approximately four to nine times higher—factoring in life-cycle costs encompassing structure, maintenance, and retrofitting expenses could potentially lead to a total cost reduction of approximately 20 to 25%.[11,12] Hence, stainless steel presents itself as a cost-effective solution, especially for structures designed for extended service life (75 to 100 years) and those exposed to harsh marine environments.[13] The pursuit of cost-effective materials has led to the embrace of more budget-friendly stainless-steel grades, notably ferritic stainless steel, distinguished by diminished chromium and nickel content. However, this economical option comes with reduced corrosion resistance compared to its counterparts. Corrosion resistance significantly relies on chromium, nickel, and molybdenum content, where higher content correlates with heightened corrosion resistance.[14,15] In aggressive settings such as high temperatures and acidic and marine environments, stainless steel may corrode in the long run, necessitating an examination of the impact of corrosion on the mechanical properties of ferritic stainless-steel reinforcing bar.

ACI Materials Journal, V. 122, No. 1, January 2025.

MS No. M-2024-058.R2, doi: 10.14359/51744377, received October 5, 2024, and reviewed under Institute publication policies.

Table 1—Chemical composition of ferritic stainless-steel and conventional carbon-steel reinforcing bars, %

Type	Grade	C (max)	Cr (max)	Ni (max)	Mn (max)	Si (max)	P (max)	S (max)	N (max)
Ferritic	EN 1.4003	0.03	10.5 to 12.6	0.3 to 1	1.5	1.0	0.03	0.015	0.03
Carbon	Fe 500SD	0.25	—	—	—	—	0.04	0.04	—

The corrosion of a reinforcing bar significantly diminishes the diameter and ductility of the material, consequently leading to a notable reduction in the load-bearing capacity of both the reinforcing bar and the reinforced member.[3,16-18] The fundamental contrast in the corrosion behavior of carbon and stainless steel lies in carbon steel exhibiting uniform to localized corrosion within concrete, while stainless steel tends to experience severe pitting corrosion. Various studies have investigated the impact of corrosion on carbon-steel reinforcing bar, reporting a considerable decrease in reinforcing bar diameter, which significantly affects its strength, along with observed accelerated degradation in ductility.[19-22] In stainless steel, the effect of corrosion-induced diameter reduction is anticipated to be more severe due to the pronounced pitting corrosion, exacerbating the decline in strength and ductility compared to carbon steel. Managing the reduction in the cross-sectional area of a stainless-steel reinforcing bar presents a more intricate challenge due to the irregular and nonuniform shapes and sizes of corrosion pits along its length, a characteristic notably pronounced in stainless steel, where pitting is both severe and considerably more irregular than in carbon steel. Several parameters such as mass loss percentage, average cross-section area loss percentage, and maximum cross-section area loss percentage have been proposed to quantify the degree of corrosion. It has been noted that the minimum cross-section area loss better aligns with the performance degradation resulting from corrosion.[23] Recent studies have employed three-dimensional (3-D) scanners to precisely measure cross-sectional variations along the length of the reinforcing bar more accurately.[23-26] Using these parameters, regression models have been proposed to correlate degradation in mechanical properties—such as yield load, ultimate load, and elongation percentage—with corrosion degree (mass loss percentage, maximum cross-section loss percentage, and average cross-section loss percentage).[14,16,24,27-31]

In this study, accelerated corrosion was induced using the impressed-current technique to corrode the reinforcing bar, which is used by various researchers to corrode samples within a considerable duration.[14,32-35] Research has demonstrated that accelerated corrosion methods are an effective approach for investigating the relationship between mass loss and the deterioration of tensile strength.[26,36] Three different levels of corrosion, characterized by mass losses of 5, 10, and 20%, were targeted for each diameter reinforcing bar. The duration for which the current was supplied was calculated based on Faraday's law.[24,28,34,35] Following the corrosion process, the reinforcing bars were thoroughly cleaned to determine the mass loss. Tensile tests were subsequently conducted on the corroded reinforcing bars to obtain data on yield load, ultimate load, and elongation percentages. Using the acquired experimental data, regression models were developed to predict yield load, ultimate load, and elongation based on different mass loss percentages. Additionally, a regression model predicting the maximum reduction in cross section for a given mass loss was also provided.

RESEARCH SIGNIFICANCE

Reinforcing bar corrosion causes a reduction in the diameter of the reinforcement, thereby decreasing the load-carrying capacity of reinforced members and potentially leading to failure under service loads. Assessing this reduction in diameter is crucial, and using easily measurable field variables such as mass loss is essential. While previous studies have primarily focused on carbon-steel reinforcing bars, there is growing interest in stainless steel due to its superior strength and higher resistance to chloride corrosion. However, given the uncertainties surrounding corrosion, stainless-steel reinforcing bars, especially low-cost variants such as 410L with lower chromium content, may still corrode in severe environments. Additionally, the tendency of stainless steel to experience pitting corrosion suggests that the reduction in diameter due to corrosion will be more pronounced compared to carbon-steel reinforcing bars for a given mass loss. This study aims to investigate the mechanical degradation in 410L stainless-steel reinforcing bars due to corrosion and establish correlations with mass loss, a parameter easily measured in the field.

EXPERIMENTAL PROGRAM

To investigate mechanical degradation due to the corrosion of ferritic stainless-steel (410L grade) reinforcing bars with diameters of 8, 10, 12, and 16 mm, three distinct corrosion levels were induced. The general chemical composition of the ferritic stainless steel used is provided in Table 1, alongside the chemical composition of conventional carbon steel for comparison. After the corrosion process, the samples were chemically cleaned, and the mass loss was measured using the galvanometric method. Subsequently, the corroded reinforcing bar samples were subjected to tensile tests to obtain load-deflection curves.

Accelerated corrosion test

To initiate corrosion, an electrochemical cell setup was prepared, consisting of a reinforcing bar sample as the anode and a galvanized wire mesh as the cathode (refer to Fig. 1); 3.5% salt (NaCl) solution served as the electrolyte, contained within a polyvinyl chloride (PVC) pipe. For 12 and 16 mm diameter reinforcing bars, 2 m length was used, while 8 and 10 mm diameter reinforcing bars used a 1.5 m length. The 2 m reinforcing bar was connected as the anode to the positive side of a direct current (DC) power source, and simultaneously, a galvanized iron mesh surrounding

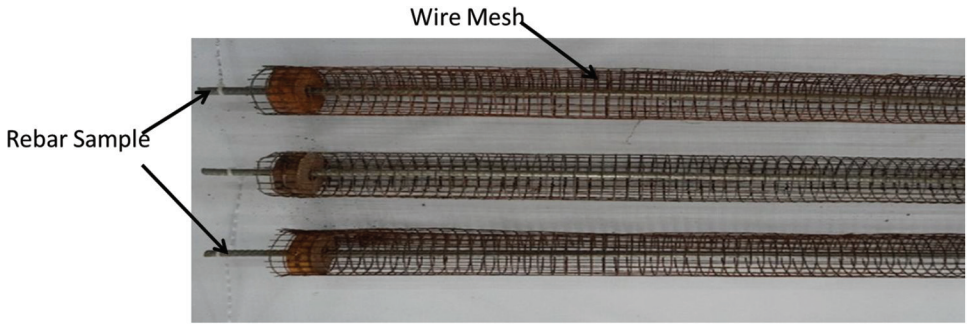

Fig. 1—Samples prepared for corrosion.

the reinforcing bar served as the cathode, connected to the negative side of the DC power source. Maintaining a constant current density of 500 μA/cm^2, three distinct corrosion levels were targeted, aiming for 5, 10, and 20% mass loss. The duration of the current application was estimated based on Faraday's law.[34,35] Samples of each diameter were connected in series, starting from those targeting 20% mass loss to those aiming for 5% mass loss (as depicted in Fig. 2), to maintain a consistent current throughout the circuit. Once the calculated duration for a specific mass loss was achieved, the corresponding sample was disconnected from the circuit. Post-removal, the reinforcing bar underwent sectioning into four samples (three samples for 12 to 16 mm and 8 to 10 mm, respectively) and underwent cleaning using a chemical method following the guidelines of ASTM G1-90(1999)e1.[37] The mass loss (mass percentage) for each 500 mm segment, cut from the initial 2 and 1.5 m corroded reinforcing bar samples, is detailed in Table 2. Accelerated corrosion testing is a commonly used technique for assessing chloride-induced corrosion; however, it is essential to recognize the differences between this approach and actual field conditions. Specifically, artificially corroded reinforcing bar typically exhibits more uniform corrosion along its length than naturally corroded reinforcing bar. A comparative analysis of naturally and artificially corroded reinforcing bars is presented in the studies by Ou et al.[38] and Papadopoulos et al.[39] Furthermore, the differences between corroded bare reinforcing bar and corroded reinforcing bar embedded in concrete are addressed in the work referenced by Du et al.[40] This acknowledgment highlights the limitations of the accelerated corrosion testing method employed in this study and the need for further exploration of real-world conditions.

Tensile test

Tensile tests were conducted on 500 reinforcing bar samples using a universal testing machine with a 1000 kN capacity and automatic hydraulic grips (Fig. 3). A constant deflection rate of 2 mm/min was monotonically applied, maintaining a parallel length of 250 mm for each sample.[24] A gauge length of five times the diameter (5d) was demarcated along the reinforcing bar's length to assess elongation (ε %) at fracture. The load-displacement curve derived from the tensile test was used for subsequent analyses to obtain the ultimate load (F_u) and yield load (F_y).

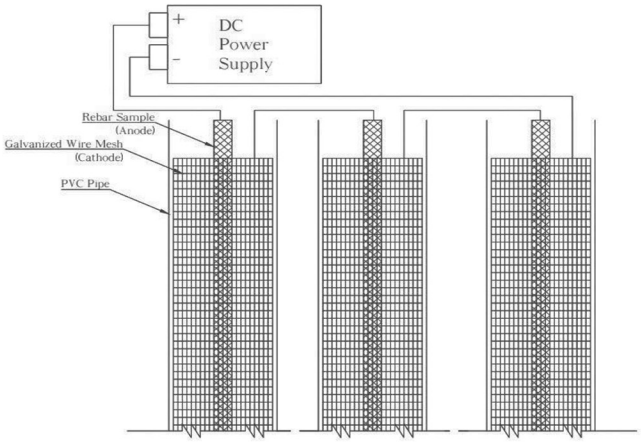

Fig. 2—Electrochemical cell connected in series.

RESULTS AND DISCUSSION

To delineate the stress-strain curve of corroded stainless-steel reinforcing bar, the placement of an extensometer on the reinforcing bar's gauge length, precisely at the minimum cross-section area along the parallel length, was crucial. However, due to the random nature of pitting in terms of shape, size, and depth along the length, the exact location of the minimum cross-section area was initially unknown. Consequently, the load-deflection curve derived from the tensile tests proved instrumental in determining the yield load and ultimate load. Given the absence of a well-defined yield point in stainless steel, the yield load was identified, as illustrated in Fig. 4. Initial data in the load-deflection curve were disregarded due to initial slips, and subsequent analysis involved fitting trend lines for the load-deflection data. One trend line considered data up to 50% of the ultimate load, while another encompassed the relatively linear data after the yield region of the load-deflection curve up to the ultimate load. The resulting equations from these trend lines were then solved to obtain the yield load (F_y). Figure 5 shows the load-deflection curve of corroded reinforcing bar; it can be clearly observed that the shape of the curve remains the same. Hence, the method discussed previously can effectively capture the yield load degradation (F_{yc}/F_{yo}) ratio for corroded reinforcing bars in the regression model developed. A similar approach was used in the bilinear idealization of the stress-strain curve of stainless-steel reinforcing bars.[41,42] The calculated yield and ultimate loads for different samples are presented in Table 2, alongside the observed degree of corrosion (n_{ML} %). The average load-deflection curves for

Table 2—Experimental data

Specimen No.	Sample ID	Mass loss, %	F_y	F_u	Elongation (ε_u), %
1	080001	0	30.68	33.01	22.12
2	080002	0	31.01	32.80	23.07
3	080003	0	31.03	32.75	22.75
4	080501	6.8	25.74	27.9	14.90
5	080502	6.66	25.9	27.6	17.50
6	080503	6.5	24.96	27.3	15.62
7	081001	12.05	22.89	24.1	16.75
8	081002	10.55	21.43	23.3	14.75
9	081003	11.41	20.86	23	12.5
10	082001	24.25	17.52	18.95	10.55
11	082002	22.14	Grip fail	Grip fail	Grip fail
12	082003	25.00	16.66	19.1	11.72
13	100001	0	52.55	55.2	24.22
14	100002	0	50.64	52.5	24.44
15	100003	0	52.12	54.1	23.86
16	100501	7.26	40.36	43.86	17.95
17	100502	6.04	41.58	44.9	18.02
18	100503	5.89	41.05	45.36	—
19	101001	9.25	45.45	48.9	17.22
20	101002	9.34	41.58	44.9	18.02
21	101003	10.24	Grip fail	Grip fail	Grip fail
22	102001	19.40	33.31	36	14.8
23	102002	17.81	28.37	32.9	14.02
24	102003	18.36	30.34	36.1	14.6
25	120001	0	57.11	60	26.44
26	120002	0	56.22	60.4	26.73
27	120003	0	56.54	59.4	25.93
28	120004	0	57.6	61.2	26.93
29	120501	4.11	50.5	55.3	21.26
30	120502	3.88	58.59	61	22.8
31	120503	3.22	51.72	56.2	22.83
32	120504	3.96	56.38	60.4	19.76
33	121001	11.54	48.07	52.7	14.36
34	121002	16.07	47.57	50.3	17.81
35	121003	11.50	46.23	49.9	21.96
36	121004	9.74	49.65	54.3	17.11
37	122001	21.22	36.53	41.2	14.68
38	122002	19.57	34.117	39.1	15.55
39	122003	26.94	28.15	33	14.30
40	122004	22.07	36.42	40.6	15.33
41	160001	0	177.28	186.4	17.65
42	160002	0	176.96	186	17.58
43	160003	0	175.52	183.5	17.25
44	160501	2.72	165	179.3	12.125

Table 2 (cont.)—Experimental data

Specimen No.	Sample ID	Mass loss, %	F_y	F_u	Elongation (ε_u), %
45	160502	3.54	166.88	180.6	15
46	160503	4.14	167.34	177.2	14.11
47	160504	4.30	151.25	178.1	14.31
48	161001	9.40	156.72	166.4	11.21
49	161002	9.16	154.49	165.7	13.21
50	161003	9.76	149.46	163.1	10.21
51	161004	10.72	153.69	164.2	14.37
52	162001	21.63	110.04	120	12.4
53	162002	23.50	88.63	111.7	9.65
54	162003	24.94	100.02	106	12.71
55	162004	21.05	112.48	121	13.11

Note: For Sample ID, first two digits represent diameter, following two digits represent target corrosion level, and last two digits denote sample number (example: 120501 signifies sample with 12 mm diameter, subjected to 5% target mass loss, and labeled as sample number 01).

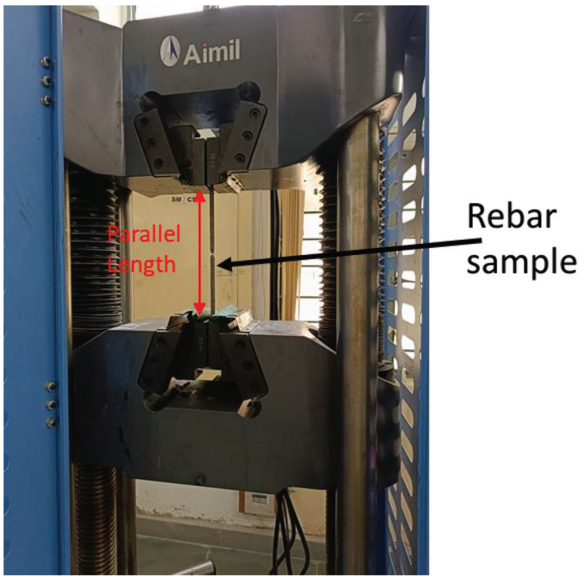

Fig. 3—Tensile test on reinforcing bar.

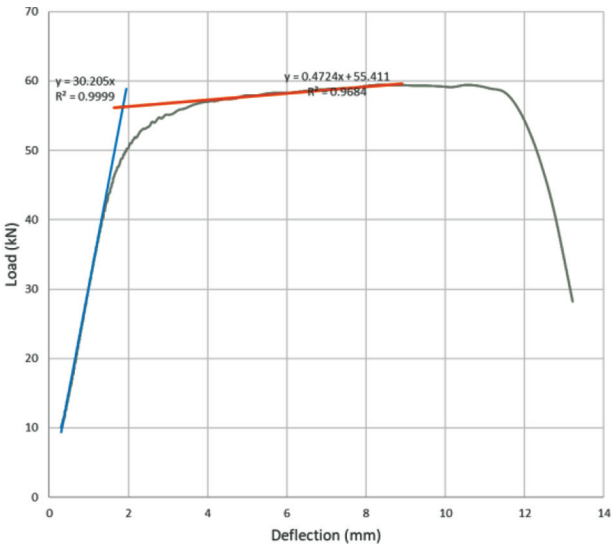

Fig. 4—Yield load idealization from load-deflection curve.

different diameter reinforcing bars subjected to various target corrosion levels (5, 10, and 20%) are shown in Fig. 5(a) to (d). It can be observed that there is no change in the shape of the load-deflection curve, but there is a reduction in the yield zone as the target mass loss increases. While minimum cross-section loss offers a more precise quantification, its measurement complexity, requiring instruments such as 3-D scanners, prompted consideration of mass loss as a simpler alternative that can be easily measured in the field. Consequently, regression models predicting yield load, ultimate load, and elongation percentage were presented based on mass loss (n_{ML} %). Previous studies by several authors demonstrated a linear variation between ultimate load, yield load, and corrosion degree and linear and exponential variation for elongation percentage.[14,21,24,27-29,34]

A notable distinction between the studies of Wu et al.[14] and other authors[14,21,24,27-29] lies in the materials used, with other authors using carbon-steel reinforcement and Wu et al. investigating duplex stainless steel to study mechanical degradation due to corrosion. The key difference in their corrosion behavior lies in stainless steel exhibiting a higher reduction in area for a given mass loss due to its relatively predominant pitting corrosion.[14] Although the corrosion rates differ between duplex and ferritic stainless steel, both suffer from similar types of pitting corrosion (Fig. 6). Hence, the maximum cross-section loss (n_{AL} %) was calculated based on the experimental ultimate load ratio using the equation provided by Wu et al.[14] (Eq. (1) and (2)). Linear regression was employed to establish the relationship between the degradation of mechanical properties and an increase in mass loss

$$\frac{F_{uc}}{F_{uo}} = 1 - 0.0188 n_{AL} \quad (1)$$

$$n_{AL}(\%) = \frac{A_0 - A_{min}}{A_0} \times 100 \quad (2)$$

where F_{uc} is the ultimate load after corrosion; F_{uo} is the ultimate load before corrosion; A_{min} is the minimum cross-section area after corrosion; and A_0 is the initial cross-section area.

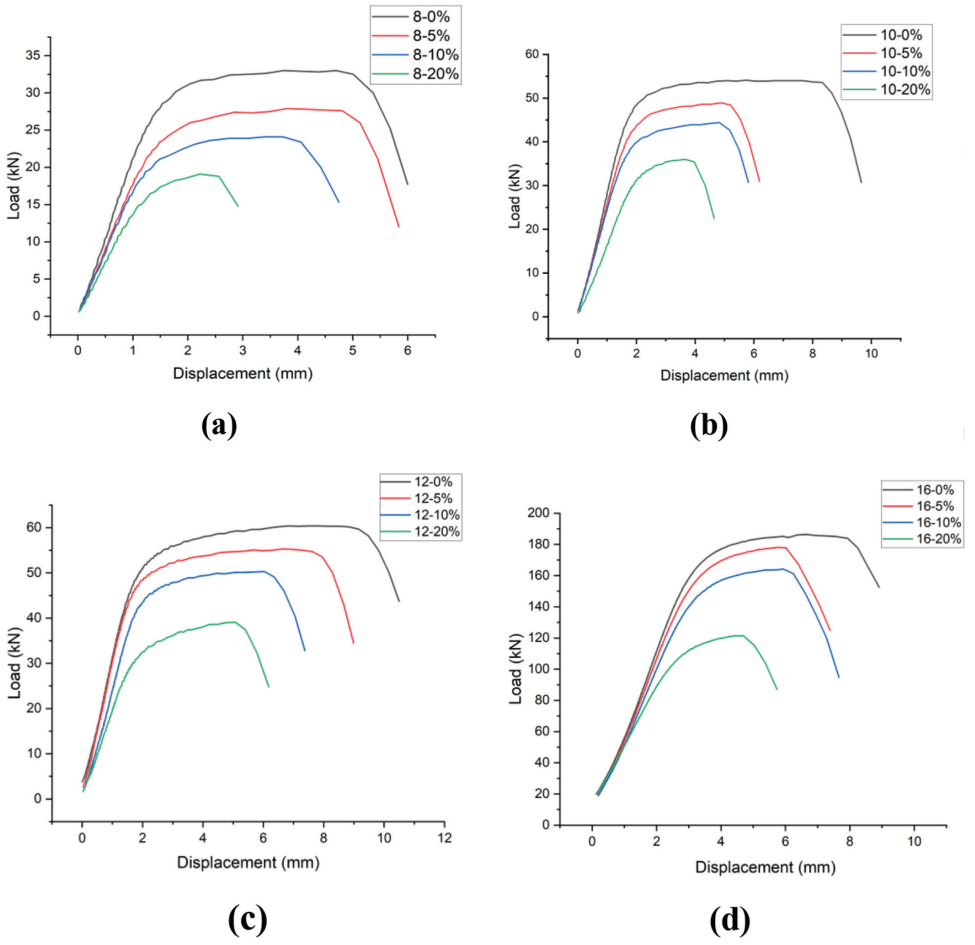

Fig. 5—Experimental load-deflection curve different diameters: (a) 8 mm; (b) 10 mm; (c) 12 mm; and (d) 16 mm.

Linear regression was employed to establish the relationship between the degradation of mechanical properties and the increase in mass loss. To quantify the degree of corrosion in this study, mass loss (n_{ML}) was considered as an independent parameter (Eq. (3)), while ultimate load, yield load, and elongation percentage were taken as dependent parameters. Linear fit, as shown in Fig. 7(a), (b), and (d), was used for ultimate load, yield load, and maximum cross-section area loss, and exponential fit, as shown in Fig. 7(c), was used for elongation percentage[24]

$$n_{mass}(\%) = \frac{m_0 - m}{m_0} \times 100 \quad (3)$$

where m_0 is the initial mass; and m is the measured mass after corrosion.

Visual observation

Figure 6 illustrates the ferritic stainless-steel reinforcing bar after corrosion, revealing noticeable pitting corrosion. Each image showcases the reinforcing bar before and after corrosion, subjected to target mass losses of 5, 10, and 20%, arranged from bottom to top in Fig. 6 to represent the variability in pit formation that can be visually observed. For the reinforcing bar subjected to a 5% mass loss, pits were less dense, primarily occurring near the ribs, and their shape could be approximated as circular. As the mass loss increased to 10%, the density of pits intensified, and some pits became interconnected. Subsequently, for a 20% mass loss, the pit density further increased, with a higher number of interconnected pits forming larger-diameter pits. With the increase in mass loss, pit density intensified, and there is a tendency for pits to become wider and connect rather than get deeper and perforate the reinforcing bar. This suggests that the effect of stress concentration is more pronounced at lower mass loss when the diameter of the pit is smaller. At higher mass loss, pits connect, and their effective diameter increases. A study conducted by Cerit et al.[43] found that the stress concentration effect is proportional to the diameter-to-depth ratio of pits, reducing when the diameter of pits increased for a given diameter-to-depth ratio. As mass loss increases, pits become interconnected, the diameter of pits increases, and, consequently, the stress concentration effects on mechanical properties tend to decrease.

Degradation in mechanical properties

Table 2 presents the calculated mass loss for various samples, along with the corresponding yield load, ultimate load, and elongation percentage at fracture obtained in this study. Samples that failed inside the grips were excluded from the analysis and were not reported. Equations (4) to (6) predict mechanical degradation after corrosion, and Eq. (7) predicts the maximum cross-section area loss (n_{AL} %) based on mass loss (n_{ML} %). Results obtained from tensile testing exhibit scatter, which is expected due to the severe pitting

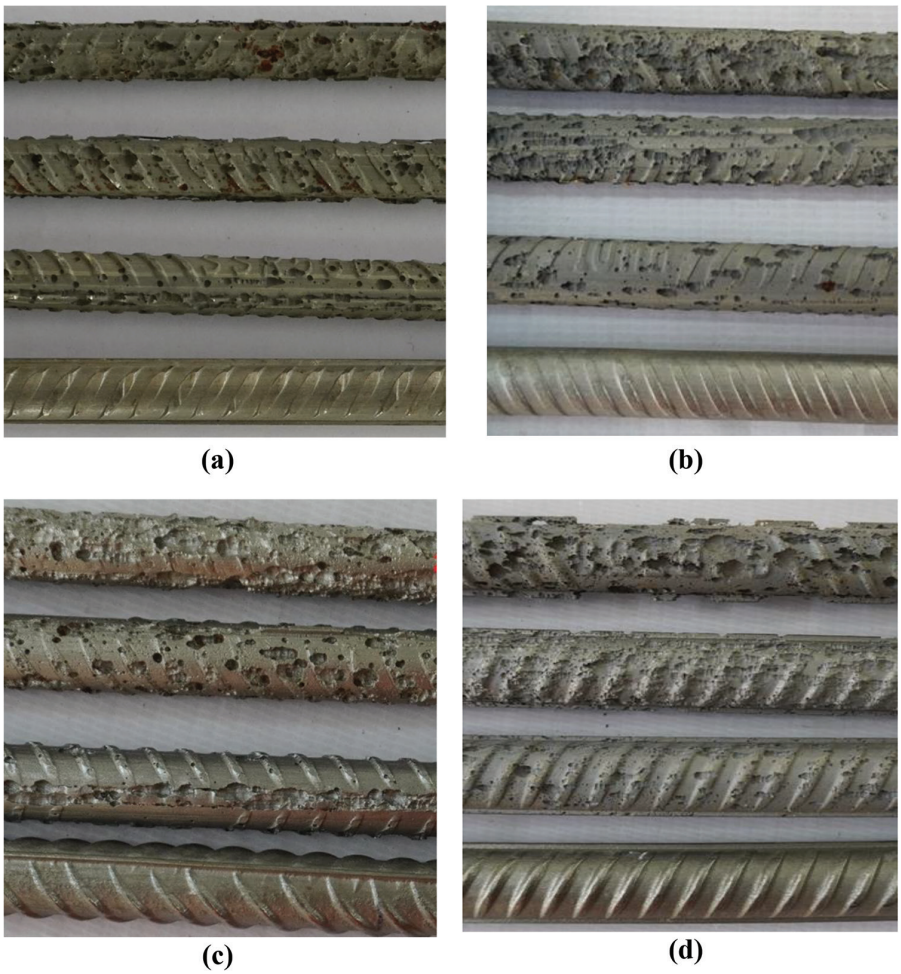

Fig. 6—Reinforcing bar before and after being subjected to target 5, 10, and 20% mass loss (bottom to top): (a) 8 mm; (b) 10 mm; (c) 12 mm; and (d) 16 mm.

of the reinforcing bar, resulting in varying shapes, sizes, and depths of pits in stainless-steel reinforcing bar. Therefore, a 95% prediction band is presented alongside the fitted curve, indicating that almost all data fall within this band. This band should be considered in practice due to the scattering in experimental data and uncertainties arising from severe pitting in stainless steel. Replicating the effects of severe pitting on mechanical properties is challenging, and this prediction band accounts for such uncertainties.

$$\frac{F_{uc}}{F_{uo}} = 1 - 0.017n_{ML} \tag{4}$$

$$\frac{F_{yc}}{F_{yo}} = 1 - 0.0187n_{ML} \tag{5}$$

$$\frac{\varepsilon_{uc}}{\varepsilon_{uo}} = 0.55 - 0.45e^{-0.138n_{ML}} \tag{6}$$

$$n_{AL} = 0.125 + 1.4n_{ML} \tag{7}$$

where F_{yc} is the yield load after corrosion; F_{yo} is the yield load before corrosion; ε_{uc} is the elongation percentage after corrosion; and ε_{uo} is the elongation percentage before corrosion.

Figure 7 illustrates a decrease in yield load, ultimate load, and elongation with an increase in mass loss. The decrease in yield load was higher than the ultimate load, possibly attributed to nonuniform pitting along the reinforcing bar that might affect the material before reaching the yield zone. This effect diminished at higher loads. The study also notes that the shape, size, density, and depth of pits have a more substantial impact on yield load and elongation than on ultimate load, consistent with previous research.[26,29,40] The decrease in elongation was even higher than the yield and ultimate loads with an increase in mass loss, indicating a more significant reduction in ductility than strength.[6,14,24,30,44] Figure 7(c) displays a pronounced decrease in elongation during initial mass loss, likely due to smaller pits resulting in higher stress concentration. This effect diminished as the size of pits increased and became interconnected at a higher mass loss, aligning with the visual observations discussed earlier.

Figure 7(d) demonstrates that the reduction in cross section is higher than the mass loss. Data are more scattered at moderate (10 to 15% mass loss) corrosion levels, but at lower and higher mass loss, the reduction in cross section closely relates to mass loss percentage.

Several authors have investigated the effect of corrosion and induced mass loss on the mechanical behavior

of reinforcing bar, proposing models using data-fitting methods. These proposed equations can be generalized as linear equations (Eq. (8)), where Y represents the degrading parameter ratio (F_{uc}/F_{uo} and F_{yc}/F_{yo}), m represents the degradation constant, X is the mass loss percentage (n_{ML} %), and C is a constant ($C = 1$). Table 3 shows the degradation constant (m) obtained by various authors. The basic difference in this experiment is the material used; this study used ferritic stainless steel, while other studies used carbon-steel reinforcement. Stainless-steel reinforcing bar exhibits severe pitting corrosion, while carbon steel suffers relatively uniform to localized corrosion. It is observed that the degradation constant (m) proposed by Tang et al.[24] and Moreno et al.[27] is lower than observed in this study. The m value for yield load proposed by Lee and Cho[28] closely aligns with the results of this study, but the m value for ultimate load is higher than that proposed by Lee and Cho.[28]

Figures 8(a) and (b) show the ultimate load degradation ratio and yield load degradation ratio predicted by other studies along with the current study. Figure 8(c) displays the elongation degradation ratio predicted by the current study compared with other studies. The models proposed by Lee and Cho[28] and Sheng and Xia[29] overpredict the degradation elongation ratio for mass loss up to approximately 20% while underpredicting for mass loss above 20%. The model proposed by Tang et al.[24] more closely aligns with the proposed model for mass loss up to approximately 5% while underpredicting the degradation elongation ratio for higher mass loss. This suggests that the loss in ductility is quite severe and nearly the same as carbon steel for initial mass loss, but for higher mass loss, the ductility loss in stainless steel is lower than in conventional carbon steel.

Table 3—Results comparison

Author	Yield load	Ultimate load
This study	0.0187	0.017
Lee and Cho[28]	0.0198	0.0157
Tang et al.[24]	0.017	0.017
Moreno et al.[27]	0.0144	0.0134

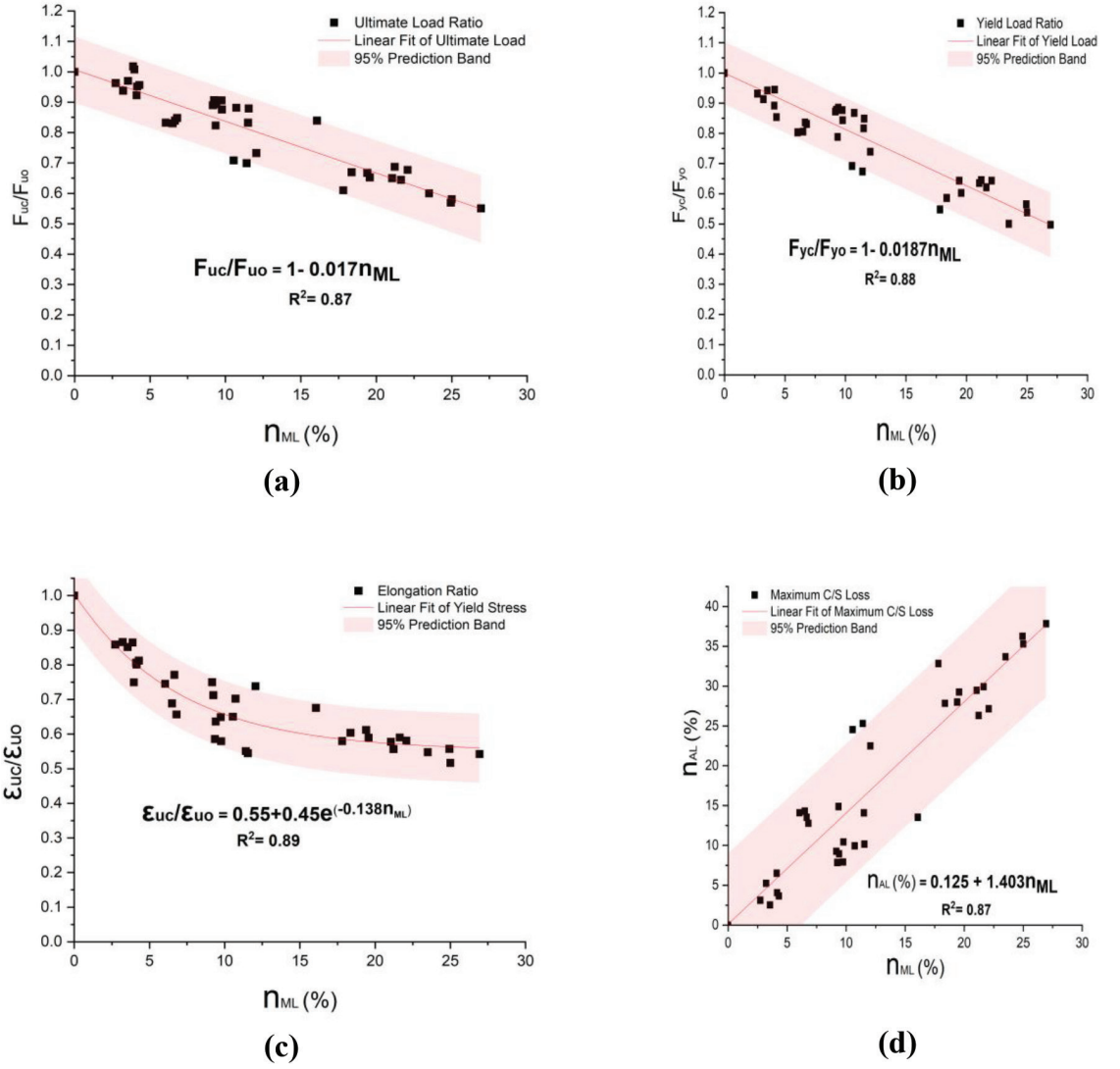

Fig. 7—Relationship between: (a) ultimate load degradation ratio versus mass loss percentage; (b) yield load degradation ratio versus mass loss percentage; (c) elongation degradation ratio versus mass loss percentage; and (d) maximum area loss versus mass loss percentage.

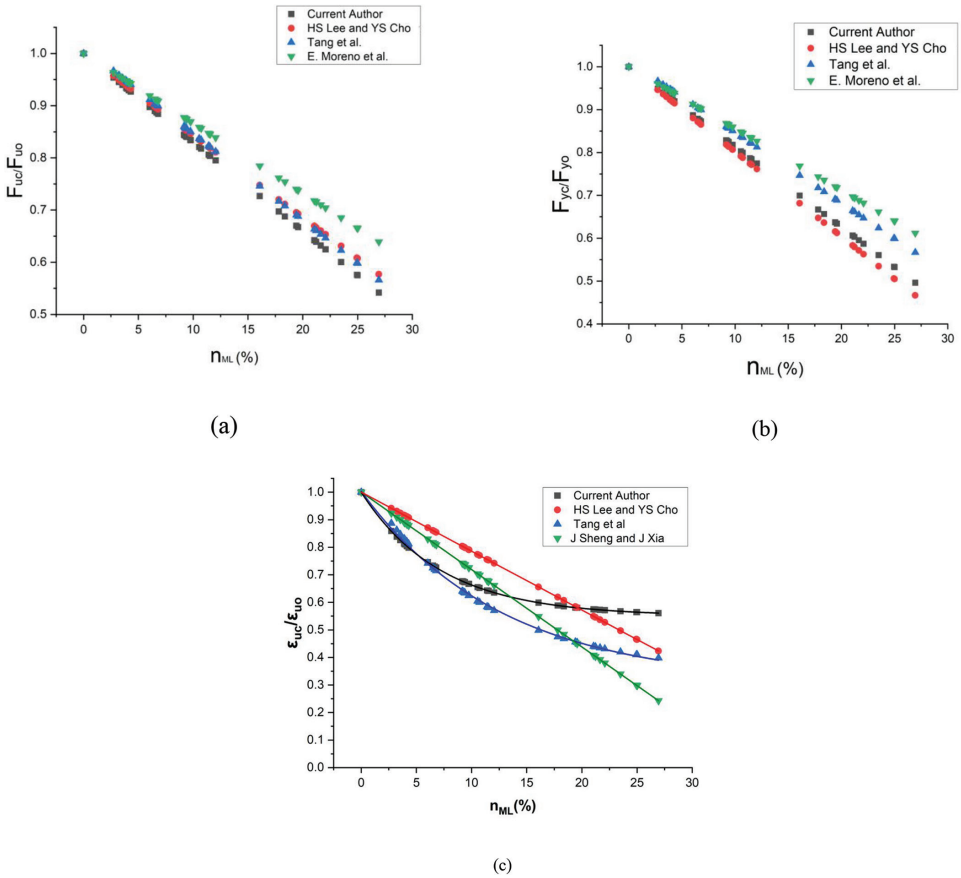

Fig. 8—Prediction model proposed by various authors: (a) ultimate load degradation ratio versus mass loss percentage; (b) yield load degradation ratio versus mass loss percentage; and (c) elongation degradation ratio versus mass loss percentage.

$$Y = C - mX \tag{8}$$

It is important to highlight that, in this study, the reduction in elongation capacity was particularly severe across the tested samples. For average mass loss percentages of 3.73%, 6.53%, 10.73%, and 23.76%, the corresponding reductions in elongation were 19.45%, 27.46%, 31.28%, and 41.52%, respectively. Significant reductions in yield and ultimate loads were observed in samples with mass loss greater than 3.73%. Specifically, the yield load decreased by 6.21%, 19.10%, 29.09%, and 46.56%, while the ultimate load dropped by 3.43%, 16.55%, 23.91%, and 42.69% for the respective mass loss levels.

Comparing these findings to previous studies, Du et al.[40] reported a 14 and 15% reduction in yield and ultimate loads at a 10% mass loss in carbon-steel reinforcing bars. In contrast, the present study on stainless-steel reinforcing bar shows more severe reductions of 19.1% in yield load and 29.09% in ultimate load at just a 6.53% mass loss. Apostolopoulos et al.[21] observed a 31.4% reduction in yield strength and a 22.9% reduction in ultimate strength at a 13.55% mass loss for carbon-steel reinforcing bars exposed to salt spray. Additionally, Andisheh et al.[26] reported a 31% reduction in elongation for reinforcing bars with a 10% mass loss, while Du et al.[45] reported a 29% reduction in elongation at the same level of mass loss percentage for carbon-steel reinforcing bar.

CONCLUSIONS

This study examined the impact of corrosion on the mechanical properties of ferritic stainless-steel reinforcing bar. The key observations and findings are summarized as follows:

1. Ferritic stainless-steel reinforcing bar exhibited pitting corrosion, which initiated at the interface of the reinforcing bar ribs and the body. As the mass loss increased, pit density rose, and larger pits began to interconnect rather than deepen further.

2. Corrosion-induced mass loss led to significant reductions in mechanical properties. Ferritic stainless steel showed a more pronounced reduction in both yield and ultimate loads than carbon steel, with degradation being more severe as mass loss increased.

3. The reduction in elongation was notably more severe than that in yield and ultimate loads. At lower mass loss (~5%), the reduction in percentage elongation was comparable with carbon steel; however, it became much more pronounced than carbon steel with an increase in mass loss levels.

4. Elongation at fracture for stainless steel can experience a significant reduction, even at relatively low mass loss percentages.

The findings of this study on the corrosion-induced behavior of ferritic stainless-steel reinforcing bar, along with the developed predictive models for mechanical properties, offer valuable insights. Future research could extend

these findings by exploring the impact of factors such as the shape, size, and density of corrosion on reinforcing bar's mechanical behavior. Additionally, investigating reinforcing bar behavior when embedded in concrete, where localized corrosion is common, would provide more realistic insights. Exploring more realistic corrosion methods, such as salt spray or alternate wetting-and-drying cycles, could enhance the applicability of the study's conclusions. Correlating accelerated corrosion methods with realistic scenarios would contribute to a comprehensive understanding, leading to robust predictive models for varied environmental conditions.

AUTHOR BIOS

Ankit Kumar Jaiswal *is a Research Scholar pursuing his PhD in the Department of Applied Mechanics at Visvesvaraya National Institute of Technology (VNIT) Nagpur, Nagpur, Maharashtra, India.*

Sangeeta Gadve *is a Professor in the Department of Applied Mechanics at VNIT Nagpur. She received her PhD in structural engineering from the Indian Institute of Technology (IIT) Bombay, Mumbai, Maharashtra, India. Her research interests include structural health monitoring, corrosion of reinforced concrete (RC) structures, concrete, reinforcements, and experimentation in structural engineering.*

REFERENCES

1. Valcarce, M. B., and Vázquez, M., "Carbon Steel Passivity Examined in Solutions with a Low Degree of Carbonation: The Effect of Chloride and Nitrite Ions," *Materials Chemistry and Physics*, V. 115, No. 1, May 2009, pp. 313-321. doi: 10.1016/j.matchemphys.2008.12.007

2. Wang, J.-H.; Cai, G.; and Wu, Q., "Basic Mechanical Behaviours and Deterioration Mechanism of RC Beams under Chloride-Sulphate Environment," *Construction and Building Materials*, V. 160, Jan. 2018, pp. 450-461. doi: 10.1016/j.conbuildmat.2017.11.092

3. NSBA, "Corrosion Protection of Steel Bridges," *Steel Bridge Design Handbook*, National Steel Bridge Alliance, American Institute of Steel Construction, Chicago, IL, 2006.

4. Cramer, S. D.; Covino, B. S. Jr.; Bullard, S. J.; Holcomb, G. R.; Russell, J. H.; Nelson, F. J.; Laylor, H. M.; and Soltesz, S. M., "Corrosion Prevention and Remediation Strategies for Reinforced Concrete Coastal Bridges," *Cement and Concrete Composites*, V. 24, No. 1, Feb. 2002, pp. 101-117. doi: 10.1016/S0958-9465(01)00031-2

5. Tang, F.; Chen, G.; Brow, R. K.; Volz, J. S.; and Koenigstein, M. L., "Corrosion Resistance and Mechanism of Steel Rebar Coated with Three Types of Enamel," *Corrosion Science*, V. 59, June 2012, pp. 157-168. doi: 10.1016/j.corsci.2012.02.024

6. Al-Mehthel, M.; Al-Dulaijan, S.; Al-Idi, S. H.; Shameem, M.; Ali, M. R.; and Maslehuddin, M., "Performance of Generic and Proprietary Corrosion Inhibitors in Chloride-Contaminated Silica Fume Cement Concrete," *Construction and Building Materials*, V. 23, No. 5, May 2009, pp. 1768-1774. doi: 10.1016/j.conbuildmat.2008.10.010

7. Sheelavantar, P. G.; Pandit, P.; Prashanth, S.; Nishit, N.; and Jadhav, M., "Taguchi-Integrated Grey Relational Analysis for Multi-Response Optimization of Mix Design for Alkali-Activated Concrete," *Materials Research Express*, V. 11, No. 7, July 2024, Article No. 075505. doi: 10.1088/2053-1591/ad592c

8. Bhagwat, Y.; Nayak, G.; Pandit, P.; and Lakshmi, A., "Effect of Polypropylene Fibres on Strength and Durability Performance of M-Sand Self Compacting Concrete," *Cogent Engineering*, V. 10, No. 1, 2023, Article No. 2233783. doi: 10.1080/23311916.2023.2233783

9. Hamsashree; Pandit, P.; Prashanth, S.; and Katpady, D. N., "Durability of Alkali-Activated Fly Ash-Slag Concrete-State of Art," *Innovative Infrastructure Solutions*, V. 9, No. 6, June 2024, Article No. 222.

10. Wang, X.-H.; Chen, B.; Gao, Y.; Wang, J.; and Gao, L., "Influence of External Loading and Loading Type on Corrosion Behavior of RC Beams with Epoxy-Coated Reinforcements," *Construction and Building Materials*, V. 93, Sept. 2015, pp. 746-765. doi: 10.1016/j.conbuildmat.2015.05.101

11. Huerta, E. O., *Corrosión y Degradación de Materiales*, Editorial Síntesis SA, Madrid, Spain, 2001, 368 pp.

12. Castro, H.; Rodriguez, C.; Belzunce, F. J.; and Canteli, A. F., "Mechanical Properties and Corrosion Behaviour of Stainless-Steel Reinforcing Bars," *Journal of Materials Processing Technology*, V. 143-144, Dec. 2003, pp. 134-137. doi: 10.1016/S0924-0136(03)00393-5

13. Calderon-Uriszar-Aldaca, I.; Briz, E.; Larrinaga, P.; and Garcia, H., "Bonding Strength of Stainless Steel Rebars in Concretes Exposed to Marine Environments," *Construction and Building Materials*, V. 172, May 2018, pp. 125-133. doi: 10.1016/j.conbuildmat.2018.03.156

14. Wu, X.; Ye, D.; Li, H.; and Yu, H., "Corrosion Characteristics of S23043 Duplex Stainless Steel Bars," *Construction and Building Materials*, V. 178, July 2018, pp. 135-143. doi: 10.1016/j.conbuildmat.2018.05.008

15. Shinomiya, H.; Kato, Z.; Enari, K.; and Hashimoto, K., "Effects of Corrosion-Resistant Elements on the Corrosion Resistance of Amorphous Bulk Ni-Cr-Mo-Ta-Nb-4P Alloys in Concentrated Hydrochloric Acids," *ECS Transactions*, V. 16, No. 32, 2009, pp. 9-18. doi: 10.1149/1.3091902

16. Lakshmi, A.; Pandit, P.; Kumar, A.; Bhagwat, Y.; Nayak, G.; and Shetty, A., "Study on Bond Behaviour of Corroded Reinforced Concrete Beam – Finite Element Analysis," *Cogent Engineering*, V. 11, No. 1, 2024, Article No. 2340298. doi: 10.1080/23311916.2024.2340298

17. Pandit, P., "Experimental Study on Accelerated Corrosion Technique of OPC and PPC Beams in Coastal Environment," *Journal of Corrosion Science and Engineering*, V. 22, 2019, 18 pp.

18. Papadopoulos, M. P.; Apostolopoulos, C. A.; Alexopoulos, N. D.; and Pantelakis, S. G., "Effect of Salt Spray Corrosion Exposure on the Mechanical Performance of Different Technical Class Reinforcing Steel Bars," *Materials & Design*, V. 28, No. 8, 2007, pp. 2318-2328. doi: 10.1016/j.matdes.2006.07.017

19. Apostolopoulos, C. A.; Papadopoulos, M. P.; and Pantelakis, S. G., "Tensile Behavior of Corroded Reinforcing Steel Bars BSt 500_S," *Construction and Building Materials*, V. 20, No. 9, Nov. 2006, pp. 782-789. doi: 10.1016/j.conbuildmat.2005.01.065

20. Cairns, J.; Plizzari, G. A.; Du, Y.; Law, D. W.; and Franzoni, C., "Mechanical Properties of Corrosion-Damaged Reinforcement," *ACI Materials Journal*, V. 102, No. 4, July-Aug. 2005, pp. 256-264.

21. Apostolopoulos, C. A.; Demis, S.; and Papadakis, V. G., "Chloride-Induced Corrosion of Steel Reinforcement – Mechanical Performance and Pit Depth Analysis," *Construction and Building Materials*, V. 38, Jan. 2013, pp. 139-146. doi: 10.1016/j.conbuildmat.2012.07.087

22. Palsson, R., and Mirza, M. S., "Mechanical Response of Corroded Steel Reinforcement of Abandoned Concrete Bridge," *ACI Structural Journal*, V. 99, No. 2, Mar.-Apr. 2002, pp. 157-162.

23. Wang, X.-G.; Zhang, W.-P.; Gu, X.-L.; and Dai, H.-C., "Determination of Residual Cross-Sectional Areas of Corroded Bars in Reinforced Concrete Structures Using Easy-to-Measure Variables," *Construction and Building Materials*, V. 38, Jan. 2013, pp. 846-853. doi: 10.1016/j.conbuildmat.2012.09.060

24. Tang, F.; Lin, Z.; Chen, G.; and Yi, W., "Three-Dimensional Corrosion Pit Measurement and Statistical Mechanical Degradation Analysis of Deformed Steel Bars Subjected to Accelerated Corrosion," *Construction and Building Materials*, V. 70, Nov. 2014, pp. 104-117. doi: 10.1016/j.conbuildmat.2014.08.001

25. Kashani, M. M.; Crewe, A. J.; and Alexander, N. A., "Use of a 3D Optical Measurement Technique for Stochastic Corrosion Pattern Analysis of Reinforcing Bars Subjected to Accelerated Corrosion," *Corrosion Science*, V. 73, Aug. 2013, pp. 208-221. doi: 10.1016/j.corsci.2013.03.037

26. Andisheh, K.; Scott, A.; Palermo, A.; and Clucas, D., "Influence of Chloride Corrosion on the Effective Mechanical Properties of Steel Reinforcement," *Structure and Infrastructure Engineering*, V. 15, No. 8, 2019, pp. 1036-1048. doi: 10.1080/15732479.2019.1594313

27. Moreno, E.; Cobo, A.; Palomo, G.; and Nieves González, M., "Mathematical Models to Predict the Mechanical Behavior of Reinforcements Depending on Their Degree of Corrosion and the Diameter of the Rebars," *Construction and Building Materials*, V. 61, June 2014, pp. 156-163. doi: 10.1016/j.conbuildmat.2014.03.003

28. Lee, H.-S., and Cho, Y.-S., "Evaluation of the Mechanical Properties of Steel Reinforcement Embedded in Concrete Specimen as a Function of the Degree of Reinforcement Corrosion," *International Journal of Fracture*, V. 157, No. 1-2, May 2009, pp. 81-88. doi: 10.1007/s10704-009-9334-7

29. Sheng, J., and Xia, J., "Effect of Simulated Pitting Corrosion on the Tensile Properties of Steel," *Construction and Building Materials*, V. 131, Jan. 2017, pp. 90-100. doi: 10.1016/j.conbuildmat.2016.11.037

30. Zhang, W.; Song, X.; Gu, X.; and Li, S., "Tensile and Fatigue Behavior of Corroded Rebars," *Construction and Building Materials*, V. 34, Sept. 2012, pp. 409-417. doi: 10.1016/j.conbuildmat.2012.02.071

31. François, R.; Khan, I.; and Dang, V. H., "Impact of Corrosion on Mechanical Properties of Steel Embedded in 27-Year-Old Corroded Reinforced Concrete Beams," *Materials and Structures*, V. 46, No. 6, June 2013, pp. 899-910. doi: 10.1617/s11527-012-9941-z

32. Austin, S. A.; Lyons, R.; and Ing, M. J., "Electrochemical Behavior of Steel-Reinforced Concrete During Accelerated Corrosion Testing," *CORROSION*, V. 60, No. 2, Feb. 2004, pp. 203-212. doi: 10.5006/1.3287722

33. El Maaddawy, T. A., and Soudki, K. A., "Effectiveness of Impressed Current Technique to Simulate Corrosion of Steel Reinforcement in

Concrete," *Journal of Materials in Civil Engineering*, ASCE, V. 15, No. 1, Feb. 2003, pp. 41-47. doi: 10.1061/(ASCE)0899-1561(2003)15:1(41)

34. Haris, N., and Gadve, S., "Mechanical Properties of Reinforcing Steel Bars Corroded at Different Levels," *ACI Materials Journal*, V. 118, No. 4, July 2021, pp. 109-120.

35. Jaiswal, A. K., and Gadve, S. S., "Residual Bond Strength of Highly Corroded Reinforced Concrete," *CORROSION*, V. 79, No. 11, Nov. 2023, pp. 1324-1335. doi: 10.5006/4333

36. Lakshmi, A.; Pandit, P.; Nayak, G.; Bhagwat, Y.; and Kumar, S., "Influence of Corrosion-Based Section Loss on Morphology and Tensile Capacity of Pre-stressing Strands," *Journal of Structural Integrity and Maintenance*, V. 9, No. 1, 2024, Article No. 2302655. doi: 10.1080/24705314.2024.2302655

37. ASTM G1-90(1999)e1, "Standard Practice for Preparing, Cleaning, and Evaluating Corrosion Test Specimens," ASTM International, West Conshohocken, PA, 1999, 8 pp.

38. Ou, Y.-C.; Susanto, Y. T. T.; and Roh, H., "Tensile Behavior of Naturally and Artificially Corroded Steel Bars," *Construction and Building Materials*, V. 103, Jan. 2016, pp. 93-104. doi: 10.1016/j.conbuildmat.2015.10.075

39. Papadopoulos, M. P.; Apostolopoulos, C. A.; Zervaki, A. D.; and Haidemenopoulos, G. N., "Corrosion of Exposed Rebars, Associated Mechanical Degradation and Correlation with Accelerated Corrosion Tests," *Construction and Building Materials*, V. 25, No. 8, Aug. 2011, pp. 3367-3374. doi: 10.1016/j.conbuildmat.2011.03.027

40. Du, Y. G.; Clark, L. A.; and Chan, A. H. C., "Residual Capacity of Corroded Reinforcing Bars," *Magazine of Concrete Research*, V. 57, No. 3, Apr. 2005, pp. 135-147. doi: 10.1680/macr.2005.57.3.135

41. Medina, E.; Medina, J. M.; Cobo, A.; and Bastidas, D. M., "Evaluation of Mechanical and Structural Behavior of Austenitic and Duplex Stainless Steel Reinforcements," *Construction and Building Materials*, V. 78, Mar. 2015, pp. 1-7. doi: 10.1016/j.conbuildmat.2015.01.008

42. Rabi, M.; Cashell, K. A.; and Shamass, R., "Flexural Analysis and Design of Stainless Steel Reinforced Concrete Beams," *Engineering Structures*, V. 198, Nov. 2019, Article No. 109432. doi: 10.1016/j.engstruct.2019.109432

43. Cerit, M.; Genel, K.; and Eksi, S., "Numerical Investigation on Stress Concentration of Corrosion Pit," *Engineering Failure Analysis*, V. 16, No. 7, Oct. 2009, pp. 2467-2472. doi: 10.1016/j.engfailanal.2009.04.004

44. Imperatore, S.; Rinaldi, Z.; and Drago, C., "Degradation Relationships for the Mechanical Properties of Corroded Steel Rebars," *Construction and Building Materials*, V. 148, Sept. 2017, pp. 219-230. doi: 10.1016/j.conbuildmat.2017.04.209

45. Du, Y. G.; Clark, L. A.; and Chan, A. H. C., "Effect of Corrosion on Ductility of Reinforcing Bars," *Magazine of Concrete Research*, V. 57, No. 7, Sept. 2005, pp. 407-419. doi: 10.1680/macr.2005.57.7.407

ACI Faculty Network

Why Join the Faculty Network?

The Faculty Network is a support group for educators interested in ACI and the concrete industry. Members receive notifications about classroom resources, fellowships and scholarships, funding for research, online learning, and calls for papers and presenters.

Free 1-Year Educator Membership

ACI offers complimentary membership to teaching professionals who have not been an ACI member within the past 5 years.

Free Desk Copies

Faculty Network members can request a complimentary print or PDF copy of:

- ACI CODE-318 Building Code Requirements for Structural Concrete and Commentary (includes a free subscription to ACI 318 PLUS)
- ACI CODE-530 Building Code Requirements and Specification for Masonry Structures and Companion Commentaries
- ACI CODE-562 Assessment, Repair, and Rehabilitation of Existing Concrete Structures—Code and Commentary
- MNL-3(20) Guide to the Code for Assessment, Repair, and Rehabilitation of Existing Concrete Structures
- MNL-5(19) Contractor's Guide to Quality Concrete Construction, 4th Edition
- MNL-17(21) ACI Reinforced Concrete Design Handbook (available digitally with ACI 318 PLUS subscription)
- MNL-66(20) ACI Detailing Manual (available digitally with ACI 318 PLUS subscription)

Networking

ACI hosts a Faculty Network Reception twice a year during the ACI Concrete Conventions, giving an opportunity to exchange ideas and network.

aci 318PLUS+

Faculty Network members receive a complimentary annual subscription that provides users with convenient digital interactive access to ACI CODE-318-25, ACI CODE-318-19, the ACI Detailing Manual, and the numerous design examples in the ACI Reinforced Concrete Design Handbook. The platform allows professors to create custom user notes that can be distributed to the students to view alongside the Code. Student members are provided 1-year access to ACI 318 PLUS when they purchase their printed copy of ACI 318-25 or ACI 318-19 at the student price of $105 (plus shipping).

aci Professors' Workshop
Materials | Pavements | Structures
Sponsor: aci Foundation

The Professors' Workshop is designed to provide instructors in civil engineering, architecture, architectural engineering, materials science, and construction management programs the tools to engage students in the latest developments in concrete design, construction, and materials.

aci Foundation
Building the Future

The Concrete Research Council (CRC) seeks concrete research projects that further the knowledge and sustainability of concrete materials, construction, and structures in coordination with ACI Committees. Annual Request for Proposals (RFP) are received annually between August 1 and December 1.

aci
American Concrete Institute
Always advancing

ADVANCE YOUR CLASSROOM WITH ACI

JOIN OR RENEW TODAY! concrete.org/educatorsandresearchers

ACI MATERIALS JOURNAL TECHNICAL PAPER

Title No. 122-M05

Effect of Surface Preparation Techniques on Concrete-Grout Interfaces

by Anthony Addai Boateng, Garrett Tatum, and Natassia Brenkus

Pourbacks and overlays are commonly used in bridge elements and repairs, as it is crucial to corrosion protection that the bond between grout and concrete in these regions is carefully constructed. The integrity of the bond is crucial to ensure a barrier against water, chloride ions, moisture, and contaminants; bond failure can compromise the durability of concrete structures' long-term performance. This study examines the influence of surface preparation methods on the bond durability and chloride permeability between concrete substrate and grouts, including both non-shrink cementitious and epoxy grouts. A microstructural analysis of scanning electron microscopic (SEM) images was conducted to characterize the porosity of specimen interfaces. Pulloff testing was performed to quantify tensile strength. Results show that a water-blasted surface preparation technique improved the tensile bond strength for cementitious grout interfaces and reduced porosity at the interface. In contrast, epoxy grout interfaces were less affected by surface preparation. The study establishes a relationship between chloride ion permeability, porosity, and bond strength. The findings highlight the importance of surface preparation in ensuring the durability of concrete-grout interfaces.

Keywords: cementitious grout; chloride ion; epoxy grout; surface preparation; tensile bond strength.

INTRODUCTION

In concrete composite systems, concrete-to-concrete or concrete-to-grout interfaces are common in both new construction and in the repair and strengthening of existing structures. The addition of fresh concrete or grout as an overlay to a hardened concrete substrate is frequent in the repair and maintenance of existing concrete structures.

Repair procedures involving secondary pours include the removal of any distressed concrete substrate layer, preparation of the surface of the concrete substrate is prepared to ensure a strong bond between the substrate and the secondary material, and, finally, the application of the bonded concrete or grout overlay (Espeche and León 2011). This study evaluates the effects of concrete substrate surface preparation techniques on bond performance and permeability. This work was conducted in the context of post-tensioned (PT) bridge structures. However, the results herein can be applied to concrete repair applications, PT pocket details for monostrand, and other pourback scenarios.

BACKGROUND

The nature of the interface bond between a concrete substrate and overlay has been investigated by several researchers (Babaei and Hawkins 1990; Bissonnette et al. 2012; Courard et al. 2011; De la Varga and Graybeal 2015; Momayez et al. 2005; Santos et al. 2012; Silfwerbrand 2003). Identified variables that influence the bond strength include the concrete substrate preparation technique, application of bonding agents, mechanical properties of the substrate and overlay, roughness of the interface, and method of testing used to evaluate the bond strength (Bentz et al. 2018; Kay and Beushausen 2018; Momayez et al. 2005). The surface roughness of the concrete substrate is one key parameter. Bond strength increases with concrete substrate roughness (Bentz et al. 2018; Bissonnette et al. 2012). The substrate interface roughness can influence the pourback material bond strength significantly. Reasons for substrate roughening are the eradication of delaminated concrete without introducing microcracks and exposing the aggregate at the surface to promote stronger interlock between the substrate and the overlay (Silfwerbrand 2009). Sand-blasted and water-jetted/blasted are often considered the best surface preparation techniques for achieving a suitable interface (Júlio et al. 2004).

Another variable is moisture availability at the concrete substrate surface before the casting of the overlay (De la Varga et al. 2015; Kay and Beushausen 2018). While there is disagreement over the effect of the saturation condition of the concrete substrate surface before casting the overlay (Kay and Beushausen 2018), several researchers recommend a saturated surface-dry (SSD) condition, which is the application of moisture before pouring the overlay (De la Varga et al. 2015, 2017). The practice of pre-moistening concrete substrate surface to attain an SSD condition has become widespread in the construction industries (Bissonnette et al. 2012).

Of particular consideration of the researchers is the integrity of PT systems' pourbacks. Protecting PT anchorages is critical for the long-term durability of PT structures. Hence, the strands under tensile force are protected, increasing the structure's life span. The PT anchorage comprises three layers, which shield the strands from corrosion (Tatum and Brenkus 2021): a permanent grout, a plastic cap, and a pourback material.

The typical PT pourback detail requires a secondary pour against a vertical face; the orientation of this pour lends itself to unequal distribution of the mixture. Surface preparation

ACI Materials Journal, V. 122, No. 1, January 2025.
MS No. M-2024-071.R3, doi: 10.14359/51744378, received October 10, 2024, and reviewed under Institute publication policies.

Table 1—Concrete mixture

Material	Weight, lb	Weight, kg
Sand	2660	1207
Coarse limestone aggregate	2720	1234
Fine limestone aggregate	540	245
Type 1L cement	895	406
Slag cement	410	186
Water	378	172

is often not explicitly considered; as a result, the bond and interface in these critical details may be less than optimal. Further complicating the integrity of this critical region, anchorages may be located in locations in a bridge structure of reduced accessibility, making their inspection and repair difficult. Researchers argue that failures attributed to both physical and chemical deficiencies in grout allow chloride ions and water, which act as corrosion agents, to penetrate regions where grout quality is compromised, including areas surrounding PT tendons (Hartt 2018; Miller et al. 2017).

Chloride ion penetration and contamination are proven initiators of PT tendon deterioration. Liao (2017) highlighted that even in the absence of external sources, defects such as voids and improper grouting methods result in pockets of moisture, allowing chloride ions to concentrate locally and initiate corrosion. Similarly, Whitmore et al. (2014) confirmed that chloride contamination leads to accelerated corrosion of PT tendons. Chloride ions may exist in the original mixture before casting a concrete structure from the external environment. Instances of considerable corrosion in jetty substructures have occurred due to chloride contamination in marine environments (Liam et al. 1992).

This study evaluates the effects of concrete substrate surface preparation techniques on bond performance and permeability. This work was conducted in the context of PT bridge structures. However, the results herein can be applied to concrete repair applications, PT pocket details for monostrand, and other pourback scenarios. The surface of the concrete substrate was prepared according to the current practice of the selected state departments of transportation (DOTs) (FDOT 2019; ODOT 2019). The bond strength between the concrete substrate and the grout was assessed by the direct tensile strength test, also known as the pulloff bond strength test, ASTM C1583/C1583M-20 (2020). To describe the ion permeability along the interfaces, chloride profiling was conducted to measure the chloride ion diffusion by ASTM C1152/C1152M-20 (2020) and ASTM C1556-22 (2022). Additionally, porosity was evaluated through scanning electron microscopy (SEM) images in the grout materials along the concrete-grout interface and correlated to bond strength.

RESEARCH SIGNIFICANCE

This study investigates the traditional practices associated with pourback and overlay placements, considering the regularly specified constitutive materials and the types of surface preparations. It recommends improvements to construction and testing approaches to enhance overall structural durability.

Table 2—4 x 8 in. (102 x 203 mm) concrete cylinder compressive strength test results

Age	Specimen	Ultimate compressive stress, psi (MPa)	Average f_c', psi (MPa)	Standard deviation
28 days	1	6528 (45)	6831 (47)	621.2707
	2	7546 (52)		
	3	6420 (44)		

Table 3—2 x 2 in. (50 x 50 mm) grout cubes' compressive strength test results

Age	Specimen	Ultimate compressive stress, psi (MPa)	Average f_c', psi (MPa)	Standard deviation
Epoxy grout				
28 days	1	12,199 (84)	11,473 (79)	667.0055
	2	10,887 (75)		
	3	11,334 (78)		
Cementitious grout				
28 days	1	8656 (60)	7305 (50)	1221.506
	2	6279 (43)		
	3	6979 (48)		

EXPERIMENTAL INVESTIGATION

Material properties

A concrete mixture conforming to the Ohio DOT QC2 specification (ODOT 2019) was used for the concrete substrate. The concrete used in this study was designed with a slump of 4 in. (102 mm), a 28-day design compressive strength of 6831 psi (47 MPa), a minimum cementitious content of 520 lb (236 kg), and incorporated a well-graded aggregate. The concrete mixture (Table 1) comprised of the following materials: sand; coarse limestone aggregate (following ASTM C33/C33M-24 [2024]), with no more than 3.8% passing a No. 200 sieve); fine limestone aggregate (natural sand, per ASTM C33/C33M); Type 1L cement (complying with ASTM C595/C595M-24 [2024]); and slag cement (according to ASTM C989/C989M-24 [2024]). It is essential to note that the inclusion of slag cement contributes to the reduction of permeability, enhancing the long-term durability of concrete. A non-shrink cementitious grout was considered for this study, with a manufacturer-specified 28-day compressive strength of 9000 psi (63 MPa). Following the manufacturer's recommendations, the grout was mixed with a minimum amount of water to provide the desired workability. The grout required a water-to-solid ratio (w/s) of 0.16, which is 9 lb (4.08 kg) of water per 55 lb (25 kg) bag. However, the tested compressive strength conducted per ASTM C579-23 (2023) was 7305 psi (50.4 MPa) (Table 2), which is lower than expected. Also used was a three-component modified epoxy-resin-based grout with a manufacturer-specified strength of 16,000 psi (110 MPa). Compression testing of the prepared materials presented 11,473 psi (79 MPa) (Table 3). These variations may be due to differences in curing conditions, mixing procedures, or

Fig. 1—Surface preparation methods: (a) wet-sand blasting; and (b) water blasting.

Table 4—Experimental groups

Pourback material	Surface preparation procedure		
	Wet sand-blasted (SB) with 3000 psi (21 MPa) nozzle	Water-blasted (WB) with a 3000 psi (21 MPa) nozzle	No preparation (N)
Cementitious grout (CG)	CGSB	CGWB	CGN
Epoxy grout (EG)	EGSB	EGWB	EGN

environmental factors during testing. The tested materials, however, displayed acceptable performance for the intended purpose of this study, and the measured strengths were used in the analysis.

Experimental groups

The concrete substrate surface was prepared by considering wet sand-blasted and water-blasted (Fig. 1), both at a 3300 psi (23 MPa) nozzle pressure and no surface preparation method, as given in Table 4.

A prepared concrete surface was achieved using a commercial 3300 psi (23 MPa) rated washer pressure and a 15-degree spray nozzle 4 in. (102 mm) from the concrete surface. Figure 2 illustrates the concrete surface conditions after roughening, corresponding to Concrete Surface Profiles (CSP) 6 to 7 as classified by the International Concrete Repair Institute (ICRI) under ICRI 310.2R (2013). The water-blasted technique was achieved at 0.004 in.^{2}/s (2.58 mm^2/s) by striking the surface with only water to expose the coarse aggregate. Subsequently, the wet sand-blasted procedure had a rate of 0.02 in.^{2}/s (12.9 mm^2/s) to expose the coarse aggregate using fine-graded play sand and water.

Concrete-grout specimen preparation

A concrete slab with dimensions 54 x 39 x 5 in. (1372 x 991 x 127 mm) was used as the substrate for the direct tensile strength pulloff tests. The area of interest had a thickness of 3 in. (76 mm) of the concrete substrate and 2 in. (50 mm) thickness of the grout (overlay). The concrete slab was covered with burlap and plastic and cured for 28 days at a standard laboratory temperature of 68°F (20°C) and a relative humidity of 50%. Before casting the grout, the surface preparation was performed. The substrate was ponded with water for 48 hours and then prepared in SSD condition. The surface was clean from dirt and dust. A 2 in. (50 mm) thick grout overlay was cast over the prepared exposed concrete slab surface, creating an interface between the concrete substrate and the grout material. No vibration was necessary throughout the grout casting because both materials demonstrated self-consolidation properties.

TEST METHODS

Bond strength by pulloff testing

The bond strength assessment was conducted on the concrete grout slab in accordance with ASTM C1583/C1583M. Tests were performed when the concrete substrate and grout overlay were 90 and 60 days of age, respectively. The slabs were designed such that the coring rig could be directly mounted to the face of the slab to eliminate differential movement between the test site and the coring rig. The slabs were also sufficiently large enough that the concrete mass could dampen vibrations during coring and not

Fig. 2—Surface of prepared specimens: (a) wet-sand-blasted; and (b) water-blasted.

Fig. 3—Pulloff testing: (a) coring; and (b) testing.

transmit to the test sites. Specimens were cast and tested in the horizontal orientation. Troughs in the concrete for each pourback were constructed by blocking out the forms with wood framing and plastic tarps during concrete casting. The test locations were cored through the grout and penetrated the concrete by approximately 0.5 in. (13 mm) (Fig. 3(a)). For each test, a 2 in. (50 mm) diameter steel disc was glued to the cored locations. The specimens were dried for 7 days before attaching test dollies. The surface of each pulloff test site was cleaned with acetone and compressed air immediately before gluing test dollies with epoxy gel. The epoxy was allowed to cure for 24 hours before pulloff testing. A tensile load was applied using an adhesion tester, and the failure modes were recorded. As required by ASTM C1583/C1583M, at least three valid tests were completed, with results documented for each failure mode. Figure 4 presents the types of tensile failures encountered.

Chloride ion permeability testing

The presence of chloride ions is a primary cause of reinforcing steel corrosion. The chloride ions penetrate concrete through diffusion, capillary absorption, and hydrostatic pressure mechanisms; however, the principal mechanism is diffusion through pore fluid (Mutitu and Wachira 2014). Various tests are accessible for direct and indirect assessment of chloride ion penetration into concrete. These include the Rapid Chloride Penetration Test (RCPT) (ASTM C1202-22e1 2022), chloride diffusion tests (ASTM C1556), resistivity measurements, absorption tests, and electrical migration tests, among others. The chloride diffusion test method is considered for this study because it is meant to produce a property known as the apparent diffusion coefficient. This property illustrates the resistance faced by chloride ions as they penetrate concrete principally by diffusion rather than capillary transport. This method required approximately 60 days to complete. Chloride ion permeability was determined with concrete cylinder specimens of 6 x 12 in. (152 x

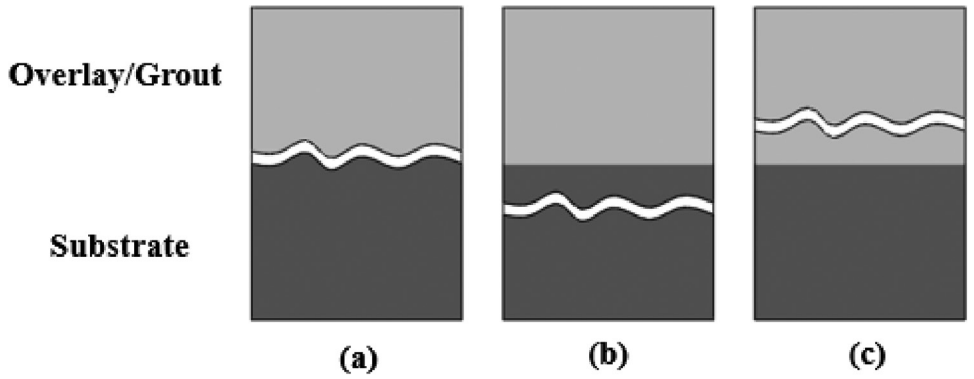

Fig. 4—Interface bond failure modes: (a) interface failure; (b) failure in concrete substrate; and (c) failure in overlay/grout.

305 mm) with one half filled with concrete and the other half grout (Fig. 4(a)). It is important to note that the concrete substrate was 120 days old, and the grout overlay was 90 days old at the testing time. While a 4 x 8 in. (102 x 203 mm) cylinder specimen is specified for conducting this test per ASTM C1556, a 6 x 12 in. (152 x 305 mm) cylinder was used instead to ensure enough material could be milled at the interface site to perform the test. This test specimen was constructed by casting the substrate material in a half-cylinder mold followed by the same curing and surface preparation regimes described previously. When casting the pourback, the half cylinder was placed into a new 6 x 12 in. (152 x 305 mm) cylinder mold, and the void space was filled with grout. Specimens were prepared by cutting a 3 in. (72 mm) thick slice to expose the surfaces of the concrete and grout material to salt water. Prior trials (data not presented here) using an interface specimen constructed of a 4 x 8 in. (102 x 203 mm) cylinder mold allowed for only 1 to 2 g (0.035 to 0.071 oz) of material to be milled along the interface for each 0.08 in. (2 mm) of depth, requiring the use of many test samples and potential increases in errors. Using a test specimen developed from a 6 in. (152 mm) diameter cylinder allowed much more material to be ground from a single test sample. The samples were exposed to a lime water bath for 48 hours prior to saltwater exposure. Per ASTM C1556, the saltwater used was a mixture of deionized water and technical-grade sodium chloride at a concentration of 165 g/L (5.82 oz/gal.); no other compounds were present in the solution. The specimens were immersed in the salt solution for 35 days. Profile grinding was performed using a milling machine with a 5/16 in. (7.9 mm) diameter concrete coring bit to obtain powdered samples (Fig. 5(d)). Eight-layer thicknesses were ground in 0.04 in. (1 mm) increments in each constitutive material and along the concrete-grout interface for each surface preparation technique. Initial chloride concentration was determined using specimens not exposed to the salt solution. The profile milling was performed to gather samples for chloride profiling, acid dissolution, determination equivalence point, and to obtain chloride content at several depths by titration with silver nitrate using an auto titrator per ASTM C1152/C1152M (Fig. 5(b)). A nonlinear regression analysis was run on the data to determine the diffusion coefficient.

Sampling and microstructural analysis

Three cored sample specimens that measured 2 in. (50 mm) diameter were extracted and prepared for microstructural analysis. These samples were extracted so that the concrete-grout interface was exposed. At the time of sampling, the concrete substrate was 150 days old, and the grout overlay was 120 days old. The selection of these ages intentionally captured the stabilized microstructure of the concrete and the grout. The ages of the microstructural specimens represent a mature period with well-developed hydration products, granting an accurate assessment of its long-term porosity characteristics. Removing any water particles in the cored specimens before the preparation (particularly during epoxy impregnation) is essential because water particles can interfere with the polymerization of the stabilizing epoxy (Kjellsen et al. 2003; Struble and Stutzman 1989). The specimens were immersed in isopropanol for 48 hours after coring and then dried in an oven at 122°F (50°C). Before performing polishing and grading, the specimens were impregnated with a low-viscosity (LV) resin because stabilizing and keeping the pore structure is essential (Struble and Stutzman 1989; Stutzman and Clifton 1999). Sequential grinding, lapping, and polishing with progressively finer abrasion were performed to obtain a flat-polished surface for imaging (Fig. 6). The quality of the polished surfaces was examined using an optical microscope in a reflected light mode.

After preparing the sample, the microstructure of the final polished specimens was examined using SEM. Images were collected using a backscattered electron detector. Imaging was accomplished under a low vacuum detector (LVD) at 20 kV and a 0.39 in. (10 mm) working distance. Each map had an area of 24 tiles with a magnification of 3000×, stitched together to form a large backscatter electron (BSE) map with a total area of 216 fields. Each tile set has an area of 0.005 in.^{2} (3.54 mm^2). Large BSE maps were collected using microanalysis software. For each specimen, nine maps were collected from random areas to ensure the analysis was representative of the sample.

Porosity profiles were obtained from the images by extracting successive 10 µm wide bands (Diamond and Huang 2001; Elsharief et al. 2003) (Fig. 7(c)) in both the concrete and grout. Segmentation was performed on the obtained original large BSE map for the quantification of porosity (Beyene et al. 2017; Igarashi et al. 2005; Lange

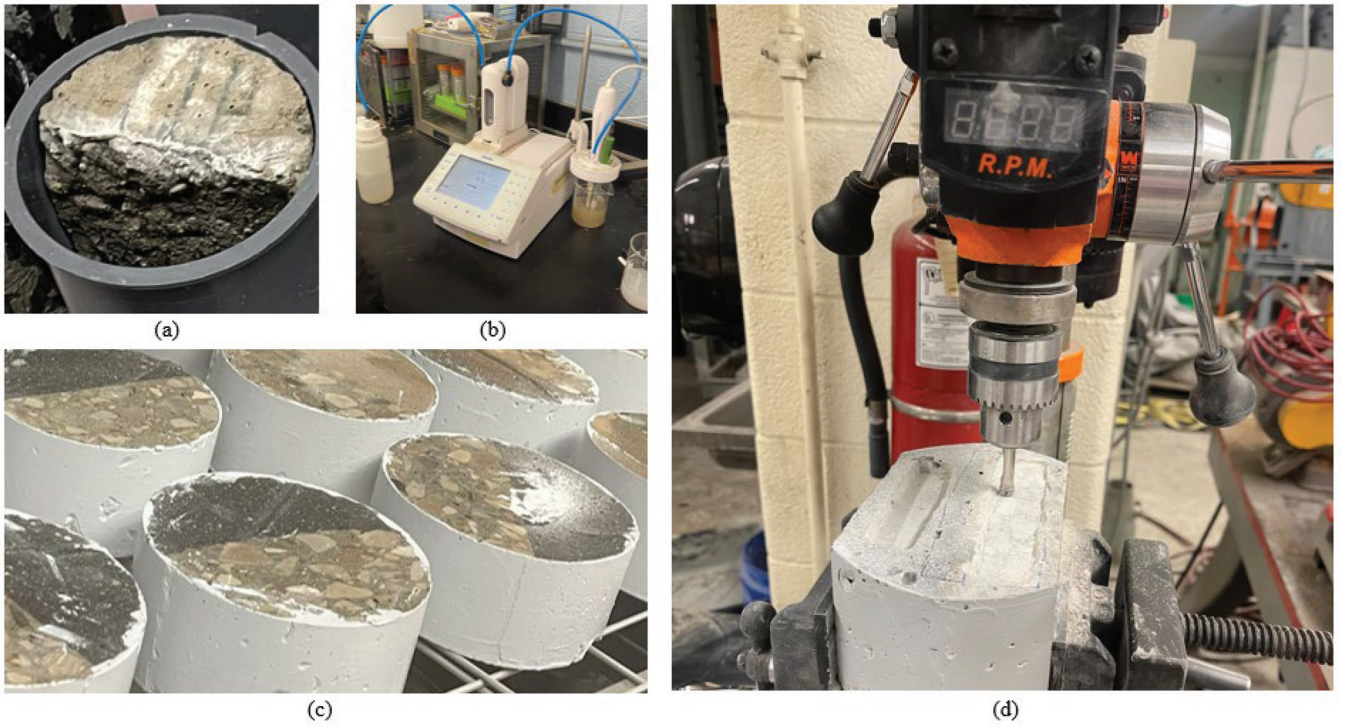

Fig. 5—Ion permeability testing: (a) half concrete cylinder mold; (b) determining acid-soluble chloride content; (c) sliced samples; and (d) milling sample.

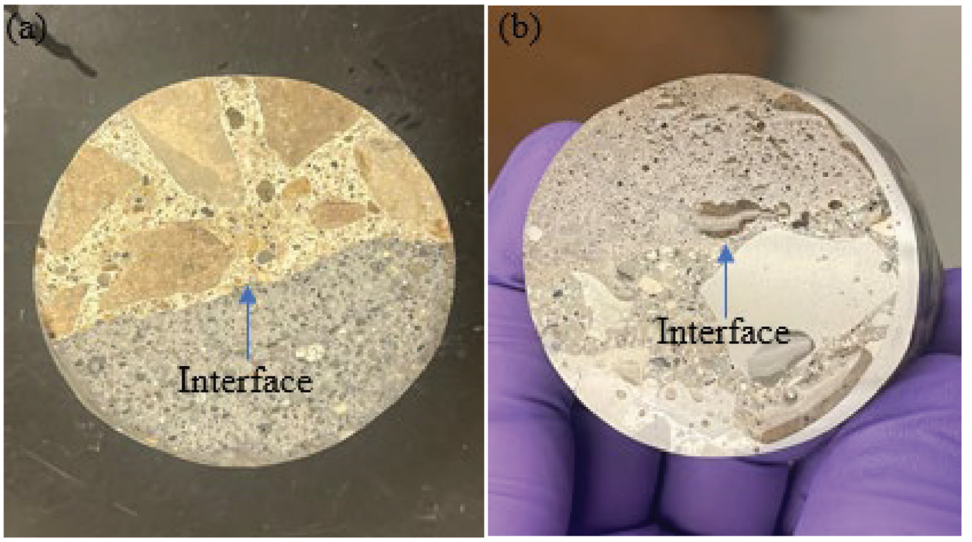

Fig. 6—Polished samples: (a) concrete-cementitious grout; and (b) concrete-epoxy grout.

et al. 1994; Zhao and Darwin 1992). The segmentation of the pores from the collected BSE images was performed using ImageJ software, which has an automatic thresholding technique that differentiates between the pore spaces and the solid phases based on greyscale intensity. The threshold was adjusted manually, as required, to ensure accurate pore identification, specifically in areas where the greyscale contrast was less distinct. Porosity fractions were calculated by measuring the percentage of pore area relative to the total mapped area for each band, with an average value obtained from the nine randomly collected maps. This process allowed for an accurate representation of the porosity distribution. Errors in porosity calculation were minimized by collecting multiple maps. An example of the large BSE map with a typical 10 µm wide bands and segmentation process is presented in Fig. 7(d).

RESULTS AND DISCUSSION

Pulloff tests

Figure 8 shows the bond strength results, representing the mean values obtained from the epoxy and cementitious grout interface specimens used for this study. These results were obtained from 90 days of concrete substrate and 60 days of old grout. All observed failure types were interface failures. Results presented by the epoxy grout specimens' pulloff strength values were more significant than those of

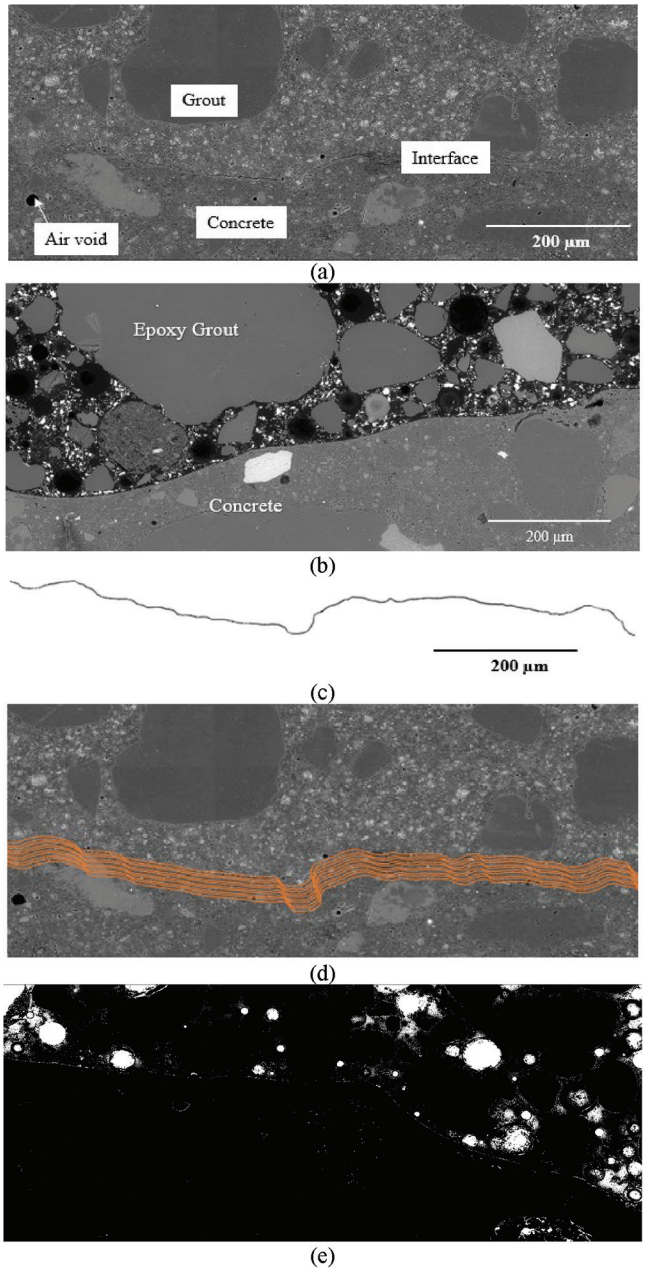

Fig. 7—SEM imaging: (a) and (b) large BSE map; (c) example 10 µm wide band; (d) location along the interface of 10 µm wide bands; and (e) example segmentation process.

the cementitious grout specimens; all the epoxy grout test samples within the no-preparation and water-blasted groups did not fail at 580.2 psi (4 MPa), which is the capacity of the test equipment (Fig. 9(a)). The epoxy grout wet sand-blasted interface test specimens failed at an average strength of 287.5 psi (1.98 MPa) with an interface failure mode (Fig. 9(b)). On the contrary, the cementitious grout interface specimens exhibited significantly lower bond strength values. The average for the no-preparation specimens was 43.6 psi (0.3 MPa); wet sand-blasted presented 75.2 psi (0.52 MPa), and water-blasted 150.4 psi (1.04 MPa) pulloff strength values. The types of bond failure modes observed in the cementitious grout interface specimens predominantly occurred at the concrete grout interface (Fig. 10). The mean values from the epoxy and cementitious grout interface

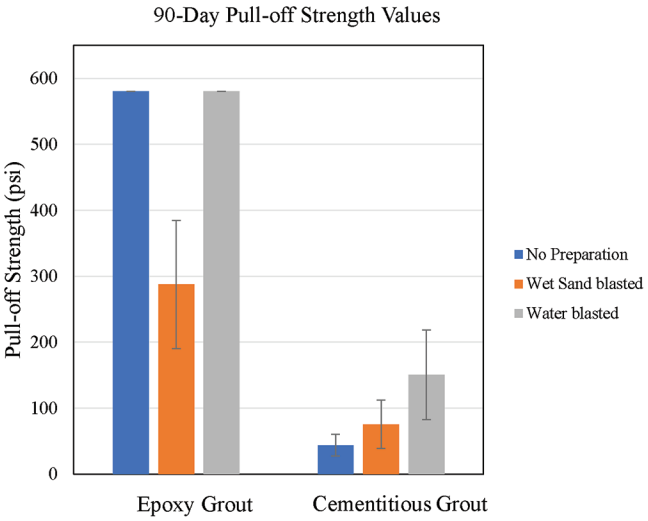

Fig. 8—Pulloff bond strength tests: influence of surface preparation.

specimens displayed a more significant scatter, as indicated by the standard deviations in the figure.

The experimental results clearly show that the type of surface preparation technique does not result in higher tensile bond strength for the epoxy grout interface specimens, as both the no-preparation and water-blasted surfaces presented the same bond strength. For the epoxy grout interface specimens, it is suspected that during the surface preparation, the moisture did not penetrate the surface of the concrete substrate in the no-preparation and water-blasted interfaces. Because epoxy is water-insoluble, it is possible that this produced deeper epoxy penetration in the no-preparation and water-blasted test specimens and higher tensile strength.

For the cementitious grout interface specimens, the results presented are evident that the type of surface preparation technique influences the bond strength. The water-blasted interface specimens presented a higher bond strength for the cementitious grout group. Results are in agreement with Silfwerbrand (2009); high-pressure water blasting is efficient on concrete surfaces, does not damage concrete, and improves the working environment.

All the bond strength values from the cementitious grout interface specimens were lower than the minimum pull-off strength value of 175 psi (1.2 MPa) specified by some states' DOTs (FDOT 2019; ODOT 2019) with failure mode at the interface.

Influence of surface preparation

Composite specimens with a concrete substrate and grout overlay exhibit a significant increase in bond strength when the interface surface is prepared using the water-blasted preparation technique. This observation is valid for only the concrete-cementitious interface specimens, revealing that the type of surface preparation technique controls the bond strength for these specimens.

Chloride profiling

The depth of absorptivity measurements was determined from chloride profiling per ASTM C1556, with chloride

Fig. 9—Post-test of epoxy core samples after pulloff testing, showing fracture surface: (a) no failure observed; and (b) interface failure.

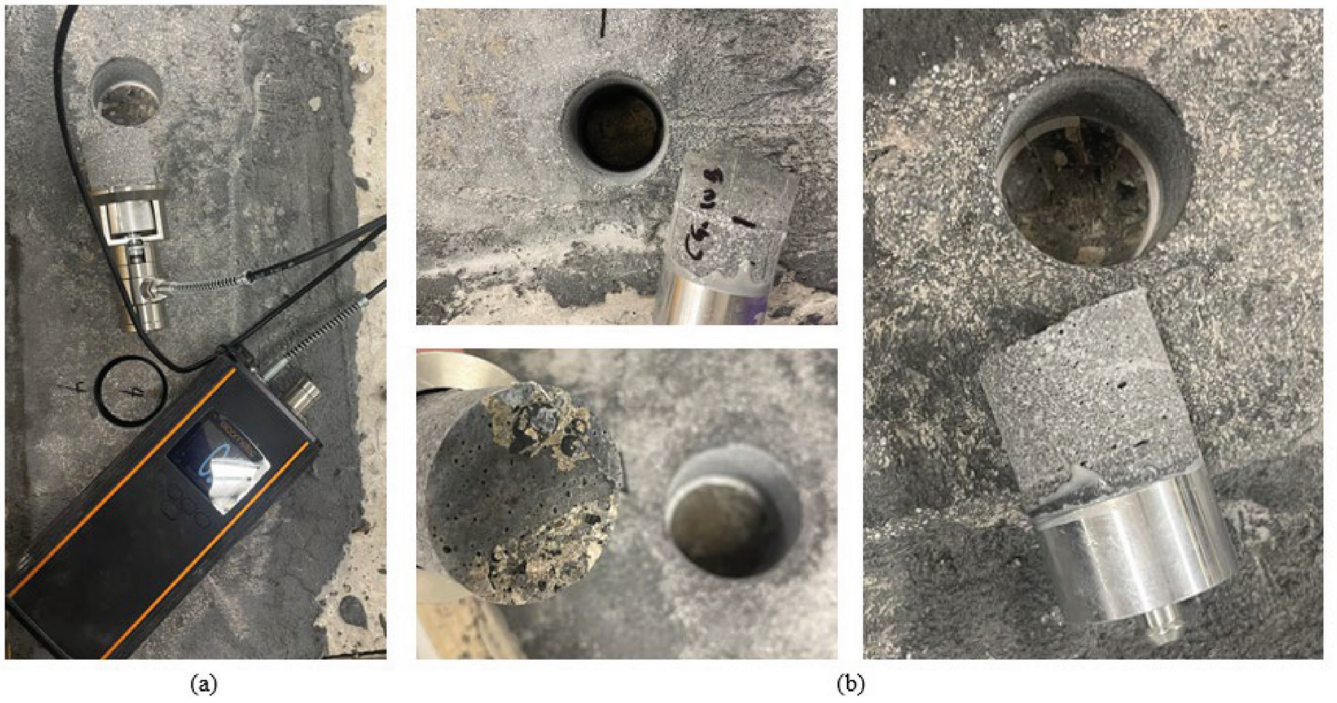

Fig. 10—Post-test of cementitious core samples after pulloff testing, showing fracture surface: (a) pulloff testing; and (b) interface failures.

contents at each depth determined by ASTM C1152/C1152M. Profiles were measured after test samples (Fig. 5(c)) were exposed to saltwater for 35 days. Least-squares regression was then used to determine the material's apparent diffusion, *Da*, and to predict the concentration of chloride ions at the surface of test samples. Results for each experimental group are presented in Table 5. The data points show the minimum average of each sample at an average depth from the exposed surfaces. The table presents each constitutive material's initial chloride content, C_i, before exposure to salt water. C_s is the estimated chloride content of the material at its exposed face. Figure 11 presents the apparent diffusion coefficient and *Da* for each constitutive material and interface area.

The diffusion coefficient assesses how swiftly ions can diffuse through a material. A lower diffusion coefficient implies that ions will take longer to diffuse through the material, which is associated with more excellent durability. Initial chloride concentrations, C_i, vary between 0.0030% by sample weight for epoxy grout and 0.0457% by sample weight for cementitious sand-blasted interface specimens. The initial chloride content of the concrete design mixture is 0.19% by weight of cement; this is greater than the recommended limit specified by ACI 222.2R-01 (ACI Committee 222 2001) for prestressed concrete construction (0.08%) but

Table 5—Chloride profiling results

Material		Initial chloride content C_i, % sample weight	Calculated surface chloride content C_s, % sample weight	Apparent diffusion coefficient Da, m^2/s
Concrete		0.0442	0.7308	5.412×10^{-12}
Epoxy grout		0.0030	0.4401	3.280×10^{-14}
Cementitious grout		0.0306	0.7219	1.397×10^{-12}
Interface	Sand-blasted epoxy grout	0.0457	0.4483	4.073×10^{-12}
	Epoxy grout with no preparation	0.0439	0.4401	5.156×10^{-12}
	Water-blasted epoxy grout	0.0447	0.4401	5.341×10^{-12}
	Sand-blasted cementitious grout	0.0365	1.6794	1.957×10^{-12}
	Cementitious grout with no preparation	0.0420	0.6522	5.544×10^{-12}
	Water-blasted cementitious grout	0.0386	0.5202	4.118×10^{-12}

less than that specified for ordinary reinforced concrete in severe exposure (0.20%). It is essential to state that though the measured initial chloride content of the concrete is outside of recommendations for PT concrete, this study pursued the characterization of chloride ion diffusion, which is negligibly impacted by the increased chloride ion presence as the diffusion model considered by ASTM C1556 does not generally consider chloride ion binding.

The surface chloride contents, C_s, ranged from 0.4401 to 1.6794% by sample weight for the test specimens and agree with values reported by Song et al. (2008) and Burris and Riding (2014). Ion contents at the surface were high; these are expected because the surfaces were the exposure faces. The epoxy grout group with its interface specimens presented the lowest C_i (0.4401 to 0.4483%), suggesting a low chance of chloride concentration throughout the sample.

The concrete material presented a calculated diffusion coefficient of 8.4×10^{-9} $in.^2/s$ (5.4×10^{-12} m^2/s). The epoxy and cementitious grouts presented diffusion coefficients of 5.1×10^{-11} $in.^2/s$ (3.3×10^{-14} m^2/s) and 2.2×10^{-9} $in.^2/s$ (1.4×10^{-12} m^2/s). The diffusion coefficients of all the interface specimens but for cementitious grout, no surface preparation specimens (CGN) were determined to be between concrete and grout. These results were expected as the chloride profiling technique for the interface region required milling approximately 0.08 in. (2 mm) for grouts and concrete material on either side of the interface. Epoxy grout water-blasted (EGWB) and no-preparation interface specimens (EGN) had diffusion coefficients closer to concrete, whereas sand-blasted (EGSB) presented a lower value. For the cementitious grout interface specimens, the wet sand (CGSB) and water-blasted (CGWB) techniques had diffusion coefficients less than those of epoxy grout counterparts, possibly due to the increasing matrix of cement hydration products along the interface during curing. However, cementitious grout with no preparation presented a diffusion coefficient greater than constitutive materials and the other interface specimens. This indicates that the cementitious grout specimens with no surface preparation (CGN) are more susceptible to chloride ion intrusion than either of the constitutive materials and could serve as a fast track for chloride ions to initiate corrosion of the PT anchorage, possibly due to localized increased porosity at the interface and a lack of mechanical interlock

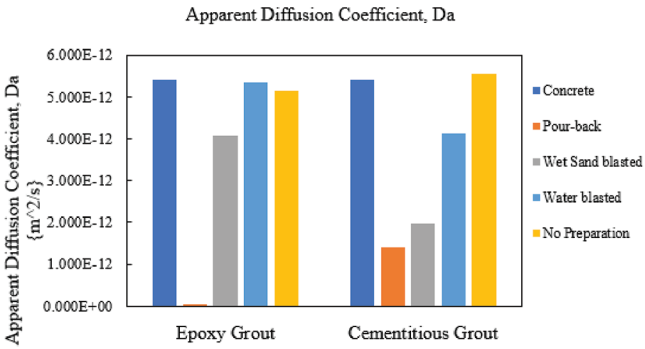

Fig. 11—Apparent diffusion coefficients.

between materials. The material interface between concrete and grout should have a predicted diffusion coefficient that is less than that of concrete to mitigate the risks of premature corrosion of the anchorage.

Time required to initiate corrosion

To present how the apparent diffusion coefficients relate to the durability of a concrete structure, the time required to initiate corrosion of mild steel reinforcement was modeled with Life-365 service life-prediction model software based on chloride profiling measurements and calculated diffusion coefficients. This concrete life cycle assessment model was developed by a consortium including the American Concrete Institute (ACI) and was released in August 2001. For this analysis, the apparent diffusion coefficient for each constitutive material and the interface specimens was input, considering a 12 x 12 in. (305 x 305 mm) square column with a cross-sectional area of 144 $in.^2$ (92,903 mm^2) and a 2 in. (50 mm) clear concrete cover. The chloride exposure scenario was based on conditions of an urban highway bridge in Columbus, OH.

The model predicted that the concrete, with a relatively higher apparent diffusion coefficient, would have the shortest time required for corrosion initiation. It presented the lowest predicted time of 38 years. In contrast, the cementitious grout, reflecting a low apparent diffusion coefficient and a high resistance to chloride ingress, predicted 127 years required for corrosion initiation. The epoxy grout demonstrated significant chloride penetration resistance, with an estimated time to corrosion initiation of 156 years (Fig. 12)

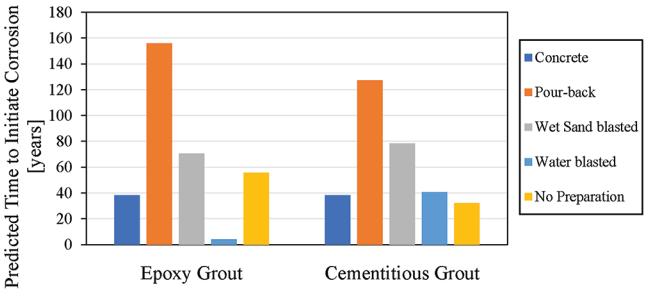

Fig. 12—Predicted time to initiate corrosion.

For the interface specimens, the epoxy grout sand-blasted interface specimen presented the most significant time to corrosion initiation at 70 years among the epoxy grout interface groups. The epoxy grout with no surface preparation was predicted to resist corrosion for 55 years, with the water-blasted surface preparation at 54 years (Fig. 12). Similarly, the cementitious grout sand-blasted interface specimen presented 78 years of prediction before corrosion initiation. The water-blasted interface predicted 41 years, and the no-surface preparation showed 32 years (Fig. 12)

Microstructural analysis

The microstructural analysis presented corresponds to the grout segment of the interface. The concrete-grout interface was analyzed on 6 in. (152.4 mm) diameter cylinder specimens. The cylinder specimens were chosen because they were moist-cured. The interface between the substrate and the grout is generally seen as a line bisecting these materials during imaging. Therefore, the interface region is evaluated in 10 um wide bands extending from the interface into the grout. The grout material was evaluated at a distance extending 100 µm from the interface, like what was reported by De La Varga et al. (2018). The SEM images of the cementitious grout interface specimens presented a dense microstructure of the grout particles at the interface, specifically for wet sand-blasted and water-blasted surface preparation techniques. This contributed to minimizing an interfacial zone in the vicinity of the exposed aggregate surface, generally known as the "wall effect" (Diamond and Huang 2001; Scrivener et al. 2004). The dense microstructure of the grout contributed to reduced porosity in the grout.

The total porosity distribution of the grout is measured as a function of the distance from the concrete surface. When quantifying the amount of porosity in the grout interfaces, it is observed that the type of surface preparation influences the total porosity. The results of the image analysis are presented in Fig. 13 and 14, where sudden increases in the porosity fraction were identified in the no-surface preparation technique for both grout materials.

In most cases, porosity at each strip linearly decreased with increasing distance from the material interface for the cementitious interface specimens. Several observations can be presented from these results. The cementitious grout specimen without surface preparation presented significant porosity values within the analyzed 100 µm wide band. The porosity fraction was 42% (0 to 10 µm) closer to the concrete surface. The porosity values gradually decreased,

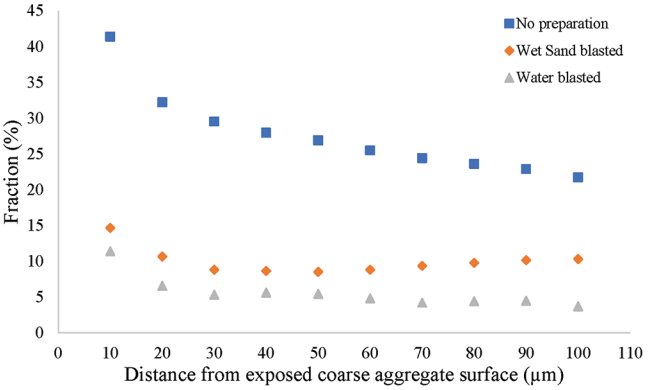

Fig. 13—Overall porosity distribution in cementitious grout.

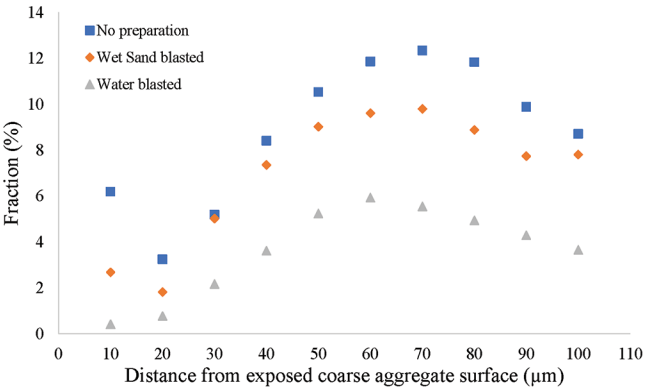

Fig. 14—Overall porosity distribution in epoxy grout.

moving away from the concrete interface to a value of 22% at 100 µm from the interface. Higher capillary pores likely cause the significant porosity measurements recorded in the cementitious no-surface preparation specimen. The cementitious water-blasted interface specimens presented porosity values ranging from approximately 4 to 12%, and the wet sand-blasted presented values ranging from approximately 9 to 15%. These results are mainly due to the improved interfaces between the concrete and the grout. According to previous studies (Branch et al. 2018; Elsharief et al. 2003; Wu et al. 2016; Xie et al. 2015), the porosities in the interfacial transition zone (ITZ) depend on the distance from the interface range from approximately 5 to 32%.

For epoxy grout interface specimens, it is acknowledged that it is challenging to differentiate the pores and the epoxy grout in the BSE images because their gray values are virtually the same (Liu et al. 2019). The results presented in Fig. 14 show that the epoxy grout can permeate into the substrate and fill the pores. Due to the filling effect, the porosity at the interfacial zone for the epoxy grout interface specimens could be reduced. When contrasting epoxy grout outcomes with cementitious grout, a notable decrease in porosity values was observed. Additionally, the method of surface preparation exerts an influence on the recorded porosity measurements. The porosity measurement at the region of 0 to 10 µm away from the interface into the grout of the epoxy grout was reduced to approximately 83% for the no-surface preparation. The wet sand-blasted presented a reduced porosity measurement of approximately 30%, and the water-blasted, approximately 60%. A possible

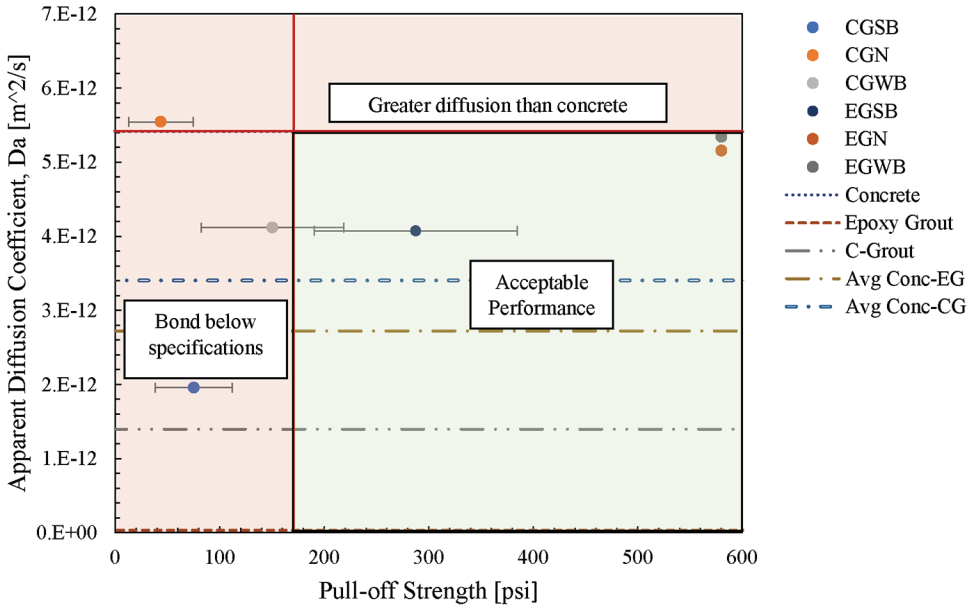

Fig. 15—Relation between apparent diffusion and pulloff strength.

explanation for the epoxy grout porosity measurement is the formation of polymer films that reduce porosity at the interface region, as confirmed by Anagnostopoulos et al. (2016).

After carefully examining the bond performance at the interface by direct tensile pulloff testing and chloride penetration by the diffusion method, there was sufficient data to evaluate the relationship between bond strength and chloride permeability. The surface preparation techniques likely substantially influence interfacial mechanical strength and chloride ion permeability. Results indicated that types of surface preparation presented significant differences in the bond strength and, to an extent, chloride ion permeability. Results were plotted in a graph with the x-axis as the bond strength and the y-axis as the apparent diffusion coefficient (Fig. 15). Generally, a well-performing interface should meet the minimum strength of 175 psi (1.2 MPa) (ODOT 2019) and have a lower apparent diffusion coefficient than concrete. Diffusion coefficients less than concrete indicate that the expected chloride ion intrusion along the interface would not exceed the concrete's and that the interface is not a fast-track for ion penetration.

Additionally, data from BSE and bond strength was used to evaluate the relationship between bond strength and average porosity (Fig. 16). The results present a correlation between the cementitious and epoxy grout interface specimens, emphasizing the influence of surface preparation techniques on porosity and bond strength. For cementitious grout, deficiencies in particle packing were observed in SEM images, potentially due to non-optimal sand and filler gradation. Surface preparation, particularly wet sand and water-blasted, improved porosity and bond strength. Water movement from the cementitious grout into concrete was identified as a potential cause for reduced grout hydration and mechanical weakness at the interface. In this case, the interface may develop a plane for mechanical weakness (Tatum and Brenkus 2021). In contrast, epoxy grout interfaces exhibited low porosity, with water-blasted surfaces having the least porosity. The epoxy grout's low viscosity

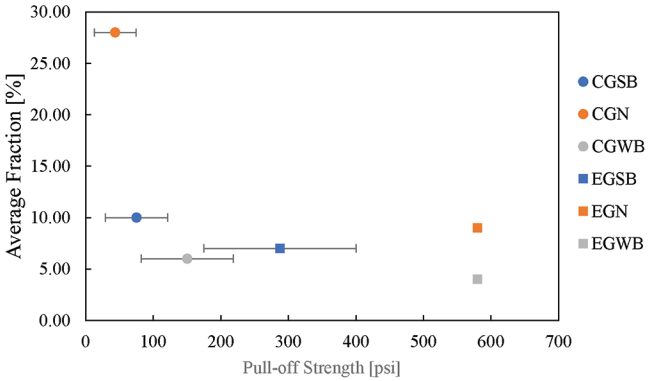

Fig. 16—Relation between porosity and pulloff strength.

allowed it to fill voids on the concrete surface. SEM images of epoxy grout interface specimens showed minimal defects and bond strength values exceeded specified minimums.

SUMMARY AND CONCLUSIONS

Based on the experimental results, the following conclusions are drawn:

- The interface zone between the concrete substrate and grout overlay is a region of weaker tensile strength.
- Surface preparation matters: water-blasted preparation of the concrete before grouting significantly improved the bond strength of cementitious grout but not epoxy grout.
- Reduced porosity at the interface is critical to the durability of the structure: water-blasted resulted in less porosity at the grout interface, contributing to a stronger bond for cementitious grout.
- Epoxy grout excels in reduced permeability: as a bulk material, epoxy grout showed greater resistance to chloride ion penetration compared to cementitious grout. However, the cementitious grout interface specimens demonstrated superior performance compared to the epoxy grout interface counterparts.

- Bond strength and permeability are linked: stronger bond strength in cementitious grout was associated with lower chloride ion permeability.

AUTHOR BIOS

ACI member **Anthony Addai Boateng** *is a PhD Student and a Research Assistant at the Department of Civil, Environmental, and Geodetic Engineering, The Ohio State University, Columbus, OH. He received his BS from Takoradi Technical University, Sekondi-Takoradi, Ghana, and his MS from Cleveland State University, Cleveland, OH, both in civil engineering. His research interests include the durability of post-tensioned concrete.*

ACI member **Garrett Tatum** *is an Assistant Professor at the Department of Civil and Architectural Engineering and Construction Management, University of Wyoming, Laramie, WY. He received his BS in civil engineering from the University of Arkansas, Fayetteville, AR, and his PhD from The Ohio State University. He is a member of ACI Committees 209, Creep and Shrinkage in Concrete; 239, Ultra-High-Performance Concrete; and S802, Teaching Methods and Educational Materials. His research interests include characterizing the durability of timber and concrete structural systems through both experimental and computational approaches.*

ACI member **Natassia Brenkus** *is an Assistant Professor at the Department of Civil, Environmental, and Geodetic Engineering, The Ohio State University. She received her BS, MS, and PhD from the University of Florida, Gainesville, FL. She is a member of ACI Committee 123, Research and Current Developments. Her research interests include the design and durability of reinforced and prestressed concrete structures, with particular interest in understanding how minor details change structural behavior.*

ACKNOWLEDGMENTS

The authors appreciate the financial support of The ACI Foundation, which provided the funding for this research. This article does not necessarily indicate the endorsement of the findings, opinions, and conclusions by the American Concrete Institute or the ACI Foundation, but instead reflects the authors' views. Acknowledgments are extended to CEMAS at The Ohio State University for helping perform the SEM imaging. The authors greatly appreciate the support of the project's advisory board, including T. Keller, L. Burris, J. Tatar, and D. Miller.

REFERENCES

ACI Committee 222, 2001, "Report on Corrosion of Prestressing Steels (ACI 222.2R-01) (Reapproved 2010)," American Concrete Institute, Farmington Hills, MI, 43 pp.

Anagnostopoulos, C. A.; Sapidis, G.; and Papastergiadis, E., 2016, "Fundamental Properties of Epoxy Resin-Modified Cement Grouts," *Construction and Building Materials*, V. 125, pp. 184-195. doi: 10.1016/j.conbuildmat.2016.08.050

ASTM C33/C33M-24, 2024, "Specification for Concrete Aggregates," ASTM International, West Conshohocken, PA. doi: 10.1520/C0033_C0033M-24

ASTM C579-23, 2023, "Standard Test Methods for Compressive Strength of Chemical-Resistant Mortars, Grouts, Monolithic Surfacings, and Polymer Concretes," ASTM International, West Conshohocken, PA. doi: 10.1520/C0579-23

ASTM C595/C595M-24, 2024, "Specification for Blended Hydraulic Cements," ASTM International, West Conshohocken, PA.

ASTM C989/C989M-24, 2024, "Specification for Slag Cement for Use in Concrete and Mortars," ASTM International, West Conshohocken, PA. doi: 10.1520/C0989_C0989M-24

ASTM C1152/C1152M-20, 2020, "Test Method for Acid-Soluble Chloride in Mortar and Concrete," ASTM International, West Conshohocken, PA. doi: 10.1520/C1152_C1152M-20

ASTM C1202-22e1, 2022, "Test Method for Electrical Indication of Concrete's Ability to Resist Chloride Ion Penetration," ASTM International, West Conshohocken, PA. doi: 10.1520/C1202-22E01

ASTM C1556-22, 2022, "Determining the Apparent Chloride Diffusion Coefficient of Cementitious Mixtures by Bulk Diffusion," ASTM International, West Conshohocken, PA. doi: 10.1520/C1556-22

ASTM C1583/C1583M-20, 2020b, "Test Method for Tensile Strength of Concrete Surfaces and the Bond Strength or Tensile Strength of Concrete Repair and Overlay Materials by Direct Tension (Pull-off Method)," ASTM International, West Conshohocken, PA. doi: 10.1520/C1583_C1583M-20

Babaei, K., and Hawkins, N. M., 1990, "Performance of Bridge Deck Concrete Overlays," *Extending the Life of Bridges*, ASTM International, West Conshohocken, PA, pp. 95-108. doi: 10.1520/STP14544S

Bentz, D. P.; De la Varga, I.; Muñoz, J. F.; Spragg, R. P.; Graybeal, B. A.; Hussey, D. S.; Jacobson, D. L.; Jones, S. Z.; and LaManna, J. M., 2018, "Influence of Substrate Moisture State and Roughness on Interface Microstructure and Bond Strength: Slant Shear vs. Pull-Off Testing," *Cement and Concrete Composites*, V. 87, pp. 63-72. doi: 10.1016/j.cemconcomp.2017.12.005

Beyene, M. A.; Munoz, J. F.; Meininger, R. C.; and Di Bella, C., 2017, "Effect of Internal Curing as Mitigation to Minimize Alkali-Silica Reaction Damage," *ACI Materials Journal*, V. 114, No. 3, May-June, pp. 417-428. doi: 10.14359/51689562

Bissonnette, B.; Vaysburd, A. M.; and von Fay, K. F., 2012, "Best Practices for Preparing Concrete Surfaces Prior to Repairs and Overlays," U.S. Department of the Interior Bureau of Reclamation Technical Service Center, Denver, CO, May, 92 pp.

Branch, J. L.; Epps, R.; and Kosson, D. S., 2018, "The Impact of Carbonation on Bulk and ITZ Porosity in Microconcrete Materials with Fly Ash Replacement," *Cement and Concrete Research*, V. 103, pp. 170-178. doi: 10.1016/j.cemconres.2017.10.012

Burris, L. E., and Riding, K. A., 2014, "Diffusivity of Binary and Ternary Concrete Mixture Blends," *ACI Materials Journal*, V. 111, No. 4, July-Aug., pp. 373-382. doi: 10.14359/51686826

Courard, L.; Lenaers, J.-F.; Michel, F.; and Garbacz, A., 2011, "Saturation Level of the Superficial Zone of Concrete and Adhesion of Repair Systems," *Construction and Building Materials*, V. 25, No. 5, pp. 2488-2494. doi: 10.1016/j.conbuildmat.2010.11.076

De la Varga, I., and Graybeal, B. A., 2015, "Dimensional Stability of Grout-Type Materials Used as Connections between Prefabricated Concrete Elements," *Journal of Materials in Civil Engineering*, ASCE, V. 27, No. 9, p. 04014246. doi: 10.1061/(ASCE)MT.1943-5533.0001212

De la Varga, I.; Muñoz, J.; Bentz, D.; and Graybeal, B., 2015, "Effect of Interface Moisture Content on the Bond Performance between a Concrete Substrate and a Non-Shrink Cement-Based Grout," *National Accelerated Bridge Construction Conference*, May 2016, pp. 371-375.

De la Varga, I.; Muñoz, J. F.; Bentz, D. P.; Spragg, R. P.; Stutzman, P. E.; and Graybeal, B. A., 2018, "Grout-Concrete Interface Bond Performance: Effect of Interface Moisture on the Tensile Bond Strength and Grout Microstructure," *Construction and Building Materials*, V. 170, pp. 747-756. doi: 10.1016/j.conbuildmat.2018.03.076

De La Varga, I.; Muñoz, J. F.; Bentz, D. P.; Stutzman, P. E.; and Graybeal, B. A., 2017, "Grout-Concrete Interface Bond Performance: Effect of Interface Moisture on the Tensile Bond Strength and Grout Microstructure," *Cement and Concrete Composites*, V. 170, pp. 747-756.

Diamond, S., and Huang, J., 2001, "The ITZ in Concrete – A Different View Based on Image Analysis and SEM Observations," *Cement and Concrete Composites*, V. 23, No. 2-3, pp. 179-188. doi: 10.1016/S0958-9465(00)00065-2

Elsharief, A.; Cohen, M. D.; and Olek, J., 2003, "Influence of Aggregate Size, Water Cement Ratio and Age on the Microstructure of the Interfacial Transition Zone," *Cement and Concrete Research*, V. 33, No. 11, pp. 1837-1849. doi: 10.1016/S0008-8846(03)00205-9

Espeche, A. D., and León, J., 2011, "Estimation of Bond Strength Envelopes for Old-to-New Concrete Interfaces Based on a Cylinder Splitting Test," *Construction and Building Materials*, V. 25, No. 3, pp. 1222-1235. doi: 10.1016/j.conbuildmat.2010.09.032

FDOT, 2019, *Standard Specifications for Road and Bridge Construction—July 2019*, Florida Department of Transportation, Tallahassee, FL, 1230 pp.

Hartt, W. H., 2018, "Effect of Modeling Variables upon Projection of Corrosion-Induced Bridge Post-Tension Tendon Failures," *Corrosion*, V. 74, No. 7, pp. 768-775. doi: 10.5006/2710

ICRI 310.2R-13, 2013, "Selecting and Specifying Concrete Surface Preparation for Sealers, Coatings, Polymer Overlays, and Concrete Repair," International Concrete Repair Institute, Minneapolis, MN, 54 pp.

Igarashi, S.; Watanabe, A.; and Kawamura, M., 2005, "Evaluation of Capillary Pore Size Characteristics in High-Strength Concrete at Early Ages," *Cement and Concrete Research*, V. 35, No. 3, pp. 513-519. doi: 10.1016/j.cemconres.2004.06.036

Júlio, E. N. B. S.; Branco, F. A. B.; and Silva, V. D., 2004, "Concrete-to-Concrete Bond Strength. Influence of the Roughness of the Substrate Surface," *Construction and Building Materials*, V. 18, No. 9, pp. 675-681. doi: 10.1016/j.conbuildmat.2004.04.023

Kay, S., and Beushausen, H., 2018, "The Influence of Concrete Substrate Moisture Condition on the Tensile Pull-Off Strength of Protective Coatings," *MATEC Web of Conferences*, V. 199, p. 07016. doi: 10.1051/matecconf/201819907016

Kjellsen, K. O.; Monsøy, A.; Isachsen, K.; and Detwiler, R. J., 2003, "Preparation of Flat-Polished Specimens for SEM-Backscattered Electron Imaging and X-Ray Microanalysis—Importance of Epoxy Impregnation,"

Cement and Concrete Research, V. 33, No. 4, pp. 611-616. doi: 10.1016/S0008-8846(02)01029-3

Lange, D. A.; Jennings, H. M.; and Shah, S. P., 1994, "Image Analysis Techniques for Characterization of Pore Structure of Cement-Based Materials," *Cement and Concrete Research*, V. 24, No. 5, pp. 841-853. doi: 10.1016/0008-8846(94)90004-3

Liam, K. C.; Roy, S. K.; and Northwood, D. O., 1992, "Chloride Ingress Measurements and Corrosion Potential Mapping Study of a 24-Year-Old Reinforced Concrete Jetty Structure in a Tropical Marine Environment," *Magazine of Concrete Research*, V. 44, No. 160, pp. 205-215. doi: 10.1680/macr.1992.44.160.205

Liao, H., 2017, "Grouted Post-Tensioning Tendon Evaluation," *PTI Journal*, V. 13, No. 2, pp. 23-27.

Liu, H.; Huang, H.; Wu, X.; Peng, H.; Li, Z.; Hu, J.; and Yu, Q., 2019, "Effects of External Multi-Ions and Wet-Dry Cycles in a Marine Environment on Autogenous Self-Healing of Cracks in Cement Paste," *Cement and Concrete Research*, V. 120, pp. 198-206. doi: 10.1016/j.cemconres.2019.03.014

Miller, E.; White, B.; Haskins, R.; Ebeling, R.; and Evans, J., 2017, *An Investigation of Corrosion Mitigation Strategies for Aging Post-Tensioned Cables*. U.S. Army Engineer Research and Development Center, Vicksburg, MS, 66 pp. doi: 10.21079/11681/21478

Momayez, A.; Ehsani, M. R.; Ramezanianpour, A. A.; and Rajaie, H., 2005, "Comparison of Methods for Evaluating Bond Strength between Concrete Substrate and Repair Materials," *Cement and Concrete Research*, V. 35, No. 4, pp. 748-757. doi: 10.1016/j.cemconres.2004.05.027

Mutitu, D. K. K. J. K., and Wachira, J. M., 2014, "Diffusivity of Chloride Ion in Mortar Cubes Made Using Ordinary Portland and Portland Pozzolana Cements," *IOSR Journal of Applied Chemistry*, V. 7, No. 2, pp. 67-73. doi: 10.9790/5736-07216773

ODOT, 2019, *Construction & Material Specifications*, Ohio Department of Transportation, Columbus, OH, 928 pp.

Santos, D. S.; Santos, P. M. D.; and Dias-Da-Costa, D., 2012, "Effect of Surface Preparation and Bonding Agent on the Concrete-to-Concrete Interface Strength," *Construction and Building Materials*, V. 37, pp. 102-110. doi: 10.1016/j.conbuildmat.2012.07.028

Scrivener, K. L.; Crumbie, A. K.; and Laugesen, P., 2004, "The Interfacial Transition Zone (ITZ) Between Cement Paste and Aggregate in Concrete," *Interface Science*, V. 12, No. 4, pp. 411-421. doi: 10.1023/B:INTS.0000042339.92990.4c

Silfwerbrand, J., 2003, "Shear Bond Strength in Repaired Concrete Structures," *Materials and Structures*, V. 36, No. 6, pp. 419-424. doi: 10.1007/BF02481068

Silfwerbrand, J. L., 2009, "Bonded Concrete Overlays for Repairing Concrete Structures," *Failure, Distress and Repair of Concrete Structures*, Elsevier, pp. 208-243. doi: 10.1533/9781845697037.2.208

Song, H.-W.; Lee, C.-H.; and Ann, K. Y., 2008, "Factors Influencing Chloride Transport in Concrete Structures Exposed to Marine Environments," *Cement and Concrete Composites*, V. 30, No. 2, pp. 113-121. doi: 10.1016/j.cemconcomp.2007.09.005

Struble, L., and Stutzman, P., 1989, "Epoxy Impregnation of Hardened Cement for Microstructural Characterization," *Journal of Materials Science Letters*, V. 8, No. 6, pp. 632-634. doi: 10.1007/BF01730426

Stutzman, P. E., and Clifton, J. R., 1999, "Specimen Preparation for Scanning Electron Microscopy," *Proceedings of the Twenty-First International Conference on Cement Microscopy*, L. Jany and A. Nisperos, eds., Las Vegas, NV, pp. 10-22.

Tatum, G., and Brenkus, N., 2021, "Division of Engineering Research On-Call Services Task 7: Durability of Anchorage Pour-Backs and Improvements," FHWA/OH-2021-02, Ohio State University Department of Civil and Environmental Engineering and Geodetic Science, Columbus, OH, https://rosap.ntl.bts.gov/view/dot/59032. (last accessed Jan. 9, 2025)

Whitmore, D.; Fallis, G.; Liao, H.; Strombeck, S.; and Lasa, I., 2014, "Tendon Impregnation Technology Mitigates Corrosion and Protects Post-Tensioned Tendons," *PTI Journal*, V. 10, No. 1, pp. 17-21.

Wu, K.; Shi, H.; Xu, L.; Ye, G.; and De Schutter, G., 2016, "Microstructural Characterization of ITZ in Blended Cement Concretes and its Relation to Transport Properties," *Cement and Concrete Research*, V. 79, pp. 243-256. doi: 10.1016/j.cemconres.2015.09.018

Xie, Y.; Corr, D. J.; Jin, F.; Zhou, H.; and Shah, S. P., 2015, "Experimental Study of the Interfacial Transition Zone (ITZ) of Model Rock-Filled Concrete (RFC)," *Cement and Concrete Composites*, V. 55, pp. 223-231. doi: 10.1016/j.cemconcomp.2014.09.002

Zhao, H., and Darwin, D., 1992, "Quantitative Backscattered Electron Analysis of Cement Paste," *Cement and Concrete Research*, V. 22, No. 4, pp. 695-706. doi: 10.1016/0008-8846(92)90022-N

CALL FOR ACTION

ACI Invites You To...

Share your expertise

Do you have EXPERTISE in any of these areas?

- BIM
- Chimneys
- Circular Concrete Structures Prestressed by Wrapping with Wire and Strand
- Circular Concrete Structures Prestressed with Circumferential Tendons
- Concrete Properties
- Demolition
- Deterioration of Concrete in Hydraulic Structures
- Electronic Data Exchange
- Insulating Concrete Forms, Design, and Construction
- Nuclear Reactors, Concrete Components
- Pedestal Water Towers
- Pipe, Cast-in-Place
- Strengthening of Concrete Members
- Sustainability

Then become a REVIEWER for the *ACI Structural Journal* or the *ACI Materials Journal*.

Become a Reviewer for the ACI Journals

How to become a Reviewer:

1. Go to: **http://mc.manuscriptcentral.com/aci**;
2. Click on "Create Account" in the upper right-hand corner; and
3. Enter your E-mail/Name, Address, User ID and Password, and Area(s) of Expertise.

Update your Manuscript Central user account information

Did you know that the database for MANUSCRIPT CENTRAL, our manuscript submission program, is separate from the ACI membership database?

How to update your user account:

1. Go to **http://mc.manuscriptcentral.com/aci**;
2. Log in with your current User ID & Password; and
3. Update your E-mail/Name, Address, User ID and Password, and Area(s) of Expertise.

QUESTIONS?

E-mail any questions to Journals.Manuscripts@concrete.org.

American Concrete Institute

Always advancing

ACI MATERIALS JOURNAL TECHNICAL PAPER

Title No. 122-M06

Assessment of Threshold Chloride of Reinforced Concrete Structures in Hot Tropical Climate

by Mshtaq Ahmed, Abdulrahman Alhozaimy, Abdulaziz Al-Negheimish, and Raja Rizwan Hussain

Chloride threshold values for steel reinforcing bars in reinforced concrete under the effect of varying temperatures and extended long-term conditions in hot climate are investigated. This investigation covers a gap in the current codes, including ACI 318, where the effect of temperature on the chloride threshold is not addressed. A total of 96 concrete specimens reinforced with carbon steel reinforcing bars sourced from two manufacturers were cast with different chloride contents and exposed to four temperatures of 20, 35, 50, and 65°C (68, 95, 122, and 149°F) for a period of more than 2 years. The chloride threshold values were determined based on corrosion potential, corrosion rate, and mass loss at the end of the exposure period. The results of the three techniques showed a consistent trend of significant dependency of the chloride threshold value on temperature. The average water-soluble chloride threshold values based on mass loss were found to be 0.77%, 0.72%, 0.47%, and 0.12% by weight of cement for temperatures of 20, 35, 50, and 65°C (68, 95, 122, and 149°F), respectively. These findings are significant as they showed a dramatic drop in the chloride threshold values at high temperature. This research highlights the need for reassessment of ACI Code limits considering hot climate.

Keywords: chloride threshold (CT) value; corrosion potential; corrosion rate; mass loss; microstructure; steel reinforcing bars, sustainability; temperature.

INTRODUCTION

The detrimental effect of chloride-induced corrosion on the durability of reinforced concrete (RC) structures is one of the major sustainability issues worldwide. Several governments around the world spend huge funds on maintaining infrastructure that has deteriorated due to reinforcing bar corrosion. In the Arabian Gulf region, the rate of concrete deterioration is as much as five times that in Europe.[1] The main cause of concrete deterioration in the Arabian Gulf region is chloride-induced reinforcement corrosion, as indicated by many researchers.[1-5] This deterioration is associated with the presence of chloride in quantities large enough to initiate and propagate corrosion under the harsh climatic conditions of high ambient temperature and high seasonal humidity.

Standards prescribe strict limits on the allowed chloride content in concrete from ingredients. For example, the European Standard EN 206[6] limits the total allowed chloride in RC to 0.4% by weight of cement. The ACI 318 Code[7] limits the maximum allowed water-soluble chloride ions in RC members to 0.15% by weight of cement if the member is exposed to an external source of chlorides, or to 0.3% if the member is not exposed to external chlorides. The chloride ions attack the protective oxide film that forms on the steel reinforcing bars due to the highly alkaline environment of pore solution in concrete. If oxygen and moisture are also available, the corrosion process will progress. The risk of corrosion increases as the chloride content in concrete increases. Reinforcement corrosion can only start once the chloride content at the steel surface has reached a certain threshold value.[8] In the literature, the amount of chloride needed to initiate steel corrosion is often referred to as critical chloride content or chloride threshold value. In this paper, the term "chloride threshold (CT) value" will be used. Schiessl and Raupach[9] defined CT value as the content of chloride at the steel depth that is necessary to sustain local passive film breakdown, and hence initiate the corrosion process.

Many factors affect the corrosion initiation and the rate of corrosion after the corrosion starts in RC structures. In tropical-climate regions, RC structures are more prone to corrosion due to the combined effect of high temperature and seasonal humidity. In hot climates, the ambient temperature in the shade often exceeds 40°C (104°F), and the temperature of concrete may increase by more than 20°C (68°F) under direct sun.[10,11] The effect of temperature on the corrosion rate of reinforcing bars embedded in concrete, mortar, or pore solution is extensively investigated in the literature.[12-21] Different studies showed different results on the effect of temperature due to the complexity of the corrosion process. Some studies found that the increase in temperature results in a continuous increase in the corrosion rate of actively corroded reinforcing bars.[14-18] Other studies reported that the increase in temperature to a specific value in the range of 40 to 45°C (104 to 113°F) increases the corrosion rate, and the trend is reversed.[19-21] The decrease in corrosion rate with the increase in temperature after a certain temperature, as reported by the last three studies, may be attributed to the reduction in internal humidity that accompanies higher temperatures.[19-21] López et al.[12] found that the increase in temperature increases the corrosion rate with the availability of moisture and decreases the corrosion rate in dry concrete.

In-depth studies on the effect of temperature on the CT value are very limited and contradictory. Hussain et al.[22] studied the effect of two temperatures using only one technique for determining the CT values. They found that an increase in temperature from 20 to 70°C (68 to 158°F) caused a dramatic reduction in CT values. Matsumura et al.[23] studied the effect of temperature on corrosion in RC specimens under

ACI Materials Journal, V. 122, No. 1, January 2025.
MS No. M-2024-095.R2, doi: 10.14359/51744379, received October 6, 2024, and reviewed under Institute publication policies.

high temperature of 65 and 90°C (149 and 194°F) to simulate nuclear RC structures exposed to elevated temperature. They found that an increase in temperature from 65 to 90°C (149 and 194°F) caused an increase in the CT value, which is inconsistent with that reported by Hussain et al.[22] Another study using stainless steel reinforcing bars rather than carbon steel found a significant reduction in the CT when the temperature increased from 20 to 60°C (68 to 140°F).[24]

The effect of a tropical climate with high temperature and humidity on the CT value of carbon steel reinforcing bars in concrete is the focus of a comprehensive multi-phase investigations by the authors. The current phase covered the influence of temperature on CT values due to chlorides from concrete ingredients. Two types of carbon steel reinforcing bars were cast in concrete with varying amounts of admixed chloride and later subjected to four levels of temperature for a period of more than 2 years. Short-term results of this investigation were reported by the authors in a previous publication.[25] The current paper presents long-term results and discussion of the effect of temperature on CT values. The corrosion potential and corrosion rate for the specimens were measured regularly during the extended long-term exposure period. The specimens were broken at the end of the exposure period to visually observe the condition of the reinforcing bars and the extent of corrosion and calculate their mass loss. The effects of temperature with respect to microstructure, elemental composition, mass loss, and nanotechnology under extended long-term conditions are also reported in this paper.

RESEARCH SIGNIFICANCE

Deterioration of RC structures in the Arabian Gulf region due to corrosion is an alarming issue. The ACI 318 Code, which is the basis of several local building codes in the region, provides limits to the water-soluble chlorides in concrete coming from the ingredients. The Code does not specifically address the coupled effect of high temperature and humidity prevalent in tropical-climate regions where the temperature of RC members exposed directly to the sun may exceed 60°C (140°F). This investigation showed the significant effect of high temperature on the CT value of steel reinforcing bars embedded in concrete. The maximum allowable limits of chlorides in concrete from ingredients in current building codes are shown to underestimate the risk of corrosion under such temperatures. This research highlights the need for reassessment of code limits considering hot climates.

Fig. 1—Carbon steel reinforcing bars glued to copper wires for electrical connection.

EXPERIMENTAL PROGRAM

Materials, casting, curing, and temperature treatment

Carbon steel reinforcing bars collected from two different manufacturers were used, designated as Source A and Source B. The microstructure of steel reinforcing bars from Source A consisted of pearlite-ferrite at the core and tempered martensite at the rim. The reinforcing bars from Source B were alloy steel produced by the normal heating of rolls without quenching and tempering treatment. Copper wires were wound around grooves made at the ends of the steel reinforcing bars and were coated with epoxy resin for proper electrical connection, as shown in Fig. 1. Ordinary portland cement was used to cast concrete specimens of 200 x 200 x 55 mm (8.0 x 8.0 x 2.2 in.) dimensions as per the mixture proportions given in Table 1. Chloride ions were introduced to the concrete by solving pre-calculated amounts of pure NaCl in the mixing water, emulating the chloride ions that exist in concrete ingredients. Plain concrete specimens were cast from the same concrete mixtures used to cast the RC specimens to measure the actual chloride ions in the hardened concrete specimens. Two types of chloride were analyzed: water-soluble and acid-soluble chlorides. Samples were prepared for both types of chloride as per ASTM C1218/C1218M[26] for water-soluble chloride and ASTM C1152/C1152M[27] for acid-soluble chloride.

After demolding, the specimens were moist-cured for 28 days and then exposed to four different temperatures (20, 35, 50, and 65°C [68, 95, 122, and 149°F]) in environmental chambers for approximately 2 years. These temperatures were chosen considering the typical temperature range in tropical climates. In the first 6 months of the exposure period, relative humidity (RH) was kept constant at 80%, which is in the range of optimum RH for corrosion.[28] After that, the specimens were subjected to wetting-and-drying cycles for the remaining exposure period to simulate the fluctuation of humidity in hot weather regions. Each wetting-and-drying cycle was 2 weeks dry and 2 weeks wet. The RH in the chambers was maintained below 30% for the dry-half cycle and approximately 80% for the wet-half cycle. The measurements of corrosion potential and corrosion rate were taken periodically every week in the first 3 months and every 2 weeks in the next 3 months using a corrosion meter device. Then, during the period of wetting-and-drying cycles,

Table 1—Mixture proportions for material used in casting concrete specimens

Materials	Cement	Aggregate	Crushed sand	White sand	Water	NaCl
Proportions, kg/m^3	350	1040	210	490	175	Variable

Table 2—Parameters investigated in this study

Parameter	Temperature, °C (°F)	Added chlorides, % cement weight	Reinforcing bar sources
Variables	20, 35, 50, 65 (68, 95, 122, 149)	0, 0.15, 0.3, 0.6, 0.9, 1.2	Source A, Source B

measurements of corrosion potential and corrosion rate were taken at the end of the wet-half cycles. Table 2 summarizes the test parameters investigated, where two duplicate RC specimens were used in this study for each parameter, giving a total of 96 specimens. The corrosion potential and corrosion rate measurements for any duplicate specimens were mostly close to each other. The measurement was repeated if one reading was far from the other for accuracy and reproducibility. Details of the experimental procedure and techniques used are given in Alhozaimy et al.[25]

Specimen break-up and characterization of corrosion products

At the end of the exposure period, specimens were split to inspect the condition of the reinforcing bars and check the extent of corrosion. Samples of some reinforcing bars and corrosion products were collected for microstructural analysis. The steel reinforcing bars were then subjected to a cleaning procedure according to ASTM G1[29] to calculate their gravimetric mass loss according to Eq. (1)

$$\text{Mass loss (\%)} = \frac{W_1 - W_2}{W_1} \times 100 \quad (1)$$

where W_1 is the original weight of the steel reinforcing bar before casting; and W_2 is the weight of the reinforcing bar after removing the corrosion products.

A scanning electron microscope (SEM) was used to study the morphology of corrosion products. In addition to morphological analysis, energy-dispersive X-ray spectroscopy (EDX) was used in conjunction with the SEM to conduct a compositional analysis of the corrosion products. For phase analysis, a dispersive micro-Raman spectroscope was employed. To excite the samples, a diode green laser with a 532 nm wavelength was used. The laser power of 0.15 mW was employed to illuminate the surface to prevent the oxide phases from transforming into other phases by localized heating. The areas of interest of the specimens were observed using an optical microscope at 50× magnification.

RESULTS AND DISCUSSION

Chloride content

The average results of acid-soluble and water-soluble chlorides for the hardened concrete specimens with varying chloride contents are given in Table 3. Every measurement in this table is an average of four chloride measurements of four powder samples taken separately from plain concrete specimens. The standard deviation for all added-chloride contents is included in Table 3. The source of chlorides in the zero-added-chloride specimens was the chloride ions existing in the concrete ingredients. This was confirmed by measuring the chlorides in each ingredient separately and summing the total amount of chlorides. The total chlorides

Table 3—Water-soluble and acid-soluble chlorides for hardened concrete samples

Added Cl, % weight of cement	Water-soluble Cl, % weight of cement		Acid-soluble Cl, % weight of cement	
	Average value	Std Dev.	Average value	Std Dev.
0.00	0.07	0.017	0.10	0.008
0.15	0.20	0.013	0.25	0.030
0.30	0.33	0.021	0.40	0.015
0.60	0.58	0.024	0.69	0.010
0.90	0.83	0.010	0.97	0.010
1.20	1.12	0.048	1.28	0.022

Note: Std Dev. is standard deviation.

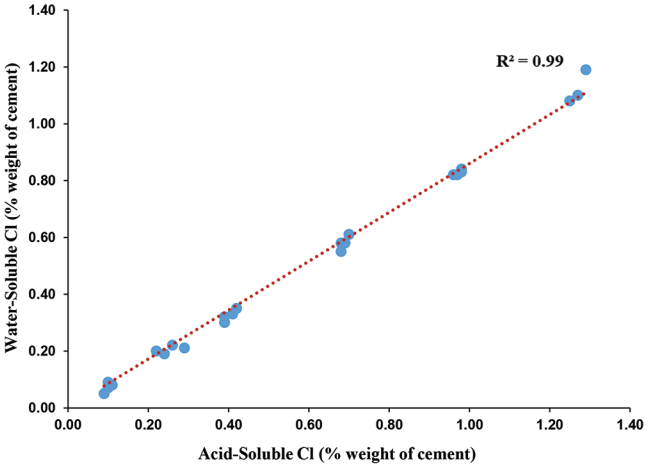

Fig. 2—Water-soluble (free) chloride versus acid-soluble (total) chloride.

when converted to a percentage value by the weight of cement was approximately 0.1%. This is the same value obtained from measuring the acid-soluble chloride of hardened concrete for zero-added-chloride specimens as reported in Table 3. The correlation between the water-soluble and acid-soluble chlorides is shown in Fig. 2. It is clear from Fig. 2 that there is a strong linear relationship between the water-soluble (free) chloride and the acid-soluble (total) chloride in the form of Eq. (2)

$$y = ax \quad (2)$$

where y is the water-soluble chloride as percent by weight of cement; x is the acid-soluble chloride as percent by weight of cement; and $a = 0.85$; $R^2 = 0.99$ from regression analysis. This ratio of water-soluble chloride to acid-soluble chloride is almost identical to the a-value of 0.86 reported by Mohammed and Hamada[30] for concrete specimens with ordinary portland cement after long exposure to seawater.

Corrosion potential

Measurements of corrosion potential during the whole period of exposure showed that corrosion potential had high variations with time at the early age of specimens. These variations diminished with time, and corrosion potential finally stabilized after a few months. Figure 3 shows the

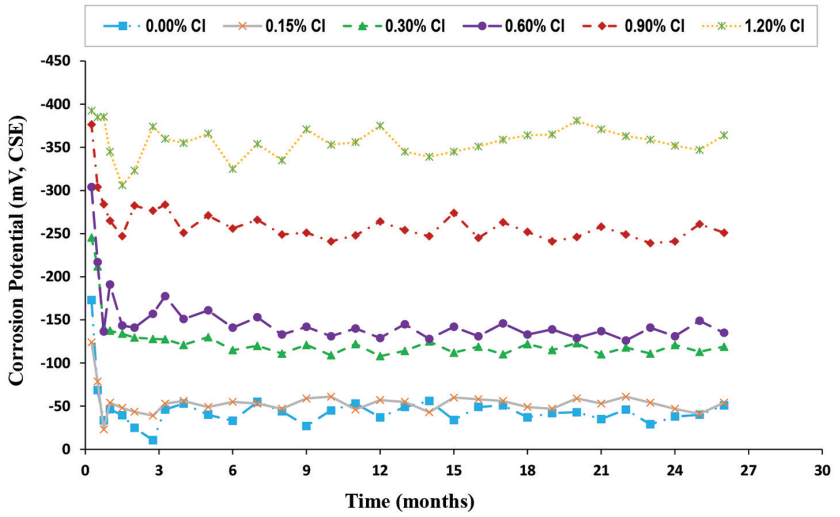

Fig. 3—Variations of corrosion potential with time for specimens exposed to temperature of 20°C (68°F) (Source A).

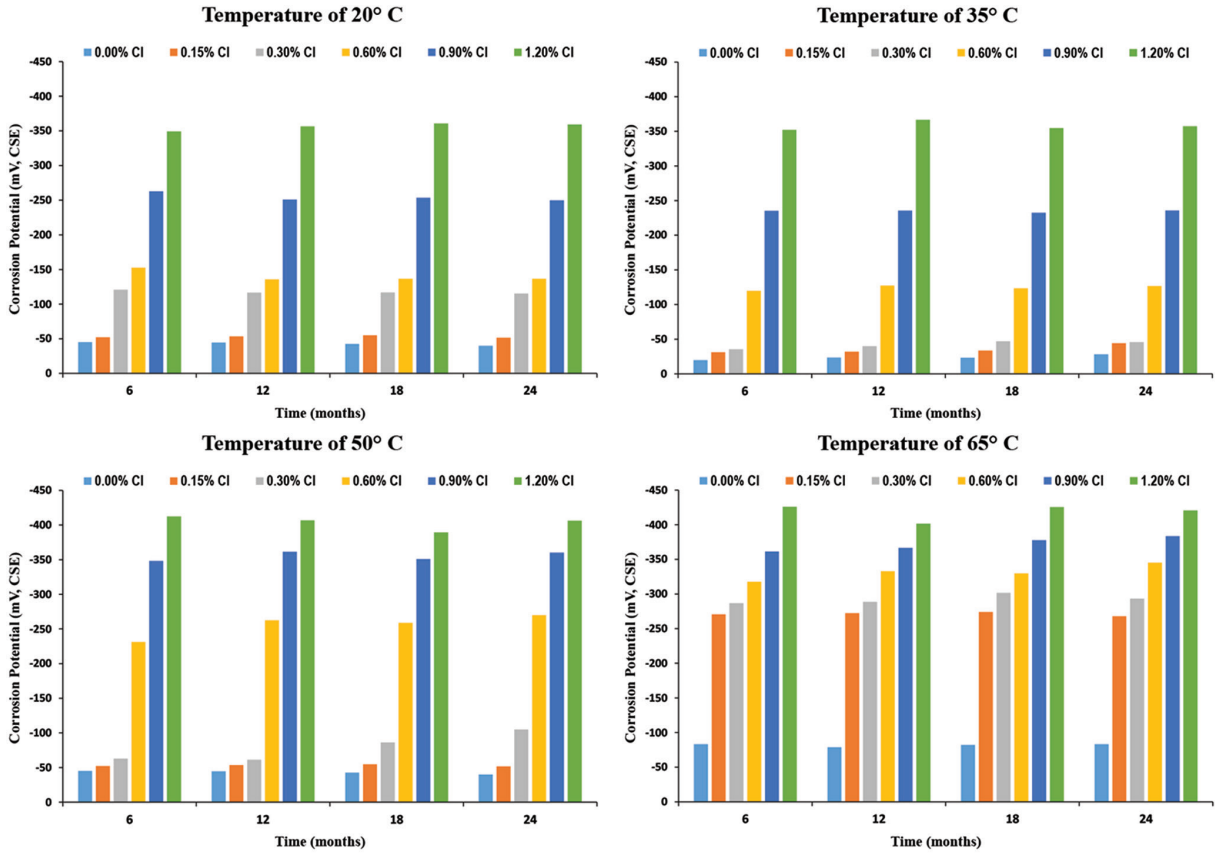

Fig. 4—Corrosion potential versus time at different temperatures and chloride contents (Source A).

variation of corrosion potential with time for specimens of Source A exposed to the temperature of 20°C (68°F), which can be considered as a typical behavior for all investigated specimens. In Fig. 3, every point is an average of corrosion potential measurements taken for two duplicate specimens. The measurements of corrosion potential with time for all chloride contents and temperatures are presented as bar charts in Fig. 4 for reinforcing bars of Source A, which presents a summary of the results at a glance. Similar results were also recorded for reinforcing bars of Source B but not included in the paper due to length limitation. In Fig. 4, the readings of corrosion potential were averaged at periods of 6 months to show the stabilization of corrosion potential with time. Every column in this figure represents the average of corrosion potential measurements taken within periods of 6 months. In the first 6-month period, the first 3 months were excluded due to the high variation of corrosion potential at the early age of specimens. During the initial exposure, the passive layer, which is essential for protecting the steel from corrosion, had not yet fully developed or stabilized. This, in addition to evolving concrete microstructure, led to fluctuations in the corrosion potential at early age as the layer undergoes changes in thickness, composition, and effectiveness. Similar behavior was also observed in previous

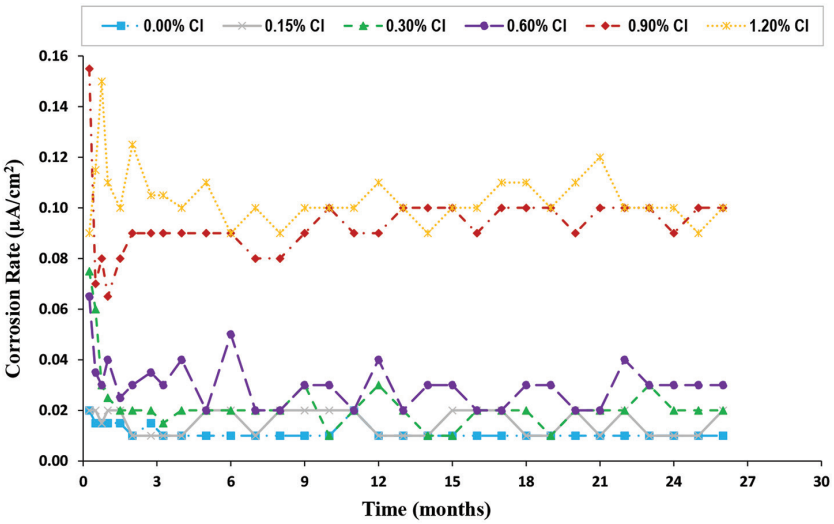

Fig. 5—Variations of corrosion rate with time for specimens exposed to temperature of 20°C (68°F) (Source A).

studies.[20,31,32] As shown in Fig. 4, the corrosion potential at the same chloride content and temperature stabilized over the long term, with the average values of corrosion potential after 2 years being largely unchanged from those after 6 months. It can also be seen from Fig. 4 that corrosion potential increases negatively with the increase in chloride content and temperature. Specimens exposed to higher temperatures always had higher corrosion potential than those with lower temperatures at the same level of chloride content. It is worth mentioning that an increase in temperature makes the potential to shift more negative, even at 0% Cl, as per the Nernst equation (Eq. (3))

$$E = E^0 - \frac{RT}{nF}\ln Q \tag{3}$$

where E^0 is standard redox potential; T is the temperature in kelvin; R is the universal gas constant; and F is Faraday's constant. Thus, an increase in temperature will decrease cell potential. Similar results for the negative increase in potential with the increase in temperature were reported in recent studies.[18,33] The results also clearly show no adverse effect due to the change in the environment from constant RH of 80% to the more aggressive wetting-and-drying condition in this case. It should be mentioned here that the limited effect of cyclic wetting-and-drying treatment can be related to the fact that specimens were not exposed to an external source of chloride and to the availability of sufficient moisture and oxygen under the constant RH of 80%.

Corrosion rate

The behavior of corrosion rate with time was similar to that of corrosion potential. At the early age of specimens, the corrosion rate had high variations, then stabilized after a few months. Figure 5 shows this behavior for specimens exposed to the temperature of 20°C (68°F) of Source A. In Fig. 5, every point is an average of corrosion rate measurements taken for two duplicate specimens. To show the stabilization of the corrosion rate over the long-term period, its variations with time for the coupled effect of all chloride contents and all four temperature conditions are presented as column charts in Fig. 6. Both reinforcing bar sources exhibited a similar trend, so the corrosion rate measurements for only reinforcing bars of Source A are presented in Fig. 6. As shown in Fig. 6, corrosion rates increase with the increase in chloride content and temperature. At chloride contents less than 0.90% and low temperatures of 20 and 35°C (68 and 95°F), the corrosion rate is negligible, which confirms that the pre-existing small amount of chlorides in fresh concrete did not affect the formation of the passive layer, as will be discussed in the "Microstructural analysis" section. The increase in corrosion rate is significant at temperatures of 50°C (122°F) for high chloride contents compared to temperatures of 20 and 35°C (68 and 95°F). This increase in corrosion rate becomes very noticeable for specimens exposed to a temperature of 65°C (149°F) at all added chloride contents. The significant increase in corrosion rate with the increase in temperature, especially at 65°C (149°F), can be attributed to the increase in free chloride contents in pore water and the increase in the mobility of chloride ions at high temperature. It is theoretically known that the increase in temperature can activate a chemical reaction according to the Arrhenius law, shown in Eq. (4)

$$k = A \cdot \exp\left(-\frac{\Delta E}{RT}\right) \tag{4}$$

where k is the rate constant; T is the temperature; ΔE is the activation energy; R is the gas constant; and A is the frequency factor (constant). The corrosion process is an electrochemical reaction, so the increase in temperature can accelerate the transfer rate of ions between the cathode and anode, thus increasing the corrosion rate. The chloride concentration at which there is a clear jump in corrosion rate is temperature-dependent, indicating the increased Arrhenius law activation energy of corrosion reaction at the points 0.9% for temperatures of 20 and 35°C (68 and 95°F), 0.6% for 50°C (122°F), and 0.15% for 65°C (149°F).

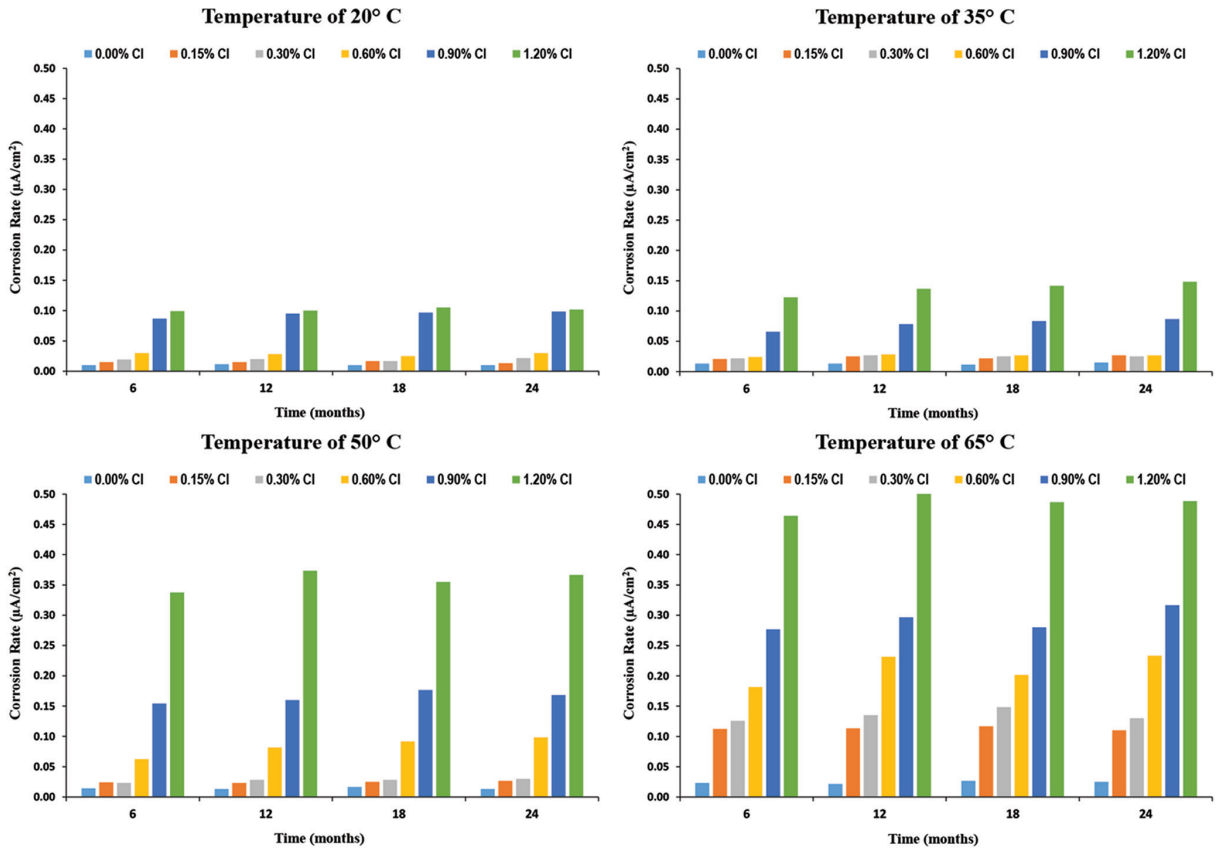

Fig. 6—Corrosion rate versus time at different temperatures and chloride contents (Source A).

Visual inspection and mass loss measurements

During the exposure period, the specimens were monitored periodically and visually inspected for any cracks on the concrete surface. Corrosion cracks along the reinforcing bars were observed on the surface of specimens with high chloride contents (0.6, 0.9, and 1.2% Cl) exposed to the temperature of 65°C (149°F) for both sources of reinforcing bars. First-appeared cracks were observed on specimens with 1.2% Cl after 6 months of exposure. Cracks on specimens with 0.9% and 0.6% Cl were first observed after 12 months and 18 months, respectively. At the end of the exposure period, specimens with chloride contents of 0.9 and 1.2% Cl exposed to the temperature of 65°C (149°F) were already split under the expansive pressure of the corrosion products. Figure 7 shows pictures of some cracked specimens at the end of the exposure period. No cracks were observed for all other specimens exposed to temperatures lower than 65°C (149°F) regardless of the chloride content.

At the end of the exposure period, all specimens were broken to extract and inspect the steel reinforcing bars. All reinforcing bars exposed to the temperature of 65°C (149°F) were corroded except those with zero-added chloride. Reinforcing bars with high chloride contents in this category were severely corroded. Signs of corrosion also appeared on reinforcing bars with high chloride contents exposed to the lower temperatures. Figures 8 and 9 present photos of the extracted reinforcing bars exposed to the different levels of chlorides and various temperatures for Sources A and B, respectively. It can be seen from the figures that the rusting of reinforcing bars increases with the increase in chloride content and temperature. The mass losses for these reinforcing bars were calculated after cleaning according to ASTM G1.[29] The values of mass loss for both reinforcing bar sources at the four investigated temperatures (20, 35, 50, and 65°C [68, 95, 122, and 149°F]) are presented as a column chart in Fig. 10. Every column in this chart is an average of two values for two reinforcing bars extracted from two duplicate concrete specimens. The two values are generally very close to each other, as shown by the error bars representing the range. The results of mass loss for the two reinforcing bar sources show a similar trend, as can be observed from Fig. 10 and agree with the visual observations in Fig. 8 and 9. These mass loss measurements carried out at the end of the experimentation strongly substantiate the results of half-cell potential and corrosion rate measurements.

Microstructural analysis

Morphologies and EDX analysis of corrosion products—The morphologies of corrosion products deposited on the surface of reinforcing bars were examined using SEM at different chloride concentrations and temperature conditions. The results showed that the morphologies of the film formed on the steel surface are similar at 20 and 35°C (68 and 95°F) exposure in concrete with chloride concentrations ranging from 0.15 to 0.6%. No trace of rust was observed on the surfaces of the reinforcing bars exposed to these temperatures at this range of chloride concentrations (0.15 to 0.6%). Due to space limitation, only the results of Source A are incorporated and discussed. The morphologies of the passive film on exposed steel reinforcing bars at a chloride

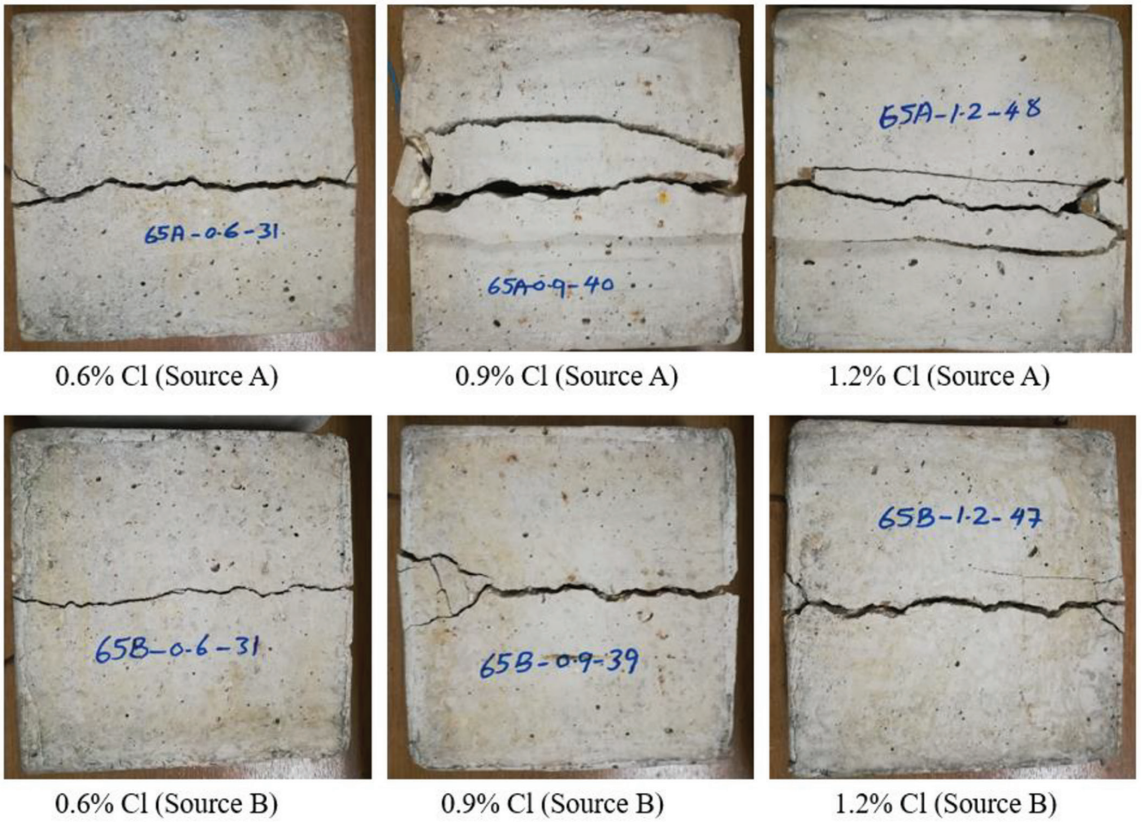

Fig. 7—Pictures of cracked specimens exposed to temperature of 65°C (149°F) at end of exposure period.

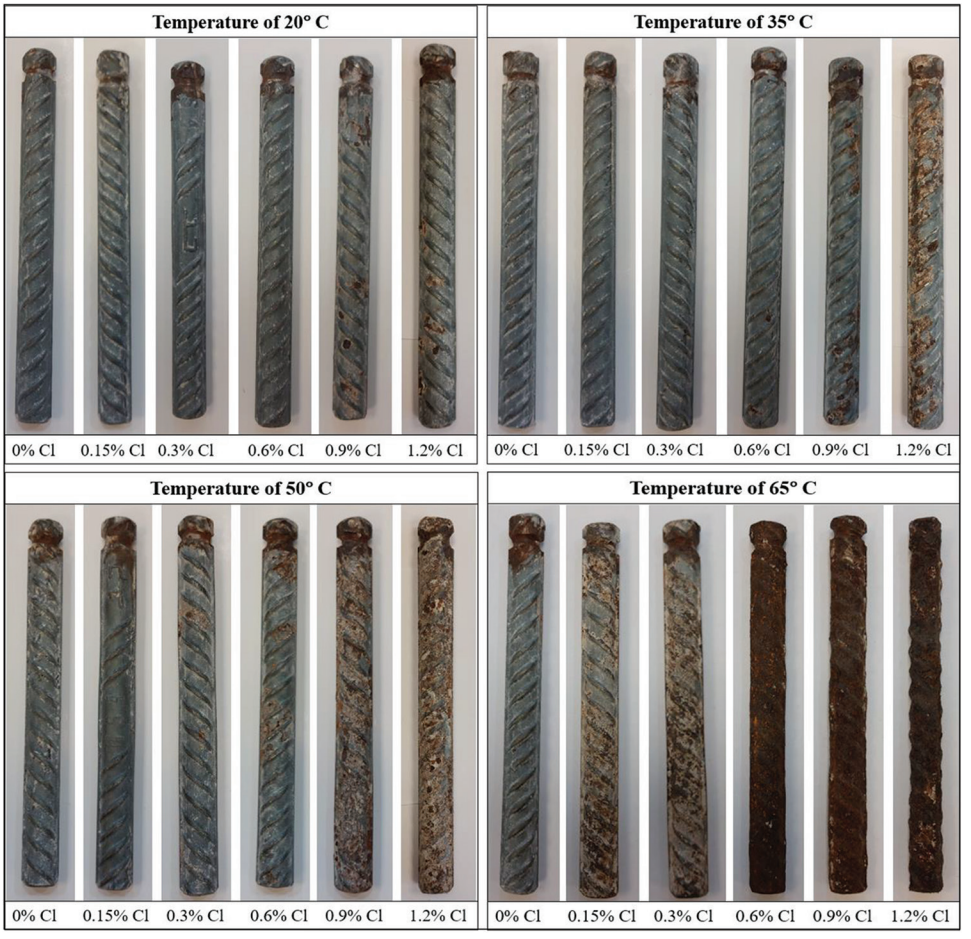

Fig. 8—Photos of reinforcing bars exposed to different temperatures and chloride contents (Source A).

Fig. 9—Photos of reinforcing bars exposed to different temperatures and chloride contents (Source B).

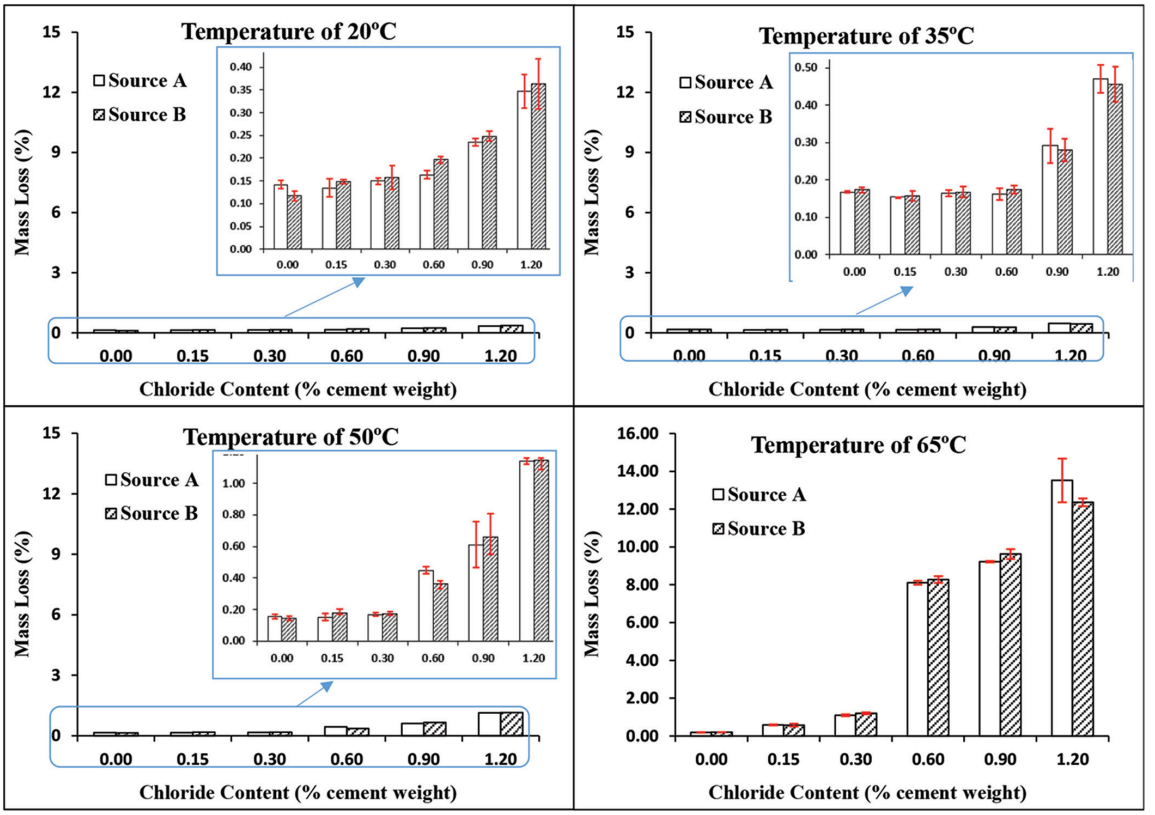

Fig. 10—Mass loss of reinforcing bars as percentages to original mass for both Sources A and B at different temperatures.

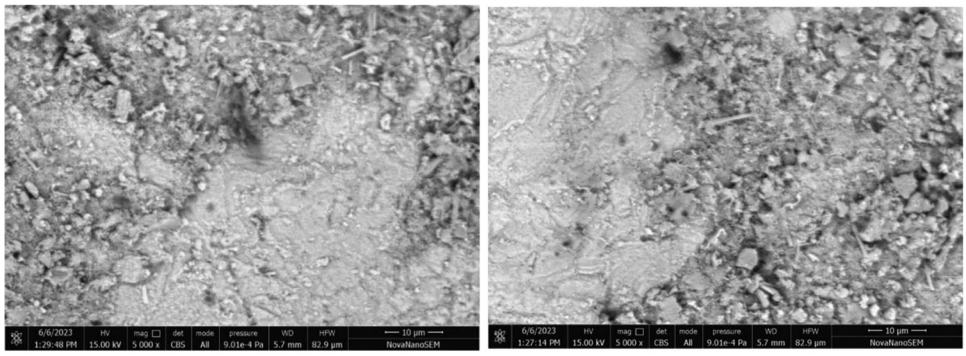

a) 20º C **b)** 35º C

Fig. 11—Morphology of film formed on surface of steel reinforcing bars of Source A at 0.60% Cl exposed to: (a) 20°C (68°F); and (b) 35°C (95°F).

concentration of 0.6% are presented in Fig. 11 for temperatures of 20 and 35°C (68 and 95°F). These results suggest that the nature of the film formed on the steel surface probably remained unchanged at these temperatures and low chloride contents (0.15 to 0.6%). To probe it further, the EDX analyses were performed for the film formed on the exposed steel reinforcing bars under the previously described conditions. The analysis results are recorded in Table 4.

It is pertinent to mention here that though the EDX analysis does not provide very accurate results, it certainly gives an idea about the approximate elements present in the tested materials. Interestingly, despite adding chloride content in concrete, chloride ions were unable to reach the steel surface exposed to temperatures of 20 and 35°C (68 and 95°F) (no chloride was detected on the surface; refer to Table 4) during the test period. It is reported that the natural passive film formed on the steel surface in chloride-free alkaline concrete pore solution is composed of maghemite (λ-Fe_2O_3) and magnetite (Fe_3O_4).[34,35] Theoretically, the iron and oxygen contents in these types of film are 70% and 30% (λ-Fe_2O_3), and 72% and 28% (Fe_3O_4), respectively. The data recorded in Table 4 are approximately in this range for oxygen and iron, indicating that chloride addition in concrete at these tested temperatures (20 and 35°C [68 and 95°F]) had no deteriorating effects on the natural passive film developed on the steel reinforcing bars' surface. In addition to these phases, $CaCO_3$ was also detected, indicating that portlandite from the concrete was also deposited on the reinforcing bars' surface. Interestingly, Ca content was considerably reduced with an increase in temperature from 20 to 35°C (68 and 95°F). It is known that the co-deposition of alkaline portlandite with phases of passive film strengthens its protective properties. To confirm it further, a small sample cut from the retrieved reinforcing bar from concrete blended with 0.6% chloride kept at 35°C (95°C) was subjected to phase analysis using X-ray diffraction (XRD). The results did not yield any peak, probably due to the very thin layer of film, which was below the limit of XRD sensitivity. The Raman spectroscopy, however, yielded the peaks of Raman shift, as shown in Fig. 12. The analyzed results indicate that the major peaks of maghemite (λ-Fe_2O_3) with some peaks of calcium carbonate are formed on the surface of the reinforcing bar.

Table 4—Elemental analysis of film formed on steel reinforcing bars of Source A at 20 and 35°C with chloride contents of 0.15 and 0.60%

	Chloride, %					
	0.15			0.60		
Temperature	Fe	O	Ca	Fe	O	Ca
20°C (68°F)	71.6	27.3	1.1	73.2	26.4	0.4
35°C (95°F)	73.1	25.4	1.5	70.8	28.6	0.6

These findings corroborate the results of SEM and EDX analysis recorded in Fig. 11 and Table 4, indicating the formation of an identical thin layer of maghemite with portlandite, which resisted the attack of chloride on the surface of reinforcing bars embedded in concrete.

Effect of higher temperature on morphology of corrosion products—Specimens with 1.2% of chloride content kept at 50 and 65°C (122 and 149°F) exhibited a thick crust of rust on the surface of exposed reinforcing bars. SEM and EDX analyses of corrosion products formed under the previous test conditions for the steel reinforcing bars of Source A were conducted. The microphotographs of corrosion products formed on the surface of reinforcing bars embedded in concrete with 1.2% chloride at 50°C (122°F) and with different concentrations of chloride kept at 65°C (149°F) are shown in Fig. 13 and 14. Because the addition of chloride below 1.2% at 50°C (122°F) did not exhibit visible rust, the detailed studies were performed only at 1.2% addition of chloride for 50°C (122°F) specimens and for the other sets of reinforcing bars embedded in 65°C (149°F) specimens with different concentrations of chloride. For comparison purposes, the magnification of images for all samples was fixed at 5000×.

Microphotographs shown in the previous figures exhibit different features with variations in chloride concentrations. It appears that different types of phases are formed in the layer of rust. The shapes of corrosion products deposited in the rust layer are considerably bigger in specimens with 1.2% chloride exposed to 65°C (149°F) than those noted for 50°C (122°F) specimens (Fig. 13 and 14(d)). EDX analysis of the rust was performed, and results are summarized in Table 5. It is seen from the data recorded in the table that element Ca, which probably came due to the co-deposition

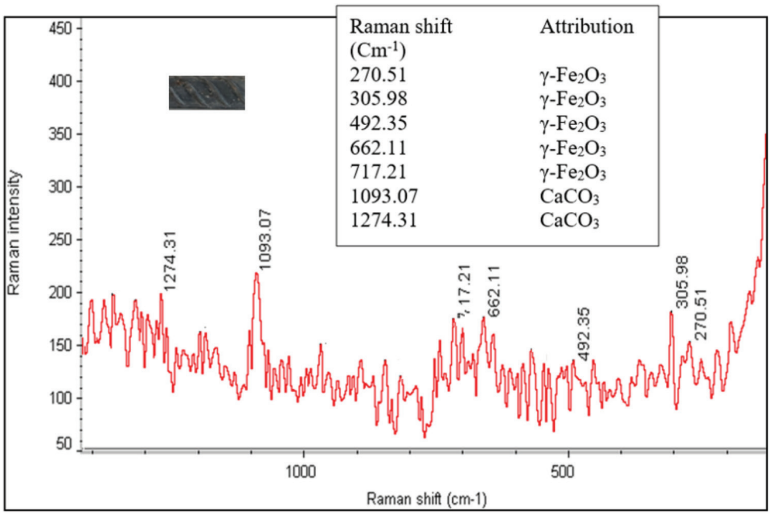

Fig. 12—Raman spectra of passive film formed on surface of steel reinforcing bars of Source A at 0.60% Cl and 35°C (95°F).

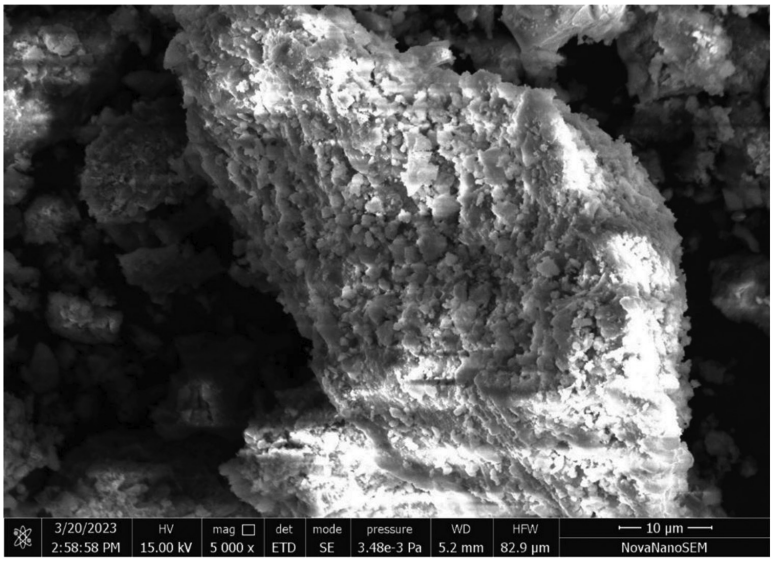

Fig. 13—Morphology of corrosion products formed on surface of steel reinforcing bars of Source A at 1.2% Cl and 50°C (122°F).

of portlandite in the rust layer, is detected in rust of 50°C (122°F) specimens (1.2% chloride) and in corrosion products formed in lower chloride concentrations (0.15 and 0.30%) of 65°C (149°F) specimens. However, it was not detected at higher chloride concentrations of 65°C (149°F) specimens. These facts suggest that elevated temperature and chloride content in concrete discouraged portlandite from getting adsorbed on the steel surface. Further, chloride content in rust is noted to increase with the rise in the addition of chloride in concrete (Table 5).

In view of very distinct differences in morphologies of rusts of 50 and 65°C (122 and 149°F) specimens with 1.2% chloride, it was considered important to identify the phases present in these two types of rusts. Raman spectra of the previous stated two types of rusts were collected and are shown in Fig. 15 and 16. Multiple phases of rust formed on the surface of both reinforcing bars are detected. Distinct peaks of hematite and a very strong peak of magnetite are detected in this rust. In the case of 65°C (149°F) with 1.20% chloride, the peaks of hematite disappeared. Very distinct peaks of lepidocrocite (λ-FeOOH), akageneite (β-FeOOH), magnetite, and a strong peak of quartz (1291.77 cm^{-1}) are detected. In this case, the absence of the akageneite phase of rust at 50°C (122°F) but its appearance in the rust formed at the higher temperature of 65°C (149°F) is a conspicuous observation and needs special attention. The akageneite form of rust is formed in the presence of higher contents of chloride in corroding media, and its formation is facilitated in the presence of certain cations and anions and decreased pH values.[36] The formation of this phase of rust may be attributed to increased diffusion of chloride in the pore solution, which was catalyzed by an increase in temperature from 50 to 65°C (122 to 149°F). It is interesting to note that though 1.2% chloride was present at 50°C (122°F) as well as at lower temperatures, the akageneite phase of rust was detected only when the temperature was increased to 65°C (149°F). This indicates that the diffusion of chloride at the corroding interface is predominantly controlled by temperature and not chloride concentration.

Corrosion initiation

Corrosion potential and corrosion current of steel reinforcing bars embedded in concrete are good indicators

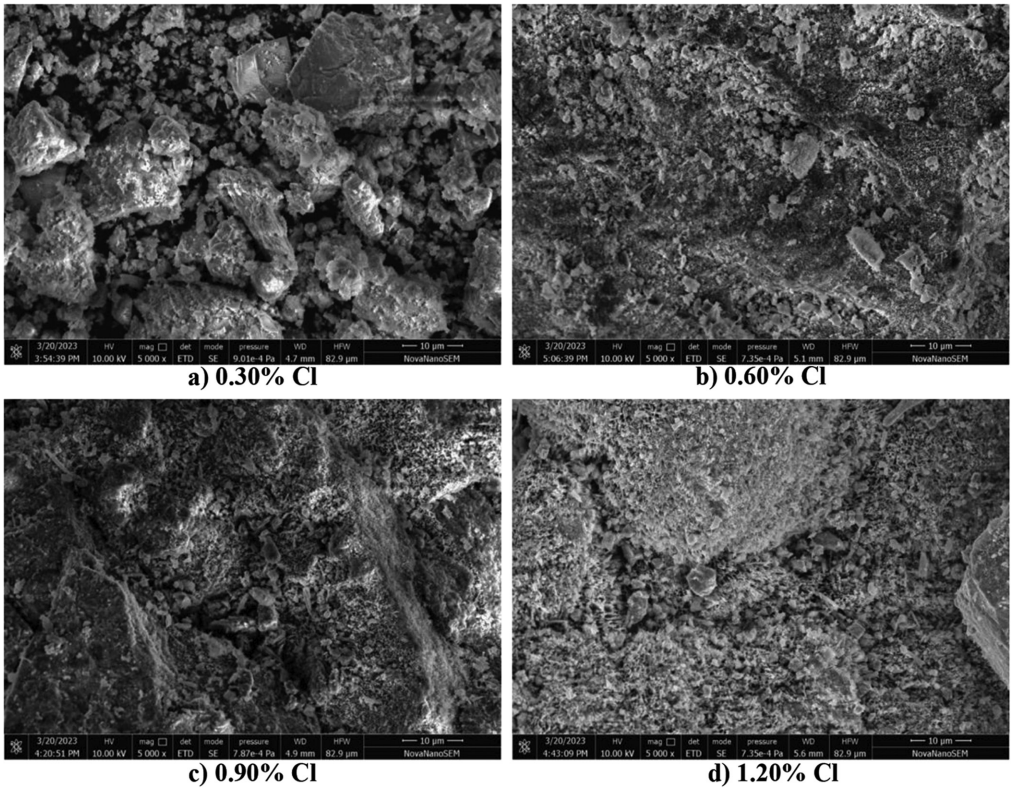

Fig. 14—Morphology of corrosion products formed on surface of steel reinforcing bars of Source A exposed to 65°C (149°F) at: (a) 0.30% Cl; (b) 0.60% Cl; (c) 0.90% Cl; and (d) 1.20% Cl.

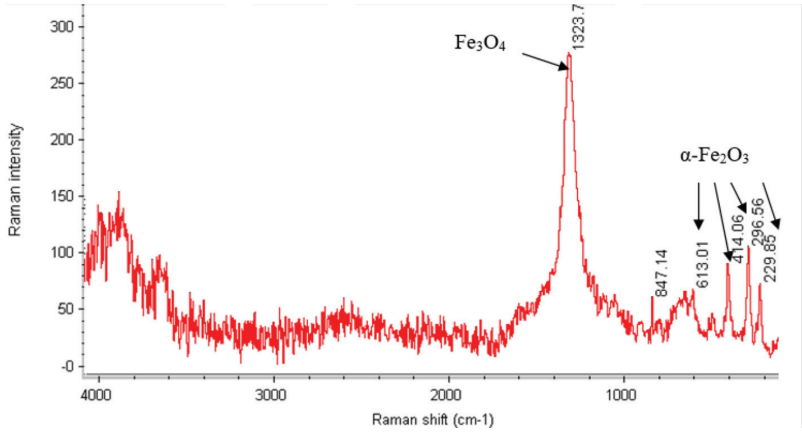

Fig. 15—Raman spectra of rust formed on steel reinforcing bars of Source A at 1.2% Cl and 50°C (122°F).

Table 5—Elemental analysis of film formed on steel reinforcing bars exposed to 50 and 65°C with different chloride contents

Temperature	Chloride, %				
	0.15	0.30	0.60	0.90	1.20
50°C (122°F)	—	—	—	—	Fe = 14.96 O = 51.92 Si = 7.66 Ca = 25.46
65°C (149°F)	Fe = 16.99 O = 51.08 Si = 5.80 Ca = 26.13	Fe = 11.28 O = 51.54 Si = 10.92 Ca = 26.26	Fe = 48.38 O = 50.94 Cl = 0.68	Fe = 55.06 O = 44.14 Cl = 0.80	Fe = 54.45 O = 44.54 Cl = 1.01

for corrosion initiation. In ASTM C876,[37] the probability of corrosion is more than 10% if the corrosion potential of the reinforcing bar is negatively greater than 200 mV versus copper sulfate electrode (CSE). If the corrosion potential of the reinforcing bar is negatively greater than 350 mV versus CSE, then the probability of corrosion is more than 90%. For corrosion rate, the steel reinforcing bars can be classified as passive if the corrosion rate is less than 0.1 μA/cm^2; the range values of 0.1 to 0.2 μA/cm^2 can be considered the transition zone between active and

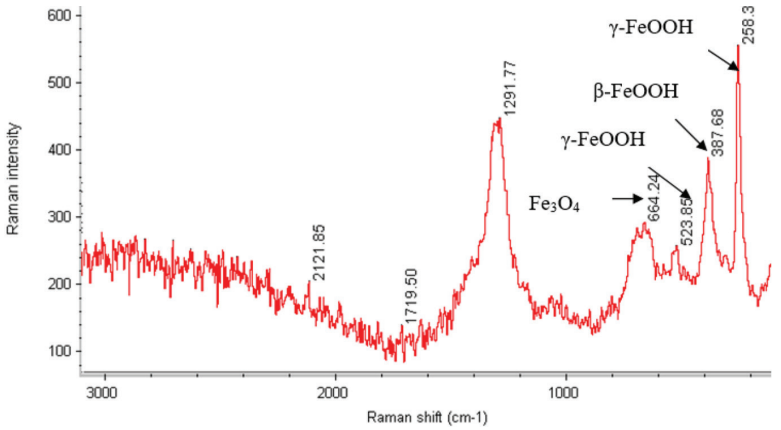

Fig. 16—Raman spectra of rust formed on steel reinforcing bars of Source A at 1.2% Cl and 65°C (149°F).

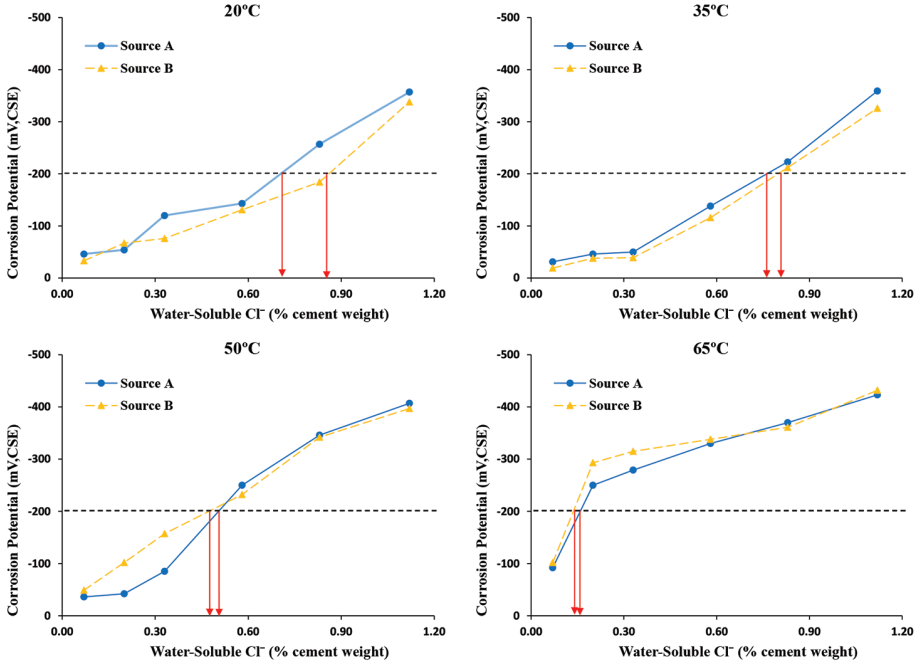

Fig. 17—Determination of CT values based on corrosion potential for different exposure temperatures.

passive corrosion.[38] The value of 0.1 μA/cm^2 is widely accepted in the literature to distinguish the corrosion activity zone from the passivity zone.[39-43] Mass loss can also be used to verify the depassivation of reinforcing bars embedded in concrete if they are exposed to an aggressive environment for long enough to allow the appearance of corrosion signs and the formation of corrosion products. The amount of mass loss of uncorroded reinforcing bars due to the oxidizing material used in cleaning reinforcing bars can be used as a criterion to identify the corrosion activity zone. This value of mass loss, which is called processing loss, varies according to the cleaning procedure adopted for removing corrosion dust from the reinforcing bars.

CT values based on corrosion potential—In this study, the criterion of 10% probability of corrosion adopted by ASTM C876 is used to establish the CT values for the steel reinforcing bars exposed to the four investigated temperatures (20, 35, 50, and 65°C [68, 95, 122, and 149°F]). The average corrosion potential values of the reinforcing bars of Sources A and B are plotted against the water-soluble chloride to predict the CT values for the four investigated temperatures, as shown in Fig. 17. It can be seen from this figure that the CT values are almost comparable for both sources of reinforcing bars at all investigated temperatures. Based on the adopted value of –200 mV CSE (the 10% probability of corrosion in ASTM C876), CT values, expressed as water-soluble chlorides, are determined and listed in Table 6 for both reinforcing bar sources.

CT values based on corrosion rate—The corrosion rate value of 0.1 μA/cm^2 is adopted in this paper to consider the corrosion initiation of carbon steel reinforcing bars embedded in concrete, as discussed earlier. The average corrosion rate values of steel reinforcing bars of Sources A and B are plotted against the water-soluble chloride to predict the CT values for the four investigated temperatures, as shown in Fig. 18. Similar to the results of corrosion potential, the figure shows that the CT values are approximately comparable for both sources of reinforcing bars at all investigated temperatures. The obtained CT values expressed as water-soluble chlorides are listed in Table 6 for both sources of reinforcing bars. The acid-soluble (commonly referred to as

Table 6—Water-soluble CT values based on corrosion potential, corrosion rate, and mass loss at different temperatures

Exposure temperature	Water-soluble CT values, % cement weight					
	Corrosion potential		Corrosion rate		Mass loss	
	Source A	Source B	Source A	Source B	Source A	Source B
20°C (68°F)	0.74	0.87	1.04	1.05	0.79	0.76
35°C (95°F)	0.78	0.81	0.96	1.00	0.72	0.73
50°C (122°F)	0.51	0.48	0.67	0.64	0.46	0.49
65°C (149°F)	0.14	0.13	0.18	0.18	0.11	0.12

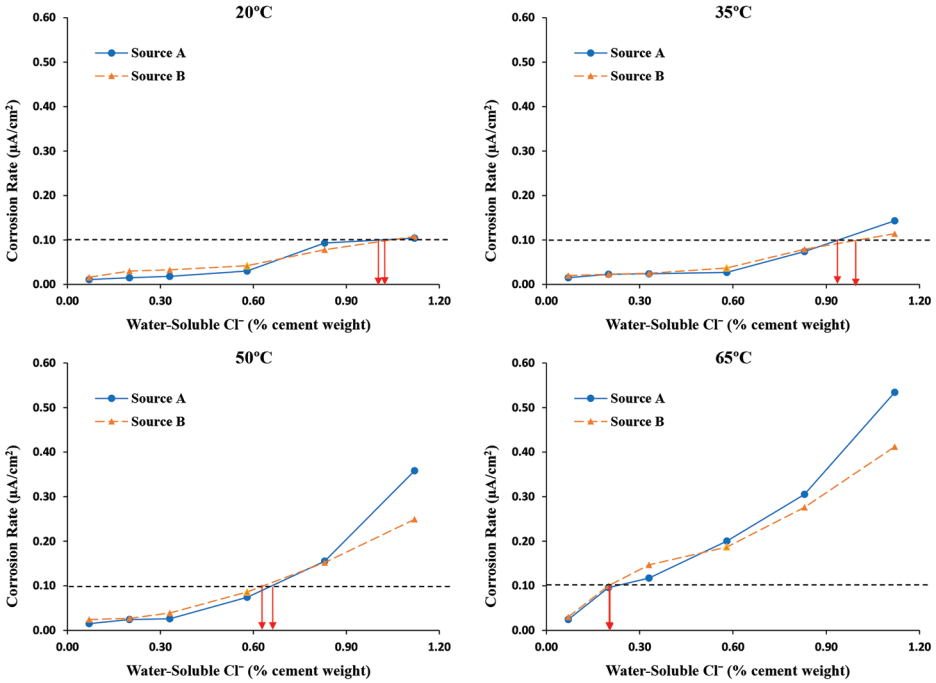

Fig. 18—Determination of CT values based on corrosion rate for different exposure temperatures.

total) CT values can be obtained from the water-soluble values using Eq. (2). The acid-soluble CT values of 1.22 and 1.24% by weight of cement for Sources A and B, respectively, at the normal temperature of 20°C (68°F) are similar to the total CT value of 1.24% obtained by Alonso et al.[40] and that of 1.10% by weight of cement obtained by Manera et al.[41] considering the same criterion of 0.1 μA/cm^2 used to distinguish the active corrosion region from the passive region.

CT values based on mass loss—The concept for determining the CT values based on the measurements of mass loss of corroded reinforcing bars and processing loss of uncorroded reinforcing bars is adopted from previous research.[44-46] To get a standard value for mass loss that can be considered as a criterion to distinguish passive steel reinforcing bars from corroded ones in this study, the cleaning procedure for removing corrosion products was applied to 16 uncorroded samples (the samples with zero added Cl in this study). The mean processing loss was 0.163% with a standard deviation of 0.026, and 0.158% with a standard deviation of 0.033 for reinforcing bar samples of Sources A and B, respectively. For simplicity, the overall average mass processing loss plus two times the standard deviation of all samples (0.16 + 0.06%) was chosen as a transition value between the uncorroded and corroded reinforcing bars for the purpose of determining the CT values of the reinforcing bars in this study. The criterion of using the mean processing loss plus twice the standard deviation was adopted based on the work of Thomas.[45] The mass loss values of all reinforcing bars are plotted against the water-soluble chloride to predict the CT values for the four investigated temperatures as shown in Fig. 19. Due to the high mass loss of reinforcing bars exposed to 65°C (149°F) at high added chlorides (0.6, 0.9, and 1.2%), only those with low chlorides (0, 0.15, and 0.3%) were considered to determine the CT values so that the scale on the vertical axis would be appropriate. It can be seen from this figure that there are two trends for the variation of mass loss with the variation of chloride content. First, the increase in chloride content does not affect the mass loss up to specified values of chloride content. Then, the increase in chloride content increases the mass loss of reinforcing bars in a linear trend. The abscissa of the intersection point between this trend line and the horizontal border line of the adopted mass loss transition value can be considered as the CT value for depassivation of steel reinforcing bars. The obtained CT values by this method at all investigated temperatures expressed as water-soluble chlorides are listed

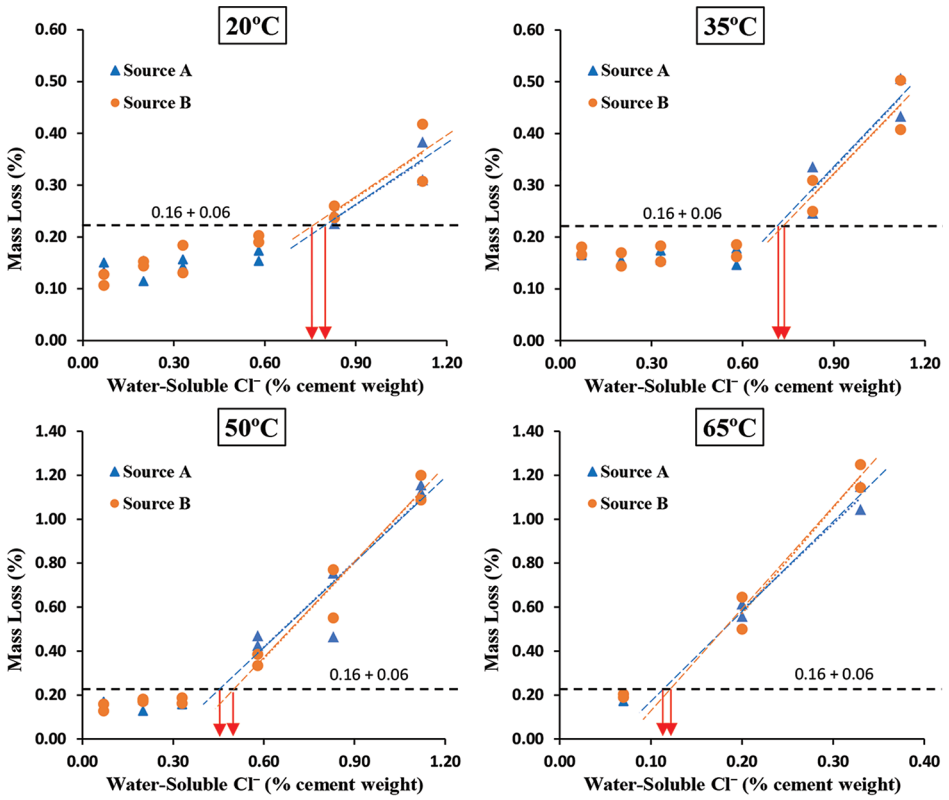

Fig. 19—Determination of CT values based on mass loss for different exposure temperatures.

in Table 6 for both reinforcing bar sources. The acid-soluble CT values obtained in the current study for 20°C (68°F) lay in between the two values of 0.70% and 0.96% by weight of cement found by Thomas[45] and Treadaway et al.,[44] respectively, under similar conditions, which validate the findings of this research.

The values obtained in Table 6 for the two reinforcing bar sources at the different examined temperatures are verified by the visual inspection of reinforcing bars presented in Fig. 8 and 9. For temperatures of 20 and 35°C (68 and 95°F), it can be seen from the photos of the reinforcing bars that there are no signs of corrosion for reinforcing bars with added chlorides up to 0.6% (0.58% water-soluble Cl). Clear signs of corrosion are seen on reinforcing bars with added chlorides of 0.9% (0.83% water-soluble Cl) and 1.2% for both reinforcing bars sources. This indicates that the CT value is in the range of 0.6 to 0.9%, which conforms to the values reported in Table 6. For a temperature of 50°C (122°F), signs of corrosion can be seen for reinforcing bars with added chlorides of 0.6% and higher for both reinforcing bar sources. On the other hand, no signs of corrosion for reinforcing bars with added chlorides of 0.3% (0.33% water-soluble Cl) and lower were observed. This indicates that the water-soluble CT value for 50°C (122°F) is in the range of 0.30 to 0.6%, which is consistent with the values reported in Table 6. The photos of the reinforcing bars exposed to 65°C (149°F) show signs of corrosion for added chloride of 0.15% (0.20% water-soluble Cl) and higher Cl contents. The only reinforcing bars that do not exhibit corrosion are those with zero added chloride, which indicates that the water-soluble CT value at this temperature should be in the range of 0.0 to 0.20% by weight of cement.

It is obvious from Table 6 that for every different method used to determine the CT values, the results are similar for both sources of steel reinforcing bars (A and B) at the same investigated temperature. It should be noted that the available literature data investigating the effect of metallurgy of steel reinforcement on the corrosion initiation in alkaline environments are limited, and the output results are contradictory, as reported by RILEM TC 262-SCI.[47] Nair and Pillai[48] found a slight difference in the CT values for coupon specimens cut from a tempered martensite periphery and a ferrite-pearlite core of a quenched and tempered steel reinforcing bar, which were immersed in simulated pore solutions (pH ≈ 13) with various chloride contents. The average CT values for the ferrite-pearlite specimens were slightly lesser (by approximately 10 to 15%) than for the tempered martensite specimens.

In this study, the effect of the metallurgy on the corrosion initiation was not significant. Therefore, the average CT values from both sources (A and B) are used in Fig. 20 to summarize the effect of temperature on the CT values. As shown in this figure, the CT values obtained by the corrosion potential are relatively lower than those obtained by the corrosion rate method, which is consistent with what was found by Xu et al.[49] for normal temperature. The CT values obtained by mass loss are the lowest. In general, the CT values decrease with the increase in temperature regardless of the method used. The increase in temperature from 20 to 65°C (68 to 149°F) causes a significant reduction in the CT value by approximately 80%, which is consistent with the results presented by Hussain et al.[22] The CT values obtained by the three methods at 65°C (149°F) have a particular significance because they are below the limits specified

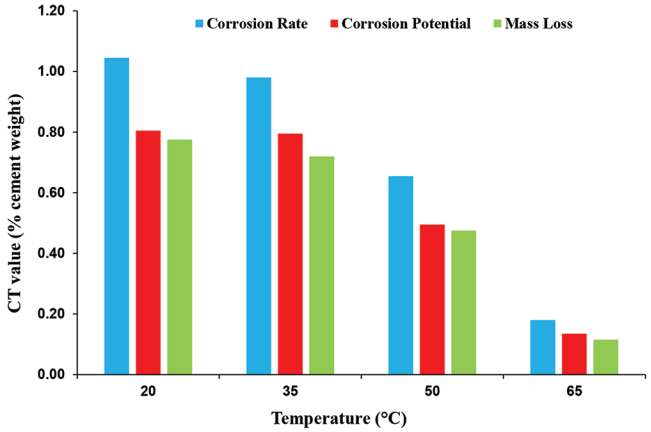

Fig. 20—Average water-soluble CT values versus temperature.

in most local and international codes, such as ACI 318[7] and SBC 304[50] for RC members, even those not exposed to an external source of chloride. This condition is very critical for RC structures in hot climate regions exposed to direct sun.

CONCLUSIONS

The effect of a tropical climate with high temperature and humidity on the chloride threshold (CT) value of carbon steel reinforcing bars in concrete was investigated. The following conclusions can be made based on the results reported in this paper:

- The CT value for corrosion of steel reinforcing bars in concrete displayed significant temperature dependency. The CT values obtained from corrosion potential, corrosion rate, and mass loss showed a consistent trend of lower values at higher temperatures.
- At temperatures of 50 and 65°C (122 and 149°F), a dramatic drop in CT values was observed from the results of the three measurement techniques, with the CT value at 65°C falling below the boundary limits specified in codes such as ACI 318 and SBC 304.
- Based on the results of mass loss, the average CT values, expressed as water-soluble chloride, are 0.77% at 20°C (68°F), 0.72% at 35°C (95°F), 0.47% at 50°C (122°F), and 0.12% at 65°C (149°F) by weight of cement.

The findings of this study highlight the need to reassess current code limits considering hot climates. It is recommended to investigate the effect of temperature on the CT value of steel reinforcement in concrete considering the use of supplementary cementitious materials, external sources of chloride, and different water-cementitious materials ratios.

AUTHOR BIOS

Mshtaq Ahmed *is a PhD Student in the Department of Civil Engineering at King Saud University, Riyadh, Saudi Arabia. His research interests include corrosion of steel in concrete, durability, and sustainability of concrete structures.*

Abdulrahman Alhozaimy *is a Professor in the Department of Civil Engineering and the Center of Excellence for Concrete Research and Testing at King Saud University. He received his PhD from Michigan State University, East Lansing, MI, in concrete materials and technology in 1993. His research interests include the durability and sustainability of concrete materials, especially corrosion.*

Abdulaziz Al-Negheimish *is a Professor in the Department of Civil Engineering and Executive Director of the Center of Excellence for Concrete Research and Testing at King Saud University. He received his BS and MS from the University of Michigan, Ann Arbor, MI, and his PhD from The University of Texas at Austin, Austin, TX, in 1988. His research interests include durability and sustainability of concrete construction and rehabilitation of concrete structures.*

Raja Rizwan Hussain *is a Professor in the Department of Civil Engineering and the Center of Excellence for Concrete Research and Testing at King Saud University. He received his PhD and MSc in civil engineering from the University of Tokyo, Tokyo, Japan. His research interests include the corrosion of steel-reinforced concrete.*

ACKNOWLEDGMENTS

This research was supported by Center of Excellence for Concrete Research and Testing (CoE-CRT), College of Engineering, King Saud University, Riyadh, Saudi Arabia.

REFERENCES

1. Rasheeduzzafar, M.; Al-Sulaimani, G.; Al-Gahtani, A.; and Al-Saadoun, S., "An Overview of Concrete Reinforcement Corrosion Research At KFUPM," *Arabian Journal for Science and Engineering*, V. 14, No. 2, 1989, pp. 219-233.

2. Walker, M., "The General Problems for Reinforced Concrete in the Gulf Region and the Use of Design Life and Life Cycle Costing to Justify Improvements," *Proceedings of the First International Conference on Deterioration and Repair of Reinforced Concrete in the Arabian Gulf*, 1985, pp. 1-11.

3. RILEM Committee 2-HC, "Concrete and Reinforced Concrete in Hot Countries," *Materials and Structures*, V. 11, 1978, pp. 127-131.

4. RILEM Committee 2-HC, "Concrete and Reinforced Concrete in Hot Countries," *Materials and Structures*, V. 13, 1980, pp. 255-258.

5. Simms, J., and Fookes, P., "Improving Reinforced Concrete Durability in the Middle East During the Period 1960–1985: An Analytical Review," *Proceedings of the Institution of Civil Engineers*, 1989, pp. 333-358.

6. EN 206, "Béton – Spécification, Performances, Production et Conformité," European Committee for Standardization, Brussels, Belgium, 2014.

7. ACI Committee 318, "Building Code Requirement for Structural Concrete (ACI 318-19) and Commentary (ACI 318R-19) (Reapproved 2022)," American Concrete Institute, Farmington Hills, MI, 2019, 624 pp.

8. Page, C., and Treadaway, K., "Aspects of the Electrochemistry of Steel in Concrete," *Nature*, V. 297, No. 5862, 1982, pp. 109-115. doi: 10.1038/297109a0

9. Schiessl, P., and Raupach, M., "Influence of Concrete Composition and Microclimate on the Critical Chloride Content in Concrete," *Corrosion of Reinforcement in Concrete: Proceedings of the Third International Symposium on Corrosion of Reinforcement in Concrete Construction*, C. L. Page, K. W. J. Treadaway, and P. B. Bamforth, eds., Wishaw, Warwickshire, UK, 1990, pp. 49-58.

10. Jaegerman, C. H.; Raveena, D.; and Pundak, B., "Accelerated Curing of Concrete by Solar Radiation," *Proceedings of International RILEM Symposium on Concrete and Reinforced Concrete in Hot Countries*, V. 2, Haifa, Israel, 1971, pp. 339-362.

11. Chestovich, P. J.; Saroukhanoff, R. Z.; Moujaes, S. F.; Flores, C. E.; Carroll, J. T.; and Saquib, S. F., "Temperature Profiles of Sunlight-Exposed Surfaces in a Desert Climate: Determining the Risk for Pavement Burns," *Journal of Burn Care and Research*, V. 44, No. 2, 2023, pp. 438-445. doi: 10.1093/jbcr/irac136

12. López, W.; González, J. A.; and Andrade, C., "Influence of Temperature on the Service Life of Rebars," *Cement and Concrete Research*, V. 23, No. 5, 1993, pp. 1130-1140. doi: 10.1016/0008-8846(93)90173-7

13. Andrade, C.; Alonso, C.; and Sarría, J., "Corrosion Rate Evolution in Concrete Structures Exposed to the Atmosphere," *Cement and Concrete Composites*, V. 24, No. 1, 2002, pp. 55-64. doi: 10.1016/S0958-9465(01)00026-9

14. Liu, T., and Weyers, R. W., "Modeling the Dynamic Corrosion Process in Chloride Contaminated Concrete Structures," *Cement and Concrete Research*, V. 28, No. 3, 1998, pp. 365-379. doi: 10.1016/S0008-8846(98)00259-2

15. Jiang, J. H., and Yuan, Y. S., "Development and Prediction Strategy of Steel Corrosion Rate in Concrete Under Natural Climate," *Construction and Building Materials*, V. 44, 2013, pp. 287-292. doi: 10.1016/j.conbuildmat.2013.03.033

16. Michel, A.; Nygaard, P. V.; and Geiker, M. R., "Experimental Investigation on the Short-Term Impact of Temperature and Moisture on Reinforcement Corrosion," *Corrosion Science*, V. 72, 2013, pp. 26-34. doi: 10.1016/j.corsci.2013.02.006

17. Qiu, J.; Li, Y.; Xu, Y.; Wu, A.; and Macdonald, D. D., "Effect of Temperature on Corrosion of Carbon Steel in Simulated Concrete Pore Solution Under Anoxic Conditions," *Corrosion Science*, V. 175, 2020, p. 108886. doi: 10.1016/j.corsci.2020.108886

18. Xia, S.; Luo, Y.; Li, Y.; Liu, W.; Ding, X.; and Tang, L., "Effects of Temperature on Corrosion Behavior of Reinforcements in Simulated Sea-Sand Concrete Pore Solution," *Buildings*, V. 12, No. 4, 2022, p. 407. doi: 10.3390/buildings12040407

19. Živica, V.; Krajči, L.; Bágel', L.; and Vargová, M., "Significance of the Ambient Temperature and the Steel Material in the Process of Concrete Reinforcement Corrosion," *Construction and Building Materials*, V. 11, No. 2, 1997, pp. 99-103. doi: 10.1016/S0950-0618(97)00001-9

20. Alhozaimy, A.; Hussain, R. R.; Al-Zaid, R.; and Al-Negheimish, A., "Coupled Effect of Ambient High Relative Humidity and Varying Temperature Marine Environment on Corrosion of Reinforced Concrete," *Construction and Building Materials*, V. 28, No. 1, 2012, pp. 670-679. doi: 10.1016/j.conbuildmat.2011.10.008

21. Cheng, L., and Maruyama, I., "Effect of Relative Humidity and Temperature on Steel Corrosion Rate in Chloride Contaminated Mortar," *Cement Science and Concrete Technology*, V. 75, No. 1, 2022, pp. 225-232. doi: 10.14250/cement.75.225

22. Hussain, S. E.; Rasheeduzzafar; Al-Musallam, A.; and Al-Gahtani, A. S., "Factors Affecting Threshold Chloride for Reinforcement Corrosion in Concrete," *Cement and Concrete Research*, V. 25, No. 7, 1995, pp. 1543-1555. doi: 10.1016/0008-8846(95)00148-6

23. Matsumura, T.; Shirai, K.; and Saegusa, T., "Verification Method for Durability of Reinforced Concrete Structures Subjected to Salt Attack Under High Temperature Conditions," *Nuclear Engineering and Design*, V. 238, No. 5, 2008, pp. 1181-1188. doi: 10.1016/j.nucengdes.2007.03.032

24. Gastaldi, M., and Bertolini, L., "Effect of Temperature on the Corrosion Behaviour of Low-Nickel Duplex Stainless Steel Bars in Concrete," *Cement and Concrete Research*, V. 56, 2014, pp. 52-60. doi: 10.1016/j.cemconres.2013.11.004

25. Alhozaimy, A. M.; Ahmed, M.; Hussain, R. R.; and Al-Negheimish, A., "Quantitative Non-Linear Effect of High Ambient Temperature on Chloride Threshold Value for Steel Reinforcement Corrosion in Concrete Under Extreme Boundary Conditions," *Materials*, V. 14, No. 24, 2021, p. 7595. doi: 10.3390/ma14247595

26. ASTM C1218/C1218M-15, "Standard Test Method for Water-Soluble Chloride in Mortar and Concrete," ASTM International, West Conshohocken, PA, 2015.

27. ASTM C1152/C1152M-04(2012)e1, "Standard Test Method for Acid-Soluble Chloride in Mortar And Concrete," ASTM International, West Conshohocken, PA, 2012.

28. Neville, A., "Chloride Attack of Reinforced Concrete: An Overview," *Materials and Structures*, V. 28, No. 2, 1995, pp. 63-70. doi: 10.1007/BF02473172

29. ASTM G1-03(2017)e1, "Standard Practice for Preparing, Cleaning, and Evaluating Corrosion Test Specimens," ASTM International, West Conshohocken, PA, 2017.

30. Mohammed, T. U., and Hamada, H., "Relationship Between Free Chloride and Total Chloride Contents in Concrete," *Cement and Concrete Research*, V. 33, No. 9, 2003, pp. 1487-1490. doi: 10.1016/S0008-8846(03)00065-6

31. Alhozaimy, A.; Hussain, R. R.; and Al-Negheimish, A., "Significance of Oxygen Concentration on the Quality of Passive Film Formation for Steel Reinforced Concrete Structures During the Initial Curing of Concrete," *Cement and Concrete Composites*, V. 65, 2016, pp. 171-176. doi: 10.1016/j.cemconcomp.2015.10.022

32. Hussain, R. R.; Alhozaimy, A. M.; and Al-Negheimish, A., "Effect of Curing Compounds on the Quality Of Passive Layer Development Under Varying Oxygen Concentration for RC Structures in the Course of Early Curing of Concrete," *Construction and Building Materials*, V. 350, 2022, p. 128842. doi: 10.1016/j.conbuildmat.2022.128842

33. Wasim, M.; Ngo, T. D.; and Abid, M., "Investigation of Long-Term Corrosion Resistance of Reinforced Concrete Structures Constructed With Various Types of Concretes in Marine and Various Climate Environments," *Construction and Building Materials*, V. 237, 2020, p. 117701. doi: 10.1016/j.conbuildmat.2019.117701

34. Yonezawa, T.; Ashworth, V.; and Procter, R. P. M., "Pore Solution Composition and Chloride Effects on the Corrosion of Steel in Concrete," *Corrosion*, V. 44, No. 7, 1988, pp. 489-499. doi: 10.5006/1.3583967

35. Alhozaimy, A.; Hussain, R. R.; Al-Negheimish, A.; Al-Zaid, R.; and Singh, D. D. N., "Effect of Simulated Concrete Pore Solution Chemistry, Chloride Ions, and Temperature on Passive Layer Formed on Steel Reinforcement," *ACI Materials Journal*, V. 111, No. 4, July-Aug. 2014, pp. 411-422. doi: 10.14359/51686829

36. Misawa, T.; Hashimoto, K.; and Shimodaira, S., "The Mechanism of Formation of Iron Oxides and Hydroxides in Aqueous Solutions at Room Temperature," *Corrosion Science*, V. 14, No. 2, 1974, pp. 131-149.

37. ASTM C876-15, "Standard Test Method for Corrosion Potentials of Uncoated Reinforcing Steel in Concrete," ASTM International, West Conshohocken, PA, 2015.

38. RILEM TC-154-EMC; Andrade, C.; Alonso, C.; Gulikers, J.; Polder, R. B.; Cigna, R.; Vennesland, Ø.; and Salta, M., "Electrochemical Techniques for Measuring Metallic Corrosion: Test Methods for On-Site Corrosion Rate Measurement of Steel Reinforcement in Concrete by Means of the Polarization Resistance Method," *Materials and Structures*, V. 37, No. 273, 2004, pp. 623-643.

39. González, J., and Andrade, C., "Effect of Carbonation and Relative Ambient Humidity on the Corrosion of Galvanised Rebars Embedded in Concrete," *British Corrosion Journal*, V. 17, No. 1, 1982, pp. 21-28. doi: 10.1179/000705982798274589

40. Alonso, C.; Andrade, C.; Castellote, M.; and Castro, P., "Chloride Threshold Values to Depassivate Reinforcing Bars Embedded in a Standardized OPC Mortar," *Cement and Concrete Research*, V. 30, No. 7, 2000, pp. 1047-1055. doi: 10.1016/S0008-8846(00)00265-9

41. Manera, M.; Vennesland, Ø.; and Bertolini, L., "Chloride Threshold for Rebar Corrosion in Concrete With Addition of Silica Fume," *Corrosion Science*, V. 50, No. 2, 2008, pp. 554-560. doi: 10.1016/j.corsci.2007.07.007

42. Bouteiller, V.; Cremona, C.; Baroghel-Bouny, V.; and Maloula, A., "Corrosion Initiation of Reinforced Concretes Based on Portland or GGBS Cements: Chloride Contents and Electrochemical Characterizations Versus Time," *Cement and Concrete Research*, V. 42, No. 11, 2012, pp. 1456-1467. doi: 10.1016/j.cemconres.2012.07.004

43. Figueira, R. B.; Sadovski, A.; Melo, A. P.; and Pereira, E. V., "Chloride Threshold Value to Initiate Reinforcement Corrosion in Simulated Concrete Pore Solutions: The Influence of Surface Finishing and pH," *Construction and Building Materials*, V. 141, 2017, pp. 183-200. doi: 10.1016/j.conbuildmat.2017.03.004

44. Treadaway, K. W. J.; Cox, R. N.; and Brown, B. L., "Durability of Corrosion Resisting Steels in Concrete," *Proceedings of the Institution of Civil Engineers*, V. 86, No. 2, 1989, pp. 305-331. doi: 10.1680/iicep.1989.1628

45. Thomas, M., "Chloride Thresholds in Marine Concrete," *Cement and Concrete Research*, V. 26, No. 4, 1996, pp. 513-519. doi: 10.1016/0008-8846(96)00035-X

46. Reou, J. S., and Ann, K. Y., "Electrochemical Assessment on the Corrosion Risk of Steel Embedment in OPC Concrete Depending on the Corrosion Detection Techniques," *Materials Chemistry and Physics*, V. 113, No. 1, 2009, pp. 78-84. doi: 10.1016/j.matchemphys.2008.07.063

47. Angst, U. M.; Geiker, M. R.; Alonso, M. C.; Polder, R.; Isgor, O. B.; and Elsener, B., Wong, H.; Michel, A.; Hornbostel, K.; Gehlen, C.; François, R.; Sanchez, M.; Criado, M.; Sørensen, H.; Hansson, C.; Pillai, R.; Mundra, S.; Gulikers, J.; Raupach, M.; Pacheco, J.; and Sagüés, A., "The Effect of the Steel–Concrete Interface on Chloride-Induced Corrosion Initiation in Concrete: A Critical Review by RILEM TC 262-SCI," *Materials and Structures*, V. 52, No. 4, 2019, pp. 1-25. doi: 10.1617/s11527-019-1387-0

48. Nair, S. A., and Pillai, R. G., "Microstructural and Corrosion Characteristics of Quenched and Self-Tempered (QST) Steel Reinforcing Bars," *Construction and Building Materials*, V. 231, 2020, p. 117109. doi: 10.1016/j.conbuildmat.2019.117109

49. Xu, J.; Jiang, L.; and Wang, J., "Influence of Detection Methods on Chloride Threshold Value for the Corrosion of Steel Reinforcement," *Construction and Building Materials*, V. 23, No. 5, 2009, pp. 1902-1908. doi: 10.1016/j.conbuildmat.2008.09.011

50. SBC 304, "Building Code Requirements for Structural Concrete (SBC 304-18: Code)," Saudi Building Code National Committee, Riyadh, Saudi Arabia, 2018.

ACI MATERIALS JOURNAL

The American Concrete Institute (ACI) is a leading authority and resource worldwide for the development and distribution of consensus-based standards and technical resources, educational programs, and certifications for individuals and organizations involved in concrete design, construction, and materials, who share a commitment to pursuing the best use of concrete.

Individuals interested in the activities of ACI are encouraged to explore the ACI website for membership opportunities, committee activities, and a wide variety of concrete resources. As a volunteer member-driven organization, ACI invites partnerships and welcomes all concrete professionals who wish to be part of a respected, connected, social group that provides an opportunity for professional growth, networking, and enjoyment.

American Concrete Institute